Inaugural dissertation

for

obtaining the doctoral degree

of the

Combined Faculty of Mathematics, Engineering and Natural Sciences

of the

Ruprecht - Karls - University

Heidelberg

Presented by

M. Sc. Liesa-Marie Pilger

born in Bad Kreuznach, Germany

Oral examination: July 30th, 2026

Investigation of brain metastasis infiltrating T cells and mechanisms of T cell suppression within the brain metastatic tumor microenvironment

Referees:

Prof. Dr. Peter Angel

Prof. Dr. Peter Lichter

Abstract

Brain metastases (BrM) show limited responses to immunotherapy, raising the question of whether these lesions lack tumor-reactive T cells or whether local anti-tumor immunity is actively constrained. In this thesis, I characterized the T cell compartment of BrM from non-small cell lung cancer (NSCLC) by combining single-cell RNA and paired T cell receptor (TCR) sequencing, matched peripheral blood T cell analysis, functional *in vitro* assays, and multiplexed spatial imaging across independent patient cohorts.

Single-cell profiling revealed $CD103^+$ tissue-resident memory (T_{RM}) $CD8^+$ T cells that exhibited pronounced clonal expansion and transcriptional features consistent with chronic antigen exposure, whereas $CD103^-$ T cells were largely non-expanded and displayed a transcriptional memory profile. Tumor reactivity was assessed by candidate TCRs tested against autologous tumor material. Thereby, I identified a tumor-reactive TCR derived from a $CD103^+$ T cell population, providing direct evidence for the presence of tumor-specific tissue resident T cells in brain metastases. In contrast, a virus-reactive TCR was identified from a $CD103^-$ T cell population.

Spatial analyses demonstrated a clear segregation of these populations: $CD103^+$ T cells were preferentially located within tumor cell-rich regions, whereas $CD103^-$ T cells predominantly resided in the surrounding stroma. In addition, T cell extravasation from the vasculature and subsequent infiltration into the tumor parenchyma was partially restricted by a preserved blood-brain barrier and the tumor-stroma interface. Within the stromal compartment, T cells were further subject to local immunosuppression by IL4I1-expressing pro-tumorigenic macrophages and activated T_{REGs}, which were observed in close proximity to $CD8^+$ T cells and may mediate suppressive effects via the granzyme B/perforin axis.

Collectively, these findings suggest that brain metastases harbor spatially and functionally distinct T cell populations, with clonally expanded $CD103^+$ T cells representing a tumor-reactive intratumoral compartment. However, their anti-tumor reactivity is likely locally constrained by physical barriers and suppressive cell interactions. These results indicate that anti-tumor immunity in BrM is not absent but spatially restricted and functionally constrained.

Zusammenfassung

Hirnmetastasen sprechen nur begrenzt auf Immuntherapien an, was die Frage aufwirft, ob diesen Läsionen tumorreaktive T Zellen fehlen oder ob die lokale Antitumorimmunität aktiv unterdrückt wird. In dieser Arbeit habe ich das T Zell-Kompartiment von Hirnmetastasen des nicht-kleinzelligen Lungenkarzinoms charakterisiert, indem ich Einzelzell-RNA-Sequenzierung und gepaarte T Zell-Rezeptor-Sequenzierung mit der Analyse von T Zellen aus dem peripheren Blut, funktionellen In-vitro-Assays sowie multiplexer räumlicher Bildgebung über unabhängige Patientenkohorten hinweg kombiniert habe.

Durch die Einzelzell-RNA-Sequenzierung wurden $CD103^+$ gewebsresidente $CD8^+$ T Zellen identifiziert, die eine ausgeprägte klonale Expansion und Transkriptionsmerkmale aufwiesen, die mit einer chronischen Antigenexposition übereinstimmen. Im Gegensatz dazu waren $CD103^-$ T Zellen weitgehend nicht expandiert und zeigten ein transkriptionelles Gedächtnisprofil. Die Tumorreaktivität wurde anhand ausgewählter TCRs gegenüber autologem Tumormaterial getestet. Dabei konnte ich einen tumorreaktiven TCR identifizieren, der von einer $CD103^+$ T Zellpopulation stammte, was einen direkten Nachweis für das Vorhandensein tumorspezifischer gewebsresidenter T Zellen in Hirnmetastasen liefert. Im Gegensatz dazu wurde aus einer $CD103^-$ Population ein virusreaktiver TCR identifiziert.

Räumliche Analysen zeigten eine deutliche Trennung dieser Populationen: $CD103^+$ T Zellen befanden sich vorwiegend in tumorzellreichen Bereichen, während $CD103^-$ T Zellen überwiegend im umgebenden Stroma lokalisiert waren. Zudem war die Extravasation von T Zellen aus dem Gefäßsystem und deren anschließende Infiltration in das Tumorparenchym teilweise eingeschränkt, was mit einer teilweise erhaltenen Blut-Hirn-Schranke sowie der Tumor-Stroma-Grenze assoziiert war. Innerhalb des Stromakompartments waren T Zellen zudem einer lokalen Immunsuppression ausgesetzt, zum einen durch pro-tumorigene, IL4I1-exprimierenden Makrophagen und zum anderen durch aktivierte T_{REGs}, die in enger räumlicher Nähe zu $CD8^+$ T Zellen beobachtet wurden und möglicherweise suppressive Effekte über die Granzyme-B/Perforin-Achse vermitteln.

Zusammengenommen zeigen diese Ergebnisse, dass Hirnmetastasen räumlich und funktionell unterschiedliche T Zell-Populationen beherbergen. Insbesondere definieren klonal expandierte $CD103^+$ T Zellen ein tumorreaktives, intratumorales Kompartiment.

Allerdings sprechen die Daten dafür, dass deren Tumorreaktivität lokal durch physische Barrieren und suppressive Zellinteraktionen eingeschränkt ist. Diese Ergebnisse deuten darauf hin, dass die Antitumorimmunität in Hirnmetastasen nicht fehlt, sondern räumlich und funktionell eingeschränkt ist.

Table of contents

List of figures i

List of tables ii

List of appendix figures ii

List of abbreviations (A-Z) iii

1. Introduction 1

1.1. The role of the immune system in cancer 1

1.1.1. Cancer cell recognition by T cells 3

1.2. Epidemiology and clinical burden of lung cancer 9

1.2.1. The Mechanisms of metastasis and brain tropism 10

1.2.2. Brain metastases and the brain metastatic niche 12

1.2.3. T cell infiltration into brain metastases 13

1.2.4. Treatment of lung cancer and brain metastases 14

2. Aims of the thesis 18

2.1. Characterization of the T cell landscape in NSCLC brain metastases 18

2.2. Functional assessment of tumor-reactive T cells 18

2.3. Spatial organization and regulation of T cells in the metastatic microenvironment 19

3. Materials and methods 21

3.1. Materials 21

3.1.1. Human fresh frozen single cell suspension samples 21

3.1.2. Human FFPE tissue samples 22

3.1.3. Antibodies and oligonucleotides 23

3.1.4. Primers 28

3.1.5. Chemicals and reagents 28

3.1.6. Buffers, solutions and media 30

3.1.7. Kits 31

3.1.8. Consumables 32

3.1.9. Equipment and devices 33

3.1.10. Software 35

3.2. Methods 36

3.2.1. Single-cell transcriptome and TCR analysis 36
3.2.2. Bulk-TCRβ sequencing 49
3.2.3. Generation of TCR-transgenic cells 50
3.2.4. TCR validation by co-culture of tumor cells with TCR-transgenic Jurkat reporter cells 54
3.2.5. TCR validation by co-culture of tumor cells with TCR-transgenic autologous T cells 57
3.2.6. Multiplexed tissue imaging using co-detection by indexing (CODEX) 62
3.2.7. Author contributions and collaborations 64

4. Results 67

4.1. Single-cell profiling of the transcriptomic landscape and TCR repertoire of brain metastases-infiltrating T cells 67

4.1.1. Distinct transcriptional T cell phenotypes in NSCLC brain metastases 68
4.1.2. $CD4^+$ T cells in NSCLC brain metastases comprise distinct memory, regulatory, and helper subsets 70
4.1.3. Distinct differentiation states and tissue-resident subsets define the $CD8^+$ T cell compartment in NSCLC brain metastases 72
4.1.4. Clonal expansion is enriched in tissue-resident $CD8^+$ T cell subsets in NSCLC brain metastases 74
4.1.5. Low clonal expansion in peripheral blood T cells contrasts with the tumor-infiltrating compartment 77
4.1.6. Heterogeneous and limited TCR sharing between brain metastasis-infiltrating and peripheral blood T cells 80

4.2. Functional validation of tumor reactivity of selected TCRs from brain metastases-infiltrating T cells 82

4.2.1. Selection and characterization of candidate TCR clonotypes for functional testing 83

4.3. Spatial organization of T cell populations in brain metastases 94

4.3.1. Design and application of a high-dimensional CODEX panel for spatial profiling of brain metastases 96
4.3.2. Spatial heterogeneity of immune infiltration in human brain metastases 99
4.3.3. Spatially defined barriers to T cell infiltration and function in brain metastases 101
4.3.4. Macrophage-driven T cell suppression and T_{REG} induced $CD8^+$ T cell apoptosis 104

4.3.5. Spatial analysis of tertiary lymphoid-like structures in brain metastases 106

5. Discussion 111

5.1. Spatial organization of the brain metastatic niche constrains T cell access and function 112

5.1.1. Heterogeneous vascular remodeling enables but spatially restricts immune cell entry into brain metastases 112

5.1.2. Structural barriers at the tumor-stroma interface restrict T cell infiltration into the metastatic parenchyma 113

5.1.3. Myeloid and regulatory T cells contribute to suppression of infiltrating T cells in the tumor stroma 115

5.2. Clonally expanded CD103$^+$ tissue-resident T cells define a spatially localized and tumor-reactive T cell compartment in NSCLC brain metastases 117

5.2.1. Functional validation reveals tumor-reactive TCRs within the CD103$^+$ T_{RM} compartment but highlights technical and biological constraints.....119

5.3. Integrated analysis of TCR repertoire and lymphoid architecture supports localized T cell immunity in NSCLC brain metastases 122

5.3.1. Differential TCR repertoire overlap between peripheral blood and brain metastases suggests localized T cell responses 122

5.3.2. TLS-like structures suggest local T cell activation within NSCLC brain metastases 125

6. Conclusion and Perspectives 128

6.1. Summary of findings.....128

6.2. Therapeutic perspectives and future directions 131

7. Appendix.....134

8. List of publications 137

9. References 138

10. Acknowledgements.....154

List of figures

Figure 1: Experimental workflow for single-cell profiling and functional analysis of T cells. 68

Figure 2: Single-cell transcriptomic landscape of brain metastases (BrM)-infiltrating T cells. 69

Figure 3: Sub-clustering of $CD4^+$ brain metastases (BrM)-infiltrating T cells. 71

Figure 4: Sub-clustering of $CD8^+$ brain metastases (BrM)-infiltrating T cells. 73

Figure 5: Clonal architecture of brain metastases (BrM)-infiltrating T cells. 76

Figure 6: Single-cell transcriptomic and clonal profiling of peripheral blood (PB) T cells…79

Figure 7: Limited and heterogeneous TCR sharing between brain metastasis-infiltrating and peripheral blood T cells 81

Figure 8: Workflow for functional validation of candidate T cell receptors (TCRs). 82

Figure 9: Distribution of TCR clonotypes selected from sample NCH8937 for functional validation. 84

Figure 10: Distribution of TCR clonotypes selected from sample NCH9348 for functional validation. 85

Figure 12: Functional identification of a tumor-reactive TCR in NCH8937 using a Jurkat reporter assay 91

Figure 13: Functional assessment of NCH9348-derived TCRs in autologous primary T cells. 93

Figure 14: Multiplexed tissue imaging by CODEX (PhenoCycler). 96

Figure 15: Spatial heterogeneity of immune infiltration in NSCLC brain metastases. 100

Figure 16: Structural barriers in NSCLC brain metastases. 102

Figure 17: Phenotype of tumor-infiltrating T cells in NSCLC brain metastases. 103

Figure 18: Spatial mapping of immunosuppressive interactions in NSCLC brain metastases. 106

Figure 19: Tertiary lymphoid structures (TLS) in NSCLC brain metastases. 109

Figure 20: Integrated model of spatial and functional mechanisms of anti-tumor immunity in NSCLC brain metastases. 131

List of tables

Table 1: Sequence features of selected TCR clonotypes. 86

Table 2: Multiplexed antibody panel for spatial immune profiling. 98

List of appendix figures

Appendix Figure 1: Cell count of T cells from scRNA/TCR-seq analysis including clonotype group 134

Appendix Figure 2: Lentiviral TCR construct and baseline reporter activation in JE6-1-NF-κB::eGFP cells 135

Appendix Figure 3: Representative multiplexed CODEX imaging of marker expression in brain metastases..... 136

List of abbreviations (A-Z)

ADCC	Antibody-dependent cellular cytotoxicity
AHR	Aryl hydrocarbon receptor
APC	Antigen-presenting cell
APC	Allophycocyanin
BBB	Blood-brain barrier
BrM	Brain Metastasis
BSA	Bovine serum albumin
BTB	Blood-tumor barrier
CAF	Cancer-associated fibroblast
cDC	Conventional dendritic cell
CDR	Complementarity-determining regions
CK19	Cytokeratin-19
CNS	Central nervous system
CODEX	Co-detection by indexing
CT	Cancer testis
CTC	Circulating tumor cell
CTL	Cytotoxic T lymphocyte
DAMPs	Damage-associated molecular patterns
DAPI	4’,6-diamidino-2-phenylindole
DC	Dendritic cells
ddH_2O	Double-distilled water
DEG	Differentially expressed genes
DMEM	Dulbecco`s modified eagle medium
EB	Elusion buffer
ECM	Extracellular matrix
ECM	Extra cranial metastasis

eGFP	Enhanced Green Fluorescent Protein
EMT	Epithelial-to-mesenchymal transition
FACS	Fluorescence-activated cell sorting
FBS	Fetal bovine serum
FC	Flow cytometry
FDA	Food and Drug Administration (United States)
fDC	Follicular dendritic cell
FFPE	Formalin-fixed paraffin-embedded
GC	Germinal center
GC	Glucocorticoid
GEX	Gene expression
GZMK	Granzyme K
HEV	High endothelial venules
HLA	Human leukocyte antigen
HSP	Heat shock proteins
IFN-γ	interferon-γ
IL	Interleukin
IVT	*In vitro* transcription
ICI	Immune checkpoint inhibitors
ITAM	Immunoreceptor tyrosine-based activation motifs
IVT	*In vitro* transcription
LC	Lung cancer
LCMV	Lymphocytic choriomeningitis virus
LN	Lymph Node
LUAD	Lung adenocarcinoma
MDM	Monocyte-derived macrophages
MET	Mesenchymal-to-epithelial transition

MFI	Mean Fluorescence Intensity
MHC	Major histocompatibility complex
mIF	Multiplexed immunofluorescence
MMP	Matrix metalloproteinase
mTLS	Mature tertiary lymphoid structures
NaN_3	Sodium azide
NCT	National Center of Tumor Diseases
NK	Natural killer cell
NSCLC	Non-small cell lung cancer
PB	Peripheral blood
PBMC	Peripheral blood mononuclear cells
PBS	Phosphate-buffered saline
PCR	Polymerase chain reaction
PD-L1	Programmed death-ligand 1
PDPN	Podoplanin
pMHC	Peptide/major histocompatibility complex
PNAd	Peripheral lymph node addressin
QC	Quality control
RT	Room temperature
S1PR	Sphingosine-1-phosphate receptors
SCC	Squamous cell carcinoma
SCLC	Small cell lung cancer
scRNA-seq	Single-cell RNA sequencing
TAA	Tumor-associated antigen
TAM	Tumor-associated macrophage
T_{CM}	Central memory T cell
T_{CYCL}	Cycling/proliferative T cells

TCR	T cell receptor
tdLN	Tumor-draining lymph node
T_{EM}	Effector memory T cell
T_{EX}	Terminally exhausted T cell
T_{FH}	T follicular helper cell
TGF-β	Transforming growth factor-β
TILs	Tumor-infiltrating lymphocytes
TLS	Tertiary lymphoid structures
TME	Tumor microenvironment
T_{PEX}	Progenitor exhausted T cell
T_{REG}	Regulatory T cell
T_{RM}	Tissue-resident memory T cells
T_{scm}	Stem-like memory T cell
UMAP	Uniform Manifold Approximation and Projection
UMI	Unique molecular identifiers
VDJdb	VDJ-database
WHO	World Health Organization

1. Introduction

1.1. The role of the immune system in cancer

The concept of the hallmarks of cancer was first introduced by Douglas Hanahan and Robert A. Weinberg in 2000, describing tumor development as a multistep process primarily driven by intrinsic properties of malignant cells (Hanahan & Weinberg, 2000). Approximately a decade later, this framework was revised to incorporate the critical contribution of the tumor microenvironment (TME) to tumor initiation and progression (Hanahan & Weinberg, 2011). The tumor microenvironment (TME) extends beyond malignant cells and includes endothelial cells and pericytes that constitute the tumor vasculature, cancer-associated fibroblasts (CAFs), as well as a broad range of immune and inflammatory cell populations. This more comprehensive view highlights that immune responses in cancer are not uniformly protective but can exert opposing effects, contributing either to tumor control or to tumor progression depending on the context.

The anti-tumor arm of this response, referred to as immune surveillance, was initially supported by clinical observations demonstrating an increased incidence of malignancies in immunosuppressed organ transplant recipients (Buell et al., 2005). These findings were further substantiated by experimental studies in mice, including lymphocyte-deficient $RAG2^{-/-}$ and interferon gamma receptor 1-deficient ($IFNGR1^{-/-}$) models, which exhibit an approximately threefold increased susceptibility to carcinogen-induced tumorigenesis (Shankaran, 2001). Consistent results were reported in models of spontaneous tumor development in IFN-γ-deficient mice (Street et al., 2002). The contribution of cytotoxic $CD8^+$ T cells to tumor surveillance was further demonstrated in transplantation models, where effective lymphoma clearance was observed following depletion of NK cells using anti-NK1.1 antibodies, thereby isolating T cell-mediated effects (Smyth, 2000).

Under homeostatic conditions, distinct memory T cell subsets exhibit specialized trafficking patterns: circulating central memory T cells (T_{CM}) preferentially localize to secondary lymphoid organs, effector memory T cells (T_{EM}) patrol non-lymphoid tissues, and tissue-resident memory T cells (T_{RM}) provide localized immune protection within non-lymphoid organs throughout the body (Christo et al., 2024). Notably, elevated intratumoral T_{RM} abundance has been associated with favorable clinical outcomes across multiple human cancers, as discussed in section 1.1.1.4 (Park et al., 2019).

In 2013, Daniel S. Chen and Ira Mellman proposed the “Cancer-Immunity Cycle”, a conceptual framework outlining seven sequential steps required for an effective anti-tumor

immune response (Chen & Mellman, 2013). The cycle is initiated within the tumor, where cancer cell death results in the release of tumor antigens that are captured by dendritic cells (DCs). These cells then relocate to the draining lymph nodes, where tumor-derived peptides are presented to T cells, leading to their activation upon recognition of these antigens as non-self. Activated cytotoxic T cells then traffic via the vasculature to the tumor site, infiltrate the tissue, recognize malignant cells through their T cell receptor (TCR) (see sections 1.1.1 and section 1.1.1.2), and mediate target cell killing. This process results in further antigen release, thereby sustaining and amplifying the cycle. Notably, T cell-dependent phases of this cycle are particularly vulnerable to disruption, as chronic antigen exposure during repeated cycles promotes progressive T cell dysfunction. In cancer, this cycle is frequently impaired, as tumors develop mechanisms to evade or suppress the immune response, ultimately enabling disease progression.

These dynamic interactions between the immune system and tumor cells led to the refinement of classical immunosurveillance theory into the concept of the “three Es of cancer immunoediting”: elimination, equilibrium, and escape (Dunn et al., 2004). The elimination phase reflects effective immunosurveillance, during which transformed cells are recognized and eradicated. However, this immune-mediated pressure imposes selective constraints on tumor cells, favoring the survival of variants with reduced immunogenicity or acquired immune evasion mechanisms. Tumor cells that are not completely eliminated enter the equilibrium phase, characterized by a dynamic balance between immune-mediated killing and tumor cell proliferation. Sustained immune pressure during this phase drives the gradual selection and expansion of tumor variants with enhanced immune evasive capacity. For example, in autochthonous lung adenocarcinoma mouse models, pre-existing lung-resident T_{RM}-like cells were shown to facilitate immune escape through the coordinated loss of a defined tumor neoantigen and reduced major histocompatibility complex (MHC) class I expression on tumor cells (Weeden et al., 2023). Eventually, tumors transition from the equilibrium phase into the escape phase, during which immune control is lost and clinically manifest disease emerges. Mechanistically, tumor escape is driven by a range of processes within the TME, including defects in antigen processing and presentation, downregulation of MHC molecules, resulting in impaired peptide presentation to T cells. In addition, the TME fosters an immunosuppressive milieu that constrains effector T cell function, partly through the accumulation and expansion of regulatory cell populations such as tumor-associated macrophages (TAMs) and regulatory T cells (T_{REGs}). Concurrently, tumor and myeloid cells upregulate inhibitory checkpoint ligands, including programmed death-ligand 1 (PD-L1), thereby limiting T cell activity. Furthermore, cancer-associated fibroblasts (CAFs) contribute to the establishment of structural barriers that can

further restrict effective immune cell infiltration and function. Chronic antigen exposure additionally promotes progressive T cell exhaustion (section 1.1.1.3), characterized by sustained expression of inhibitory receptors including PD-1, TIM-3, and LAG-3 (Dhatchinamoorthy et al., 2021; Galassi et al., 2024).

1.1.1. Cancer cell recognition by T cells

All nucleated cells continuously present short peptides derived from intracellular protein degradation on their surface via major histocompatibility complex class I (MHC-I) molecules. The term MHC refers to a set of antigen-presenting molecules conserved across vertebrates, whereas in humans it is designated as human leukocyte antigen (HLA). HLA class I molecules consist of an invariant β2-microglobulin (β2M) subunit paired with a polymorphic α heavy chain, encoded by the highly variable genes HLA-A, HLA-B, and HLA-C. These genes exhibit extensive diversity across populations, with more than 28,000 distinct alleles reported for HLA-A, -B, and -C as of July 2025. This diversity is predominantly concentrated within the peptide-binding groove, enabling the presentation of a broad repertoire of peptide ligands (Barker et al., 2025). Such polymorphism ensures wide coverage of potential antigenic threats.

Under physiological conditions, presented peptides predominantly originate from normal protein turnover. Intracellular proteins are degraded by the proteasome into peptide fragments, which are subsequently transported into the endoplasmic reticulum, trimmed to optimal length, and loaded onto nascent HLA class I molecules before being trafficked to the cell surface. This process enables continuous surveillance of intracellular protein integrity.

In cancer, somatic mutations give rise to neoepitopes, which are altered peptides absent from healthy tissues and recognized as non-self by T cells. In addition, tumor cells frequently overexpress or aberrantly express non-mutated endogenous proteins, referred to as tumor-associated antigens (TAAs), which are typically restricted to low or absent expression in normal tissues and are often linked to cellular differentiation programs (Shah et al., 2023). A specific category of tumor-associated antigens comprises cancer-testis (CT) antigens, which have a highly restricted physiological expression pattern limited to immune-privileged germline tissues, such as the testis, yet they are aberrantly re-expressed across multiple cancer types. CT antigens are capable of eliciting spontaneous cytotoxic T cell responses (Scanlan et al., 2002). A well-characterized example is NY-ESO-1, first described in 1997, which is expressed in testis and ovary under physiological conditions but is also detected

in a wide variety of human cancers (Chen et al., 1997). These peptide-HLA complexes constitute key targets for immune recognition. $CD8^+$ cytotoxic T lymphocytes survey these complexes via their αβ T cell receptors, which specifically engage the composite peptide-HLA surface (section 1.1.1.2). This interaction forms the basis for subsequent T cell priming and activation, ultimately enabling antigen-specific recognition and elimination of tumor cells.

1.1.1.1. T cell priming and activation in malignancies

Lymph nodes (LNs), as secondary lymphoid organs distributed throughout the body, serve as key sites for immune surveillance, where naïve and memory T and B lymphocytes encounter cognate antigens presented by antigen-presenting cells (APCs). Conventional dendritic cells (cDCs), as professional APCs, play a central role in priming and activating T cells within LNs by capturing and presenting exogenous antigens, including tumor-derived material. In this context, cDC1s specialize in cross-presentation of exogenous antigens on MHC class I molecules to $CD8^+$ T cells, whereas cDC2s primarily present antigens on MHC class II molecules to $CD4^+$ T cells (Borst et al., 2018). Productive T cell activation arises from the integration of three essential signals, comprising antigen recognition via TCR interaction with peptide–MHC complexes, co-stimulatory signaling (e.g., CD28–B7), and cytokine-driven instructions (e.g., by interleukin-12 of type I interferons) that guide T cell differentiation, as further detailed in section 1.1.1.2. Upon antigen-specific activation, $CD4^+$ T cells upregulate CD40 ligand (CD40L), which, in combination with interferon-γ (IFN-γ), licenses cDC1s to enhance MHC-I cross-presentation of peptides to $CD8^+$ T cells, thereby promoting cytotoxic T cell responses (Flinsenberg et al., 2015; Lei et al., 2024). This $CD4^+$ T cell help induces a transcriptional program in $CD8^+$ T cells that supports clonal expansion, effector differentiation, survival, metabolic fitness, tissue infiltration, and cytotoxic function.
Beyond classical priming in secondary lymphoid organs, as outlined in the Cancer-Immunity Cycle (Chen & Mellman, 2013), sustained anti-tumor T cell responses can also be maintained within the tumor microenvironment (TME) (Mellman et al., 2023). Within the TME, T cells interact with dendritic cells in organized immune cell aggregates, often referred to as tertiary lymphoid structures (TLS), which support $CD8^+$ cytotoxic T lymphocyte (CTL) survival and function (Di Pilato et al., 2021). TLS arise under chronic inflammatory conditions and exhibit varying degrees of structural organization. Early or immature TLS consist of loosely arranged T and B cell clusters with limited dendritic cell presence and lack follicular dendritic cells (fDCs), whereas mature TLS display defined B cell follicles enriched

in fDCs, surrounded by $CD4^+$ T follicular helper cells (T_{FH}), tissue-resident memory T cells (T_{RM}; see section 1.1.1.4), and mature dendritic cells (Fridman et al., 2023).
TLS are frequently located in proximity to high endothelial venules (HEVs), which facilitate lymphocyte recruitment from the circulation. Increased TLS density has been associated with enhanced T cell receptor (TCR) clonality, consistent with local T cell priming and expansion (Zhu et al., 2015). Moreover, the presence of mature TLS correlates with improved clinical outcomes across multiple tumor types and with enhanced responses to immune checkpoint inhibition (ICI) targeting PD-1 or PD-L1 (Fridman et al., 2022; Kroeger et al., 2016a; Zhao et al., 2022). This prognostic benefit can amongst others be attributed to TLS-driven intratumoral immune cycles, in which B cell maturation gives rise to plasma cells secreting high-affinity antibodies. These antibodies opsonize tumor cells and trigger macrophage- or natural killer (NK) cell-mediated apoptosis. The resulting antigen-antibody complexes are subsequently internalized by dendritic cells, thereby enhancing T cell cross-priming (Kroeger et al., 2016b). Collectively, TLS function as dynamic niches that support local T and B cell activation and sustain anti-tumor immunity within the TME.

1.1.1.2. The αβ T cell receptor and its interaction with MHC-peptide complex

In 1984, pioneering studies established that the T cell receptor (TCR) is part of a multicomponent complex composed of the antigen-binding αβ heterodimer and the cluster of differentiation 3 (CD3) signaling modules (Weiss & Stobo, 1984). This co-assembly is required for stable surface expression of the TCR and functionally couples antigen recognition to intracellular signaling via the CD3 chains, which contain immunoreceptor tyrosine-based activation motifs (ITAMs) essential for signal transduction (Shah et al., 2021).

The αβ TCR consists of an α and a β chain, each comprising a membrane-distal variable (V) domain responsible for antigen recognition and a membrane-proximal constant (C) domain that associates non-covalently with CD3 through hydrophobic interactions (Weiss & Stobo, 1984). The variable domains are generated through somatic V(D)J recombination of germline gene segments during thymocyte development in the thymus, giving rise to a highly diverse repertoire with a theoretical diversity exceeding 10^{15} unique specificities. The β chain incorporates an additional diversity (D) segment, further increasing junctional variability (Sim & Sun, 2022).

The recombination-activating proteins RAG1 and RAG2 initiate V(D)J recombination through interaction with recombination signal sequences adjacent to V, D, and J segments, resulting in the introduction of DNA double-strand breaks at defined sites. Recombination

proceeds in an ordered manner, with D-J joining preceding V-DJ rearrangement, followed by ligation via non-homologous end joining. Additional diversity is introduced through the activity of terminal deoxynucleotidyl transferase, which adds non-templated nucleotides at the junctions (Roth, 2014). Despite this immense theoretical diversity, the peripheral TCR repertoire is substantially constrained by thymic selection processes that eliminate non-functional or autoreactive clones.

During thymic development, thymocytes undergo stringent selection. Positive selection, mediated by cortical thymic epithelial cells, favors low-avidity interactions with self-peptide-MHC (pMHC) complexes, ensuring survival and MHC restriction. In contrast, high-avidity self-reactive clones are eliminated through negative selection, mediated by antigen-presenting cells, thereby preventing autoimmunity (Spits, 2002).

Binding of the TCR to peptide-MHC complexes relies on six complementarity-determining regions (CDRs), comprising three within the TCR-α chain and three within the TCR-β chain. The germline-encoded CDR1 and CDR2 primarily contact conserved regions of the MHC molecule, whereas the highly variable CDR3, formed at the V(D)J junction, determines peptide specificity (Rossjohn et al., 2015). Upon ligation with the peptide-MHC complex, conformational changes within the TCR-CD3 complex occur, facilitating signal initiation (Rudolph et al., 2006).

TCR engagement alone is insufficient for full T cell activation and requires coordinated signaling through the CD3 complex (Weiss & Stobo, 1984). The constant domains of the TCR associate with CD3 dimers (δε, γε, and ζζ), whose cytoplasmic ITAMs contain tyrosine residues that are phosphorylated by the SRC-family kinase LCK upon receptor engagement (Smith-Garvin et al., 2009). The co-receptors CD4 (MHC class II-restricted) and CD8αβ (MHC class I-restricted) bind non-polymorphic regions of MHC molecules, thereby stabilizing the TCR-pMHC interaction and recruiting LCK to the signaling complex (Shah et al., 2021). Phosphorylated ITAMs subsequently serve as docking sites for downstream signaling molecules, leading to the assembly of a signalosome and propagation of intracellular signaling cascades.

TCR engagement alone is insufficient for full T cell activation. In the absence of co-stimulatory signals, TCR stimulation can instead induce a state of anergy in naïve T cells (Schwartz, 2003). Productive activation therefore requires additional signals. Co-stimulatory signaling via CD28 binding to B7-1 (CD80) and B7-2 (CD86) on antigen-presenting cells provides a critical second signal, promoting T cell expansion, survival, and differentiation (Chen & Flies, 2013). A third signal, mediated by cytokines such as interleukin-12 or type I interferons, directs T cell polarization and effector differentiation (Curtsinger & Mescher,

2010). In contrast, engagement of co-inhibitory receptors, including CTLA-4 and PD-1, attenuates T cell activation and maintains immune homeostasis (Chen & Flies, 2013). In settings of persistent antigen exposure, such as cancer, sustained signaling can drive T cells into a dysfunctional state referred to as T cell exhaustion, as discussed in the following section.

1.1.1.3. T cell exhaustion and immune checkpoint inhibition

T cell exhaustion represents a distinct differentiation state characterized by the progressive impairment of effector $CD8^+$ T cell functions, including reduced cytotoxicity, cytokine production, and proliferative capacity. This state arises in the context of sustained antigen exposure in chronic inflammatory settings such as the tumor microenvironment (Gallimore, 1998; McLane et al., 2019). The phenomenon was first described in 1998 in studies of lymphocytic choriomeningitis virus (LCMV)-specific cytotoxic T lymphocytes, where high antigen loads resulted in functional inactivation without immediate cell deletion (Gallimore, 1998).

Effector T cells exposed to persistent antigenic input progressively adopt a receptor profile marked by PD-1 (*PDCD1*), TIM-3 (*HAVCR2*), LAG-3, and CTLA-4 expression. Engagement of these receptors with their respective ligands on antigen-presenting cells, tumor cells, or infected cells attenuates T cell receptor signaling and downstream effector functions (McLane et al., 2019; Wherry & Kurachi, 2015). Importantly, T cell exhaustion does not represent a binary state but rather a progressive and heterogeneous differentiation continuum, ranging from progenitor-like populations with retained functionality to terminally differentiated cells with profound dysfunction (H. Li et al., 2019; Miller et al., 2019; Vardhana et al., 2020). Progenitor exhausted T cells (T_{PEX}) are characterized by intermediate PD-1 expression and the expression of stemness-associated markers such as TCF-1 (encoded by *TCF7*), CD62L (encoded by *SELL*), and CXCR5. These cells retain the capacity for self-renewal and can give rise to more differentiated exhausted subsets under conditions of persistent antigen stimulation (Jansen et al., 2019; Tsui et al., 2022). By contrast, terminally exhausted T cells display a receptor profile dominated by inhibitory molecules such as PD-1, TIM-3, and LAG-3, accompanied by a marked loss of effector function. Notably, single-cell RNA sequencing (scRNA-seq) analyses of melanoma-infiltrating T cells have demonstrated that subsets with high expression of *PDCD1*, *LAG3*, and *HAVCR2* can retain proliferative signatures, further supporting the concept of a functional continuum rather than a strict dichotomy (H. Li et al., 2019).

Immune checkpoint inhibitors (ICI) counteract T cell exhaustion by blocking inhibitory receptor-ligand interactions, thereby restoring effector functions. This reinvigoration predominantly occurs in progenitor-like exhausted T cells, which retain proliferative capacity and developmental plasticity (Zebley & Youngblood, 2022). Ipilimumab, a monoclonal antibody targeting CTLA-4, was the first ICI approved in 2011 by the U.S. Food and Drug Administration (FDA) for the treatment of advanced melanoma, based on phase III trials demonstrating improved overall survival (Cameron, 2011; Hodi, 2010). This was followed in 2014 by the approval of the anti-PD-1 antibodies Pembrolizumab and Nivolumab for unresectable or metastatic melanoma, and in 2016 by the anti-PD-L1 antibody Atezolizumab for urothelial carcinoma (Gong et al., 2018). As of 2025, multiple ICIs targeting PD-1, PD-L1, and CTLA-4 have been approved across a broad range of malignancies, including melanoma, non-small cell lung cancer, renal cell carcinoma, and hepatocellular carcinoma (Park & Skalhegg, 2025). Notably, the efficacy of ICIs is closely linked to the presence of progenitor exhausted T cells, which expand and differentiate into cytotoxic effector cells following checkpoint blockade, whereas terminally exhausted subsets remain largely refractory. In melanoma patients, higher pre-treatment frequencies of $TCF1^{+}PD\text{-}1^{+}$ $CD8^{+}$ T cells have been associated with prolonged progression-free survival (Miller et al., 2019). Combination therapies, such as concurrent PD-1 and CTLA-4 blockade, can enhance therapeutic responses by targeting complementary inhibitory pathways, albeit at the cost of increased immune-related adverse events.

1.1.1.4. T resident memory cells exhibit anti-tumor efficiency

Tissue-resident memory T cells (T_{RM}) establish long-term local immunity across diverse non-lymphoid tissues and play a central role in tumor immunosurveillance and control. Upon entry into peripheral tissues, a subset of T cells undergoes phenotypic reprogramming driven by tissue-derived signals and transcriptional regulators. This process suppresses egress-associated molecules, including sphingosine-1-phosphate receptors (S1PRs) and the transcription factor KLF2, while promoting the expression of retention-associated molecules such as integrins, thereby anchoring these cells within tissue sites (Christo et al., 2024). A defining feature of T_{RM} cells is the expression of the integrin αeβ7, also known as CD103, which binds E-cadherin on epithelial cells and mediates tissue retention (Schenkel & Masopust, 2014). CD103 expression is particularly prominent in epithelial tissues and is induced by transforming growth factor-β (TGF-β) signaling, which promotes chromatin accessibility at residency-associated gene loci. Additional markers, including CD69 and CXCR6, further distinguish T_{RM} cells from circulating T cell populations.

Single-cell transcriptomic analyses have identified distinct T_{RM}-like states, including cytotoxic subsets characterized by high expression of granzyme B (*GZMB*) and perforin (*PRF1*), as well as more exhausted-like populations expressing inhibitory receptors such as PD-1 (*PDCD1*), TIM-3 (*HAVCR2*), and CTLA-4 (*CTLA4*) (Christo et al., 2024). These phenotypic states likely reflect adaptation to persistent antigen exposure within tissue environments.

Experimental models of intracranial infection have demonstrated that $CD8^+$ T cells can infiltrate the brain parenchyma, differentiate into long-lived T_{RM} cells, and persist for extended periods within specialized niches characterized by slow homeostatic proliferation. Upon antigen re-exposure, these cells mount rapid effector responses, thereby providing robust local protection (Brizic et al., 2018).

In human cancer, T_{RM} cells have been consistently associated with favorable clinical outcomes. In lung adenocarcinoma, T_{RM} cells are enriched within tumor lesions compared to adjacent tissue and correlate with improved prognosis (Zhao et al., 2022). Similarly, in stage I NSCLC, increased T_{RM} density is associated with reduced relapse and mortality (Djenidi et al., 2015). Notably, $CD8^+CD103^+$ tumor-infiltrating lymphocytes (TILs) often express inhibitory receptors such as PD-1 and TIM-3, yet display enhanced functional capacity compared to $CD103^-$ counterparts, as evidenced by increased degranulation (CD107a) and granzyme B production upon *ex vivo* stimulation. Among long-term melanoma survivors, T_{RM} cells represent a predominant and functionally potent TIL population associated with favorable clinical outcomes (Han et al., 2021). These cells, frequently characterized by high CD69 and PD-1 expression, have been shown to sustain tumor-reactive clones for extended periods following tumor resection.

1.2. Epidemiology and clinical burden of lung cancer

Lung cancer is the most commonly diagnosed malignancy worldwide, accounting for approximately one in eight newly diagnosed cancer cases, and remains the leading cause of cancer-related mortality, responsible for roughly one in five deaths (Bray et al., 2024). Tobacco use represents the predominant risk factor and is implicated in more than 80% of lung cancer cases (Thandra et al., 2021). With smoking prevalence continuing to increase in several regions globally, the incidence of lung cancer is expected to rise further. Accordingly, projections estimate a substantial increase in disease burden, with new cases rising by 86.2% and mortality by 95.2% by 2050 compared to 2022 levels (Ji et al., 2025). Lung cancers are broadly classified into non-small cell lung cancer (NSCLC), which

accounts for approximately 85% of cases, and small cell lung cancer (SCLC) (Smolarz et al., 2025). The World Health Organization classifies lung cancer subtypes based on morphological criteria, complemented by immunohistochemical and molecular features (Nicholson et al., 2022). Within NSCLC, adenocarcinoma represents the predominant histological subtype, comprising nearly 80% of cases, followed by squamous cell carcinoma (SCC) (Bray et al., 2024).

A substantial proportion of patients are diagnosed at advanced, surgically inoperable stages, resulting in poor clinical outcomes, with five-year survival rates ranging from 10% to 20% (Allemani et al., 2018). Notably, approximately 43% of patients with lung adenocarcinoma present with distant metastases at the time of diagnosis (Xie et al., 2024). The brain represents a major site of metastatic spread, affecting around 15% of patients with metastatic lung cancer (J. Li et al., 2019). The following section (1.3) outlines the mechanisms underlying metastatic dissemination, with a particular focus on brain tropism, while section 1.4 further addresses brain metastases (BrM) and their microenvironmental context.

1.3. The Mechanisms of metastasis and brain tropism

The concept of non-random metastasis was first proposed by Stephen Paget in 1889 through the “seed and soil” hypothesis, which posits that disseminating cancer cells (“seeds”) preferentially colonize distant organs (“soil”) that provide a supportive microenvironment for their survival and proliferation (Paget, 1889). Circulating tumor cells (CTCs) capable of initiating metastases display stem cell-like properties, including anchorage-independent survival, clonal expansion potential, invasive capacity, resistance to apoptosis, and the ability to evade growth-suppressive signals within foreign microenvironments. The metastatic cascade comprises a series of sequential steps, including local invasion, intravasation into the vasculature, survival in circulation, extravasation, and colonization of distant tissues (Ramakrishna & Rostomily, 2013).

Intravasation, the initial entry of tumor cells into the bloodstream, requires extensive cytoskeletal remodeling and is largely driven by epithelial-to-mesenchymal transition (EMT). During EMT, tumor cells lose epithelial characteristics such as apicobasal polarity and cell-cell adhesion while acquiring mesenchymal features that enhance motility and invasiveness (Ramakrishna & Rostomily, 2013). A central regulator of EMT is transforming growth factor-β (TGF-β), which induces transcriptional programs promoting anti-apoptotic signaling, pro-angiogenic mediators, and repression of E-cadherin expression, while simultaneously

facilitating extracellular matrix (ECM) degradation (Hao et al., 2019). This process is accompanied by the “cadherin switch”, characterized by the downregulation of E-cadherin and upregulation of N-cadherin and vimentin, further enhancing migratory and invasive capabilities (Loh et al., 2019). In parallel, tumor cells upregulate matrix metalloproteinases (MMPs), which degrade ECM components such as collagen IV and laminin, thereby enabling tissue invasion and vascular entry (Heerboth et al., 2015).

Within the circulation, CTCs are exposed to multiple stresses, including shear forces, nutrient deprivation, oxidative stress, and immune surveillance. Consequently, fewer than 0.01% of CTCs successfully give rise to macroscopic metastases (Ramakrishna & Rostomily, 2013). Upon arrest in distant capillary beds, surviving CTCs extravasate, often guided by organ-specific chemokine gradients, and may undergo mesenchymal-to-epithelial transition (MET) to re-establish proliferative epithelial phenotypes.

Prior to overt metastasis formation, primary tumors can condition distant organs through the release of soluble factors and extracellular vesicles, thereby establishing so-called pre-metastatic niches that facilitate subsequent tumor cell engraftment. In lung cancer models, tumor-derived extracellular vesicles have been shown to target brain microvascular endothelial cells, inducing autocrine secretion of Dickkopf-1 (Dkk-1), which suppresses microglial activation and promotes an anti-inflammatory microenvironment permissive for metastatic colonization (Gan et al., 2020).

Extravasation into the brain requires crossing of the blood-brain barrier (BBB), as discussed in section 1.4. This process involves tumor cell-derived proteases, such as cathepsin S, which degrade adhesion molecules including N-cadherin and thereby compromise barrier integrity (Souza et al., 2023).

Following extravasation, metastatic tumor cells further remodel the local microenvironment. They can induce polarization of resident microglia toward an M2-like, pro-tumorigenic phenotype through interleukin-6 (IL-6)-mediated signaling, resulting in the upregulation of immunosuppressive mediators (Jin et al., 2022). In turn, these microglia secrete factors that promote MET in infiltrating tumor cells, restoring epithelial characteristics such as E-cadherin expression and enabling proliferative outgrowth. Tumor invasion of the brain parenchyma is accompanied by BBB disruption and neuroinflammation, during which reactive astrocytes and microglia release damage-associated molecular patterns (DAMPs). This response facilitates the recruitment of peripheral immune cells, thereby progressively altering the immune landscape of the brain, undermining its immune privilege, and promoting metastatic spread.

1.4. Brain metastases and the brain metastatic niche

Brain metastases represent a frequent complication of advanced cancer, affecting approximately 20-40% of patients during the course of their disease and constituting the most common intracranial malignancy. Lung cancer accounts for 40-50% of cases, followed by melanoma, breast cancer, and renal cell carcinoma (Bertolini et al., 2015; Steindl et al., 2022; Valiente et al., 2018). Notably, around 28% of patients with advanced non-small cell lung cancer (NSCLC) present with brain involvement at diagnosis (Gillespie et al., 2023). Despite multimodal treatment approaches, the prognosis of patients with lung cancer brain metastases remains poor, with a median overall survival of approximately 7 months (Steindl et al., 2022).

The brain microenvironment is characterized by a distinct extracellular matrix and a specialized composition of central nervous system (CNS)-resident cells, including neurons, microglia, astrocytes, and oligodendrocytes, which collectively maintain homeostasis while limiting excessive neuroinflammation and anti-tumor responses (Laaker et al., 2023). Tumor cells exploit brain-specific signaling pathways, such as glutamate and γ-aminobutyric acid (GABA), to support their proliferation and survival, while adapting to nutrient limitations through metabolic reprogramming. In brain metastases derived from NSCLC, tumor cells have been shown to preferentially rely on glycolysis over oxidative phosphorylation, accompanied by increased amino acid catabolism and lipid biosynthesis (Valiente et al., 2025). Astrocytes, the most abundant glial cell population, regulate synaptogenesis, neurotransmission, neuronal metabolism, cerebral blood flow, and blood-brain barrier (BBB) integrity under physiological conditions (Andersen et al., 2021). The BBB, formed by endothelial cells, pericytes, and astrocytic endfeet, restricts the paracellular entry of molecules into the healthy brain. Historically, the brain was considered an “immune-privileged” site based on early observations that systemically administered dyes failed to penetrate the brain parenchyma. However, this concept has been revised in light of evidence demonstrating active immune surveillance. For example, T cells recognizing brain autoantigens contribute to neuronal differentiation and cognitive function, as immunodeficient mice exhibit impaired spatial learning that can be restored upon T cell reconstitution (Ziv et al., 2006). In addition, inflammatory conditions enable the recruitment of peripheral immune cells, including T cells and myeloid populations, into the brain parenchyma and meningeal compartments (Laaker et al., 2023). Meningeal lymphatic vessels further facilitate the drainage of CNS-derived antigens to peripheral lymph nodes, thereby supporting immune priming.

Microglia, which originate from yolk sac progenitors during embryonic development, act as resident immune cells of the CNS and contribute to debris clearance and early immune responses. Upon activation, they can upregulate MHC class II molecules and function as antigen-presenting cells (Ginhoux, 2010; Jakel & Dimou, 2017). In the context of metastasis, disruption of the BBB increases vascular permeability and permits the influx of immune cells and circulating molecules. Notably, more than 89% of experimental brain metastases exhibit permeability to molecules of chemotherapeutic size (Karimi et al., 2023; Lockman et al., 2010).

Tumor-associated macrophages (TAMs), comprising both resident microglia and infiltrating monocyte-derived macrophages (MDMs), dominate the immune landscape of brain metastases and can constitute more than 50% of the tumor mass (Andersen et al., 2021). In contrast to primary brain tumors, brain metastases are characterized by a predominance of MDMs, which exert strong tumor-promoting effects through immunosuppressive mechanisms. In addition, astrocytes contribute to the establishment of a pro-tumorigenic microenvironment by suppressing $CD8^+$ T cell function via STAT3 signaling and by modulating TAM activity through the secretion of cytokines, chemokines, and metabolites (Valiente et al., 2025).

A key mechanism of immunosuppression by myeloid cells involves the activation of the aryl hydrocarbon receptor (AHR). This pathway can be triggered by ligands produced by the L-amino acid oxidase IL4I1, which promotes monocyte recruitment and induces immunosuppressive transcriptional programs (Andersen et al., 2021). IL4I1 expression is elevated in metastatic compared to primary tumors, including melanoma and glioma (Sadik et al., 2020). Its enzymatic products inhibit T cell proliferation and are associated with increased frequencies of regulatory T cells and myeloid-derived suppressor cells, as well as enhanced tumor cell motility, ultimately correlating with poor clinical outcomes

1.4.1. T cell infiltration into brain metastases

Brain metastases (BrM) exhibit higher densities of tumor-infiltrating lymphocytes (TILs) compared to primary gliomas. The presence and extent of T cell infiltration in BrM have been consistently associated with prolonged overall survival across multiple studies (Friebel et al., 2020; Ikarashi et al., 2021; Klemm et al., 2020; Pocha et al., 2020). Comparative analyses of BrM derived from melanoma, lung, and breast cancer have revealed distinct immune compositions: melanoma-derived BrM are enriched in lymphoid cells, breast

cancer BrM are predominantly infiltrated by myeloid cells, and lung cancer BrM display a more balanced immune composition (Klemm et al., 2020).

Previous scRNA-seq studies investigating immune infiltrates in BrM have largely focused on melanoma-derived lesions (Biermann et al., 2022; Smalley et al., 2021) or included mixed primary tumor cohorts without prior immune cell enrichment (Gonzalez et al., 2022), thereby limiting sequencing depth and resolution for detailed T cell sub-clustering. In contrast, one study performed scRNA-seq on sorted PD-1$^+$ CD8$^+$ T cells from BrM of lung cancer and melanoma patients, identifying distinct transcriptional states. These included terminally differentiated effector CD8$^+$ T cells characterized by high expression of inhibitory receptors such as *CTLA4*, *ENTPD1* (CD39), *HAVCR2* (TIM-3), and *LAG3*; T_{RM}-like cells with a progenitor-like phenotype marked by *CD69*, *TCF7* (TCF-1), and *IL7R* (CD127); and proliferating cells expressing *MKI67* (Ki-67) and *TOP2A* (Sudmeier et al., 2022). This study highlights the importance of targeted cell enrichment strategies to improve transcriptional resolution and reveals the functional heterogeneity of BrM-infiltrating T cells.

Bulk TCRβ repertoire analyses of TILs in lung cancer-derived BrM have demonstrated substantial clonal expansion (Kudo et al., 2019; Mansfield et al., 2018). However, the lack of single-cell resolution and transcriptional integration limits the ability to assign clonotypes to specific T cell subsets. An integrated scRNA-seq and TCR-seq approach of sorted TILs from patients with lung cancer and melanoma brain metastases identified T_{RM}-like populations characterized by co-expression of inhibitory receptors and effector molecules such as *GZMB* and *IFNG*, as well as expression of *CXCL13* (Wischnewski et al., 2023). Notably, 42% of T cells within this population exhibited clonal expansion, with this transcriptional signature being enriched in lung cancer-derived BrM and corresponding to a neoantigen-reactive phenotype previously described in primary lung tumors (Hanada et al., 2022)

Collectively, these findings underscore the prognostic relevance of T cell infiltration in brain metastases and support the rationale for targeting these populations with immune checkpoint inhibitors, as discussed in section 1.5.

1.5. Treatment of lung cancer and brain metastases

Mortality rates in NSCLC have declined following the approval of targeted therapies directed against oncogenic driver mutations and genomic alterations (Nicholson et al., 2022). This development reflects advances in precision oncology, where molecular profiling enables the identification of actionable alterations in up to one-third of NSCLC cases, allowing for

tailored treatments that improve progression-free and overall survival in responsive patient subsets. However, approximately one-third of patients lack targetable alterations (Pakkala & Ramalingam, 2018), and even among eligible patients, acquired resistance frequently limits long-term efficacy (Bui et al., 2018; G. Recondo et al., 2018).

Lung cancer exhibits the second-highest tumor mutational burdens across malignancies, supporting its susceptibility to immunotherapeutic approaches (Sha et al., 2020). For patients without targetable mutations or with therapy resistance, ICIs represent a key treatment option under defined clinical criteria. The FDA has approved multiple ICIs for advanced NSCLC, including the PD-1 inhibitors Nivolumab and Pembrolizumab, as well as the PD-L1 inhibitors Atezolizumab and Durvalumab, for use either following chemotherapy or as first-line therapy in tumors with high PD-L1 expression (Davies, 2019).

The management of BrM in lung cancer relies on multimodal treatment strategies, including stereotactic radiosurgery, whole-brain radiotherapy, and systemic therapies guided by molecular profiling. Corticosteroids, particularly dexamethasone, are commonly used to reduce cerebral edema and improve neurological symptoms (Bertolini et al., 2015). Surgical resection is considered in selected patients with symptomatic lesions causing mass effects, followed by adjuvant radiotherapy; however, only approximately 6% of patients undergo resection, limiting the availability of BrM tissue for research (Yuan & Zheng, 2024).

Next-generation tyrosine kinase inhibitors, such as osimertinib for EGFR-mutant disease and alectinib for ALK-rearranged NSCLC, demonstrate improved intracranial progression-free survival compared to earlier-generation agents and are increasingly used upfront in patients with asymptomatic brain metastases (Layng et al., 2025; Gonzalo Recondo et al., 2018). In patients without driver mutations, combination strategies of ICIs and chemotherapy are now standard first-line treatments (Myall et al., 2021).

Immune infiltration differs between primary tumors and brain metastases. While lymphocytic infiltration is generally higher in primary NSCLC lesions, approximately half of $CD45^+$ immune cells in lung cancer BrM are lymphocytes, indicating a relatively inflamed microenvironment compared to brain metastases from breast cancer (Ikarashi et al., 2021; Klemm et al., 2020). Clinical trials have demonstrated that immunotherapy can improve outcomes in patients with brain metastases. For example, combination treatment with nivolumab (anti-PD-1) and ipilimumab (anti-CTLA-4) in addition to chemotherapy increased median overall survival from 9.2 to 17.4 months in patients with pretreated or stable BrM (Peters et al., 2025). Long-term analyses further reported improved 5-year overall survival rates compared to chemotherapy alone, alongside a reduced incidence of new brain lesions. Similarly, another study evaluating atezolizumab (anti-PD-L1) in combination with

chemotherapy demonstrated improved overall survival and an intracranial objective response rate of 43%, supporting the use of systemic immunotherapy in selected patients (Nadal et al., 2023).

Collectively, these findings highlight the potential of immunotherapy to enhance anti-tumor immune responses within the brain metastatic niche. However, a detailed understanding of the phenotypic and functional properties of T cells in lung cancer brain metastases, as well as their interactions with the immunosuppressive tumor microenvironment, remains incomplete. Addressing these questions is essential for identifying key axes of immune suppression and refining therapeutic strategies to improve patient outcomes.

2. Aims of the thesis

Despite increasing clinical implementation of immune checkpoint blockade, brain metastases frequently show limited therapeutic responses. While tumor-infiltrating lymphocytes are commonly detected in these lesions, it remains unclear whether they comprise tumor-reactive T cells or predominantly represent non-functional bystander populations. Moreover, the mechanisms that restrict effective anti-tumor immunity within the brain metastatic microenvironment are still poorly understood. Addressing these questions is essential to better define the role of T cells in brain metastasis (BrM) and to identify potential strategies to improve immunotherapeutic efficacy.

The central aim of this thesis was to address the existing knowledge gap regarding the nature and functional relevance of T cell infiltration in NSCLC brain metastasis. Specifically, this work sought to define the phenotypic landscape of infiltrating T cells, to determine whether these cells exhibit tumor-specific reactivity and thereby contribute to anti-tumor immunity, and to investigate whether and how their function is shaped or constrained by the local tumor microenvironment.

2.1. Characterization of the T cell landscape in NSCLC brain metastases

To define the phenotypic and transcriptional heterogeneity of tumor-infiltrating T cells, I performed single-cell RNA sequencing combined with paired T cell receptor (TCR) profiling of BrM samples. Bioinformatic analysis was performed in collaboration with Karol Jacek (PhD student, group of Prof. Dr. Bożena Kamińska, Nencki Institute, Warsaw) and Dr. Marc Zapatka (DKFZ). This approach enabled the identification of distinct $CD8^+$ T cell states and the assessment of their clonal expansion. A particular focus was placed on identifying T cell subsets associated with clonal expansion and potential tumor specificity. In addition, I analyzed matched peripheral blood samples to evaluate the relationship between circulating and tumor-infiltrating T cell populations.

2.2. Functional assessment of tumor-reactive T cells

To directly test whether infiltrating T cells recognize tumor-derived antigens, in collaboration with the group of Dr. Edward Green (DKFZ) I reconstructed selected TCRs identified from

single-cell analyses and evaluated their specificity using *in vitro* co-culture systems with autologous tumor material. This experimental approach was used to determine whether clonally expanded T cell populations exhibit functional tumor reactivity.

2.3. Spatial organization and regulation of T cells in the metastatic microenvironment

To investigate how T cells are organized within the tumor tissue and how their localization relates to tumor architecture, I performed multiplexed immunofluorescence imaging of BrM tissue sections in collaboration with the group of Prof. Dr. Sascha Dietrich (University clinic Düsseldorf). This allowed the spatial mapping of distinct T cell populations and their distribution between tumor cell-rich regions and the surrounding stroma.

In addition, I examined the presence of lymphoid aggregates and tertiary lymphoid structure-like regions to assess whether local immune activation and potential T cell priming may occur within the brain metastatic microenvironment. Furthermore, I analyzed the spatial context of myeloid cell populations and tumor-associated structural features to explore how local cellular interactions and physical barriers may contribute to the limitation of effective anti-tumor immunity in brain metastases.

3. Materials and methods

3.1. Materials

3.1.1. Human fresh frozen single cell suspension samples

Table M 1: Clinical characteristics of the neurosurgical NSCLC BrM cohort used for scRNA/TCR-seq.

Overall survival (OS), and progression free survival (PFS) given in months. Primary tumor (PT) histological subtypes: AC (adenocarcinoma), SCC (Squamous cell carcinoma), NSCLC-NOS (non-small cell lung cancer not otherwise specified). Presence of extracranial metastasis (ECM). Pre-treatment is defined as receipt of any systemic therapy prior to surgery excluding glucocorticoids, listed separately here as dexamethasone (Dex) administered 7 days preoperatively.

NCH#	Sample type	Sex	Dead vs. censored	OS	PFS	Age at surgery	Stage	Subtype PT	ECM	Dex 7d pre-op	Neoadjuvant therapy
8137	BrM	w	0	57	19	53	3B	AC	1	yes	RT PT, Cisplatin/ Vinorelbin concurrent, Afatinib
8559	BrM	m	0	48	48	62	4	SCC	0	Yes	0
8937	BrM	m	1	8	4	80	3A	AC	0	Yes	0
9230	BrM + PBMC	m	1	36	35	69	4	NSCLC-NOS	1	Yes	0
9348	BrM + PBMC	m	1	3	2	69	4	SCC	0	Yes	0
9427	BrM	w	0	37	37	61	3B	AC	0	Yes	Carboplatin/ Navelbine, RT PT
9488	BrM + PBMC	m	0	40	2	65	4	NSCLC-NOS	N.A.	Yes	0
9587	BrM + PBMC	m	1	12	9	81	4	AC	1	Yes	0
9904	BrM	m	0	34	34	81	3A	AC	1	yes	RT PT

3.1.2. Human FFPE tissue samples

Table M 2: Pathological classification of tumor and stroma content of human FFPE BrM tissue slides.

All FFPE tissues were obtained from the National Center for Tumor Diseases in Heidelberg. The investigation was approved by the ethics committee of the Medical Faculty, University of Heidelberg (S-074/2025).

Pseudonym	% Tumor	Tumor cells vital	Tumor cells avital	Stroma
1KZQFG	90	70	3	27
3VD1VD	100	70	5	35
1HDHP8	95	70	0	30
HYBQ1Z	97	60	10	30
10J1VP	100	70	0	20
2SX18C_I	100	80	0	20
TVR49P	100	65	5	30
14MV87	97	70	0	30
1R2OQ0	100	60	0	40
EGNCTO	80	80	0	20
MVKN8N	70	50	10	40
1O76LW	80	50	0	50
1AU7BC	60	50	5	45
14KSG1	100	50	10	40
1JK3D0	100	40	20	40
LDL8XH	95	45	25	30

Table M 3: Clinical characteristics of the FFPE tissues of brain metastases from primary NSCLC.

Data include de-identified patient pseudonyms, age, sex, NSCLC histological subtype (LUAD, lung adeno carcinoma; LCNEC, Large cell neuroendocrine carcinoma; NSCC, Non-Small Cell Carcinoma), pathological stage, preoperative glucocorticoid treatment, and *TP53* mutation status (where available). All corresponding tissues underwent multiplexed imaging by CODEX with a 52-antibody panel.

Pseudonym	Sex	Age at surgery	NSCLC subtype	Pathological stage	Gluco-corticoids	*TP53* Mutation status
1KZQFG	m	71	LUAD	4	yes	NA
3VD1VD	m	69	LUAD	4	yes	no mutation
1HDHP8	w	52	LUAD	4	no	no mutation

10J1VP	w	66	LUAD	4	no	NA
2SX18C_I	w	69	LCNEC	3	no	no mutation
HYBQ1Z	w	68	LUAD	3	no	NA
TVR49P	m	55	LCNEC	3	no	*TP53*: Exon 8, p.Arg282Trp,
14MV87	m	60	LCNEC	2	no	NA
1R2OQ0	m	61	LUAD	3	no	NA
EGNCTO	m	65	LUAD	3	no	no mutation
MVKN8N	m	59	LUAD	4	no	no mutation
1O76LW	w	60	LUAD	4	no	*TP53*: Exon 7 – p.Gly244fs*3
1AU7BC	m	71	LUAD	3	no	no mutation
14KSG1	w	66	LUAD	3	no	*TP53*: Exon 6, p.Pro190Leu;
1JK3D0	m	73	NSCC	4	yes	*TP53*:Exon7, p.Arg248Gln
LDL8XH	w	48	LUAD	3	no	NA

3.1.3. Antibodies and oligonucleotides

Table M 4: Antibodies and stains used for fluorescence-activated cell sorting and flow cytometry analysis.

Target	Fluorochrome	Dilution	Clone	Supplier	Reference
CD3	APC	1:100	OCT3	Biolegend	317318
CD8	PerCP	1:50	SK1	Biolegend	344708
CD19	APC	1:100	HIIB19	Biolegend	302212
CD45	Spark UV395	1:50	HI30	Biolegend	304095
CD45	BV421	1:50	HI30	Biolegend	304032
CD45	AF647	1:50	HI30	Biolegend	304020
CD45	AF488	1:200	HI30	Biolegend	304019
HLA-A2	APC	1:100	BB7.2	BioLegend	343308
Mouse TCRβ	APC	1:100	H57-597	Biolegend	109211
Mouse TCRβ	PE/Cy7	1:50	H57-597	Biolegend	109222
Live/Dead	eFluor 450	1:1000	/	eBioscience	65086314
Live/Dead	Near-IR	1:1000	/	Invitrogen	L10119
TNFα	BV711	1:50	Mab11	Biolegend	502940

Table M 5: Antibody for T cell stimulation

Name	Purpose	Supplier	Reference
MACS® GMP CD3 pure	T cell expansion from PBMCs	Miltenyi Biotech	170-076-124

Table M 6: Oligonucleotide-conjugated antibodies used for CODEX multiplexed immunofluorescent staining.

Target	Clone	Oligonucl.	Fluorophore	Supplier	Reference
Granzyme B	EPR20129-217	81	ATTO647	Abcam	ab219803
CCR7	2H4	6	ATTO647	DB	550937
CD11b	EPR1344	28	ATTO647	Abcam	ab216445
CD11c	EP1347Y	49	ATTO550	Abcam	ab216655
CD103	EPR4166(2)	58	ATTO550	Abcam	Ab271889
CD138	B-A38	76	ATTO647	Novus	NBP3-14568
CD15	MMA	14	ATTO550	DB	559045
CD163	EDHu-1	45	ATTO647	Novus	NB110-40686
CD20	rIGEL/773	48	ATTO550	Novus	NBP2-54591
CD206	poly	3	ATTO647	R&D	AF2534
CD21	Bu32	21	ATTO550	Biolegend	354902
CD25	4C9	24	ATTO550	Cell Marque	custom order
CD3	MRQ-39	55	ATTO550	Cell Marque	custom order
CD31	C31.3 + C31.7 + C31.10	68	ATTO550	Novus Bio	NBP2-47785
CD34	QBEnd/10 + HPCA1/763	33	ATTO647	Novus	NBP2-47909
CD39	EPR20627	43	ATTO647	Abcam	ab236038
CD4	EPR6855	20	ATTO647	Abcam	ab181724
CD45	2B11 + PD7/26	56	ATTO647	Novus	NBP2-34528
CD45RA	HI100	63	ATTO550	Biolegend	304102
CD45RO	UCH-L1	79	ATTO647	NovusBio	NBP2-33104
CD56	MRQ-42	29	ATTO550	Cell Marque	custom order

CD57	HCD57	30	ATTO647	MyBioSource, distributed by Biozol	MBS140192
CD62L	B-8	57	ATTO647	Santa Cruz	sc-390756
CD68	KP-1	41	ATTO550	Biolegend	916104
CD69	poly (AF2359)	36	ATTO550	Novus	AF2359
CD79a	JBC117	46	ATTO647	Cell Marque	custom order
CD8	C8/144B	8	ATTO647	NovusBio	NBP2-34588
CD90	EPR3132	59	ATTO647	Abcam	ab181885
CK19	A53-B/A2	111	ATTO647	BioLegend	628502
Collagen IV	EPR20966	38	ATTO550	Abcam	ab226485
CXCL13	polyclonal	75	ATTO647	R&D Systems	AF801
CXCR5	D6L3C	62	ATTO550	Cell Signaling	custom order
FoxP3	236A/E7	61	ATTO647	Invitrogen	14-4777-82
GFAP	GA5	70	ATTO647	Cell signaling	56522
HLA-DR	EPR3692	65	ATTO550	Abcam	ab215985
ICAM-1 (CD54)	2F9A8	77	ATTO550	Ptglab	60299-1-PBS
ICOS	D1K2T	74	ATTO647	CST	39740
IKZF2 (Helios)	22F6	7	ATTO550	Biolegend	137202
IKZF3	OTI7E11	15	ATTO647	OriGene	CF804396
IL4I1	EPR22070	26	ATTO550	Abcam	ab237783
KI-67	B56	2	ATTO550	BD	556003
LAG3	D2G4O	42	ATTO647	CST	25848SF
LAMP3/ CD208	1010E1.01	114	ATTO550	Novus	DDX0191P
Na+/K+-ATPase	EP1845Y	67	ATTO647	Abcam	ab283340
p53	DO-7	52	ATTO647	Santa Cruz Biotechnology	sc-47698
PAX5	D7H5X	11	ATTO550	CST	93009SF
PD-1	D4W2J	23	ATTO550	CST	63815SF
PD-L1	E1L3N	25	ATTO647	Cell Signaling Technology	85164
Podoplanin	D2-40	32	ATTO550	Biolegend	916606

SLAMF6	EPR22170	69	ATTO647	Abcam	Ab246707
TCF1	Polyclonal	5	ATTO550	R&D	AF5596
TIM3	Polyclonal	44	ATTO550	R&D	AF2365
TMEM119	EPR25865-89	72	ATTO647	Abcam	ab306584

Name	**Purpose**	**Supplier**	**Reference**
MACS® GMP CD3 pure	T cell expansion from PBMCs	Miltenyi Biotech	170-076-124

Table M 6

Table M 7: Oligonucleotide sequence and reporter oligonucleotide sequence used for CODEX.

Listed is the oligonucleotide internal number, the sequences of the oligonucleotide which is conjugated via maleimide (mal) to the antibody listed in Table M 6, and the respective reporter oligonucleotide sequence.

Oligonucleotide	**Oligonucleotide sequence (5`-3`)**	**Reporter oligonucleotide sequence (5`-3`)**
2	/mal/ATGGTTTAGGACTAC	GTAGTCCTAAACCAT
3	/mal/TACTCCTCGCCG	CGGCGAGGAGTA
5	/mal/TCTCCCATTAGTCGG	CCGACTAATGGGAGA
6	/mal/TGGATGTGTTACGAT	ATCGTAACACATCCA
7	/mal/CGCTAAGATATTCTAAG	CTTAGAATATCTTAGCG
8	/mal/CGCAGATGAATATTC	GAATATTCATCTGCG
11	/mal/GGGTTATACACTCGT	ACGAGTGTATAACCC
14	/mal/AGATTCAGTCTCTCG	CGAGAGACTGAATCT
15	/mal/CTGTAATAGGCACTA	TAGTGCCTATTACAG
20	/mal/ATGTAGGATGGTCTC	GAGACCATCCTACAT
21	/mal/CGTGCCGTTTCAC	GTGAAACGGCACG
23	/mal/GGTTTCCTCAGACAC	GTGTCTGAGGAAACC
24	/mal/ATAAGGGCTCATTGT	ACAATGAGCCCTTAT
25	/mal/GCACGCCCTTTTA	TAAAAGGGCGTGC
26	/mal/CACTTGTCTAACCAA	TTGGTTAGACAAGTG
28	/mal/TGGTCCACTAACGTA	TACGTTAGTGGACCA
29	/mal/ATAGGGCATTTGAAG	CTTCAAATGCCCTAT
30	/mal/CACATGAGCGAATCA	TGATTCGCTCATGTG

32	/mal/TACCAAATCCTGATG	CATCAGGATTTGGTA
33	/mal/TTATCATGAGGAGCG	CGCTCCTCATGATAA
36	/mal/ACCTACACAATGCTA	TAGCATTGTGTAGGT
38	/mal/GCGTCTACTTATAAG	CTTATAAGTAGACGC
41	/mal/TGTATGAGTAGTAATCT	AGATTACTACTCATACA
42	/mal/TCTAAGTCAGAGAGC	GCTCTCTGACTTAGA
43	/mal/GACATTATCCGTGAT	ATCACGGATAATGTC
44	/mal/TCACTACTATTAGTACT	AGTACTAATAGTAGTGA
45	/mal/GCCAGAATGCCA	TGGCATTCTGGC
46	/mal/GACTCGAACCTGAG	CTCAGGTTCGAGTC
48	/mal/GCACGGCAAAGTG	CACTTTGCCGTGC
49	/mal/ATAACGCCTCGTATC	GATACGAGGCGTTAT
52	/mal/ACCAGGTGATTGCAT	ATGCAATCACCTGGT
55	/mal/AGGTCAACTCGCAC	GTGCGAGTTGACCT
56	/mal/GGTCACATGGTCGTT	AACGACCATGTGACC
57	/mal/GCGGATTTCGTATTT	AAATACGAAATCCGC
58	/mal/CGTCAGTACTTTCAG	CTGAAAGTACTGACG
59	/mal/GCTTATTATGGACTTC	GAAGTCCATAATAAGC
61	/mal/TCTTATTCCCGAATA	TATTCGGGAATAAGA
62	/mal/TAGGGGAACAGGTTG	CAACCTGTTCCCCTA
63	/mal/AATTAGCTTAAGAGAGT	ACTCTCTTAAGCTAATT
65	/mal/GATAAATATTTTACAGAGT	ACTCTGTAAAATATTTATC
67	/mal/GACGACGAAGGC	GCCTTCGTCGTC
68	/mal/CTTCTTGTGGAACC	GGTTCCACAAGAAG
69	/mal/CCCGGCAGTT	AACTGCCGGG
70	/mal/AACCAAACTGACCG	CGGTCAGTTTGGTT
72	/mal/AACGCGACGGAT	ATCCGTCGCGTT
74	/mal/ATTTGCTTCGACGA	TCGTCGAAGCAAAT
75	/mal/CGCTTGGGTGTTTA	TAAACACCCAAGCG
76	/mal/CTGTCGGTCGTCA	TGACGACCGACAG
77	/mal/ATTTCAACAAATATTGTT	AACAATATTTGTTGAAAT

79	/mal/GCCGGAAGTGGT	ACCACTTCCGGC
81	/mal/CAAGGAACTACCGA	TCGGTAGTTCCTTG
111	/mal/GCTGGCTTCAAA	TTTGAAGCCAGC
114	/mal/ATTGACGCTAGC	GCTAGCGTCAAT

3.1.4. Primers

All primers used in this work were purchased from Sigma-Aldrich.

Table M 8: Primers used in this work.

Target	Reactivity	Primer	Sequence
Cloned TCR (plasmid linearization)	Human	Forward	TAAGTGCAGTAGTCGCCGTG
Cloned TCR (plasmid linearization)	Human	Reverse	GTGTGGCTGGCACGAAATTG

3.1.5. Chemicals and reagents

Table M 9: Chemicals and reagents used in this work.

Name	Purpose	Supplier	Reference
10% Tween 20	scRNA sequencing	Biomol GmbH	E108
16 % Formaldehyd (w/v), Methanol-free	CODEX	EMS	15710
4',6-diamidino-2-phenylindole (DAPI)	Flow cytometry	Sigma-Aldrich	D9542-1MG
Accumax™ solution	Lightning loading	Sigma-Aldrich	A7089
Agarose	Gel electrophoresis	Sigma-Aldrich	9012-36-6
Agencourt® AMPure® XP, 60 mL	scRNA sequencing/ PCR cleanup	Beckman Coulter	A63881
B-27 serum-free 50x	Lightning™ loading media	Gibco	17504044
Biocoll separating solution	PBMC isolation	Biochrom	BS.L6115
Bovine Serum Albumin (BSA), Fraction V	FC	Biomol	9048-46-8

Cytoseal 60 mounting medium	CODEX	EMS	18996
Dimethylsulfoxide (DMSO)	Cell culture	Sigma-Aldrich	41639
DNAseI from bovine Pancreas	Lightning™ loading media	Roche	11284932001
dNTPs	PCR linearization and amplification by PCR	Invitrogen, ThermoFisher Scientific	R0192
Dulbecco's Modified Eagle's Medium (DMEM)	Cell culture	Sigma-Aldrich	D6046
Dulbecco's Phosphate Buffered Saline (PBS)	Miscellaneous	Sigma-Aldrich	D8537
DynabeadsTM MyOneTM SILANE	scRNA sequencing	10X Genomics	PN-2000048
DynaMag™-2 magnetic separator rack	Magnetic bead seperation	Thermo Fisher Scientific	12321D
eBioscience Fixable Viability Dye eFluor 450	Flow cytometry	eBioscience	65086314
EDTA 0.5 M, pH 8.0	scRNA sequencing	ThermoFisher Scientific	R1021
Ethanol	Miscellaneous	Fischer Scientific GmbH	10342652
Fetal Bovine Serum (FBS)	Miscellaneous	Sigma-Aldrich	S0165
Gel Green	Gel electrophoresis	Biotium	41005-T
Gel loading dye, blue (6x)	Gel electrophoresis	New England Biolabs	B7021S
GeneRuler 1 kb Plus DNA Ladder	PCR	ThermoFisher Scientific	SM1331
Gibco Penicillin/Streptomycin (10,000 U/mL)	Cell culture	ThermoFisher Scientific	15140122
Glycerol (50%), Sterile Solution	scRNA sequencing	BioVision BV	B1012-100
High Sensitivity D1000 Reagents	scRNA sequencing/ FUME-TCR	Agilent Technologies	5067-5585
High Sensitivity D5000 Reagents	scRNA sequencing	Agilent Technologies	5067-5593
Human serum type AB	FACS sort	Sigma-Aldrich	H3667-100ML

Human serum type AB	*In vitro* TCR validation	Sigma-Aldrich	H4522-100ML
Methanol	CODEX	VWR	32213-2.5
PepTivator® CEF MHC Class I Plus	TCR-validation, viral target	Miltenyi Biotec	130-098-426
Phusion high fidelity proofreading DNA polymerase	TCR linearization and amplification by PCR	ThermoFisher Scientific	F530S
PureProteome™ Magnetic Beads	TCR-validation, positive control	Merck	LSKMAGT02
RPMI Medium 1640 without Phenol Red	mRNA transfection	Gibco	11835-063
Synth-a-Freeze™ medium	Freezing of BrM samples	Thermo Fisher Scientific	A1254201
TexMACS Medium without phenol red	Medium after utologous T cell transfection	Miltenyi Biotec	170-076-306
T Cell TransAct™, human	TCR-validation, TCR-independent stimulation	Miltenyi Biotec	130-111-160
Qiagen Buffer EB	scRNA sequencing/ PCR cleanup	Qiagen	19086
RNAse free water	Miscellaneous	Ambion	AM9937
RNase inhibitor	TCR transfection	New Englands Biolabs	M0307S
Tris-(2-carboxyethyl) phosphine hydrochloride (TCEP, 0.5 M, pH 7.0)	CODEX	Sigma-Aldrich	646547-10x 1ml
Tris–EDTA Buffer Solution, pH = 9.0	CODEX	Morphisto	1,232,802,500
Xylene	CODEX	Sigma-Aldrich	534056-4l

3.1.6. Buffers, solutions and media

Table M 10: Buffers, solutions and media used in this work, and their respective components.

Name	**Components**
CODEX antibody stabilizer solution	1 mL 5 M NaCl solution, 100 µL 500 mM EDTA (pH 8.0), 9 mL stock antibody stabilizer solution

CODEX Buffer C	1 mL 1 M Tris (pH 7.0), 1 mL of 1 M Tris (pH 7.5), 30 mL 5 M NaCl solution, 2 mL 0.5 M EDTA (pH 8.0), 0.02% NaN_3, and 1 L with ddH_2O.
CODEX bleaching solution	25 mL PBS, 4.5 mL 30% (w/v) H_2O_2, 0.8 mL 1 M NaOH.
CODEX blocking buffer	285.21 µL H_2 buffer, 14.29 µL salmon sperm DNA (10 mg/mL), 0.5 µL DAPI (5 mg/mL stock solution)
CODEX H_2 buffer	30 mL 5 M NaCl solution, 10 mL 1 M Tris (pH 7.5), 0.943 mL of Triton X-100, 2.03 g of $MgCl_2 \cdot 6H_2O$, 0.02% (w/v) NaN_3, and 1 L with ddH_2O
DMEM complete medium	DMEM high Glucose + 10% FBS + 1% Pen/Strep
High-salt PBS	45 mL 5 M NaCl solution, 25 mL 10× DPBS, 0.02% (w/v) NaN_3, and 250 mL with ddH_2O.
FC buffer for surface staining	PBS + 10% FBS + 0.05% NaN_3
FC buffer for T cell barcoding with anti-CD45	PBS + 3 mg/mL BSA + 2 mM EDTA
Freezing medium	90% FBS + 10% DMSO
Lightning™ loading media	basal RPMI lacking standard additives, + 20% 50x B27, + 20% Accumax, + 5 µL100 U/mL DNaseI
PBS-T (0.1% Tween-20)	500 mL PBS, 0.5 mL Tween-20
Tris–EDTA (TE) buffer	1 mL of 1 M Tris (pH 8.0), 200 µL of 500 mM EDTA (pH 8.0), 0.02% (w/v) NaN_3, and 100 mL with ddH_2O
Wash buffer for FACS sorting before scRNA sequencing	PBS + 2mM EDTA + 0.5% human Serum
MACS buffer for FACS sorting before scRNA sequencing	PBS + 5% human Serum
TAE buffer	40 mM Tris, 20 mM acetate, 1 mM EDTA, pH 8.0

3.1.7. Kits

Table M 11: Commercial kits used in this work.

Name	Purpose	Supplier	Reference
$CD8^+$ T cell isolation kit, human	$CD8^+$ T cell isolation of expansion from PBMCs	Miltenyi Biotech	130-096-495

Akoya Staining Kit: Staining, hydration and storage buffer, N-, J-, S-blocker and final fixative reagent (Akoya Biosciences).	CODEX staining	Akoya	7000008
Chromium™ Next GEM Chip K Single Cell Kit, 16 rnxs	scRNA sequencing	10X Genomics	PN-1000287
Chromium™ Next GEM Single Cell 5' Kit v2, 16 rnxs	scRNA sequencing	10X Genomics	PN-1000263
Dual Index Kit TT Set A, 96 rnxs	scRNA sequencing	10X Genomics	PN-1000215
EasySep™ Dead cell removal (Annexin V)	Dead cell removal	StemCell Technologies	17899
Library Construction Kit, 16 rnxs	scRNA sequencing	10X Genomics	PN-1000190
Neon Transfection System	mRNA transfection	Invitrogen	MPK1025
T7 mScript Standard mRNA Production System	In Vitro transcription of TCR constructs	CellScript	C-MSC100625
X-Vivo™ 20 Serum-free Hematopoietic Cell Medium	T cell expansion from PBMCs	Lonza	04-448Q

3.1.8. Consumables

Table M 12: Consumables used in this work.

Name	Purpose	Supplier	Reference
12-Well Flat Bottom Plate	Cell culture	Techno Plastic Products (TPP)	Z707775-126EA
50-kDa Amicon Ultra 0.5-mL centrifugal filter columns	Conjugation of CODEX antibodies	EMD Millipore	41104916
Black 96-well plate			
Corning® Plastic Serological Pipettes (5 mL, 10 mL, 25 mL, 50 mL)	Miscellaneous	Corning	CLS4487, CLS4488, CLS4489, CLS4490
Corning® Costar® Reagent Reservoirs (50 mL)	FC staining	Corning	CLS4870-5EA
Cryo.s, 2 mL	Cell culture	Greiner Bio-one	TPP91014, TPP91050

DNA LoBind Tubes, DNA LoBind, 1.5 mL	scRNA sequencing	Eppendorf	22431021
Eppendorf Safe-Lock Microcentrifuge Tubes	Miscellaneous	Eppendorf	22363204
Falcon® Polystyrene Round Bottom Tubes (5 mL)	FACS/ FC staining	Corning	352052
Falcon® 70 µm Cell Strainer	Cell culture	Corning	352350
Flow cells	CODEX imaging	Akoya Biosciences	240204
gentleMACS™ C Tubes	Tissue dissociation	Miltenyi Biotec	130-093-237
High Sensitivity D1000 ScreenTape	scRNA sequencing	Agilent Technologies	5067-5584
High Sensitivity D5000 ScreenTape	scRNA sequencing	Agilent Technologies	5067-5592
Leucosep™ tubes	PBMC isolation	Greiner Bio-One	227288
Pipette Tips (10 µL, 20 µL, 100 µL, 200 µL, 300 µL, 1000 µL)	Miscellaneous	Steinbenner Laborsysteme	TP50010, TP50020, TP50100, TP50200, TP50300, TP51250
Vi-CELL™ XR Tubes	Cell culture	Beckman Coulter	383721

3.1.9. Equipment and devices

Table M 13: Equipment and devices used in this work.

Name	Purpose	Supplier
10x Magnetic Separator	scRNA sequencing	10X Genomics
10x Vortex Adapter	scRNA sequencing	10X Genomics
4150 TapeStation	TCR mRNA QC	Agilent Technologies
4200 TapeStation	scRNA sequencing	Agilent Technologies
Axygen® Gel Documentation System	Length determination of PCR product	Corning, Life Sciences
Accu-jet® pro Pipette Controller	Miscellaneous	BrandTech
BD FACSAriaTM Fusion	FACS sorting	BD (Becton, Dickinson & Company)

BD LSRFortessa™	FC measurement	BD (Becton, Dickinson & Company)
C1000 Touch™ Thermal Cycler	scRNA sequencing	Bio-Rad Laboratories
Mastercycler X40	TCR mRNA generation	Eppendorf
Cell Culture Safety Cabinet, Herasafe KS	Cell culture	ThermoFisher Scientific
Centrifuge Rotina 380R	Miscellaneous	Hettich Zentrifugen
Centrifuge Varifuge 3.OR	Miscellaneous	Heraeus Sepatech
Cetntrifuge Heraeus Fresco 17	Miscellaneous	ThermoFisher Scientific
Chromium™ Next GEM Secondary Holder	scRNA sequencing	10X Genomics
Chromium™ Single Cell Controller Instrument	scRNA sequencing	10X Genomics
EasySep™ Magnet	Cell culture	StemCell Technologies
Eppendorf ThermoMixer C	scRNA sequencing	Eppendorf
FastGene Mini Centrifuge	scRNA sequencing	Nippon Genetics
Flow cell mounting device	CODEX imaging	Akoya Biosciences
gentleMACS™ Octo Dissociator	Tissue dissociation	Miltenyi Biotec
Heracell 150i Incubator	Cell culture	ThermoFisher Scientific
Heracell 240i Incubator	Cell culture	ThermoFisher Scientific
Illumina HiSeq 4000	scRNA sequencing	Illumina Inc.
LED Panel (4100-4600LUX)	CODEX staining	AGPTEK
Mr. Frosty™ Freezing Container	Cell culture	ThermoFisher Scientific
NanoDrop	RNA isolation	NanoDrop Technologies
PhenoCycler (CODEX)	CODEX imaging	Akoya Biosciences
PIPETMAN L Multichannel P8x200L, 20-200 µL	Miscellaneous	Gilson
Pipettes (2 µL, 20 µL, 100 µL, 200 µL, 1000 µL)	Miscellaneous	Gilson
Qubit 4.0 Fluorometer	scRNA sequencing	ThermoFisher Scientific
Thermo electrophoresis power supply	Gel electrophoresis	Thermo EC250-90
Vi-CELL XR 2.03	Cell culture	Beckman Coulter Inc.
Vortex Mixer Neolab 7-2020	Miscellaneous	neoLab Migge

Water Bath Julabo SW-20C	Miscellaneous	Julabo

3.1.10. Software

Table M 14: Software used in this work.

Name	Purpose	Source	Version
Affinity Designer	Figure-making	Serif Ltd, West Bridgford	V2.0
BD FACSDiva™	FC data acquisition	BD (Becton, Dickinson & Company), Franklin Lakes	V9.0
BioRender	Figure-making	BioRender, Toronto, Canada	2023
ChatGPT	Language refinement	OpenAI	GPT-5.3
EndNote™	Reference management	Thomson Reuters, Carlsbad	X 20
FlowJo	FC data analysis	BD (Becton, Dickinson & Company)	V10
GraphPad Prism	Statistical analysis, graphic-making	GraphPad Software, San Diego, USA	V9.0
Microsoft Excel	Data analysis	Microsoft, Redmond	2016
Microsoft PowerPoint	Data presentation	Microsoft, Redmond	2016
Microsoft Word	Document-writing	Microsoft, Redmond	2016
R	Bioinformatics analysis	The R Foundation	V4.2.2

3.1.11. Declaration of the use of artificial intelligence (AI)

The AI-based language model ChatGPT (OpenAI) was used exclusively for linguistic refinement; all scientific content, data analysis, and interpretation were developed and verified by me.

3.2. Methods

3.2.1. Single-cell transcriptome and TCR analysis

Fresh-frozen single-cell suspensions were provided by the research group of Prof. Dr. Herold-Mende at the University Hospital Heidelberg. The study was conducted with approval from the Ethics Committee of the Medical Faculty, Heidelberg University (reference no. 005/2003). Written informed consent was secured from all patients prior to inclusion, in accordance with the principles outlined in the Declaration of Helsinki and its subsequent amendments.

3.2.1.1. Clinical sample processing and cryopreservation of BrM tissue

Immediately following neurosurgical resection, brain metastatic tissue was transported to the laboratory. Under sterile conditions, visibly cauterized or necrotic areas were macroscopically excised. The remaining tissue was minced into approximately 1 mm^3 fragments and transferred into gentleMACS™ C Tubes (Miltenyi Biotec). Combined mechanical and enzymatic dissociation was performed utilizing a gentleMACS™ Octo Dissociator (Miltenyi Biotec) in Hank's Balanced Salt Solution (HBSS) supplemented with 0.0125% Liberase and 0.04% DNase I for subsequent functional assays. Following dissociation, erythrocytes were lysed for 3 minutes using an ammonium chloride lysis buffer (150 mM NH_4Cl, 10 mM $KHCO_3$, 0.1 mM EDTA). The resulting single-cell suspensions were filtered through 100 µm and 40 µm cell strainers, cryopreserved in Synth-a-Freeze™ medium (Thermo Fisher Scientific), and stored in liquid nitrogen.

3.2.1.2. Peripheral Blood Mononuclear Cell (PBMC)isolation

Matched peripheral blood was collected on the day of surgery for the isolation of PBMCs. Density gradient centrifugation was performed using 20 mL of heparin-anticoagulated blood loaded into Leucosep™ tubes (Greiner Bio-One) containing 15 mL of Biocoll separating solution (Biochrom). Samples were centrifuged at 700 × g for 20 minutes at room temperature. The mononuclear cell layer was carefully harvested, washed twice with PBS, cryopreserved, and stored in liquid nitrogen until further use.

3.2.1.3. Fluorescence-Activated Cell Sorting (FACS) of Lymphocytes

Cryopreserved single-cell suspensions of human BrM and matched PBMCs were processed for downstream single-cell RNA sequencing (scRNA-seq). For BrM samples,

both T cells and B cells were isolated, whereas only T cells were isolated from the PBMC samples.

Samples were thawed in 20 mL of Dulbecco's Modified Eagle Medium (DMEM) supplemented with 10% fetal bovine serum (FBS) and 1% penicillin/streptomycin. The cell suspensions were passed through a 70 µm cell strainer and centrifuged at 2000 rpm for 2 minutes at 4 °C. The resulting cell pellets were washed once in wash buffer PBS containing 2 mM EDTA and 0.5% human AB serum (Sigma-Aldrich, #H3667), centrifuged again, and resuspended to a concentration of 5×10^7 cells/mL in wash buffer.

To maximize the viability of the sorted populations, dead cells were magnetically depleted utilizing the EasySep™ Dead Cell Removal (Annexin V) Kit (STEMCELL Technologies, #17899). Briefly, 50 µL/mL of Annexin V Dead Cell Removal Cocktail and 50 µL/mL of Biotin Selection Cocktail were added to the samples and incubated for 3 minutes at room temperature (RT). Subsequently, 100 µL/mL of pre-vortexed Magnetic RapidSpheres™ were added. Immediately following mixing, 2.5 mL of wash buffer was added. The suspension was incubated for an additional 3 minutes at RT, and the supernatant containing the live cell fraction was collected into 5 mL polystyrene round-bottom tubes. Cells were washed once with 2 mL of wash buffer, centrifuged (2000 rpm, 2 minutes, 4 °C), and maintained on ice.

For flow cytometric sorting, cells were resuspended at a density of 1×10^6 cells per 100 µL of wash buffer. To exclude dead cells, eBioscience™ Fixable Viability Dye eFluor™ 450 (Thermo Fisher Scientific, #65-0863-14; 1:1000 dilution) was applied. Single-cell suspensions from BrM tissue were co-stained with APC-conjugated anti-human CD3 (BioLegend, #317318; 1:200 dilution) and APC-conjugated anti-human CD19 (BioLegend, #302212; 1:50 dilution) for 30 minutes at 4 °C in the dark. Because physical separation of T and B cells was not required for the downstream scRNA-seq pipeline, both targeting antibodies utilized the same fluorophore (APC). For PBMC samples, only the anti-CD3 antibody was utilized.

Following staining, cells were washed twice with 1 mL of ice-cold wash buffer, centrifuged, and resuspended at a concentration of 6×10^6 cells/mL in MACS buffer. Cell sorting was performed on a BD cell sorter operated with BD FACSDiva™ software (version 8.0.2; BD Biosciences), utilizing a 100 µm nozzle and the "4-way purity" sort mode. The gating strategy (Figure M 1) consisted of an initial morphological gate to identify singlets, followed by the exclusion of dead cells (eFluor 450-positive) and the positive selection of target lymphocytes (APC-positive). The sorted lymphocytes were collected directly into 1.5 mL Safe-Lock tubes and stored on ice for immediate downstream processing.

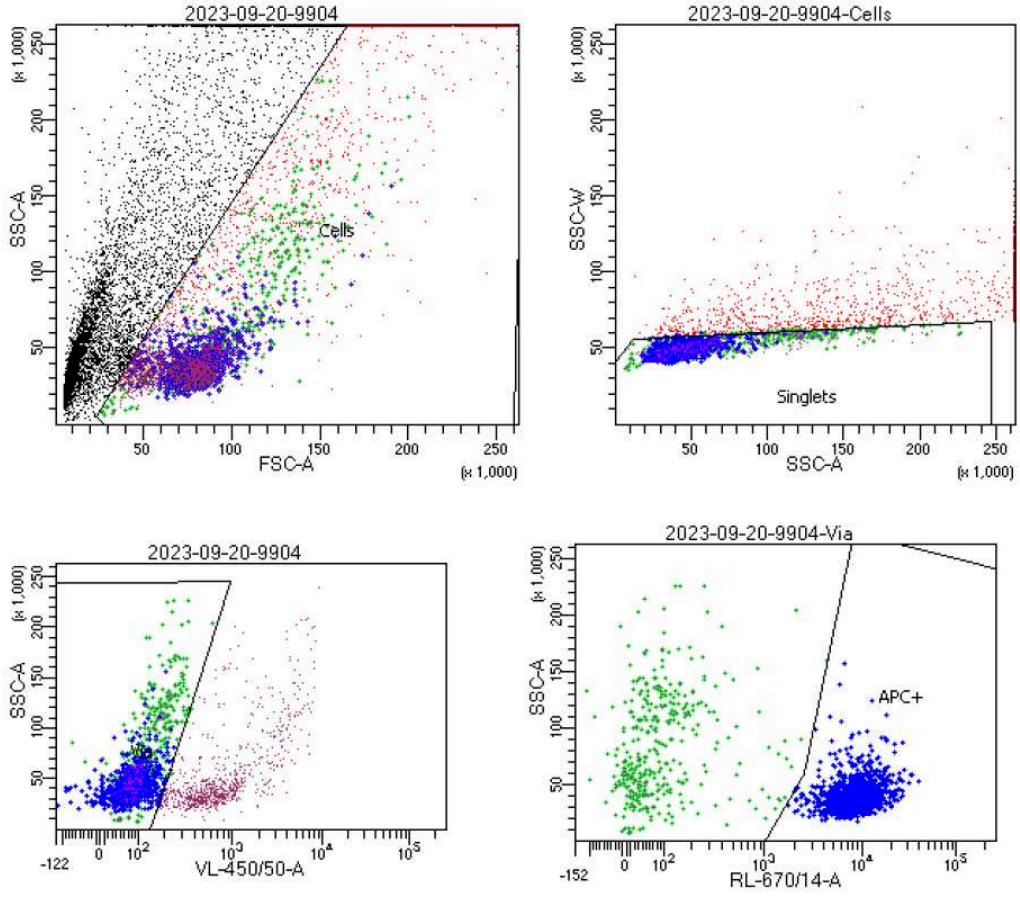


Figure M 1: Representative sorting-strategy for brain metastasis-infiltrating lymphocytes

Single cell suspensions stained with fluorescent-labelled antibodies against CD3 (APC) and CD19 (APC). Viability was assessed with the fixable viability dye eFluor450. Sorting was performed in collaboration with the FACS core facility at DKFZ at a DB FACSAria™ Fusion machine with a 100M nozzle and a 4-way purity. The plots were automatically generated in the software BD FACSDiva 9.4.

3.2.1.4. Generation of cDNA from lymphocytes coming from human BrM samples or PBMCs

Single-cell transcriptomes were generated from the samples using the Chromium Next GEM Single Cell 5' GEM Kit v2 (10X Genomics; #PN-1000190, #PN-1000263), following the manufacturer's protocol. For a target recovery of 10,000 cells per sample, 20,000 cells were loaded onto the Chromium Next GEM Chip K, except for two brain metastases samples. For NCH8937 and NCH9348, only 12,928 and 11,000 cells were loaded, respectively, due to limited lymphocytes available after FACS sorting. The loaded cells were processed in the Chromium Single Cell Controller to generate Gel Bead-in-Emulsion (GEMs), which were then transferred from the chip's recovery wells to an ice-chilled tube

strip. The tube strip underwent reverse transcription and barcoding in a thermal cycler using the following program:

Lid temperature	**Reaction volume**	**Run time**
53 ºC	125 µL	~ 55 min
Step	**Temperature**	**Time**
1	53 ºC	00:45:00
2	85 ºC	00:05:00
3	4 ºC	Hold

Before post-GEM reverse transcription cleanup, all reagents were equilibrated to room temperature (RT). The recovery agent was added to the samples in the tube strip, mixed by gentle inversion (four times), and incubated for 2 min. The oil phase was then carefully aspirated and discarded from the biphasic mixture, avoiding disturbance of the aqueous phase. Dynabeads Cleanup Mix was prepared according to the manufacturer's instructions and added to the samples, followed by thorough pipetting to resuspend. The mixture was incubated at RT for 10 min, with additional mixing after 5 min. The tube strip was placed on a 10x Magnetic Separator (High position) for 2 min; the supernatant was discarded, and beads were washed twice with 80% ethanol (30 s each). After brief centrifugation, the tube strip was repositioned on the magnet (Low position), residual ethanol was removed, and samples were air-dried for 1.5 min. The tube strip was removed from the magnet, and 35.6 µL Elution Solution I was added to each tube. Samples were incubated at RT for 1 min, placed on the magnet (Low position), and 35 µL of cleared eluate was transferred to a new tube strip. cDNA Amplification Mix was prepared on ice and added to each sample. Amplification proceeded in a thermal cycler as follows:

Lid temperature	Reaction volume	Run time
105 ºC	100 µL	~ 25-50 min
Step	**Temperature**	**Time**
1	98 ºC	00:00:45
2	98 ºC	00:00:20
3	63 ºC	00:00:30
4	72 ºC	00:01:00
5	Go to step 2 (x12)	13 cycles
6	72 ºC	00:01:00
7	4 ºC	Hold

cDNA amplification cycles were adjusted based on target cell recovery and RNA content, for a total of 13 cycles. AMPure beads (Beckman Coulter, #A63881) were vortexed and added at a 0.6× ratio to each sample, followed by thorough mixing. The mixture was incubated for 5 min at room temperature (RT), placed on a 10x Magnetic Separator (High position) for 2 min, and the supernatant was discarded. Samples were washed twice with 80% ethanol (30 s each), briefly centrifuged, repositioned on the magnet (Low position), residual ethanol removed, and air-dried for 1.5 min. The tube strip was removed from the magnet, 45.5 µL Buffer EB added, and incubated at RT for 2 min. Samples were placed on the magnet (High position) for 2 min, and 45 µL of cleared eluate transferred to a new tube strip kept on ice. cDNA concentration was quantified using a NanoDrop spectrophotometer (NanoDrop Technologies), and quality assessed via Agilent TapeStation (Agilent Technologies).

3.2.1.5. Single cell gene expression library construction

Gene expression (GEX) libraries were generated from cDNA (section 3.2.1.4) via fragmentation, end repair, and A-tailing. Fifty ng of cDNA per sample was transferred to a new tube strip and adjusted to 20 µL with Buffer EB. Fragmentation Mix (30 µL) was

prepared on ice and added to the cDNA (also on ice). Samples were incubated in a thermal cycler as follows:

Lid temperature	**Reaction volume**	**Run time**
65 ºC	50 µL	~ 35 min
Step	**Temperature**	**Time**
Pre-cool block	4 ºC	Hold
Fragmentation	32 ºC	00:05:00
End repair and A-tailing	65 ºC	00:30:00
Hold	4 ºC	Hold

Post-fragmentation, end repair, and A-tailing were performed, followed by double-sided size selection of cDNA fragments. AMPure beads (0.6×) were added to the samples, which were placed on a 10x Magnetic Separator; supernatants were collected and mixed with AMPure beads (0.8×). Two washes with 80% ethanol (30 s each) were performed as described previously. Tubes were removed from the magnet, 50.5 µL Buffer EB added, and incubated at room temperature (RT) for 2 min. Samples were placed on the magnet (High position) for 2 min, and 50 µL of cleared eluate transferred to a new tube strip.

Adaptor Ligation Mix was prepared and added at a 1:1 ratio to each sample, followed by thorough pipetting. Ligation proceeded in a thermal cycler as follows:

Lid temperature	**Reaction volume**	**Run time**
30 ºC	100 µL	~ 15 min
Step	**Temperature**	**Time**
1	20 ºC	00:15:00
2	4 ºC	Hold

Post-ligation cleanup was performed by adding 0.8× AMPure beads, followed by 80% ethanol washes as described previously. 30 µL of each sample was transferred to a new tube strip for Sample Index PCR. Amp Mix (50 µL) and 20 µL of individual Dual Index TT

Set A wells (PN-3000431) were added to each sample. Indexing proceeded in a thermal cycler as follows:

Lid temperature	Reaction volume	Run time
105 ºC	100 µL	~ 30 min
Step	**Temperature**	**Time**
1	98 ºC	00:00:45
2	98 ºC	00:00:20
3	54 ºC	00:00:30
4	72 ºC	00:00:20
5	Go to step 2 (x13)	14 cycles
6	72 ºC	00:01:00
7	4 ºC	Hold

Double-sided size selection of GEX libraries was performed using AMPure beads and 80% ethanol washes. AMPure beads (0.6×) were added to the samples, which were placed on a 10x Magnetic Separator; supernatants were collected and mixed with AMPure beads (0.8×). Two washes with 80% ethanol (30 s each) were performed as described previously. The tube strip was removed from the magnet, 35.5 µL Buffer EB added to each sample, and incubated at room temperature (RT) for 2 min. Samples were placed on the magnet (Low position), and 35 µL of cleared eluate transferred to DNA-low-binding 1.5 mL safe-lock tubes. Library quality was assessed using Agilent TapeStation, and concentrations quantified via NanoDrop (NanoDrop Technologies).

3.2.1.6. Single cell V(D)J cDNA amplification

V(D)J genes were amplified from 2 µL of amplified cDNA (section 3.2.1.4) mixed with V(D)J Amplification 1 Reaction Mix prepared on ice. A customized T cell Mix 1 v2 was obtained from the Single-cell OpenLab. Reactions were incubated in a thermal cycler as follows:

Lid temperature	Reaction volume	Run time
105 ºC	100 µL	~ 20 - 30 min
Step	**Temperature**	**Time**
1	98 ºC	00:00:45
2	98 ºC	00:00:20
3	62 ºC	00:00:30
4	72 ºC	00:01:00
5	Go to step 2 (x11)	12 cycles
6	72 ºC	00:01:00
7	4 ºC	Hold

Double-sided size selection was performed on the amplified V(D)J cDNA. AMPure beads (0.5×) were added to the samples, which were placed on a 10x Magnetic Separator; supernatants were collected and mixed with AMPure beads (0.8×). Two washes with 80% ethanol (30 s each) were performed as described previously. Tubes were removed from the magnet, 35.6 µL Buffer EB added, and incubated at room temperature (RT) for 2 min. Samples were placed on the magnet (High position) for 2 min, and 35 µL of cleared eluate transferred to a new tube strip. V(D)J Amplification 2 Reaction Mix was prepared on ice using customized T Cell Mix 2 v2 from the Single-cell OpenLab, followed by thermal cycling:

Lid temperature	Reaction volume	Run time
105 ºC	100 µL	~ 20 - 30 min
Step	**Temperature**	**Time**
1	98 ºC	00:00:45
2	98 ºC	00:00:20
3	62 ºC	00:00:30
4	72 ºC	00:01:00
5	Go to step 2 (x9)	10 cycles
6	72 ºC	00:01:00
7	4 ºC	Hold

Cleanup and double-sided size selection of V(D)J libraries were performed using AMPure beads. AMPure beads (0.5×) were added to the samples, placed on a 10x Magnetic Separator, and supernatants recovered; these were then mixed with AMPure beads (0.8×) as described previously. After two 80% ethanol washes (30 s each), beads were air-dried for 1 min, resuspended in 45.5 µL Buffer EB, and incubated at room temperature (RT) for 2 min. Samples were placed on the magnet (Low position), and 45 µL of cleared eluate transferred to new tubes. Library quality was assessed using Agilent TapeStation, and concentrations quantified via NanoDrop (NanoDrop Technologies).

3.2.1.7. Single cell V(D)J library construction

V(D)J libraries were generated from V(D)J cDNA (section 3.2.1.6) via initial fragmentation.

50 ng of V(D)J cDNA per sample was transferred to a new tube strip and adjusted to 20 µL with Buffer EB. Fragmentation Mix (30 µL) was prepared on ice and added to the cDNA (also on ice). Samples were incubated in a thermal cycler as follows:

Lid temperature	Reaction volume	Run time
65 ºC	50 µL	~ 35 min
Step	**Temperature**	**Time**
Pre-cool block	4 ºC	Hold
Fragmentation	32 ºC	00:02:00
End repair and A-tailing	65 ºC	00:30:00
Hold	4 ºC	Hold

Adaptor Ligation Mix was prepared and added at a 1:1 ratio to each sample, followed by thorough pipetting. Ligation proceeded in a thermal cycler as follows:

Lid temperature	Reaction volume	Run time
30 ºC	100 µL	~ 15 min
Step	**Temperature**	**Time**
1	20 ºC	00:15:00
2	4 ºC	Hold

Post-ligation cleanup was performed by adding 0.8× AMPure beads, followed by 80% ethanol washes as described previously. 30 µL of each sample was transferred to a new tube strip for Sample Index PCR. Amp Mix (50 µL) and 20 µL of individual Dual Index TT Set A wells (PN-3000431) were added to each sample. Indexing proceeded in a thermal cycler as follows:

Lid temperature	Reaction volume	Run time
105 ºC	100 µL	~ 30 min
Step	**Temperature**	**Time**
1	98 ºC	00:00:45
2	98 ºC	00:00:20
3	54 ºC	00:00:30
4	72 ºC	00:00:20
5	Go to step 2 (x7)	8 cycles
6	72 ºC	00:01:00
7	4 ºC	Hold

Cleanup of V(D)J libraries was performed using AMPure beads and 80% ethanol washes. AMPure beads (0.8×) were added to the samples, which were placed on a 10x Magnetic Separator. Two washes with 80% ethanol (30 s each) were performed as described previously. The tube strip was removed from the magnet, beads air-dried for 1.5 min, and 35.5 µL Buffer EB added to each sample. Samples were incubated at room temperature (RT) for 2 min, placed on the magnet (Low position), and 35 µL of cleared eluate transferred to DNA-low-binding 1.5 mL safe-lock tubes. Library quality was assessed using Agilent TapeStation, and concentrations quantified via NanoDrop (NanoDrop Technologies).

3.2.1.8. Sequencing of single cell libraries

GEX and V(D)J libraries were pooled at a 4:1 ratio (GEX:V(D)J) and sequenced on a NovaSeq 6000 (Illumina) using paired-end 150 bp reads on an S4 flow cell. Sequencing was conducted at the DKFZ Next-Generation Sequencing (NGS) Core Facility.

3.2.2. Bioinformatic processing of single cell RNA and TCR sequencing data

Processing of scRNA/TCR-seq data including dimensional reduction, cell cluster visualization and identification of differentially expressed genes was performed by Karol Jacek (PhD student, group of Prof. Dr. Bożena Kamińska, Nencki Institute, Warsaw) under supervision of Dr. Marc Zapatka (DKFZ) for the BrM-derived T cells, while Dr. Marc Zapatka

performed the bioinformatic analysis of the peripheral blood-derived T cells and the bioinformatic analysis of TCR sharing between the blood and BrM compartment.

3.2.2.1. Bioinformatic processing of brain metastasis-derived T cells

Single-cell RNA-seq data analysis was performed using R (v4.4.0) and the Seurat package. For the brain metastases dataset, raw feature-barcode matrices from 9 samples were loaded and merged. Quality control (QC) was performed by filtering cells based on mitochondrial content (percent_mito < 5%) and total unique molecular identifiers (UMIs) (nCount_RNA < 1200; see note above regarding this value). Doublets were identified and removed using the “scDblFinder” package, applying a score threshold of > 0.9 to each sample independently. Cell cycle phase scores were assigned using the “CellCycleScoring” function based on standard S and G2/M gene sets. A similar preprocessing pipeline was applied to the paired PBMC-derived T cell dataset, including independent normalization and variable feature selection.

To correct for batch effects, the data was integrated using Seurat’s Reciprocal PCA (RPCA) workflow. Features were selected for integration, and anchors were identified using “FindIntegrationAnchors” (reduction = "rpca", dims = 1:13). The integrated data was scaled and subjected to Principal Component Analysis (PCA). Uniform Manifold Approximation and Projection (UMAP) was calculated using the first 13 principal components to visualize the data. For the brain dataset, a second processing step was applied to mitigate stress-response artifacts. Heat shock protein (HSP) related genes were regressed out during the “ScaleData” step, followed by re-clustering and recalculation of UMAP visualization to better preserve local density information. Clustering was performed using the Louvain algorithm (“FindClusters”) at resolutions ranging from 0.7 to 1.1. I performed manual cluster-annotation by cross-referencing cluster-specific marker genes and canonical marker expression and visualized using “DimPlot” and “FeaturePlot”.

Single-cell TCR-seq data was processed using the “scRepertoire” package. Contig annotation files for the BrM samples were loaded, and non-cellular barcodes were removed. Clonotypes were defined based on the “CTstrict” metric (combined nucleotide sequence of TRA and TRB chains). Clonal expansion were visualized using custom scripts. The relative abundance of clonotypes was categorized into expansion groups (Hyperexpanded, Large, Medium, Small, Rare, Unique) and visualized using 100% stacked bar plots to compare the clonal landscape between samples. To identify putative virus-reactive T cells, TCRb CDR3 amino acid sequences were matched against the VDJdb database (filtered for "HomoSapiens" and "synthetic" epitopes). Matching was performed using the Levenshtein

distance metric via the “stringdist” package, allowing for a maximum edit distance of 1 amino acid mismatch to account for cross-reactivity or sequencing errors.

A composite cytotoxicity score and a memory score were calculated using the “AddModuleScore” function based on the expression of *PRF1*, *NKG7*, *GZMB*, and *FASL* (cytotoxicity score) and *IL7R*, *CCR7*, *SELL*, *CXCR3*, *EOMES*, and *CD44* (memory score). Visualization of continuous variables (gene expression and module scores) was performed using Nebulosa, which utilizes kernel density estimation to visualize expression distinctness in sparse single-cell data. Categorical data and cluster distributions were visualized using Seurat and “SCpubr”. All plots were generated using ggplot2 with custom color palettes for consistency.

3.2.2.2. Bioinformatic processing of peripheral blood-derived T cells and TCR sharing

For preprocessing and quality control raw 10x Genomics feature-barcode matrices were loaded into R (v4.5.2) using Seurat (v5.4.0). For each sample, per-cell quality metrics were computed, including the percentage of mitochondrial and ribosomal reads. Doublets were identified with “scDblFinder” using default parameters. Cells were filtered to retain those with 500–6,000 detected genes, ≤20,000 UMI counts, <5% mitochondrial reads, <60% ribosomal reads, and classified as singlets by “scDblFinder”.

For normalization, cell cycle scoring, and integration, filtered objects were normalized with “SCTransform”. Samples were integrated using the SCT workflow: 3,000 integration features were selected with “SelectIntegrationFeatures”, prepared via PrepSCTIntegration, merged, and subjected to PCA (50 PCs). Batch correction across samples was performed with “IntegrateLayers” using reciprocal PCA (RPCA). Downstream neighbor graph construction, Louvain clustering (resolutions 0.2–0.8), and UMAP embedding were computed on the first 30 RPCA dimensions.

For cell type annotation cell identities were assigned by reference mapping with Azimuth using the human PBMC reference (pbmcref), providing predicted labels at levels 1 and 2 with associated prediction scores. Annotations were retained at score thresholds of ≥0.4; cells below threshold were labeled "Unassigned." Non-T-cell populations (B naive, B memory, B intermediate, dnT) were removed, and clustering, UMAP, and Azimuth annotation were re-run on the filtered object. Marker gene expression (e.g., *PTPRC, CD3D, CD4, CD8A, FOXP3, GZMB, MKI67*) was visualized on the RNA assay after “JoinLayers” and log-normalization.

For the TCR repertoire analysis filtered contig annotations from Cell Ranger VDJ output were processed with “scRepertoire”. Per-sample TCR contigs were combined with “combineTCR”, and clonotype metadata (CTaa, CTnt, CTstrict, clonal frequency and proportion) were added to the Seurat object with “combineExpression”. Clonal expansion was categorized into homeostatic size bins (Unique, Rare, Small, Medium, Large, Hyperexpanded) based on clonal proportion. Shared clonotypes between matched blood and tumor samples from the same patient were identified on amino acid CDR3αβ sequences (CTaa) and visualized as scatter plots of per-compartment clone fractions and Venn diagrams (“ggVennDiagram”).

Known antigen specificities were annotated by querying VDJdb (human TRA/TRB entries). For each (chain, CDR3) pair the highest-confidence record was retained, and hits were mapped to cells by matching the TRA and TRB CDR3 amino acid sequences parsed from CTaa, annotating epitope, epitope gene/species, and MHC class/allele.

QC metrics, UMAPs, dot plots of marker genes, cell-type distribution bar plots, clonal expansion projections, and shared-clonotype plots were generated with ggplot2, patchwork, and Seurat visualization functions. All analyses used a fixed random seed (42) for reproducibility.

3.2.3. Bulk-TCRβ sequencing

Bulk-TCRβ sequencing was performed of T cells from cryopreserved PBMCs of patient samples NCH9230, NCH9348, NCH9488, and NCH9587 by the group of Dr. Isabel Poschke at the German Cancer Research Center (DKFZ). The raw data was obtained and bioinformatic analysis was performed by Karol Jacek (PhD student, group of Prof. Dr. Bożena Kamińska, Nencki Institute, Warsaw) under supervision of Dr. Marc Zapatka (DKFZ).

Initial quality control and basic repertoire profiling were conducted by quantifying the total number of unique clonotypes and overall sequence read depth for each sample. To evaluate the complexity and clonal evenness of the T-cell repertoires, multiple established diversity metrics were computed, specifically the D50 index, Gini-Simpson index, and Inverse-Simpson index. These metrics were chosen to provide a comprehensive assessment of both species richness and dominant clonal expansion within the tissue. All repertoire processing, diversity estimations, and subsequent visualizations were performed in the R statistical computing environment, primarily utilizing the “immunarch” framework for “immunosequencing” analysis.

3.2.4. Generation of TCR-transgenic cells

The following sub-chapters describe step by step the generation of TCR-transgenic cells.

3.2.4.1. Cloning of selected TCRs into Lentiviral Vectors

Output files containing selected TCR sequences from the 10x Genomics scRNA/TCR-seq analysis of patient samples NCH8937 and NCH9348 were processed using the open-source software platform "makeTCR" (https://maketcr.com). The selected sequences were cloned into a third-generation lentiviral transfer plasmid conferring ampicillin resistance, with the TCR cassette expressed under the control of a T7 promoter. For downstream experiments, to prevent mispairing with endogenous human TCRs and to facilitate the unambiguous detection of transgenic TCR expression via flow cytometry, murine constant regions were incorporated into the constructs. The cloning procedure was performed by the research group of Dr. Edward Green at the DKFZ, following the protocol described by (Hamberger et al., 2025).

3.2.4.2. Linearization and amplification of TCR DNA

Plasmid vectors containing the TCR sequences of interest were linearized and subsequently amplified via polymerase chain reaction (PCR). A PCR master mix was prepared on ice, consisting of 1× Phusion™ HF Buffer, 200 µM dNTPs, 0.5 µM of both forward and reverse primers (detailed in Table M 8), 0.5 ng of template vector DNA, and 0.02 U/µL of Phusion™ High-Fidelity DNA Polymerase (Thermo Fisher Scientific, # F530S). The reaction was performed in a thermal cycler according to the following protocol:

Step	Temperature	Time
Initial denaturation	95 ºC	00:03:00
Denaturation	98 ºC	00:00:20
Annealing	60 ºC	00:00:15
Extension	72 ºC	00:02:00
	Go to step 2 (x34)	35 cycles
Final extension	72 ºC	00:02:42
Hold	4 ºC	Hold

Following amplification, the PCR products were purified using AMPure XP magnetic beads (Beckman Coulter, #A63881). Briefly, a 1.8× volume of AMPure XP beads was added to each PCR sample, mixed, and incubated for 5 minutes at RT. The tubes were then placed on a magnetic rack for 2 minutes to allow for bead separation. The supernatant was carefully aspirated, and the bead pellet was washed twice with 70% ethanol. The beads were air-dried for 2 minutes and subsequently resuspended in 16 µL of Elution Buffer (EB, Qiagen, #19086). Following a 5-minute incubation at RT, the tubes were placed back on the magnetic rack for 2 minutes. The cleared supernatant containing purified DNA was transferred into a fresh DNA low-binding Safe-Lock tube. The final DNA concentration was quantified using a NanoDrop spectrophotometer (NanoDrop Technologies), and the purified DNA was stored at -20 °C until further use.

3.2.4.3. Agarose gel electrophoresis

The correct length of the PCR product was validated by gel electrophoresis. A 1.5x agarose (Sigma-Aldrich, #9012-36-6) gel was prepared containing gel-green (Biotium, #41005-T). 2 µl of the PCR product after cleanup was mixed with loading buffer (New England Biolanbs, # B7021S) and filled up to 10 µl with water. The mix was loaded into the gel chambers within 1x TAE buffer and run for 50 minutes at 130 V and 500 mA (Thermo EC250-90) taking along a gene ruler DNA ladder (Thermo Fisher, SM1331). Subsequently, DNA bands on the gel were investigated at the Axygen® gel documentation system (Corning, Life Sciences). Correctly amplified TCR DNA has a length of 2.7 kB.

3.2.4.4. Generation of TCR mRNA

TCR mRNA was performed by *in vitro* transcription (IVT) using the T7 mScript™ Standard mRNA Production System (Cellscript™, #C-MSC100625), using either the original protocol or half of the volumes mentioned in the original protocol. In case of the reduced protocol, RNA was generated by mixing 3.15 µl of linearized RNA template DNA containing the T7 RNA promoter with 1 µl mScript T7 transcription buffer, 3.6 µl NTP solution, 1µl of 100mM DTT, 0.25 µl ScriptGuard RNase Inhibitor and 1 µl mScript T7 Enzyme Solution. This mix was incubated for 60 minutes at 37°C in a headblock of a thermal cycler. Subsequently the DNA template was removed by the addition of 0.5 µl RNase-Free DNase I and incubated for 15 minutes at 37°C. RNA was purified using RNA-Clean-XP beads in a 1x ratio. For this, RNase-free water was added to the samples to reach a volume of 40 µl and then the XP beads were added (1x) and pipette mixed. After 5 minutes of incubation at RT the samples were subjected to a magnet for 2 minutes. Supernatant was aspirated and the beads washed twice with 80 % ethanol. Beads were dried for 1.5 minutes and then resuspended in 70 µl of RNase-free water. After 5 minutes of incubation at RT, magnetic separation was performed for 2 minutes and the supernatant transferred into a new tube. The RNA concentration was measured by Nanodrop. In the next step the 5´-cap was added to the RNA. 60 µg of RNA was filled up with RNase-free water to reach a volume of 72 µl and incubated for 10 minutes at 65°C followed by an incubation on ice for 2 minutes. Subsequently, 10 µl of 10X ScriptCap Capping Buffer, 5 µl of 20 mM GTP, 2.5 µl of 20 mM SAM, 2.5 µl of ScriptGuard RNase Inhibitor, and ScriptCap 2`-o-Methyltransferase, and 4 µl of ScriptCap Capping Enzyme 10 U/µl) were added to the RNA, mixed and incubated for 30 minutes at 37°C. In the next step, the 3`-Poly(A)-Tailing was performed. Therefore, 0.5 µl ScriptGuard RNase Inhibitor, 12 µl of 10X A-Plus Tailing Buffer, 6 µl of 20 mM ATP and 5 µl of A-Plus Poly(A) Polymerase (4 U/µl) were added, mixed, and incubated for 30 minutes at 37 °C. The reaction was stopped by immediately proceeding to the mRNA cleanup using 1x XP beads (Beckman Coulter, #A63881) and 80% ethanol as described previously. The mRNA was eluded in 33 µl EB buffer (Qiagen, #19086) and aliquoted in small volumes to prevent unnecessary thaw-freeze cycles and stored at -80°C. The concentration was measured by Nanodrop and the mRNA integrity by TapeStation (4150 TapeStation System, Agilent Technology).

3.2.4.5. Electroporation for transfer of TCR mRNA into recipient cells

To functionally evaluate TCR reactivity against autologous tumor single-cell suspensions, two distinct analytical platforms were employed. For the Lightning™ system (Bruker Cellular Analysis) based assay, the Jurkat JE6-1-NF-κB::eGFP-endoTCRαβ-KO-CD8αβ reporter

cell line (kindly provided by Assoc. Prof. Dr. Peter Steinberger, Medical University of Vienna; hereafter referred to as JE6-1-NF-κB::eGFP) was utilized as the recipient cell line for TCR mRNA transfection. Conversely, for the flow cytometry-based assay, primary autologous T cells expanded from patient PBMCs were used. Irrespective of the recipient cell type, mRNA transfection was performed utilizing an identical electroporation protocol. For brevity within this section, both primary autologous T cells and Jurkat reporter cells are collectively referred to as recipient T cells.

Recipient T cells were washed with PBS and resuspended in Resuspension Buffer T (Neon™ Transfection System, Invitrogen, # MPK1025) at a density of 0.5×10^6 cells per 10 µL. To prevent RNA degradation, each 10 µL reaction was supplemented with 0.25 µL of RNase inhibitor (New Englands Biolabs, #M0307S). The cell suspension was maintained on ice. A Neon™ tube filled with 3 mL of Electrolytic Buffer E2 was inserted into the electroporation pipetting station. Immediately prior to electroporation, 1 µg of in vitro-transcribed TCR mRNA was added per 0.5×10^6 cells. Using a 10 µL Neon™ tip attached to the electroporation pipette, the cell-mRNA mixture was aspirated and electroporated using the following parameters: 1600 V pulse voltage, 10 ms pulse width, and 3 pulses. Depending on the required total cell yield, this process was repeated up to four times utilizing the same Neon™ tip.

Following electroporation, cells were immediately transferred into pre-warmed culture media at a density of 0.5×10^6 cells/mL. JE6-1-NF-κB::eGFP cells were cultured in phenol red-free RPMI 1640 medium, while primary autologous T cells were cultured in phenol red-free TexMACS™ medium (Miltenyi Biotec); both media were initially unsupplemented with serum. After a 1.5-hour recovery period in a humidified incubator at 37 °C and 5% CO_2, the cultures were supplemented with serum. FBS was added to the JE6-1-NF-κB::eGFP cultures to achieve a final concentration of 10%, whereas human AB serum was added to the autologous T cell cultures to reach a final concentration of 2%. The cells were returned to the incubator and allowed to rest overnight (14 to 16 hours).

Transfection efficiency and TCR surface expression were validated via flow cytometry using a fluorophore-conjugated anti-mouse TCRβ antibody. For the JE6-1-NF-κB::eGFP cells, this validation was performed 24 hours post-electroporation, coinciding with the initiation of tumor cell co-cultures on the Lightning™ system (Bruker Cellular Analysis). For the primary autologous T cells, validation was conducted simultaneously with the functional readout experiment.

3.2.4.6. Surface staining for flow cytometry

Cells were washed with flow cytometry (FC) buffer, consisting of phosphate-buffered saline (PBS) supplemented with 2% FBS and 0.05% sodium azide (NaN_3), and centrifuged at 300 × g for 5 minutes. Cells were immunostained with a APC-conjugated anti-mouse TCRβ antibody (Biolegend, #109211) diluted 1:100 in FC buffer for 30 minutes at 4 °C in the dark. Following surface staining, the samples were washed twice with FC buffer and resuspended in an appropriate volume of FC buffer for flow cytometric data acquisition. DAPI was utilized as the viability dye and added to the final resuspended cells immediately prior to analysis.

3.2.4.7. Data acquisition and analysis of TCR expression

Expression of markers was assessed with a BD LSRFortessa™ (from BD Biosciences) flow cytometer. Data analysis was performed using FlowJo v10 software (FlowJo, LLC, BD Biosciences). Single antibody stainings were used as compensation controls. Spectral overlap was corrected before data acquisition. Expression of the transfected TCR of interest were analyzed out of all single cell, viable JE6-1-NF-κB::eGFP cells were set according to the negative mock condition (Figure M 2).

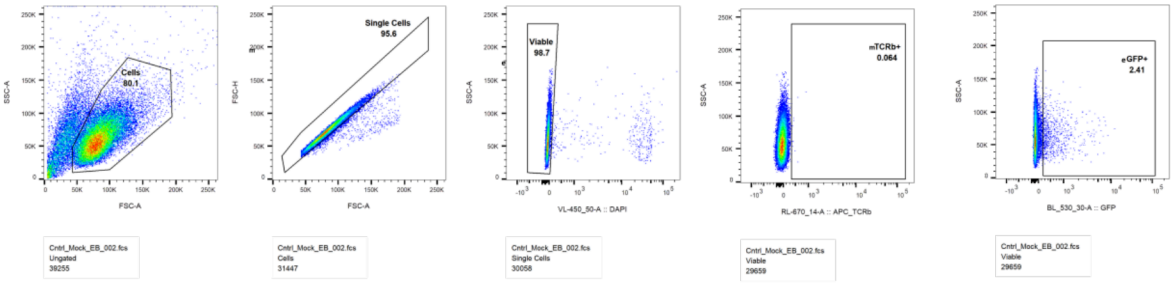


Figure M 2: Gating strategy to determine TCR expression post TCR mRNA transfection.

Gating strategy based on the mock condition. Sequential gating on cells, exclusion of doublets and dead cells, followed by selection of $mTCRb^+$ cells or $eGFP^+$ cells.

3.2.5. TCR validation by co-culture of tumor cells with TCR-transgenic Jurkat reporter cells

Reactivity of selected TCRs against respective tumor single-cell suspensions of the patient samples NCH8937 and NCH9348 were tested on the Lightning™ system equipped with OptoSelect™ 1500 chips (Bruker Cellular Analysis). For this assay the JE6-1-NF-κB::eGFP reporter cell line was transfected with the mRNA of the TCRs of interest as described in section 3.2.4.5 and expression of eGFP was used as readout for TCR-specific T cell activation. As positive control JE6-1-NF-κB::eGFP cells were transfected with mRNA

encoding the 1G4-α95LY TCR, this well-characterized TCR specifically recognizes a peptide derived from the cancer-testis antigen NY-ESO-1, and co-cultured with magnetic beads coupled with the respective cognate NY-ESO-1 peptide. Coupling of the beads and the co-culture set-up are outlined in the following sections 3.2.5.1 and 3.2.5.2.

3.2.5.1. Magnetic bead coupling

The peptide-bead coupling procedure was performed by Katharina von Werthern from the research group of Dr. Patrick Schmidt at the German Cancer Research Center (DKFZ). PureProteome™ Magnetic Beads (Merck, #LSKMAGT02; hereafter referred to as PP beads) were coupled with NY-ESO-1 single-chain trimers (SCTs; kindly provided by Marten Meyer, construct #16396.1) in accordance with the manufacturer's instructions. To minimize potential bead loss resulting from nonspecific surface adhesion, all microcentrifuge tubes were pre-coated with FBS for 20 minutes at 37 °C prior to use. Successful conjugation of NY-ESO-1 SCTs to the PP beads was verified via flow cytometry. The coupled PP beads were incubated with an APC-conjugated anti-human HLA-A2 antibody (BioLegend, clone BB7.2, 343308) for 30 minutes at 4 °C. Following incubation, the beads were washed twice utilizing a DynaMag™-2 magnetic separator rack (Thermo Fisher Scientific, #12321D) to remove unbound antibody and subsequently analyzed on a flow cytometer. Uncoupled PP beads subjected to the identical staining protocol were utilized as a negative control to establish baseline fluorescence.

3.2.5.2. *In vitro* co-culture of T cells and BrM single-cell suspension on the Lightning™ platform

Live single-cell cultivation and activation analyses were conducted using the Lightning™ system equipped with OptoSelect™ 1500 chips (Bruker Cellular Analysis). The technical operation of the machine was performed by Felix Andres from the research group of Prof. Dr. Stefan Eichmüller at the DKFZ. This platform employs Opto-Electronic Positioning (OEP) to generate non-destructive, light-induced electric fields, allowing for the precise manipulation of individual cells into the chip's 1500 NanoPen™ chambers. Before and after every workflow, a system full clean was performed as per the manufacturers` suggestion. Prior to cell loading, the microfluidic chips were flushed with wetting solution and wetting additive (Bruker Cellular Analysis), followed by priming the fluidics with a 1:1 mixture of fresh RPMI and conditioned medium. As conditioned medium, the supernatant of JE6-1-NF-kB::eGFP cultures was used, which had been centrifuged at 500 x g for 5 minutes.

Prior to on-chip loading, cryopreserved single-cell suspensions of the brain metastases (samples NCH8937 and NCH9348) single cell suspensions were carefully thawed using a fractional thawing protocol to maximize cell viability and retain not used material. The cryovial was maintained on dry ice under a tissue culture laminar flow hood, while pre-warmed complete DMEM (supplemented with 10% FBS, 100 U/mL penicillin, and 100 µg/mL streptomycin) was sequentially applied to the frozen suspension. The melted fractions were immediately transferred into a conical tube containing 20 mL of warm complete DMEM. The pooled cell suspension was centrifuged at 400 × g for 5 minutes. The supernatant was partially removed, leaving a residual volume of 1 mL in which the cell pellet was resuspended for cell counting. Following a second centrifugation step and complete removal of the supernatant, the BrM cells were resuspended at a density of 6×10^6 cells/mL in loading medium (basal RPMI lacking standard additives, supplemented with 20% 50x B27 Supplement, 20% Accumax, and 100 U/mL DNase).

Cells were loaded to the OptoSelect™ 1500 chip using a workflow utilizing a small-volume import protocol and an OEP waveform voltage of 4.7 V to maintain cell viability. First, NY-ESO-1 SLLMWITQC (WT)-pulsed beads (kindly provided by the Schmidt laboratory, DKFZ) were loaded by bulk-penning into a single positive-control designated field of view (FOV). Next, the prepared BrM NCH8937 cell suspension was imported and bulk-penned into all FOVs designated to have reporter cells transgenic for patient-individual TCRs or Mock-electroporated reporter cells. Lastly, the different TCR-transgenic JE6-1-NF-κB::eGFP reporter cells were resuspended in the aforementioned loading medium to a concentration of 3×10^6 cells/mL each. These reporter cells were sequentially loaded into their designated FOV, aiming for an occupancy of 3 to 10 cells per NanoPen. Aliquots of the remaining TCR-transgenic reporter cell suspensions were retained for flow cytometric validation of transgenic TCR expression via anti-mouse TCRβ staining. Staining and analysis was performed according to sections 3.2.4.6 and 3.2.4.7. Finally, the on-chip co-cultures were incubated under standard physiological conditions (37°C, 5% CO_2, complete RPMI supplemented 1:1 with conditioned media) on the chip for 43 hours with a constant media flow rate of 4 µL/min. During this culture, imaging was performed in the brightfield and FITC channel to assess target cell-contact dependent activation of the reporter cells, with an imaging interval of 20 minutes and 4000 ms exposure time for FITC imaging.

3.2.5.3. Analysis of tumor-reactive TCRs on the Lightning™ platform

TCR-specific activation was defined on basis of several conditions. First, in the brightfield images the TCR-transgenic JE6-1-NF-kB::eGFP needed to be in direct cell contact with the tumor cells prior to eGFP detection. Second, eGFP signal emerging earlier than 6 h after

initiation of the co-culture was excluded. Third, the strength of the eGFP signal had to exceed the threshold of 4000 MFI in the FITC channel.

3.2.6. TCR validation by co-culture of tumor cells with TCR-transgenic autologous T cells

Autologous T cells expanded from the cryopreserved PBMCs of patient NCH9348 were utilized to functionally validate selected TCRs identified via scRNA/TCR-seq. Expanded T cells were electroporated with nine distinct IVT TCR mRNAs, generated as described in section 3.2.4.4. As a negative mock-transfection control, T cells were electroporated with Elution Buffer (EB). As a positive control, T cells were transfected with NY-ESO-1 TCR mRNA and co-cultured with the A375 melanoma cell line, which endogenously expresses the cognate target peptide (SLLMWITQC).

To comprehensively evaluate TCR functionality, specificity, and background activity, the transfected T cells were subjected to five distinct co-culture conditions listed below (Table M 15). All experimental conditions were performed in biological triplicates.

Table M 15: Culture conditions of TCR-transgenic autologous NCH9348 T cells.

Condition	Stimulus/ Target cell	Purpose of assessment
Baseline	TCR-transgenic T cells cultured alone	Spontaneous background activation
Autoimmunity	Autologous PBMCs	Auto-reactivity against healthy tissue
Tumor-specific	Autologous tumor single-cell suspension	Specific recognition of tumor antigens
Activation capacity	Human T cell TransAct® (Miltenyi Biotec)	TCR-independent, universal T cell activation
Viral-specific	PepTivator® viral peptide pool (Miltenyi Biotec)	Viral-specific memory reactivity

The specific methods for T cell expansion from cryopreserved PBMCs and the subsequent co-culture setups are outlined in the sections below.

3.2.6.1. T cell expansion from cryopreserved PBMCs

T cell expansion from cryopreserved PBMCs was performed in collaboration with the research group of Prof. Dr. Eichmüller at the German Cancer Research Center (DKFZ).

Cryopreserved PBMCs (patient NCH9348) were thawed in pre-warmed X-VIVO™ 20 medium (Lonza, #04-448Q) supplemented with 2% human AB serum (hAB, Sigma-Aldrich, #H4522-100ML). Cells were centrifuged at 400 × g for 5 minutes, resuspended in 10 mL X-VIVO™ 20 / 2% hAB medium containing 60 ng/mL anti-human CD3 antibody (clone OKT3, Miltenyi Biotec, #170-076-124), and seeded into a T25 culture flask. Irradiated (30 Gy) allogeneic PBMC feeder cells, pooled from three healthy donors, were added to the culture at a 100-fold excess in 10 mL X-VIVO™ 20 / 2% hAB medium. This resulted in a final culture volume of 20 mL and a final OKT3 concentration of 30 ng/mL.

On days 1 and 4 post-thawing, 50% of the culture medium was exchanged with fresh X-VIVO™ 20 / 2% hAB medium supplemented with interleukin-2 (IL-2) to achieve a final concentration of 300 IU/mL. On day 6, $CD8^+$ T cells were isolated using the $CD8^+$ T cell isolation kit (Miltenyi Biotec, 130-096-495). The $CD8^+$ enriched and $CD8^-$ depleted fractions were subsequently cultured in parallel at a density of 0.6×10^6 cells/mL in IL-2-supplemented medium. Following a complete media exchange on day 8, cells were harvested on day 10 for downstream applications. Prior to transfection 9×10^6 $CD8^+$ enriched T cells were recombined with 2×10^6 cells from the autologous $CD8^-$ depleted fraction. The resulting mixed T cell population was subsequently subjected to TCR mRNA electroporation as detailed in Section 3.2.4.5.

3.2.6.2. Barcoding and multiplexing of TCR-transgenic T cells

At 15 hours post-electroporation, TCR-transgenic T cells were washed with FC buffer (PBS, 3 mg/mL BSA, 2 mM EDTA) and centrifuged at 400 × g for 5 minutes. To enable multiplexed functional screening within single co-culture wells, cells expressing distinct TCRs were barcoded using 4 different fluorophore-conjugated anti-human CD45 antibodies (Table M 4) as outlined below. The experiment was conducted in collaboration with Felix Andres (from the research group of Prof. Dr. Stefan Eichmüller), who established the anti-CD45 barcoding strategy for pooling of T cells with distinct TCRs.

Table M 16: Pooling of barcoded TCR-transgenic NCH9348 T cells and the respective fluorophore-conjugated anti-human CD45 antibodies.

Fluorophore	Pool 1	Pool 2	Pool 3
Spark PLUS UV395	NCH9384 TCR-1	NCH9384 TCR-4	NCH9384 TCR-7
BV421	NCH9384 TCR-2	NCH9384 TCR-5	/
AF488	NCH9384 TCR-3	/	NCH9384 TCR-13
AF647	Mock	NCH9384 TCR-6	NCH9384 TCR-14

Mock-electroporated cells (0.181 × 10^6) and NY-ESO-1 TCR-transfected positive controls (0.525 × 10^6) were equally divided and stained with all four CD45 fluorophores to serve as internal controls across all pools. Barcoding was performed in FC buffer for 15 minutes at RT in the dark. Cells were washed twice and resuspended at 1 × 10^6 cells/mL in assay medium (X-VIVO™ 20, 2% hAB) containing PE-conjugated anti-human CD107a (1:40; BioLegend, #328608). Barcoded cell populations were subsequently pooled according to the experimental design outlined above.

Co-cultures were established in a 96-well plate in technical triplicates. For each pooled TCR set, five conditions were evaluated: (1) baseline activation (TCR-transgenic T cells only); (2) auto-reactivity (co-culture with autologous PBMCs, E:T ratio 1:1); (3) tumor-reactivity (co-culture with autologous tumor single-cell suspension, E:T ratio 1:1); (4) viral reactivity (1 µg/mL PepTivator® CEF MHC Class I Plus, Miltenyi Biotec, #130-098-426); and (5) TCR-unspecific activation (1:100 T Cell TransAct™, Miltenyi Biotec, #130-111-160). Cultures were incubated at 37 °C and 5% CO_2. After 1 hour, protein transport inhibitors (Brefeldin A and Monensin; 1:1000) were added to block cytokine secretion, and cultures were incubated for an additional 5 hours. Following the 6-hour incubation, cells were harvested and subjected to surface and intracellular staining (section 3.2.6.3). Transgenic TCR expression and functional activation were quantified via flow cytometry by assessing murine TCRβ chain expression, intracellular TNFα production, and surface CD107a mobilization.

3.2.6.3. Cell surface and intra-cellular staining for flowcytometric readout

For patient sample NCH9348, flow cytometry-based functional testing of selected TCRs was performed with a modified cell surface staining protocol. Briefly, cells were washed in FC buffer (PBS supplemented with 3 mg/mL bovine serum albumin (BSA) and 2 mM EDTA) and centrifuged at 400 × g for 5 minutes. The cell pellet was resuspended in a staining master mix prepared in FC buffer, consisting of a fixable near-infrared (NIR) viability dye (Invitrogen, #L10119, 1:1000 dilution), PE/Cyanine7-conjugated anti-mouse TCRβ (BioLegend, Cat# 109222, 1:50 dilution), and PerCP-conjugated anti-human CD8 (BioLegend, Cat# 344708, 1:50 dilution). Cells were incubated in the dark for 10 minutes at room temperature (RT), followed by an additional 10 minutes at 4 °C. Following surface staining, samples were washed twice with FC buffer, resuspended in Cytofix/Cytoperm solution (BD Biosciences, Cat# 554714), and incubated for 20 minutes at 4 °C in the dark for fixation and permeabilization. Fixed and permeabilized cells were then washed twice with freshly prepared 1× Perm/Wash buffer (BD Biosciences, Cat# 554714). For intracellular cytokine detection, cells were incubated with Brilliant Violet 711-conjugated anti-human TNFα (BioLegend, Cat# 502940, 1:50 dilution in 1× Perm/Wash buffer) for 30

minutes at 4 °C in the dark. Finally, the samples were washed twice with 1× Perm/Wash buffer and resuspended in 180 µL of FC buffer prior to flow cytometric data acquisition. Data acquisition and analysis was performed as described in method section 3.2.4.7.

3.2.6.4. Data acquisition and analysis of T cell activation and TCR expression

Expression of markers was assessed with a BD LSRFortessa™ (from BD Biosciences) flow cytometer. Data analysis was performed using FlowJo X v10 software (FlowJo, LLC, BD Biosciences). Single antibody stainings were used as compensation controls. Spectral overlap was corrected before data acquisition. In the gating was established on the mock control condition (Figure M 3) and applied to all other conditions. Doublets were excluded from the cells, followed by gating on viable cells. Subsequently the differentially barcoded TCR conditions were separated by the CD45 staining. mTCRβ expression was set according to be negative for the $CD8^+$ T cell in the EB condition. To set the gates for the T cell activation marker TNFα and CD107a the non-stimulated mock control was used but first gated on all $CD8^+$ T cells for all barcoded conditions (in the mock condition mTCRβ-negative).

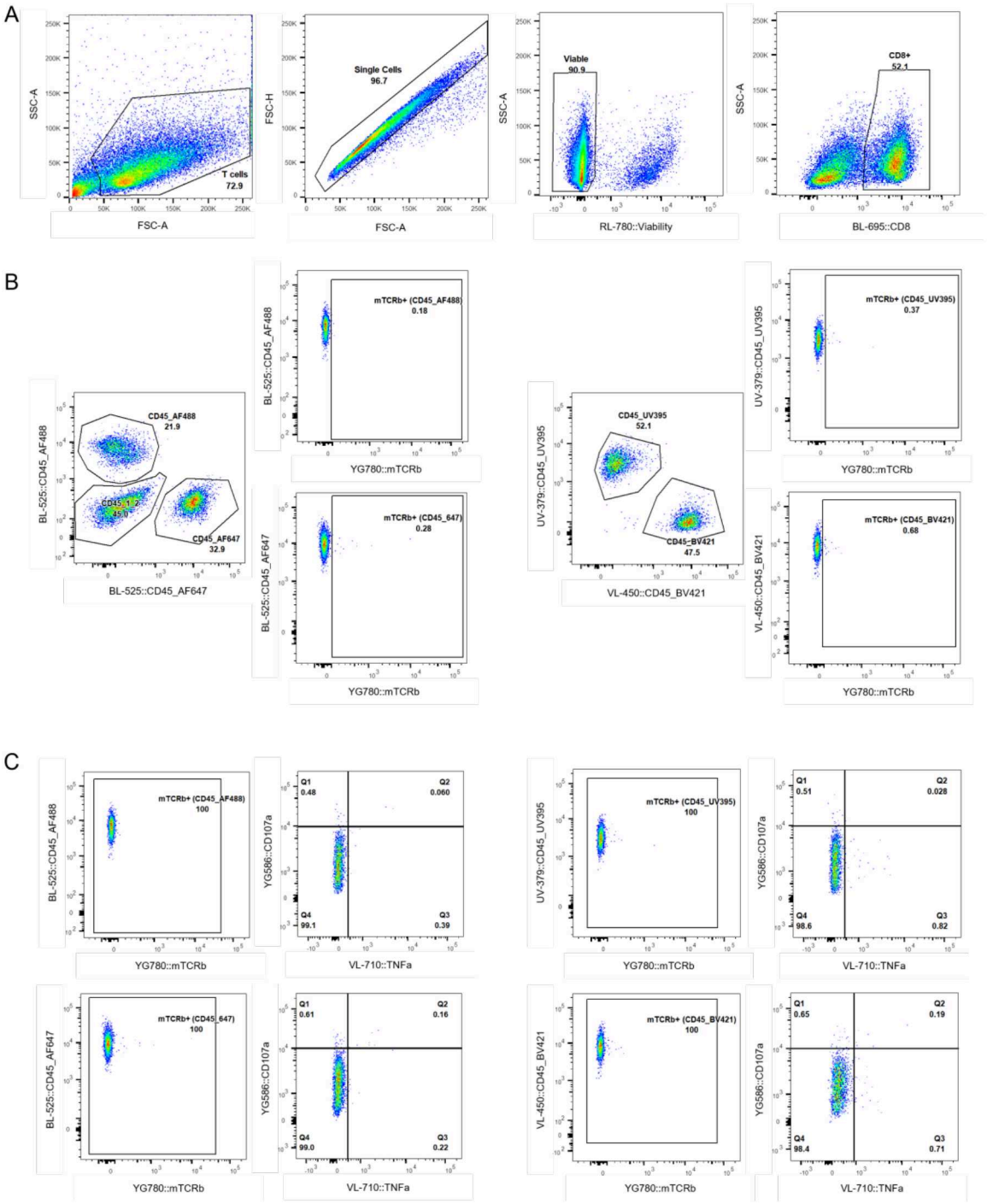


Figure M 3: Gating strategy for TCR expression and functional activation of the autologous TCR-transfected T cells.

Gating strategy based on the mock condition. (A) Sequential gating on cells, exclusion of doublets and dead cells, followed by selection of $CD8^+$ T cells. (B) Subsequent discrimination of pooled TCR conditions using four distinct CD45-barcoded fluorophores. Transgenic TCR expression was defined by detection of the murine constant TCRβ chain. (C) Functional marker gates were established by first including $mTCR^-$ cells, followed by gate setting for CD107a and TNFα.

3.2.7. Multiplexed tissue imaging using co-detection by indexing (CODEX)

3.2.7.1. Clinical samples and tissue preparation

Formalin-fixed paraffin-embedded (FFPE) tissue sections of 16 human brain metastases were received from the tissue bank of the National Center of Tumor Diseases (NCT) in Heidelberg. Pathological information and clinical characteristics are listed in Table M 2 and Table M 3 respectively. Tissue thickness was 4 µm and it was mounted on positively charged microscopy slides to avoid tissue detachment. Antibody conjugation, CODEX antibody staining of FFPE tissues, and image acquisition were performed by the group of Prof. Dr. Dietrich at the University clinic in Düsseldorf according to their published protocol (Schniederjohann et al., 2025). The main steps are described in short below.

3.2.7.2. Antibody Conjugation and validation

Custom antibody conjugation to maleimide-modified DNA oligonucleotides was performed at a 2:1 oligonucleotide-to-antibody weight ratio. Briefly, centrifugal filter columns were pre-conditioned with 0.1% PBS-Tween-20 to minimize nonspecific binding prior to antibody loading. To generate reactive thiol groups for conjugation, antibodies (≥30 µg) were partially reduced using a 2.5 mM TCEP/EDTA (Sigma-Aldrich, #646547-10x) solution for 30 minutes at RT, followed by washing with Buffer C. To prevent premature maleimide degradation, lyophilized maleimide-oligonucleotides were reconstituted in PBS under an inert nitrogen atmosphere immediately prior to use.

The reduced antibodies and activated oligonucleotides were subsequently co-incubated in the filter columns for 2 hours at room temperature to facilitate site-unspecific conjugation. Following incubation, unreacted oligonucleotides were removed via three consecutive wash steps with High Salt PBS. The conjugated antibodies were recovered by inverting the filter columns and centrifuging (3000 × g, 2 minutes) into CODEX antibody stabilizer solution at a 1:2 (w/v) ratio. Conjugated antibodies were stored at 4 °C. Functional validation of the conjugated antibodies was performed via multiplexed imaging using a standard starting dilution of 1:150 and an exposure time of 300 ms. Based on these validation runs, optimal concentrations and exposure times were titrated for subsequent experimental runs on BrM tissue.

3.2.7.3. FFPE tissue preparation and multiplexed staining

FFPE slides were baked at 65 °C for 60 minutes, deparaffinized in xylene (Sigma-Aldrich, #534056-4l) 3 × 5 min, and rehydrated through a descending ethanol gradient (100% to 30%, 5 min each) ending in double-distilled water (ddH_2O). Heat-induced epitope retrieval was performed in Tris-EDTA buffer (pH 9.0, Morphisto, #1,232,802,500) using a pressure cooker on a high-pressure setting for 20 minutes, followed by a 30-minute RT equilibration and ddH_2O rinses. To minimize intrinsic tissue autofluorescence, slides were photobleached in freshly prepared bleaching solution under high-power LED arrays for two 45-minute cycles (with reagent exchange between cycles) and subsequently washed in PBS (4 × 5 min).

Tissues were conditioned in hydration buffer (Akoya, #7000008) 2 × 2 min, equilibrated in staining buffer (20 to 30 min), and blocked for 30 minutes at RT in a humidity chamber. The multiplex antibody cocktail was prepared in staining buffer utilizing pre-centrifuged custom-conjugated antibodies and proprietary Akoya blocking buffer. The cocktail was applied to the tissues and incubated overnight at 4 °C on an orbital shaker (~30 rpm).

Post-staining, slides were washed in staining buffer (2 × 2 min) and subjected to sequential fixation to crosslink the bound antibodies: 1.6% paraformaldehyde for 10 minutes, ice-cold methanol for 5 minutes, and freshly prepared BS3 homobifunctional crosslinker (20 µL/mL in PBS) for 20 minutes at RT. Intermediate PBS washes were performed between each fixation step. Slides were then either immediately mounted with flow cells (Akoya Biosciences) or maintained in storage buffer at 4 °C for up to 5 days.

3.2.7.4. Automated CODEX image acquisition

For cyclic multiplexed imaging, 96-well reporter plates were assembled by dispensing 245 µL of reporter stock solution containing sequence-specific fluorescent oligonucleotides (10 pmol/µL each) per well, alongside blank wells for background subtraction. Plates were sealed with pierceable aluminum foil. Multiplexed automated image acquisition was executed using the PhenoCycler®-Fusion System (Akoya Biosciences) in accordance with the manufacturer's established protocols.

3.2.8. Author contributions and collaborations

Several components of this study were performed in collaboration with external partners. The respective contributions are detailed below to clearly delineate experimental, analytical, and conceptual responsibilities.

3.2.8.1. Generation and analysis of scRNA-seq, TCR-seq, and bulk RNA-seq data

The nine human brain metastasis samples and four matched PBMC samples were provided as cryopreserved single-cell suspensions by the group of Prof. Dr. Christel Herold-Mende (University Hospital Heidelberg).

The experimental generation of scRNA-seq and paired TCR-seq data from these samples was performed entirely by me. Bulk RNA sequencing experiments were conducted by the group of Dr. Isabel Poschke (German Cancer Research Center).

Bioinformatic processing of scRNA-seq, TCR-seq, and bulk RNA-seq data was performed in close collaboration with Karol Jacek (PhD student, group of Prof. Dr. Bożena Kamińska, Nencki Institute, Warsaw) and Dr. Marc Zapatka (DKFZ). Specifically, computational preprocessing and pipeline implementation were carried out by Karol Jacek, and Dr. Marc Zapatka, while I defined biologically meaningful clustering parameters, performed cluster annotation, and led the biological interpretation of the data. I directed the analytical strategy of the study, including the introduction of tumor reactivity prediction scores, developed all hypotheses and performed all data interpretations.

3.2.8.2. Selection and cloning of TCRs

Candidate TCRs for functional validation were selected based on criteria defined by me, including clonal expansion (≥4 cells per clonotype), localization within $CD103^+$ T_{RM} clusters, and predicted tumor reactivity across the two applied scoring approaches. In addition, selected clones outside predicted tumor-reactive regions were included as controls.

Based on these criteria, Karol Jacek selected and extracted TCR sequences from the 10x Genomics dataset and uploaded them to the “makeTCR” platform. The cloning of TCR-encoding DNA constructs into viral vectors was performed by the group of Dr. Edward Green.

All subsequent experimental steps, including DNA linearization, amplification, and *in vitro* transcription, were performed exclusively by me.

3.2.8.3. Functional validation of TCRs

Functional testing of the selected TCRs was performed using two complementary assay systems.

The Jurkat-based reporter assay was established in collaboration with Katharina von Werthern (PhD student, group of Dr. Patrick Schmidt, DKFZ) and Felix Andres (PhD student, group of Prof. Dr. Stefan Eichmüller, DKFZ). Katharina von Werthern provided expertise in handling the reporter cell line and established the positive control system based on an NY-ESO-1-specific TCR and peptide-loaded beads. The Lightning™ assay platform was implemented in collaboration with Felix Andres.

An alternative assay based on primary T cells was developed by Felix Andres. He expanded T cells from cryopreserved PBMCs of sample NCH9348. The pooling of T cells expressing distinct TCRs by barcoding via different anti-human CD45 fluorophore-labelled antibodies was previously established by Felix Andres (methodological publication in preparation).

For both assay systems, all experimental procedures, including TCR mRNA electroporation, co-culture setup, and flow cytometry staining, were performed by me.

3.2.8.4. CODEX multiplexed tissue imaging

An initial panel of validated antibodies was provided by the group of Prof. Dr. Sascha Dietrich (University Hospital Düsseldorf). Based on my scRNA-seq analysis and relevant literature, I selected additional antibodies to refine and extend the panel.

All experimental procedures, including tissue staining and imaging, were performed by the group of Prof. Dr. Sascha Dietrich. Following image acquisition, I received the imaging data and performed quality control, including evaluation of antibody specificity and optimization of antibody dilution and exposure parameters.

Once the antibody panel was established, patient tissue samples were stained and imaged by the collaborating group in Düsseldorf. I subsequently performed independent qualitative analysis of the imaging data. All downstream analyses, including spatial interpretation, hypothesis generation were conducted by me.

4. Results

4.1. Single-cell profiling of the transcriptomic landscape and TCR repertoire of brain metastases-infiltrating T cells

To characterize the T cell compartment in NSCLC brain metastases, I performed single-cell RNA sequencing (scRNA-seq) combined with paired T cell receptor (TCR) sequencing of FACS-sorted $CD3^+$ T cells isolated from resected brain metastasis tissue of nine patients. For four patients, matched peripheral blood mononuclear cells (PBMCs) were analyzed in parallel, enabling comparison between tumor-infiltrating and circulating T cell populations.

This approach allowed the simultaneous assessment of transcriptional states and clonal relationships of T cells at single-cell resolution. In particular, it enabled the identification of distinct $CD4^+$ and $CD8^+$ T cell populations and the direct linkage of their transcriptional profiles to TCR-defined clonal expansion. Furthermore, I functionally evaluated selected TCRs identified from the BrM single-cell analyses using *in vitro* co-culture systems with autologous tumor material (Figure 1).

The integration of matched blood samples provided a framework to assess the degree of overlap between tumor-infiltrating and circulating T cell repertoires and to investigate whether clonal expansion occurs locally within the metastatic niche. Bioinformatic processing and downstream computational analyses of the scRNA-seq and TCR-seq analysis auf der BrM-derived T cells and the bulk-TCRβ analysis were performed in collaboration with Karol Jacek (PhD student, group of Prof. Dr. Bożena Kamińska, Nencki Institute, Warsaw) under supervision of Dr. Marc Zapatka (DKFZ). Analysis of the scRNA-seq and TCR-seq for the peripheral blood-derived T cells and TCR sharing between TCRs of blood and BrM of the same patient were directly performed by Dr. Marc Zapatka (DKFZ).

Together, this dataset enables the high-resolution characterization of T cell heterogeneity and clonal expansion in NSCLC brain metastases and provides the basis for subsequent analyses of tumor reactivity and spatial organization.

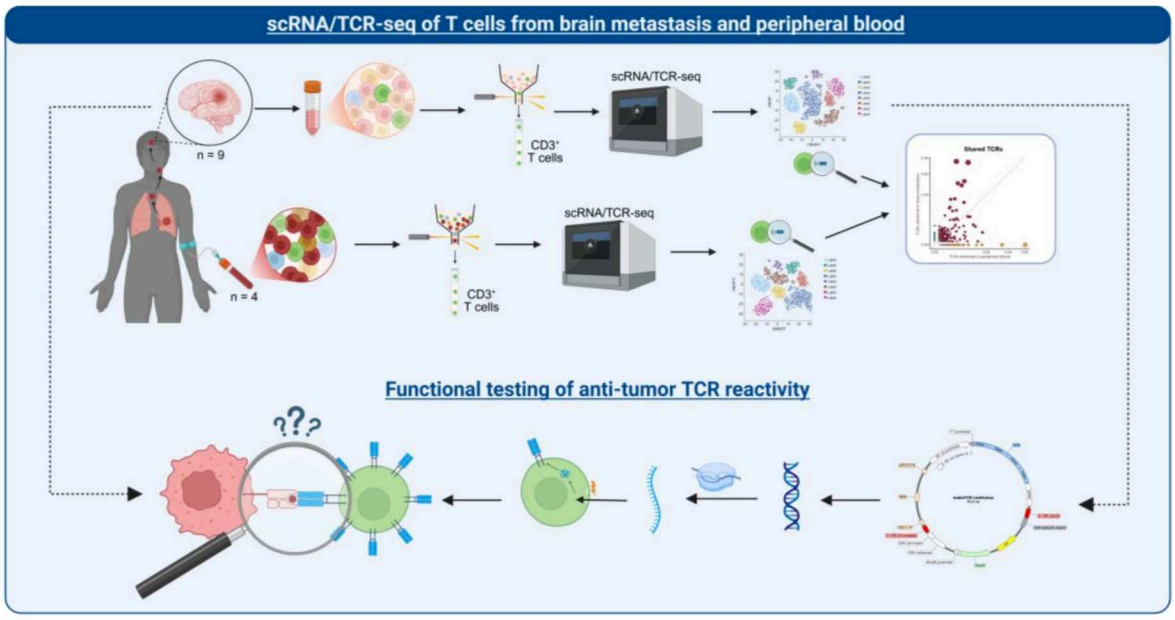


Figure 1: Experimental workflow for single-cell profiling and functional analysis of T cells.

Schematic overview of the study design. Single-cell gene expression and paired T cell receptor (TCR) libraries were generated from FACS-sorted CD3⁺ T cells isolated from brain metastases (n = 9) and matched peripheral blood (n = 4). TCR repertoire overlap between tumor and blood compartments was analyzed. Selected BrM-derived TCR sequences were reconstructed *in vitro* and functionally tested by transfection into T cells followed by co-culture with autologous tumor cells.

4.1.1. Distinct transcriptional T cell phenotypes in NSCLC brain metastases

To define the transcriptional landscape of tumor-infiltrating T cells in NSCLC brain metastases, I performed single-cell RNA sequencing on FACS-enriched CD3⁺ T cells derived from nine patient samples, yielding 53,220 high-quality cells after quality control filtering. Unsupervised clustering identified multiple transcriptionally distinct T cell populations, visualized by UMAP (Figure 2E), which were broadly assigned to CD4⁺ and CD8⁺ lineages based on the expression of *CD4* and *CD8A*, respectively (Figure 2A, Figure 2B). In addition, a small population of γδ T cells was identified by expression of *TRDV1* and *TRGV4*.

Within the CD4⁺ compartment, I identified central memory (T_{CM}) cells characterized by expression of *TCF7*, *CCR7*, and *IL7R* (Figure 2C, 2F), as well as effector memory (T_{EM}) populations with increased expression of inflammatory genes such as *GZMK* and *IFNG*. Furthermore, distinct clusters corresponding to regulatory T cells (*FOXP3*, *IL2RA*) and T follicular helper-like cells expressing *CXCL13* and *PDCD1* were observed (Figure 2F).

Proliferating T cell populations were detected in both CD4⁺ and CD8⁺ compartments based on expression of cell cycle-associated genes.

Within the CD8⁺ T cell compartment, in addition to effector memory populations, I identified a distinct subset characterized by the tissue-residency markers *ITGAE* (CD103) and *CXCR6*. Notably, this population was characterized by high expression of cytotoxic effector molecules, including *PRF1* and *GZMB*, alongside the expression of inhibitory receptors such as *PDCD1*, *HAVCR2*, and *TIGIT* (Figure 2D, 2F). Based on this transcriptional profile, I annotated this cluster as CD8⁺ tissue-resident memory T cells (TRM).

To further resolve lineage-specific differentiation states and functional programs, CD4⁺ and CD8⁺ T cells were subsequently analyzed separately.

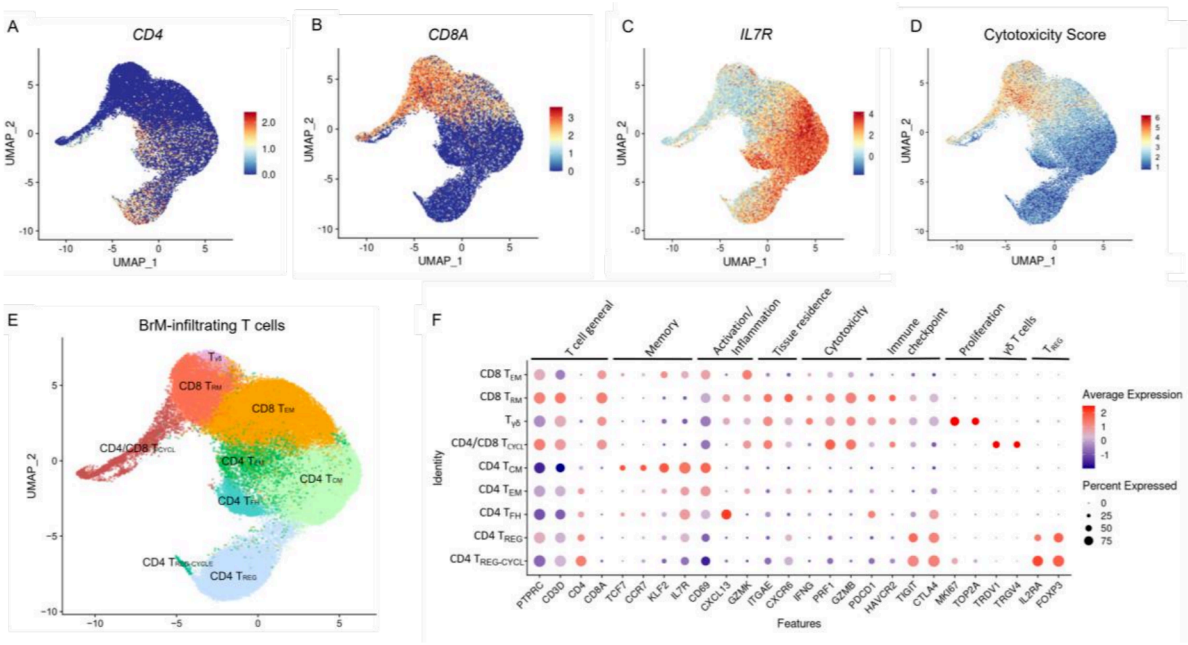


Figure 2: Single-cell transcriptomic landscape of brain metastases (BrM)-infiltrating T cells.

UMAP visualization of scRNA-seq data from T cells isolated from BrM of nine patients. (A-C) Feature plots showing expression of *CD4* (A), *CD8A* (B), and *IL7R* (C). (D) Cytotoxicity score based on expression of *GZMB*, *PRF1*, *NKG7*, and *FASLG*. (E) UMAP colored by cluster annotation. (F) Selected differentially expressed genes supporting cluster annotation.

4.1.2. CD4$^+$ T cells in NSCLC brain metastases comprise distinct memory, regulatory, and helper subsets

To further resolve the CD4$^+$ T cell compartment, CD4$^+$ T cells were extracted from the global dataset based on expression of *PTPRC* (CD45), *CD3D*, and *CD4*, yielding 25,300 high-quality cells. Independent unsupervised re-clustering identified seven transcriptionally distinct CD4$^+$ T cell states (Figure 3A), which were annotated based on characteristic marker gene expression (Figure 3B).

Three clusters exhibited memory phenotypes, including one central memory population (CD4$^+$ T_{CM}) characterized by *CCR7*, *TCF7*, *KLF2*, and *IL7R*, and two effector memory populations (CD4$^+$ T_{EM}) with increased expression of activation-associated genes such as *CD69* and *GZMK*. In addition, a distinct cluster of T follicular helper (T_{FH}) cells was identified based on expression of *CXCL13*, *PDCD1*, and *ICOS*. Regulatory T cells (T_{REG}) segregated into two subsets, including an activated population ($T_{REG\text{-}ACT}$) characterized by high expression of *FOXP3*, *IL2RA*, *CTLA4*, *TIGIT*, and *ICOS*. Notably, this activated T_{REG} population also expressed *PRF1*. A proliferative cluster (T_{CYCL}) was defined by expression of cell cycle-associated genes such as *MKI67* and *TOP2A*. This cluster showed overlapping transcriptional features with both T_{FH} and $T_{REG\text{-}ACT}$ populations, suggesting that the proliferating CD4$^+$ T cells originate from these two subsets.

Across patients, all major CD4$^+$ T cell states were consistently detected but varied in relative abundance, indicating substantial inter-patient heterogeneity (Figure 3C). Notably, the proliferative T_{CYCL} population was absent in two patients, suggesting variability in local T cell activation states across the cohort.

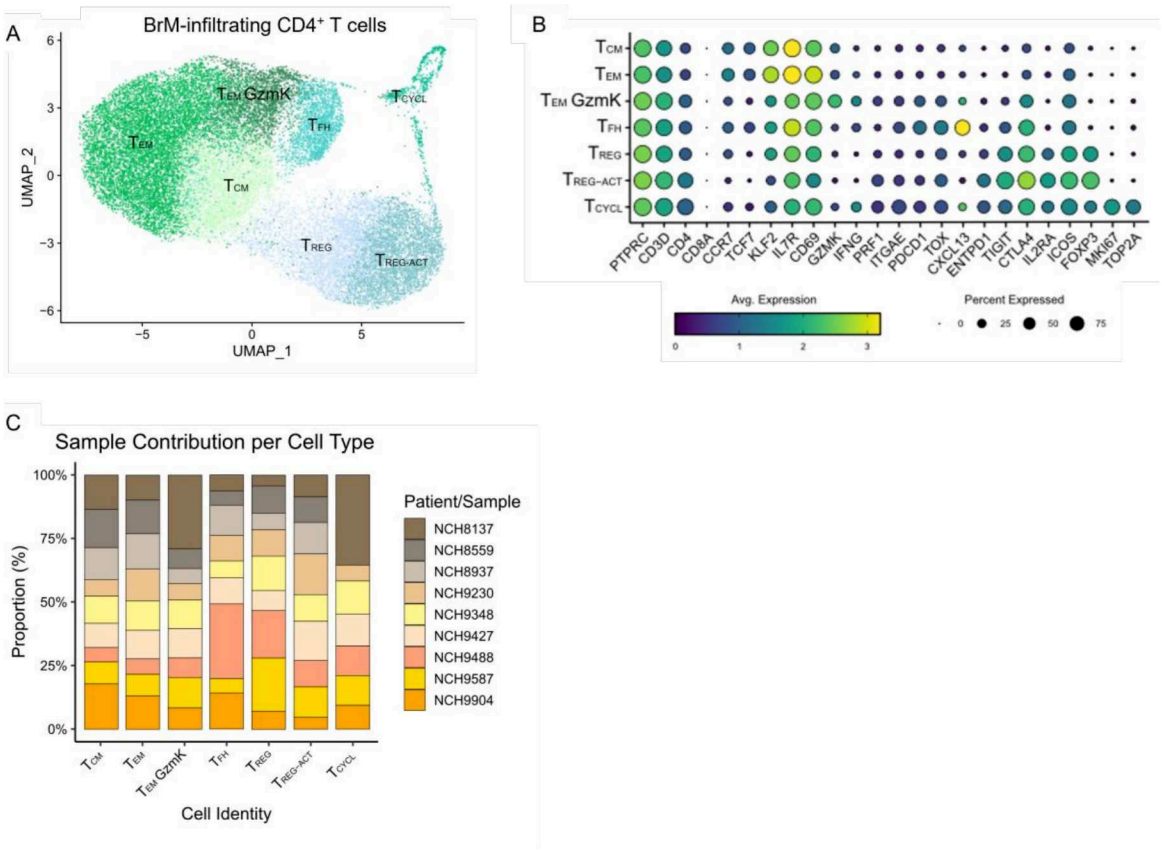


Figure 3: Sub-clustering of CD4⁺ brain metastases (BrM)-infiltrating T cells.

(A) UMAP visualization of CD4⁺ T cells colored by subclusters. (B) Dot plot showing expression of selected marker genes used for cluster annotation. (C) Proportion of cells from each patient within each subcluster.

4.1.3. Distinct differentiation states and tissue-resident subsets define the CD8⁺ T cell compartment in NSCLC brain metastases

Focusing on the CD8⁺ T cell compartment, 23,689 cells were extracted from the global dataset based on expression of *PTPRC* (CD45), *CD3D*, and *CD8A* and subjected to independent unsupervised re-clustering, identifying seven transcriptionally distinct subsets (Figure 4A, Figure 4B).

Among these, a cluster characterized by expression of *CCR7*, *TCF7*, *KLF2*, and *IL7R* was annotated as stem-like memory T cells (CD8⁺ T_{SCM}). A related population displaying elevated *GZMK* expression (CD8⁺ T_{SCM} GzmK) suggested an early transition toward effector differentiation. Two effector memory populations (CD8⁺ T_{EM} and CD8⁺ T_{EM} GzmK) were identified based on reduced expression of stemness-associated genes and increased expression of cytotoxic markers such as *GZMB* and *NKG7*. To further characterize these populations, a memory score was applied, revealing variation in memory-associated transcriptional programs across clusters (Figure 4C).

In addition to these populations, three clusters displayed features of activated and exhausted T cells (Figure 4D, Figure 4E). One cluster exhibited high expression of multiple inhibitory receptors and exhaustion markers, including *PDCD1*, *HAVCR2*, *LAG3*, *TIGIT*, and *TOX*, consistent with a terminally exhausted phenotype (T_{EX}). Two additional clusters co-expressed exhaustion markers together with tissue-residency genes, including *ITGAE* (CD103) and *CXCR6*, and were annotated as tissue-resident memory exhausted ($T_{RM\text{-}EX}$) and proliferating T_{RM} ($T_{RM\text{-}CYCL}$), the latter defined by expression of *MKI67* and *TOP2A*. Notably, both T_{RM} clusters showed strong expression of *ENTPD1* (CD39), a marker associated with chronic antigen stimulation (Figure 4B).

Across patients, all CD8⁺ T cell subsets were detected, but their relative abundance varied substantially (Figure 4F). While memory-associated populations were broadly represented across patients, activated and tissue-resident subsets displayed higher variability. In particular, the proliferative $T_{RM\text{-}CYCL}$ population was reduced or absent in selected patients, indicating inter-patient differences in T cell activation states.

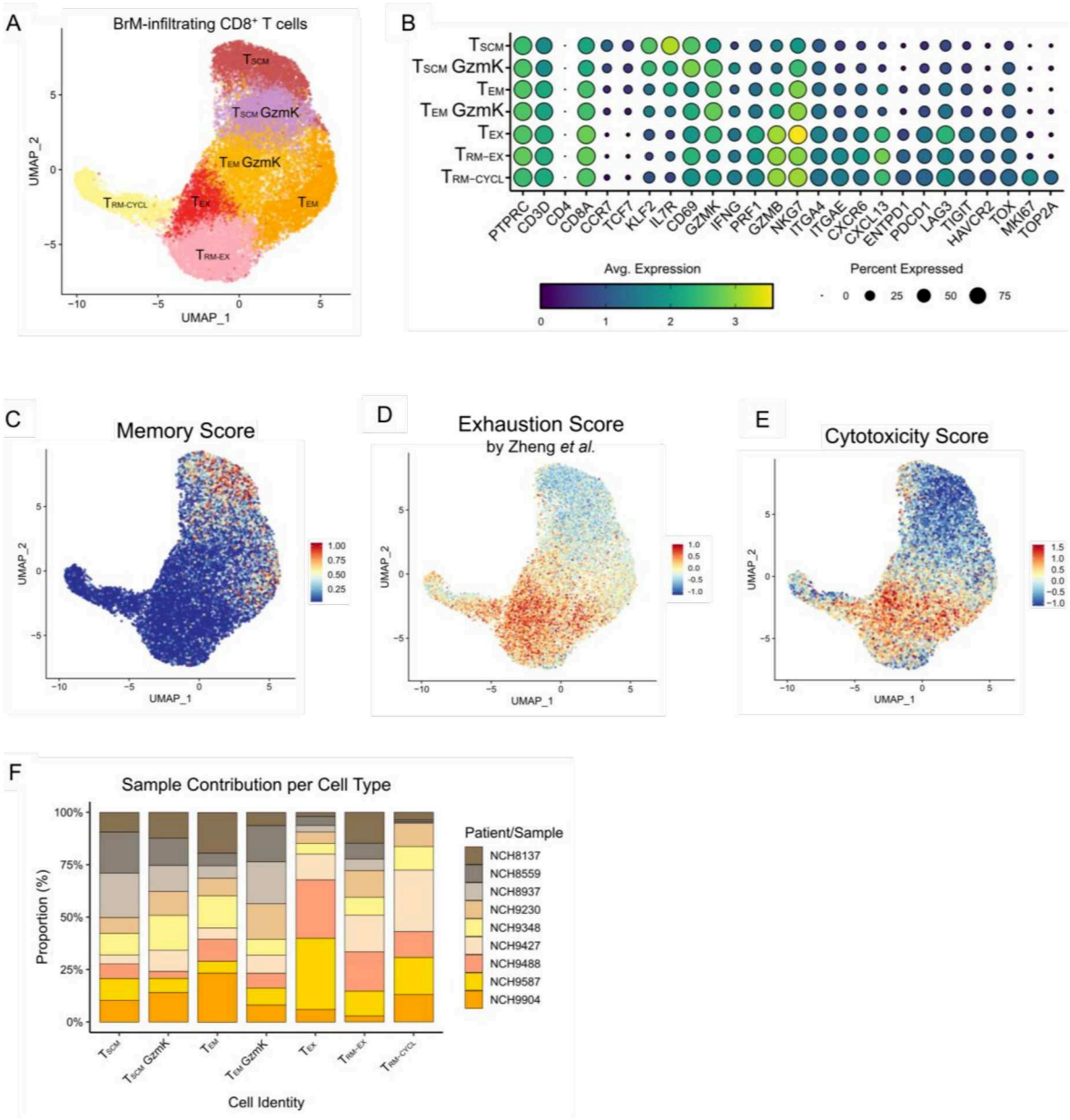


Figure 4: Sub-clustering of CD8⁺ brain metastases (BrM)-infiltrating T cells.

(A) UMAP visualization of CD8⁺ BrM-infiltrating T cells colored by subclusters. (B) Dot plot showing expression of selected differentially expressed genes used as marker genes for cluster annotation. (C-E) Feature plots over the CD8⁺ subclustered UMAP showing a memory score based on expression of genes *IL7R*, *CCR7*, *SELL*, *CXCR3*, *EOMES*, and *CD44* (C), an exhaustion score based on the transcriptomic signature of Zheng et al. (D), and the cytotoxicity score based on expression of *GZMB*, *PRF1*, *NKG7*, and *FASLG* (E). (F) Proportion of cells from each patient sample within each subcluster.

4.1.4. Clonal expansion is enriched in tissue-resident CD8⁺ T cell subsets in NSCLC brain metastases

The co-expression of CD103 and CD39 has been linked to tumor-reactive CD8⁺ T cell populations in multiple tumor types (Duhen et al., 2018; Workel et al., 2019). In line with these observations, the presence of this phenotype within my BrM dataset suggests that tumor-associated T cell populations may be enriched within the tissue-resident compartment. To further explore this possibility, I analyzed the clonal architecture of these populations, as antigen-specific T cell responses are typically associated with clonal expansion. Upon recognition of cognate antigen, T cells can undergo clonal expansion, giving rise to populations of cells sharing identical T cell receptors (TCRs) (Sanromán et al., 2023).

To investigate the clonal architecture of BrM-infiltrating T cells, I generated paired V(D)J libraries alongside the gene expression libraries, enabling integrated analysis of transcriptional state and TCR sequence at single-cell resolution. Clonotypes were defined by matching nucleotide sequences of both *TRA* and *TRB* chains.

To stratify the extent of clonal expansion, clonotypes were classified according to their relative abundance within the repertoire. TCRs detected only once were classified as singlets; clones representing ≤0.1% of the repertoire as rare; >0.1% to 0.5% as small; >0.5% to 1% as medium; >1% to 10% as large; and >10% as hyperexpanded. Clonal expansion patterns varied substantially across patients; however, in most cases, more than 50% of T cells belonged to expanded clonotypes (Figure 5A). All patients harbored large clones representing 1% to 10% of the total repertoire. While a subset of patients exhibited predominantly rare to small clones with only limited expansion, others showed a substantially higher fraction of expanded clonotypes. Notably, one patient displayed a hyperexpanded clone representing more than 10% of all recovered TCRs.

Projection of clonal fractions onto the global UMAP revealed that expanded clonotypes were not uniformly distributed across the T cell compartment, but were predominantly localized within CD8⁺ T cell clusters (Figure 5B). When mapped onto the CD8⁺ subclustered UMAP, the most expanded clonotypes were concentrated within the $T_{RM\text{-}EX}$ and $T_{RM\text{-}CYCL}$ populations (Figure 5D). In contrast, memory-associated clusters showed markedly lower degrees of clonal expansion.

This spatial restriction of expanded clonotypes to tissue-resident CD8⁺ T cell states is consistent with the hypothesis that these populations are enriched for antigen-experienced cells. Notably, the $T_{RM\text{-}EX}$ and $T_{RM\text{-}CYCL}$ clusters were defined by co-expression of *ITGAE* (CD103), *ENTPD1* (CD39), and *CXCL13* (Figure 4B), a phenotype previously associated

with tumor-reactive CD8⁺ T cells in multiple solid tumor types (Duhen et al., 2018; Hanada et al., 2022; Oliveira et al., 2021; Simoni et al., 2018; Wischnewski et al., 2023). Together, these observations support the notion that the tissue-resident compartment contains the most strongly expanded candidate tumor-associated clonotypes in the BrM microenvironment.

To further assess this possibility, we applied two complementary approaches to infer tumor reactivity. First, a transcriptional tumor-reactivity score based on the signature described by Hanada et al. was projected onto the CD8⁺ UMAP (Hanada et al., 2022). This score showed strongest enrichment within the resident-memory clusters, with lower enrichment in the T_{EX} population (Figure 5E). Second, a machine-learning-based classifier was applied to predict tumor-reactive TCRs from integrated scRNA-seq and V(D)J data (Tan et al., 2025). These predictions largely overlapped with the signature-based approach, while extending into the T_{EX} cluster and a subset of GZMK-positive populations (Figure 5F).

To assess the contribution of potential viral-reactive bystander T cells, TCRβ CDR3 amino acid sequences were cross-referenced against VDJdb, a curated database of experimentally validated antigen-specific TCRs. Only few virus-associated matches were detected within the CD4⁺ compartment, whereas a more notable fraction localized to CD8⁺ T cells (Figure 5G). Surprisingly, these hits were enriched within the T_{RM} cluster and originated exclusively from a single patient, NCH9587 (Figure 5H).

Although clonal expansion was most pronounced in CD8⁺ T cells, analysis of the isolated CD4⁺ compartment also revealed selective expansion within activated subsets. Expanded CD4⁺ clonotypes were primarily detected in T_{FH}, $T_{REG\text{-}ACT}$, and T_{EM} GzmK populations (Figure 5C). This observation is compatible with localized activation of distinct helper T cell populations within the BrM niche and further supports the presence of structured intratumoral immune responses, which are examined spatially in section 4.3.5.

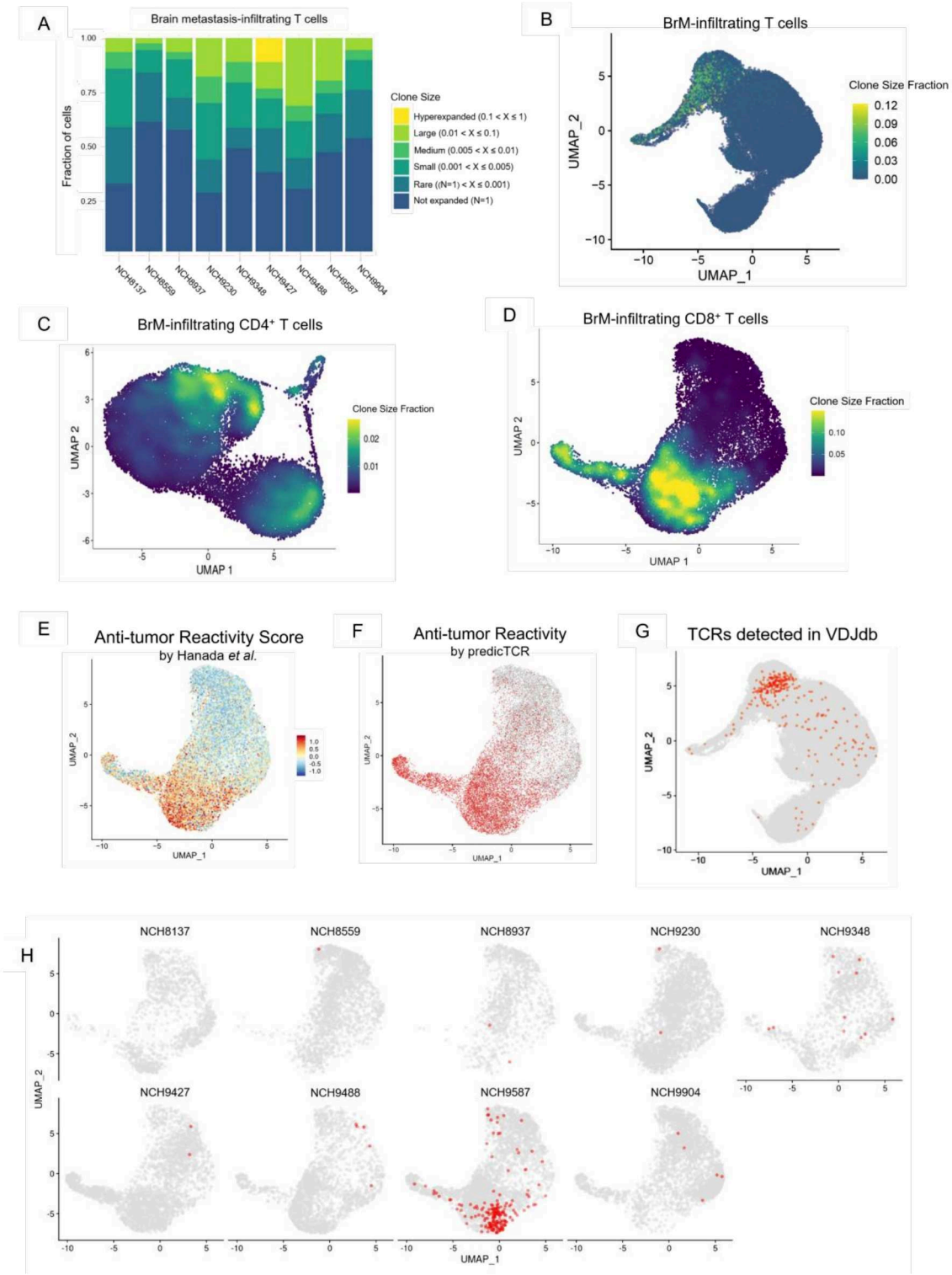


Figure 5: Clonal architecture of brain metastases (BrM)-infiltrating T cells.

(A) Distribution of clonal expansion frequencies of BrM-infiltrating T cells based on paired TCRαβ sequences. (B) UMAP of the global T cell compartment colored by clonal expansion. Projection of clonal expansion onto the CD4+ (C) and CD8+ (D) T cell UMAPs. Feature plots of the CD8+ T cell UMAP showing tumor-reactivity scores based on the Hanada et al. transcriptional signature (E) and the predicTCR classifier (F). (G) UMAP of the global T cell compartment highlighting TCRs with virus-associated matches in VDJdb. (H) CD8+ T cell UMAP shown separately for each patient, highlighting virus-associated clonotypes.

4.1.5. Low clonal expansion in peripheral blood T cells contrasts with the tumor-infiltrating compartment

The pronounced clonal expansion observed within BrM-infiltrating T cells suggested antigen-driven activation within the metastatic niche. However, it remained unclear whether these expanded clonotypes were restricted to the intracerebral compartment or were also present in the peripheral circulation. Resolving this question provides indirect insight into whether these T cells represent locally expanded populations or reflect systemic immune responses potentially primed outside the brain. To address this, I performed paired single-cell transcriptomic and TCR profiling of peripheral blood (PB) T cells and tumor-infiltrating T cells from four patients.

$CD3^+$ T cells were isolated by FACS from cryopreserved peripheral blood mononuclear cells (PBMCs) obtained from four patients whose BrM samples had been profiled previously. Unsupervised clustering identified distinct transcriptional states within the peripheral T cell compartment (Figure 6A) and cluster annotation was performed based on differentially expressed genes (Figure 6B). Naïve T cells were defined by high expression of *SELL*, *TCF7*, *CCR7*, *LEF1*, *KLF2*, and *IL7R*. Central memory T cells retained expression of *KLF2* and *IL7R* while exhibiting reduced levels of naïve-associated markers. Effector memory T cells showed further downregulation of naïve markers and upregulation of effector-associated genes, including *KLRB1* in $CD4^+$ cells and cytotoxic molecules such as *GZMB*, *PRF1*, and *NKG7* in $CD8^+$ cells. Cytotoxic $CD4^+$ T cells were defined by high expression of *PRF1* and *NKG7* in the absence of memory-associated gene expression. Regulatory T cells were identified by *FOXP3* and *IL2RA* expression together with inhibitory receptors including *TIGIT* and *CTLA4*. Natural killer (NK) cells were annotated on the expression of *NKG7*, and *KLRB1*, mucosal-associated invariant T (MAIT) cells were annotated based on *TRAV1-2*, *SLC4A10*, and *KLRB1* expression, while γδ T cells were defined by *TRGV9* and *TRDV2* expression. No cluster of proliferative cells could be detected.

Analysis of TCR clonality revealed markedly lower levels of clonal expansion in peripheral blood compared to matched BrM samples, with the majority of peripheral T cells represented by unique TCRs (Figure 6C). This observation is consistent with the expected diversity of circulating T cell repertoires. Notably, one patient (NCH9230) exhibited substantially higher clonal expansion in peripheral blood, with more than 50% of T cells belonging to expanded clonotypes, whereas the remaining patients showed markedly lower levels of expansion.

Projection of clonal expansion onto the PB UMAP revealed that expanded clonotypes were primarily localized within the $CD8^+$ effector memory compartment (Figure 6D). These T cells

co-expressed cytotoxic effector molecules and activation-associated genes in combination with memory genes, consistent with an re-activated T cell state.

To further characterize the antigen specificity of the expanded TCR repertoire, TCR sequences were compared against the VDJdb. This analysis identified some TCRs with virus-associated entries. However, only a negligible number of fully matching TCRs, defined by identical α- and β-chain pairing (Figure 6E).

Taken together, these findings indicate that clonal expansion is generally less pronounced in peripheral blood than in the tumor microenvironment, although a slight clonal expansion can be observed in one patient and is associated with activated $CD8^+$ T_{EM} cell states. Compared to the BrM T cells, T cells from the peripheral blood are more frequently annotated with known viral-reactivity in the VDJdb. These virus-directed TCRs were predominantly found in distinct clusters within the $CD4^+$ and $CD8^+$ effector memory clusters. However, the extent to which clonally expanded T cells are shared between brain metastases and the peripheral circulation remains unresolved.

To directly address this, I next performed a comparison of TCR-sequences between patient matched BrM and PB T cells, as described in section 4.1.6.

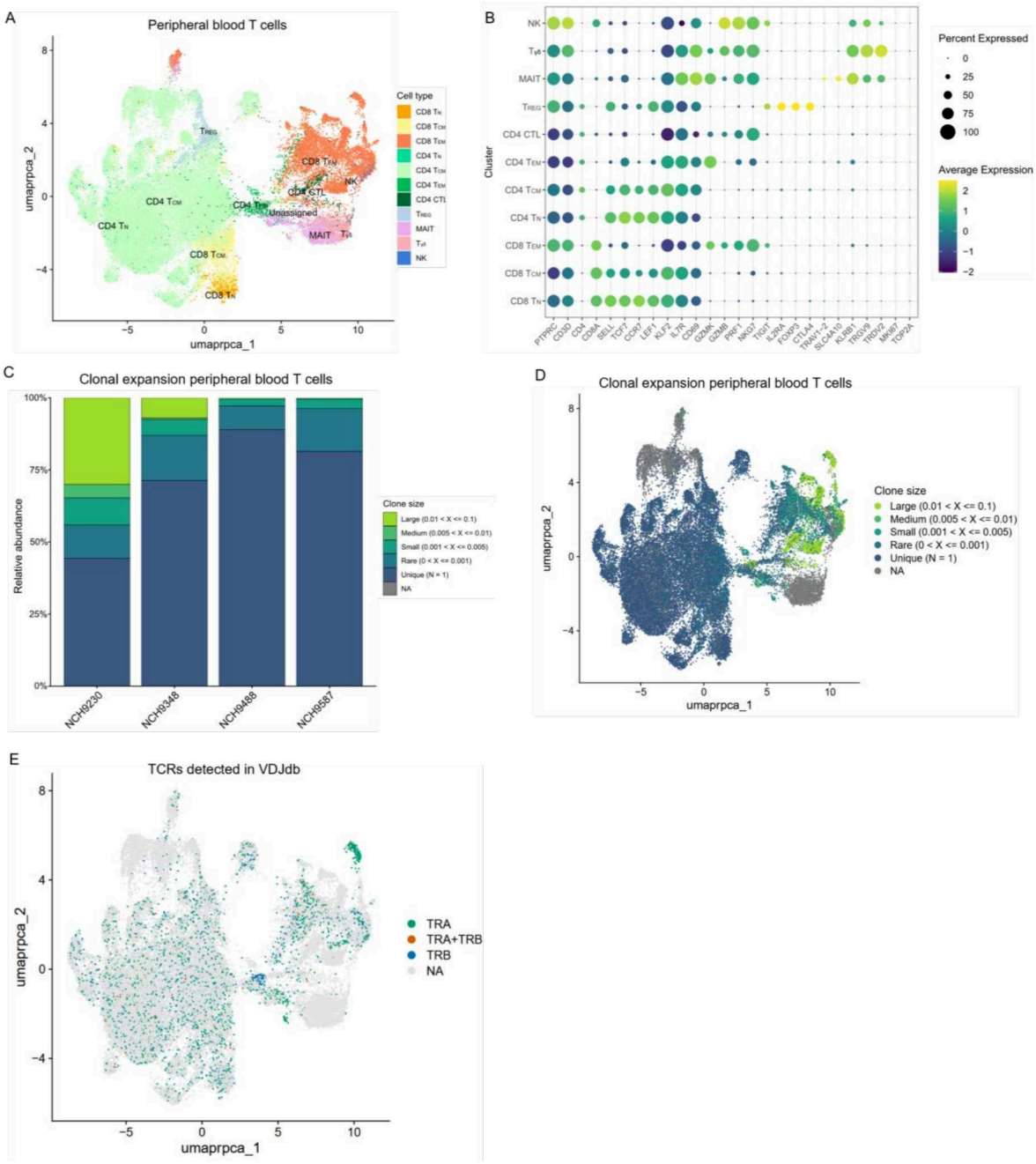


Figure 6: Single-cell transcriptomic and clonal profiling of peripheral blood (PB) T cells.

(A) UMAP of PB T cells colored by cluster annotation. (B) Dot plot showing expression of selected marker genes used for cluster annotation. (C) Distribution of clonal expansion frequencies of PB T cells based on paired TCRαβ sequences. (D) Projection of clonal expansion onto the PB T cell UMAP. (E) UMAP highlighting TCRs with virus-associated matches in VDJdb.

4.1.6. TCR sharing between brain metastasis-infiltrating and peripheral blood T cells

To assess whether clonally expanded T cells are shared between the tumor and the peripheral circulation, BrM-infiltrating and matched peripheral blood (PB) T cells were directly compared based on identical TCR amino acid sequences.

The extent of TCR sharing between compartments varied markedly across patients (Figure 7A-D). Notably, this heterogeneity was not explained by differences in the number of sequenced T cells. For example, patient NCH9348, despite having the lowest number of sequenced BrM T cells (Appendix Figure 1A), exhibited 122 shared clonotypes, whereas patient NCH9587, with the highest number of sequenced BrM T cells, displayed only 37 shared clonotypes. Beyond the absolute number of shared clonotypes, substantial variability was observed in their clonal sizes and relative distribution between compartments.

In patient NCH9230, a prominent shared clonotype comprised several hundreds of cells and represented a highly expanded population in the peripheral blood, accounting for nearly 10% of all detected TCRs, while constituting less than 1% of the BrM TCR repertoire (Figure 7A). In contrast, patient NCH9587 harbored two shared clonotypes that were highly expanded within the brain compartment, each comprising more than 100 cells and accounting for approximately 9% of all sequenced TCRs, while representing less than 0.1% of the peripheral blood repertoire (Figure 7D). Beyond these compartment-skewed extremes, a subset of smaller clonotypes displayed comparable relative frequencies across both compartments, consistent with a more balanced distribution between circulation and tumor tissue.

It is important to consider that single-cell sequencing captures only a small fraction of the highly diverse circulating TCR repertoire. As a result, rare clonotypes present in peripheral blood may not be detected, potentially leading to an underestimation of true systemic TCR sharing. To address this limitation, bulk TCRβ sequencing of peripheral blood T cells was performed to assess whether the clonal expansion patterns observed in the single-cell dataset accurately reflect the underlying peripheral TCR repertoire. While this approach does not preserve α-β chain pairing information, it provides substantially increased sampling depth and enables more sensitive detection of low-frequency clonotypes. Bulk TCR analysis showed strong concordance with the single-cell data, with similar proportions of clonally expanded T cells observed across patients (Figure 7E, Figure 6C). In addition, analysis of the 10 most expanded clonotypes revealed that peripheral clonal expansion in

patient NCH9230 was driven by a small number of dominant clones rather than broad polyclonal expansion (Figure 7F).

While these analyses provide evidence for compartmental overlap of clonally expanded T cells, they do not resolve their antigen specificity. To directly the antigen specificity of selected BrM-derived TCRs, I performed functional *in vitro* assays which are described in the next section 4.2.

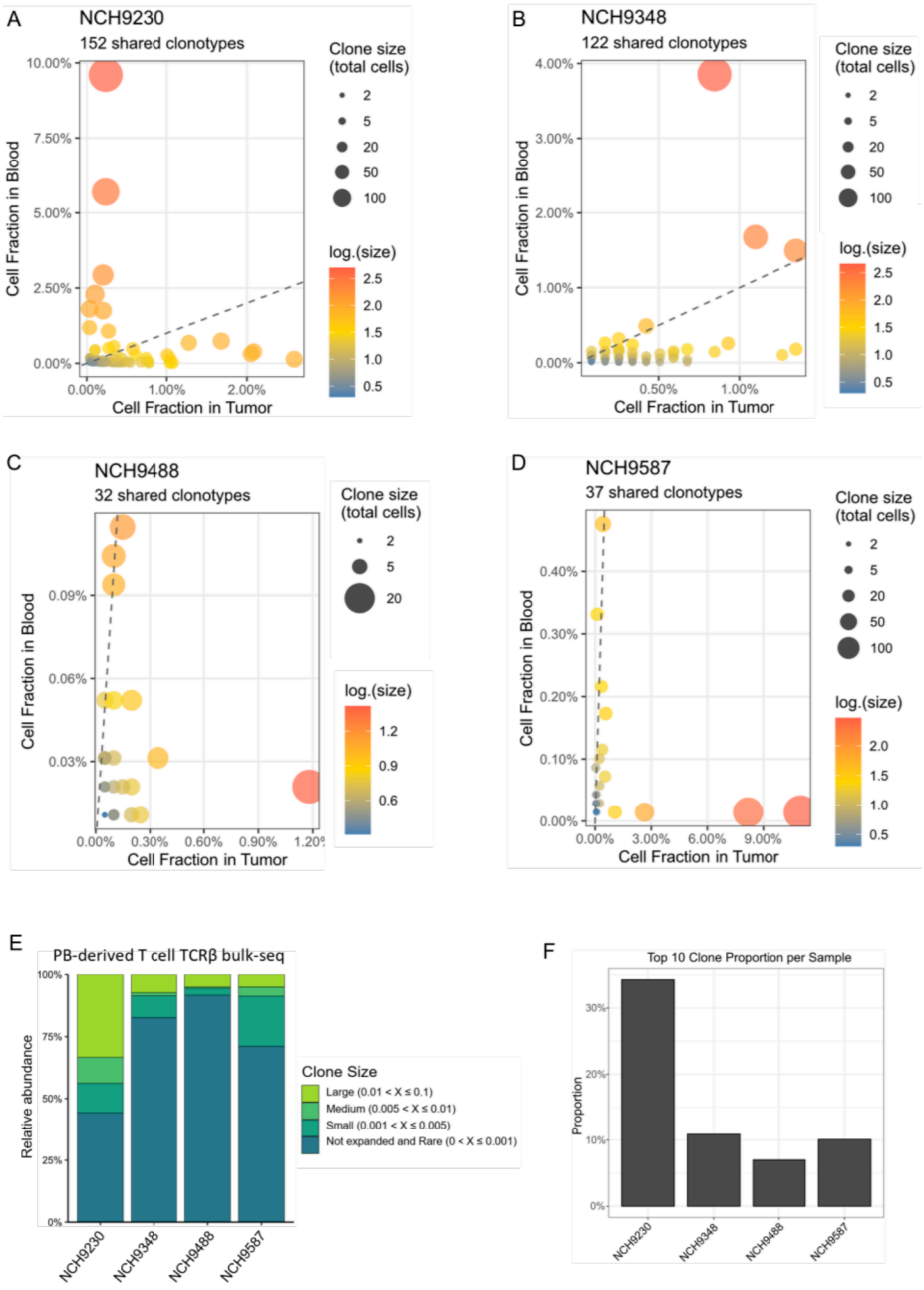


Figure 7: TCR sharing between brain metastasis-infiltrating and peripheral blood T cells

(A-D) Clonotype overlap between brain metastasis-infiltrating (tumor) and PB (blood) T cells across four patients. Dot size indicates the number of cells per clonotype, which is furthermore indicated by log. size color coding. Number of shared clonotypes are indicated. (E) Clonal fraction of the PB TCR repertoire determined by bulk TCRβ sequencing. (F) Proportion of the top 10 clonotypes per sample based on bulk TCRβ sequencing.

4.2. Functional validation of tumor reactivity of selected TCRs from brain metastases-infiltrating T cells

To directly test whether T cells identified in the BrM microenvironment recognize tumor-derived antigens, I performed in vitro functional assays using selected TCRs derived from the single-cell RNA/TCR-seq dataset.

A major limitation in studying brain metastases is the scarcity of viable patient material. For this analysis, I obtained cryopreserved single-cell suspensions of BrM tissue from two patients (NCH8937 and NCH9348), as well as matched PBMCs from patient NCH9348.

To functionally assess whether selected TCRs mediate tumor antigen-specific T cell activation, I applied two complementary experimental systems based on TCR-transgenic cells. Selected TCR sequences were cloned in collaboration with Dr. Edward Green (DKFZ), transcribed into mRNA, and transfected into either a Jurkat reporter cell line or autologous T cells. Functional responses were then measured upon co-culture with patient-derived tumor cells using reporter activation or flow cytometric readouts of T cell activation.

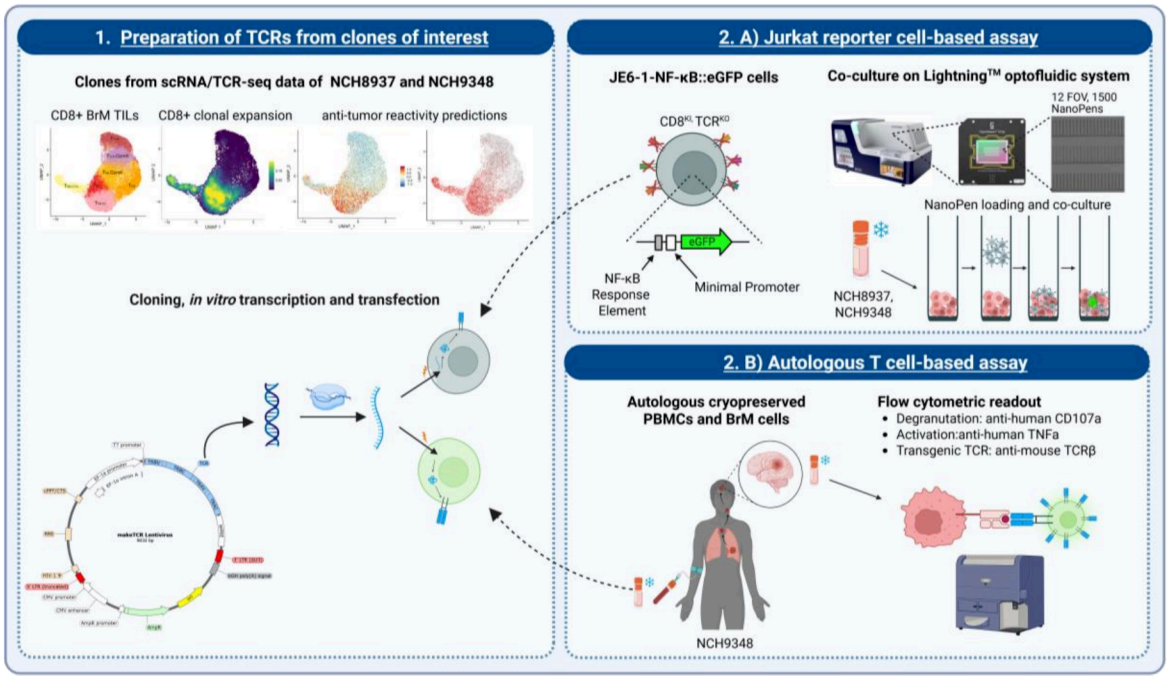


Figure 8: Workflow for functional validation of candidate T cell receptors (TCRs).

Schematic overview of the experimental pipeline for functional testing of TCRs identified from scRNA/TCR-seq of brain metastases (BrM)-infiltrating T cells from patients NCH8937 and NCH9348. (1.) Selected TCR sequences were cloned, in vitro transcribed, and transfected as mRNA into either JE6-1 reporter cells or autologous T cells (available for NCH9348). (2. A) TCR-transgenic JE6-1 reporter cells were co-cultured with patient-derived tumor cells using the Lightning™ optofluidic platform, with NF-κB-driven eGFP expression as a readout of T cell activation. (2. B) TCR-transgenic autologous T cells were co-cultured with tumor cells, and activation was assessed by flow cytometric detection of CD107a surface expression and TNFα production.

4.2.1. Selection and characterization of candidate TCR clonotypes for functional testing

TCR candidates for functional validation were selected based on the integrated single-cell transcriptomic and clonal analyses described in sections 4.1.3 and 4.1.4. I focused on clonally expanded $CD8^+$ T cells, defined as clonotypes represented by at least four cells sharing identical paired TCRαβ sequences. To capture a broad spectrum of transcriptional states, TCRs were selected from clusters associated with predicted tumor reactivity based on transcriptomic and machine learning-based approaches (Figure 4D, Figure 4E, and shown again in Figure 9B and Figure 9C for reference), as well as from clusters not classified as tumor-reactive.

For patient NCH8937, eight TCR clonotypes were selected. Three clonotypes originated from clusters predicted to be tumor-reactive based on both transcriptomic signatures and machine learning-based classification, predominantly mapping to the $T_{RM\text{-}EX}$ cluster (Figure 9D, clones 1 to 3). Three further clonotypes were selected from the GZMK-positive effector memory cluster (Figure 9D, clones 4 to 6). One additional clonotype (Figure 9D, clone 7) localized to an intermediate transcriptional state spanning features of exhausted and effector memory populations, while one clonotype mainly originated from the stem-like memory cluster (Figure 9D, clone 8).

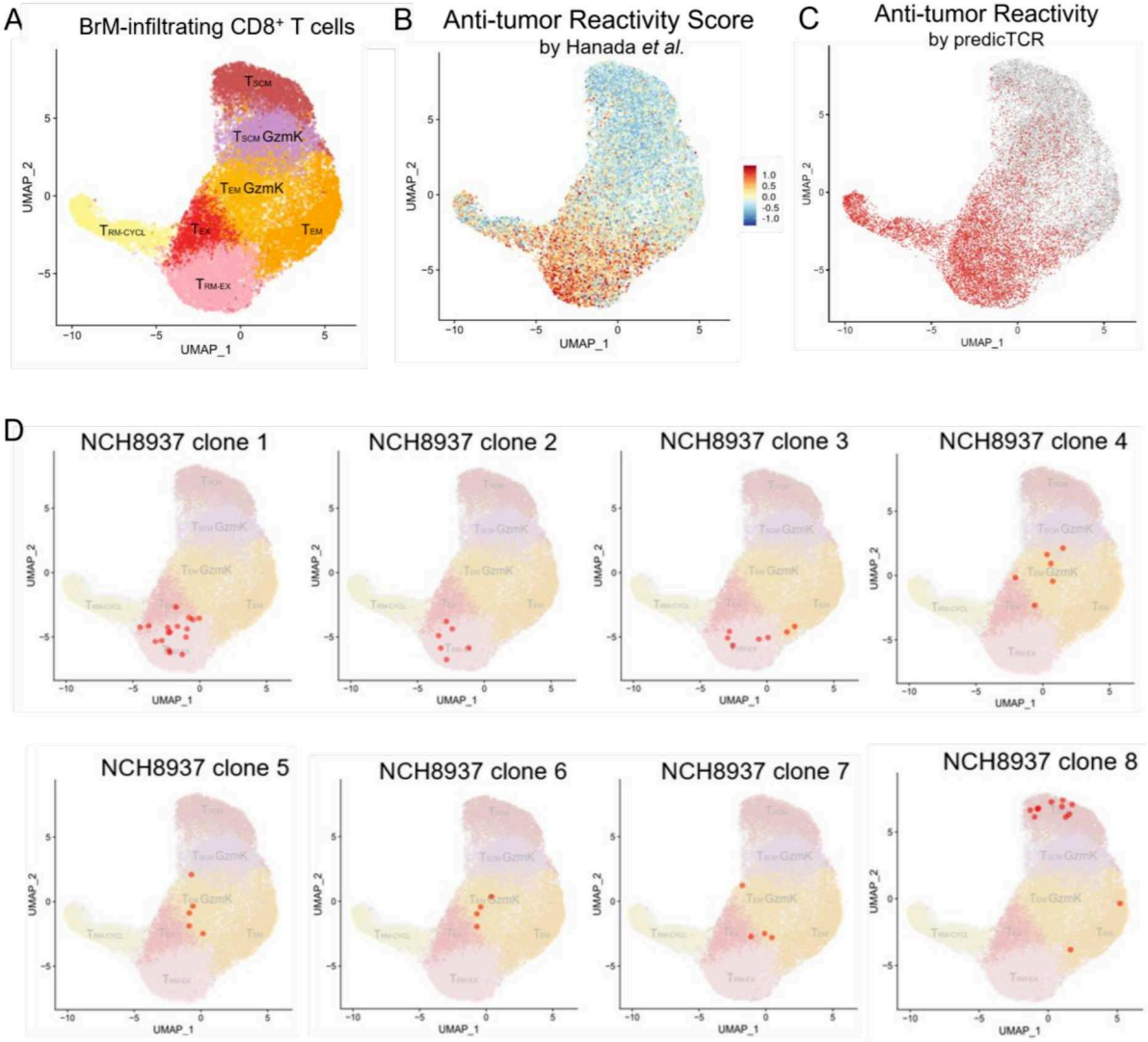


Figure 9: Distribution of TCR clonotypes selected from sample NCH8937 for functional validation.

For reference, the BrM CD8⁺ TIL UMAP (A), the anti-tumor reactivity score based on the signature by Hanada et al. (B), and the predicTCR score (C) are shown again. (D) UMAP projection of the BrM CD8⁺ T cell compartment showing the distribution of eight selected TCR clonotypes from patient NCH8937.

For patient NCH9348, nine clonotypes were selected for downstream analysis. The majority of these (clones 1-7; Figure 10A) were derived from the predicted tumor-reactive clusters $T_{RM\text{-}EX}$ and $T_{RM\text{-}CYCL}$. Two additional clonotypes (clones 8 and 9; Figure 10A) originated from T_{SCM} GZMK memory clusters, thereby extending the analysis to T cell populations outside the predicted tumor-reactive clusters.

For this patient, matched peripheral blood T cells were also profiled by scRNA-seq and TCR sequencing (see section 4.1.5). Notably, of the nine selected TCRs, only the two clonotypes derived from the BrM T_{SCM} GZMK TIL cluster (clones 8 and 9) were also detectable in the peripheral blood based on shared *TRAV* and *TRBV* gene usage as well as identical CDR3α

amino acid sequences (compare with Table 1). For each of these two clonotypes, one clonally expanded population was identified within the peripheral CD8⁺ T_{EM} compartment, accompanied by one to two additional T cells exhibiting alternative CDR3β chain pairing (Figure 6C). However, none of the remaining seven clones coming from the tumor-predicted CD103⁺ T_{RM} clones were detectable in the peripheral blood.

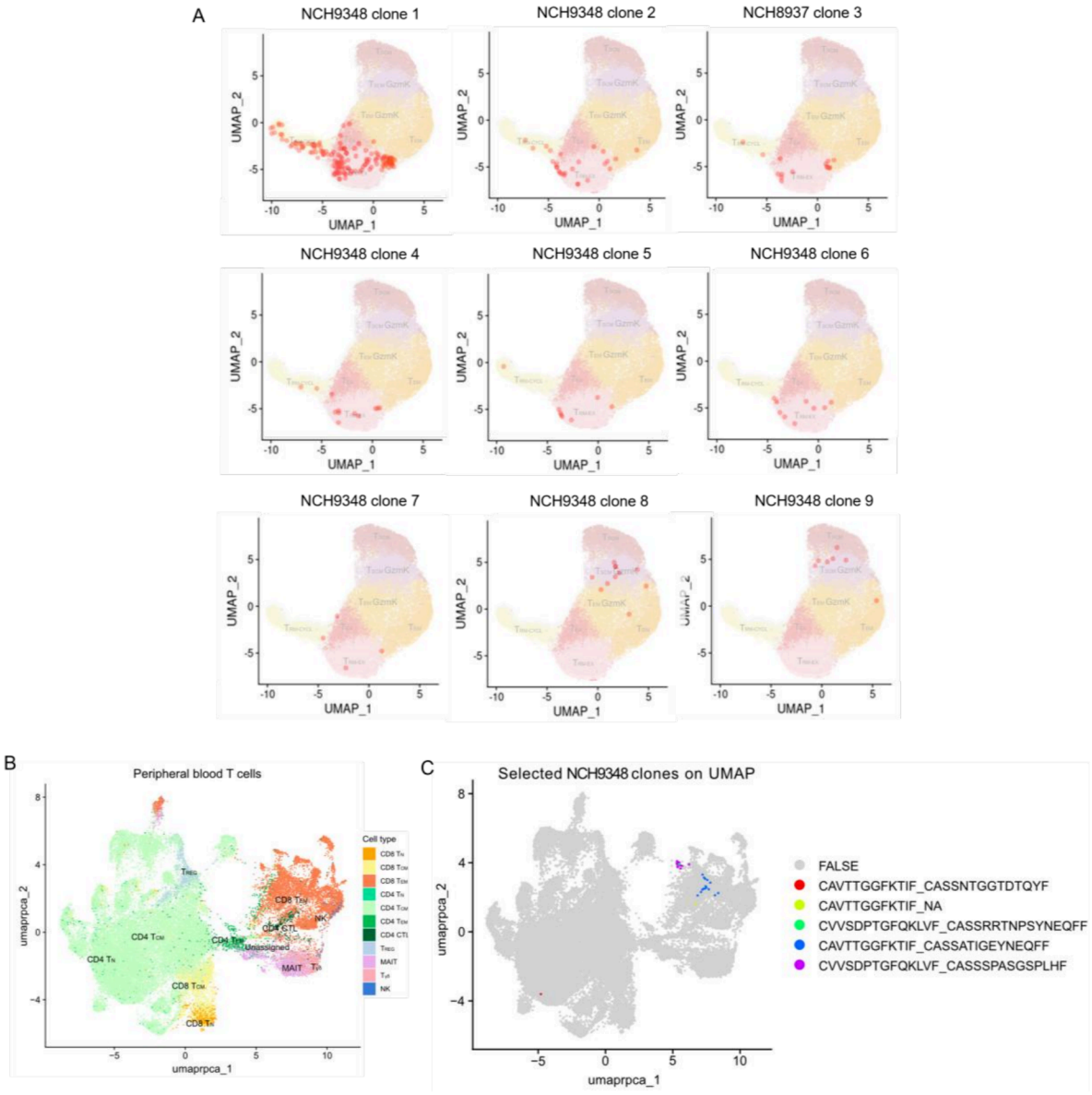


Figure 10: Distribution of TCR clonotypes selected from sample NCH9348 for functional validation.
(A) UMAP projection of the BrM CD8⁺ T cell compartment showing the distribution of eight selected TCR clonotypes from patient NCH9348. (B) For reference, the peripheral blood (PB) UMAP. (C) Localization on the PB UMAP of T cells carrying TCRs with identical *TRAV*/*TRBV* genes, and identical TCRα chain amino acid sequences to the selected clones of sample NCH9348 for the *in vitro* testing. Corresponding paired TCRα_TCRβ amino acid sequences are indicated.

The selected TCR clonotypes for both patient samples are summarized in Table 1, including their CDR3α amino acid sequences and corresponding *TRAV* and *TRBV* gene usage. Notably, several clonotypes shared identical *TRBV* gene segments while pairing with distinct *TRAV* chains. For example, in patient NCH8937, clonotypes 1 and 3 both utilized *TRBV20-1*, and clonotypes 5 and 6 shared *TRBV12-5*. Similarly, in patient NCH9348, clonotypes 1 and 2 both utilized *TRBV2* but differed in their associated *TRAV* genes. Despite sharing identical TCRβ chains, these clonotypes represent distinct TCRαβ receptors due to their unique α-chain pairing. As antigen recognition is determined by the combined αβ TCR structure, these receptors are expected to exhibit distinct antigen specificities.

Table 1: Sequence features of selected TCR clonotypes.

Selected TCR clonotypes derived from single-cell RNA/TCR sequencing of brain metastases (BrM)-infiltrating T cells from patients NCH8937 and NCH9348. The table summarizes CDR3 amino acid sequences and corresponding *TRAV* and *TRBV* gene usage for each clonotype.

Clone	**CDR3a sequence**	***TRAV***	***TRBV***
NCH8937 clone 1	CALSDWNNNARLMF	*TRAV19*	*TRBV20-1*
NCH8937 clone 2	CAGGRSTSGTYKYIF	*TRAV25*	*TRBV9*
NCH8937 clone 3	CLVVLPWMDTGRRALTF	*TRAV4*	*TRBV20-1*
NCH8937 clone 4	CAMDSNYQLIW	*TRAV38-2*	*TRBV6-5*
NCH8937 clone 5	CIVRVNNDMRF	*TRAV26-1*	*TRBV12-5*
NCH8937 clone 6	CAFIVIYNQGGKLIF	*TRAV24*	*TRBV12-5*
NCH8937 clone 7	CGTETGANNLFF	*TRAV30*	*TRBV5-1*
NCH8937 clone 8	CAVSPDGQKLLF	*TRAV12-2*	*TRBV7-8*
NCH9348 clone 1	CILGGGTSYGKLTF	*TRAV26-2*	*TRBV2*
NCH9348 clone 2	CAVKDDYKLSF	*TRAV12-2*	*TRBV2*
NCH9348 clone 3	CALSESPGGSEKLVF	*TRAV19*	*TRBV19*
NCH9348 clone 4	CAVTGDYGGSQGNLIF	*TRAV21*	*TRBV27*
NCH9348 clone 5	CAMREILRGANSKLTF	*TRAV14/DV4*	*TRBV2*
NCH9348 clone 6	CALSEQTGANNLFF	*TRAV19*	*TRBV6-5*

NCH9348 clone 7	CAVKDGADKYIF	*TRAV12-2*	*TRBV5-1*
NCH9348 clone 8	CVVSDPTGFQKLVF	*TRAV8-2*	*TRBV7-2*
NCH9348 clone 9	CAVTTGGFKTIF	*TRAV12-2*	*TRBV2*

To generate the selected TCRs for functional testing, TCR sequences were processed using the open-source “makeTCR” cloning platform and cloned in collaboration with Dr. Edward Green’s group into a T7 promoter-containing expression backbone (Appendix Figure 2A). The resulting constructs were used to generate *in vitro*-transcribed mRNA encoding both TCR α- and β-chains.

Due to the availability of autologous T cells only for patient NCH9348, two complementary experimental systems were established for functional testing. TCR mRNA was introduced either into a Jurkat-based reporter cell line or into autologous primary T cells, followed by co-culture with patient-derived tumor cells. The functional outcomes of these assays, which directly assess tumor reactivity of the selected TCRs, are presented in sections 4.2.1.1 and 4.2.1.2.

4.2.1.1. Functional assessment of TCRs using a Jurkat-reporter line identifies anti-tumor reactivity in CD103^{+} T cells

To functionally assess tumor reactivity of selected TCRs, I utilized the JE6-1-NF-κB::eGFP Jurkat reporter system, developed by the group of Assoc. Prof. Dr. Peter Steinberger (Medical University of Vienna), in which TCR engagement induces NF-κB-dependent eGFP expression as a direct readout of antigen-specific TCR signaling.

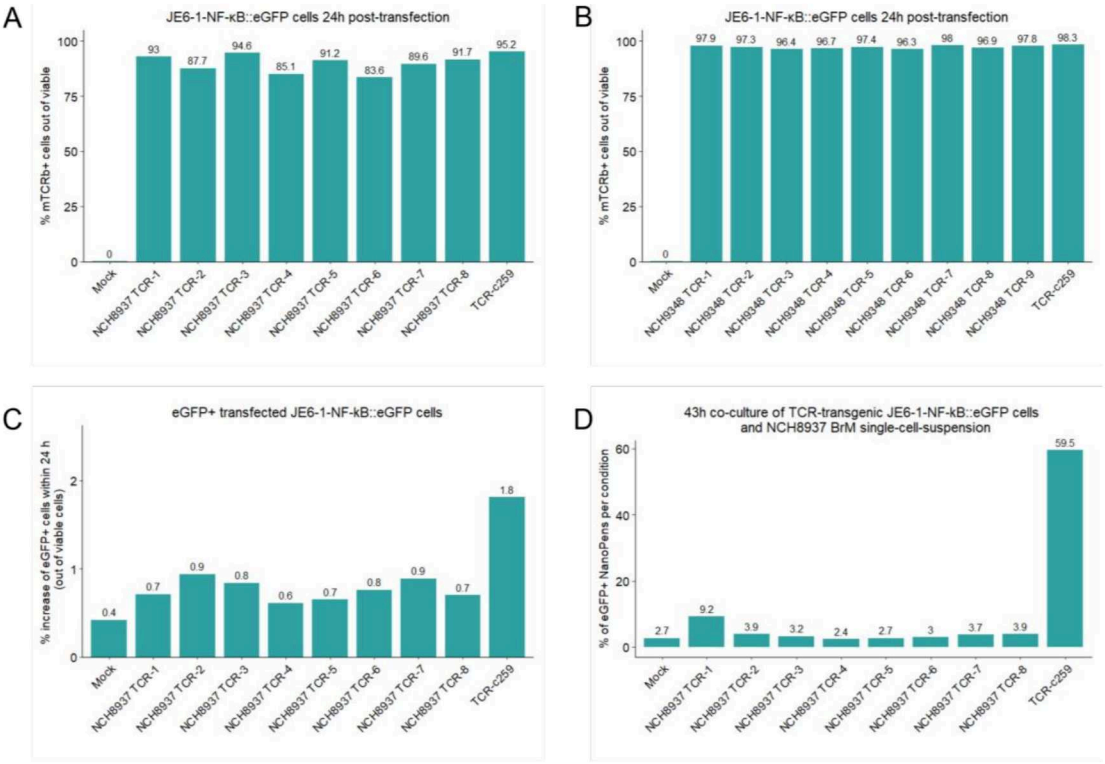
The assay was performed in two independent experiments using patient-specific TCRs and matched autologous brain metastases samples from patients NCH8937 and NCH9348. To enable high-throughput functional testing despite limited availability of primary tumor material, co-culture experiments were performed using the Lightning™ optofluidic platform (Bruker). This system allows single-cell-resolved co-culture in nanoliter-scale NanoPens™, enabling parallel analysis of more than 100 independent co-cultures per TCR candidate while minimizing consumption of BrM cells. Tumor cells were first loaded at a concentration adjusted to achieve approximately 10 cells per NanoPen™. Subsequently, TCR-transgenic Jurkat reporter cells were introduced, with each TCR condition assigned to a separate field of view comprising 101 to 156 NanoPens™. Jurkat cells were loaded at a concentration

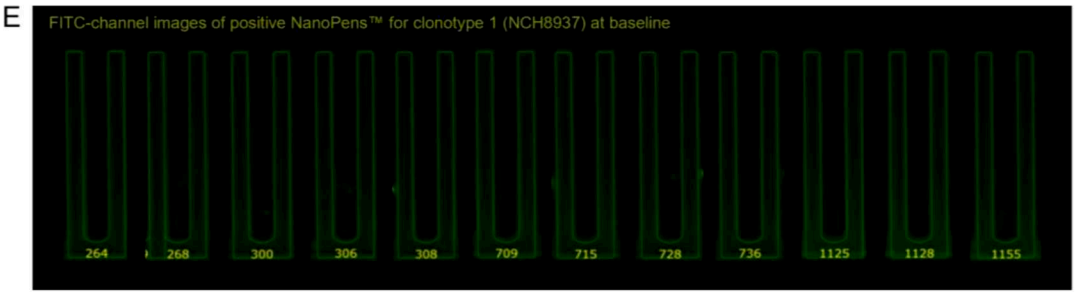
corresponding to approximately 5 cells per NanoPen™, resulting in a 1:2 effector to target ratio.

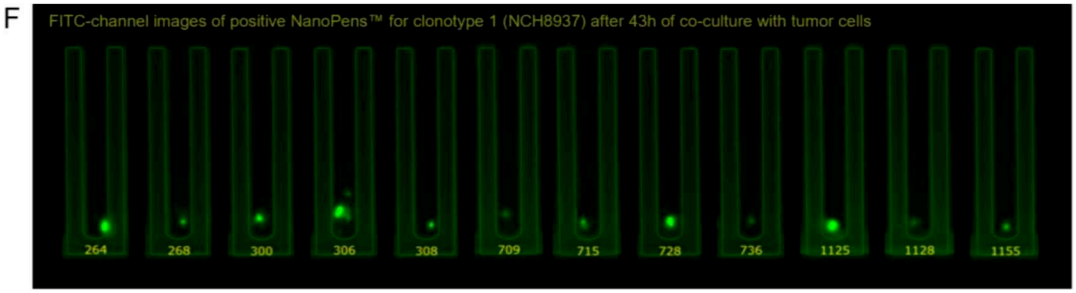
TCRs of interest were introduced into reporter cells by mRNA electroporation, resulting in efficient surface expression across all constructs (>80%) (Figure 11A, Figure 11B). Baseline reporter activity at the start of co-culture was low across all conditions, with mean eGFP positivity of approximately 4% to 5% among mRNA-transfected populations (Appendix Figure 2B-D). To further assess unspecific reporter induction in the absence of TCR stimulation, I monitored eGFP expression over an additional 24-hour period. This analysis showed only a minor increase in spontaneous eGFP positivity (Figure 11C), providing an important reference for distinguishing background reporter induction from bona fide TCR-dependent activation during co-culture. To define the dynamic range and background activity of the assay, both negative and positive controls were included. Mock-transfected cells (electroporated with elution buffer EB but without TCR mRNA) were used to quantify unspecific eGFP expression in the absence of TCR-mediated activation, thereby establishing the baseline level of reporter induction. As a positive control, reporter cells were transfected with the well-characterized NY-ESO-1-specific TCR 1G4-α95LY (referred to as TCR c259) and co-cultured with beads loaded with the cognate NY-ESO-1 peptide (SLLMWITQC). NY-ESO-1 is a highly immunogenic cancer-testis antigen frequently expressed in solid tumors (Chen et al., 2024). This condition provided a defined, antigen-specific stimulus to confirm functional responsiveness of the reporter system. Importantly, peptide presentation on beads represents a non-physiological setting with high local antigen density and therefore does not reflect endogenous antigen presentation by tumor cells. Consequently, this condition serves as a benchmark for maximal reporter activation rather than a direct comparator for physiological TCR activation in tumor co-culture experiments. Under these conditions, none of the tested TCRs from patient NCH9348 induced reporter activation above background levels (data not shown). Notably, the corresponding BrM single-cell suspension consisted entirely of non-viable cells, in contrast to the NCH8937 sample, which contained viable tumor cells. This lack of viable target cells likely limited antigen presentation and may explain the absence of detectable TCR activation in this experiment. Subsequent analyses were therefore restricted to patient sample NCH8937, in which TCR-dependent reporter activation was detectable. For this sample, one clonotype (NCH8937 clone 1) induced reporter activation, with 9.2% of NanoPens™ (12/130) containing eGFP-positive cells (Figure 11D-F). Time-resolved imaging confirmed that eGFP expression was induced upon direct contact of the TCR-transgenic Jurkat cells and the tumor cells and increased over time (Figure 11G).

Longitudinal analysis of fluorescence intensity revealed marked variability in eGFP signal strength across positive NanoPens™, reflected by differences in MFI values (Figure 11G). This variability is consistent with the peptide dose-dependent nature of the reporter system (Müller et al., 2020), in which fluorescence intensity scales with the strength of TCR-peptide interactions and the density of cognate antigen presented by target cells. Independently of signal intensity, in some NanoPens™ multiple reporter cells were simultaneously activated, suggesting that local presentation of sufficiently high levels of cognate antigen by tumor cells may enable coordinated activation of the TCR-identical reporter cells. Importantly, the activation of one T cell did not impact on the other T cells in the same NanoPen™. The magnitude of the eGFP expression for this positive hit must be interpreted in the context of the assay's dynamic range. Even under optimized conditions, the positive control reached only ~60% NanoPen™ positivity, indicating intrinsic sensitivity limitations of the reporter system. In addition, the use of unselected tumor single-cell suspensions introduces substantial cellular heterogeneity, including antigen-negative and non-malignant cells.

Taken together, the detection of contact-dependent activation in 9.2% of NanoPens™ provides strong functional evidence that the selected NCH8347 clonotype 1 recognizes antigens presented by autologous brain metastatic cells.


A
JE6-1-NF-κB::eGFP cells 24h post-transfection
% mTCRb+ cells out of viable
Mock
NCH8937 TCR-1
NCH8937 TCR-2
NCH8937 TCR-3
NCH8937 TCR-4
NCH8937 TCR-5
NCH8937 TCR-6
NCH8937 TCR-7
NCH8937 TCR-8
TCR-c259
B
JE6-1-NF-κB::eGFP cells 24h post-transfection
% mTCRb+ cells out of viable
Mock
NCH8348 TCR-1
NCH8348 TCR-2
NCH8348 TCR-3
NCH8348 TCR-4
NCH8348 TCR-5
NCH8348 TCR-6
NCH8348 TCR-7
NCH8348 TCR-8
NCH8348 TCR-9
TCR-c259
C
eGFP+ transfected JE6-1-NF-kB::eGFP cells
% increase of eGFP+ cells within 24 h (out of viable cells)
D
43h co-culture of TCR-transgenic JE6-1-NF-kB::eGFP cells and NCH8937 BrM single-cell-suspension
% of eGFP+ NanoPens per condition


E
FITC-channel images of positive NanoPens™ for clonotype 1 (NCH8937) at baseline
264
268
300
306
308
709
715
728
736
1125
1128
1155


F
FITC-channel images of positive NanoPens™ for clonotype 1 (NCH8937) after 43h of co-culture with tumor cells
264
268
300
306
308
709
715
728
736
1125
1128
1155

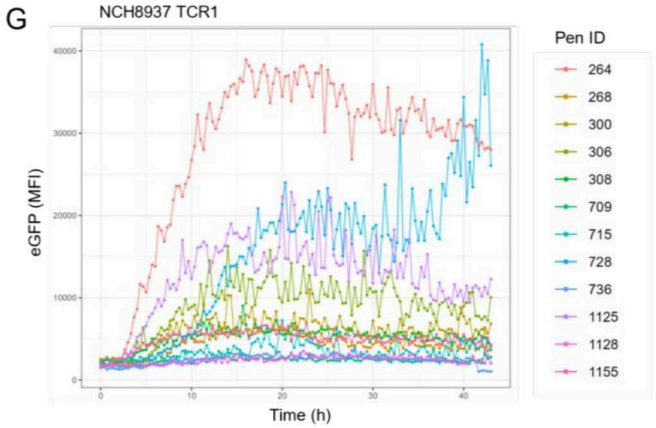

G
NCH8937 TCR1
eGFP (MFI)
Time (h)
Pen ID
264
268
300
306
308
709
715
728
736
1125
1128
1155

Figure 11: Functional identification of a tumor-reactive TCR in NCH8937 using a Jurkat reporter assay

Flow cytometric assessment of surface expression of transfected mTCRs for candidate clonotypes from NCH8937 (A) and NCH9348 (B). (C) Increase in unspecific eGFP expression in reporter cells transfected with TCRs of interest over 24 h (24-48h post-transfection) in the absence of target cell stimulation. (D) Fraction of NanoPens™ containing eGFP-positive cells after 43 h of co-culture with autologous BrM cells from NCH8937, meeting predefined criteria for TCR-dependent activation (contact-dependent signal induction and onset ≥6 h after co-culture initiation). Representative FITC-channel images of positive NanoPens™ for clonotype 1 (NCH8937) at baseline (E) and after 43 h (F). (G) Longitudinal mean fluorescence intensity (MFI) of the 12 NanoPens™ exhibiting TCR-dependent activation.

4.2.1.2. Functional assessment of TCRs using autologous T cells identifies anti-viral reactivity in T cells outside the tumor-reactive predicted cluster

To exclude that the absence of tumor reactivity observed for NCH9348-derived TCRs in the Jurkat reporter assay was due to limited assay sensitivity, I performed complementary functional testing using autologous primary T cells. T cells were expanded from cryopreserved PBMCs of patient NCH9348 and transfected with mRNA encoding the nine candidate TCRs selected from this patient. TCR-transgenic T cells were co-cultured with autologous tumor single-cell suspensions at an effector-to-target ratio of 1:1 for 6 hours. T cell activation was assessed by flow cytometric detection of degranulation by CD107a and effector function and cytokine production by TNFα.

To validate assay performance under physiological conditions, multiple control conditions were included. As a positive control for antigen-specific activation, T cells expressing the NY-ESO-1-specific TCR c259 were co-cultured with the melanoma cell line A375, which endogenously expresses high levels of NY-ESO-1. Baseline activation was assessed using TCR-transgenic T cells cultured alone, while co-culture with autologous PBMCs served to exclude nonspecific or autoreactive activation. In addition, TCR-independent stimulation using TransAct™, a polymeric nanomatrix conjugated to humanized CD3 and CD28 agonists, confirmed the general activation capacity of transfected T cells. Finally, a viral peptide pool (PepTivator®) containing 32 MHC-I-restricted peptides from cytomegalovirus (HCMV), Epstein-Barr virus (EBV), and influenza virus was used to assess potential virus-specific reactivity.

Efficient TCR expression was achieved across all constructs, with >90% of viable $CD8^+$ T cells staining positive for the transgenic TCR at the time of analysis (Figure 12A). The use of murine constant regions prevented mispairing with endogenous TCR chains and enabled specific detection of transgenic TCR expression using an anti-mouse TCRβ antibody.

No activation was observed in T cells cultured alone or in co-culture with autologous PBMCs, indicating absence of nonspecific or autoreactive responses. Upon TCR-independent stimulation, all conditions showed robust activation, with >50% of TCR-positive cells expressing CD107a and/or TNFα (Figure 12C-K), confirming functional competence of the transfected T cells.

The positive control condition (TCR-c259 + A375 cells) resulted in clear antigen-specific activation, with approximately 25% of T cells expressing CD107a and/or TNFα (Figure 12B), demonstrating that the assay is capable of detecting physiologically relevant TCR-mediated responses.

In contrast, none of the nine NCH9348-derived TCRs induced detectable activation upon co-culture with autologous tumor cells, indicating absence of measurable tumor reactivity under these conditions. This finding is consistent with the results obtained for patient NCH9348 in the Jurkat reporter assay from section 4.2.1.1 and supports the conclusion that the lack of activation is not attributable to insufficient assay sensitivity.

Notably, one clonotype (clone 9) exhibited strong activation in response to the viral peptide pool, indicating virus-specific reactivity (Figure 12K, Figure 12L). This clonotype was transcriptionally annotated as belonging predominantly to the T_{SCM} GZMK cluster (Figure 10 A), consistent with a non-tumor-specific memory phenotype.

Taken together, these results demonstrate that one of the two clonotypes selected from non-tumor-predicted transcriptional states in patient NCH9348, which was furthermore detectable in the patients peripheral blood, exhibits clear functional reactivity toward viral antigens. This finding provides direct evidence that TCRs outside of tumor-associated clusters can represent virus-specific bystander populations within the BrM-infiltrating T cell compartment.

In contrast, none of the NCH9348-derived TCRs induced detectable activation upon co-culture with autologous tumor cells. As noted above in section 4.2.1.1, the cryopreserved tumor single-cell suspension used in this assay consisted entirely of non-viable cells, likely limiting antigen presentation. Consequently, the absence of tumor-directed activation cannot be interpreted as evidence for a lack of tumor reactivity.

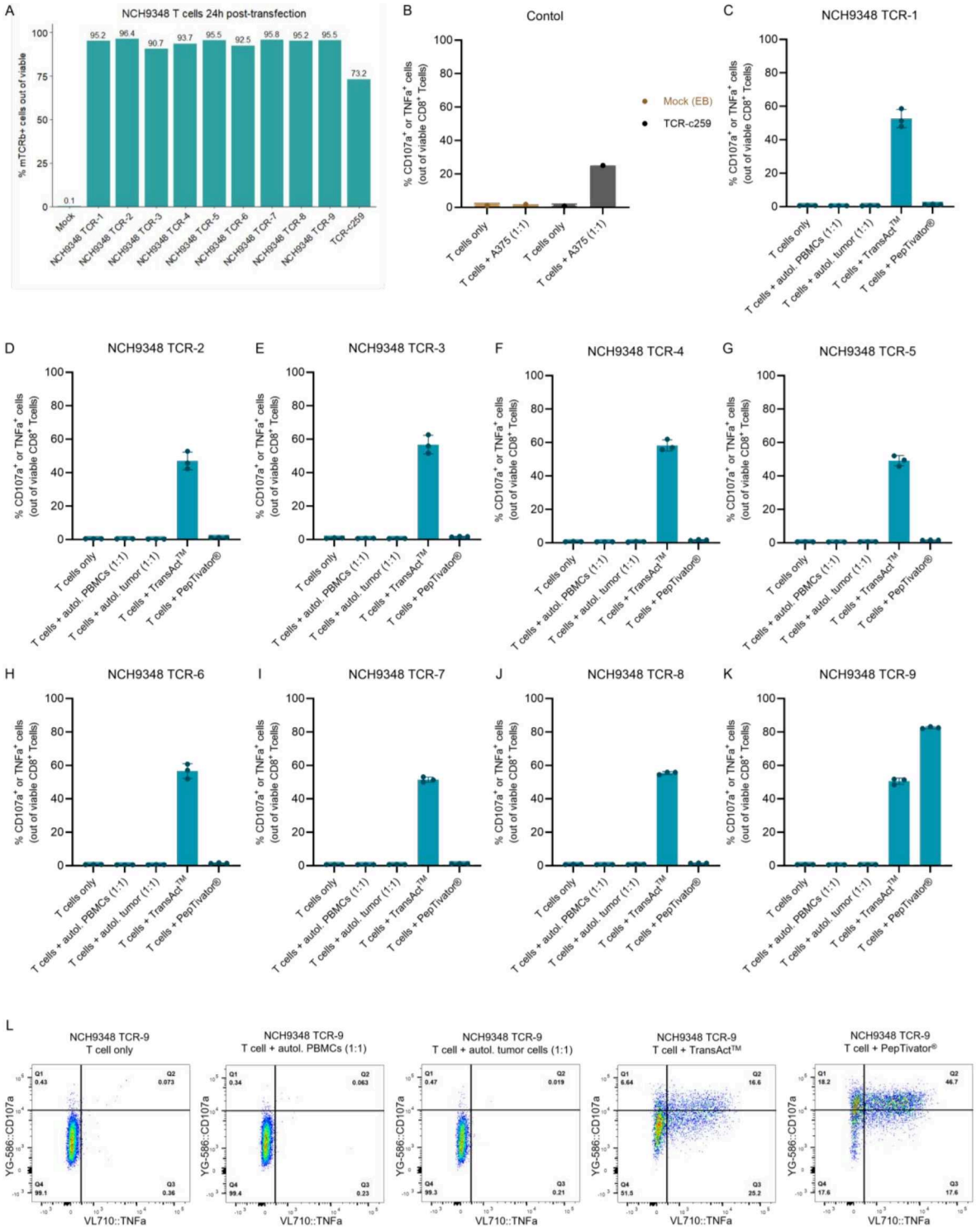


Figure 12: Functional assessment of NCH9348-derived TCRs in autologous primary T cells.

(A) Flow-cytometric assessment of transfection efficiency, showing mTCRβ expression in $CD8^+$ T cells. (B) Percentage of $CD107a^+$ and/or $TNF\alpha^+$ T cells following co-culture of mock- or c259-transfected T cells with A375 melanoma cells or culture without target cells. (C-K) Percentage of $CD107a^+$ and/or $TNF\alpha^+$ T cells transfected with NCH9348-derived TCRs following 6 h under the indicated conditions: T cells alone, co-culture with autologous PBMCs, co-culture with autologous tumor cells, TCR-independent stimulation (TransAct™), or stimulation with a viral peptide pool (PepTivator®). (L) Representative flow cytometry plots showing CD107a and TNFα expression for NCH9348 clonotype 9 under the indicated conditions.

4.3. Spatial organization of T cell populations in brain metastases

The single-cell transcriptomic and TCR-based analyses presented above identified clonally expanded $CD8^+$ T cell populations with transcriptional features consistent with antigen-driven activation within brain metastases. These populations were predominantly enriched within tissue-resident $CD103^+$ T cell states, suggesting local activation and retention within the metastatic niche. Independent tumor-reactivity prediction approaches, based on both transcriptomic signatures and machine learning-based classification, consistently predicted tumor reactivity for cells within these states.

Functional validation further demonstrated that selected TCRs can mediate antigen-specific responses. Notably, the clonotype identified as tumor-reactive originated from a tissue-resident cluster, predicted to be tumor-reactive by both transcriptomic and machine learning-based approaches, whereas the clonotype exhibiting viral specificity was derived from a non-tumor-predicted state, specifically the T_{SCM} GZMK cluster. These findings provide functional support for the predictive frameworks and highlight the functional heterogeneity of the intratumoral T cell repertoire.

The limited overlap of TCR clonotypes between peripheral blood and brain metastases, together with the presence of highly expanded $CD103^+$ tissue-resident T cells within the tumor, suggests that clonal expansion may predominantly occur locally within the metastatic niche rather than being driven by continuous recruitment from the periphery.

This observation led to the hypothesis that clonally expanded and functionally distinct T cell populations are spatially organized within defined microenvironmental niches that support local activation, differentiation, and retention. In particular, I sought to determine whether putative tumor-reactive $CD103^+$ T cells preferentially localize to specific anatomical regions and whether they engage in direct interactions with tumor cells. Furthermore, I aimed to assess the presence of tertiary lymphoid structures (TLS) as potential sites of local T cell priming.

However, dissociation-based single-cell analyses inherently lack spatial context, as tissue disruption abolishes architectural integrity and precludes assessment of cellular organization and interactions within the tumor microenvironment. Moreover, understanding anti-tumor immunity requires analysis beyond isolated T cells, incorporating the broader cellular and structural context, including other immune populations, stromal components, and tumor architecture. To address these limitations, we performed multiplexed tissue imaging using co-detection by indexing (CODEX, PhenoCycler) in collaboration with the group of Prof. Dr. Sascha Dietrich (University clinic Düsseldorf) to resolve the spatial distribution, cellular composition, and interaction networks within brain metastases.

Importantly, the presence of clonally expanded CD103$^+$ T cells with cytotoxic features did not uniformly associate with effective tumor control. For example, in patient NCH8937, I functionally validated a tumor-reactive TCR, demonstrating the presence of clonally expanded T cells capable of recognizing tumor-derived antigens. Despite this, this patient exhibited the shortest overall survival within the cohort (4 months; Table M 1). While this observation is limited to a single case and does not allow for generalizable conclusions, it highlights that the presence of tumor-reactive T cells alone may not be sufficient to mediate effective tumor control. Additional clinical and tumor-intrinsic factors are likely to critically influence patient outcome.

Resolving these mechanisms requires analysis of tumor-infiltrating lymphocytes within their native spatial context. However, existing spatial studies of brain metastases are limited by restricted multiplexing capacity, incomplete tissue coverage, or insufficient single-cell resolution, leaving the spatial organization of immune cell populations in brain metastases incompletely defined (Álvarez-Prado et al., 2023; Biermann et al., 2022; Lu et al., 2021; Widodo et al., 2023).

To address these limitations, I performed multiplexed tissue imaging using CODEX to resolve the spatial distribution, cellular composition, and interaction networks within brain metastases. All brain metastases analyzed originated from primary NSCLC. Pathological classifications and clinical characteristics are summarized in Table M 2 and Table M 3. A schematic overview of the experimental workflow is shown in Figure 13.

This analysis aimed to define the spatial organization and interaction networks of tumor-infiltrating T cells, with a particular focus on CD103$^+$ populations as a surrogate for clonally expanded T cells, in order to identify microenvironmental factors that may limit effective anti-tumor immunity. While the current analysis is based on qualitative interpretation of multiplexed imaging data, comprehensive quantitative and computational analyses of spatial architecture, cellular neighborhoods, and cell-cell interactions are ongoing and were beyond the scope of this thesis.

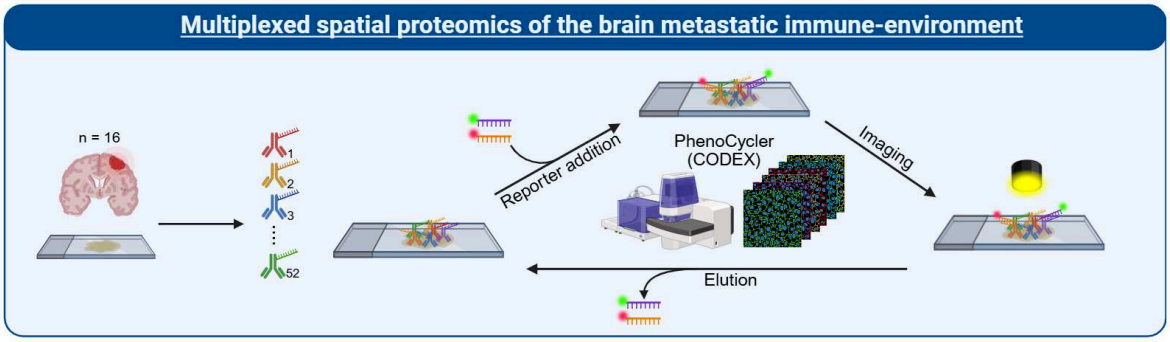


Figure 13: Multiplexed tissue imaging by CODEX (PhenoCycler).

Schematic overview of co-detection by indexing (CODEX) imaging based on iterative cycles of reporter hybridization and removal. Brain metastasis tissue sections (n = 16; NSCLC origin) were stained with a 52-plex panel of oligonucleotide-conjugated antibodies and DAPI. In each cycle, complementary fluorophore-labeled reporter oligonucleotides were hybridized, imaged, and subsequently removed to enable sequential detection of all markers.

4.3.1. Design and application of a high-dimensional CODEX panel for spatial profiling of brain metastases

To enable high-resolution spatial characterization of the brain metastatic microenvironment, we designed and optimized a custom 52-plex oligonucleotide-conjugated antibody panel (Table 2) to capture the cellular, structural, and functional complexity of the metastatic niche. I specifically designed the panel to integrate three key biological dimensions: tissue architecture, immune composition, and T cell functional states.

To delineate the tumor compartment, the epithelial marker cytokeratin-19 (CK19) was included to identify metastatic NSCLC cells. In addition, p53 was incorporated because NSCLC cells frequently harbor *TP53* alterations or exhibit p53 overexpression, resulting in intracellular protein accumulation detectable by immunostaining. Notably, such p53 accumulation has been linked to clinical outcome and response to immune checkpoint inhibition (Mathiot et al., 2024; Mogi & Kuwano, 2011). Vascular and stromal components were resolved using markers of endothelial cells and extracellular matrix organization (CD31, CD34, CD90, Collagen IV, Podoplanin), while brain-resident cell types were captured using GFAP for astrocytes and TMEM119 for microglia, to define the anatomical context of the central nervous system. CD34 was included to identify endothelial progenitor cells and thereby enable assessment of angiogenic activity (Hassanpour et al., 2023). In parallel, Podoplanin (PDPN) was incorporated to capture cancer-associated fibroblasts (CAFs), as $PDPN^{+}$ CAFs are linked to localized immunosuppression via TGF-β signaling and correlate with poor clinical outcome (Hu et al., 2018; Suzuki et al., 2021).

I comprehensively profiled the immune compartment using the lineage-defining marker CD45 to resolve major leukocyte populations, including T cells (CD3, CD4, CD8, FOXP3), B cells and plasma cells (CD20, PAX5, CD79a, CD138), myeloid cells (CD11b, CD68, CD15), dendritic cell subsets (CD11c, CD21, CD208), and NK cells (CD56). Notably, the combination of CD11b and CD56 additionally captures a subset of highly cytotoxic NK cells (Fu et al., 2011). Within the T cell compartment, particular emphasis was placed on resolving differentiation states, tissue residency, and functional phenotypes. Core lineage markers were complemented by markers of naïve, memory, and stem-like states (CD45RA, CD45RO, CD62L, TCF1), as well as markers of terminal differentiation (CD57) and tissue retention and migration (CD103, CD69, CCR7, ICAM-1). To further dissect functional states, markers of activation and proliferation were included (CD25, ICOS, Ki-67), antigen presentation (HLA-DR), and cytotoxicity (Granzyme B), alongside inhibitory receptors associated with T cell exhaustion and chronic antigen exposure (PD-1, LAG-3, TIM-3, CD39). These were paired with markers of immunosuppressive microenvironmental signals (PD-L1, CD163, CD206, IL4I1). In addition, chemokine axes associated with B cell recruitment and tertiary lymphoid structure formation (CXCL13, CXCR5) were included to facilitate identification of organized immune niches. For accurate single-cell segmentation and downstream spatial analysis, nuclear and membrane markers (DAPI, Na^+/K^+-ATPase) were integrated to enable robust cell boundary detection across heterogeneous tissue regions.

Following extensive optimization, I achieved robust signal detection for the majority of markers. Representative fluorescence images for selected markers are shown in (Appendix Figure 3). A subset of targets (CD39, CD45RO, CD62L, SLAMF6, TMEM119, CXCR5) exhibited lower signal-to-noise ratios and higher background staining, limiting direct visual interpretation. However, their suitability for downstream computational analysis remains to be determined.

Collectively, this high-dimensional panel provides a comprehensive framework to resolve the spatial organization, functional states, and interaction networks of immune and tumor cells within NSCLC brain metastases.

Table 2: Multiplexed antibody panel for spatial immune profiling.

Overview of all oligonucleotide-conjugated antibodies included in the 52-plex CODEX panel, grouped by biological category and annotated according to their primary cellular or functional associations.

Category	Subcategory	Marker
Lineage Marker	Pan-leukocyte	CD45
	T cells	CD3, CD4, CD8, FOXP3
	B cells/ Plasma cells	CD138, CD20, PAX5, CD79a
	Myeloid/ DCs	CD11b, CD11c, CD21, CD15, CD68
	NK/ Neurons	CD56
	Astrocytes	GFAP
	Microglia	TMEM119
Structural/ Vascular Marker	Vasculature	CD31
	Progenitor/ Vasculature	CD34
	Stromal /ECM	CD90, Collagen-IV, Podoplanin
Tumor Marker	Tumor/Epithelial	Cytokeratin-19
	Tumor	p53
Segmentation	Nucleus	DAPI
	Membrane	Na^+/K^+-ATPase

Category	Subcategory	Marker
Functional Marker	Activation	CD25, CD69, ICOS
	Antigen presentation	HLA-DR
	Proliferation	KI-67
	Cytotoxic	Granzyme B
	Migration/ Retention	CCR7, CD103, CXCR5, CXCL13, ICAM-1
	Differentiation	CD208, CD45RA, CD45RO, CD57, CD62L, SLAMF6, TCF1
	Exhaustion/ Inhibition/ Regulation	CD163, CD206, CD39, Helios, IKZF3, IL4I1, PD1, PD-L1, TIM3

4.3.2. Spatial heterogeneity of immune infiltration in human brain metastases

Analyses of whole-slide CODEX images across all brain metastases samples revealed that distinct microenvironmental niches coexist within individual tumors, as exemplified by the representative tissue shown in Figure 14A. Regions composed of densely packed malignant cell clusters were largely devoid of immune infiltration (Figure 14A-1), whereas adjacent areas exhibited highly inflamed stromal compartments characterized by aberrant vasculature and dense accumulation of T cells, B cells and macrophages (Figure 14A-2). In addition, localized niches at the edge of the metastasis were identified in which infiltrating immune cells were embedded within reactive astrocytic networks, reflecting the influence of the brain-specific microenvironment (Figure 14A-3). These observations demonstrate pronounced intra-tumoral heterogeneity and highlight the importance of whole-slide spatial profiling, as such contrasting niches would not be captured by spatially restricted sampling approaches such as tissue microarrays.

While immune infiltration exhibited marked intra-tumoral heterogeneity, consistent patterns emerged when assessing the overall immune landscape at the level of entire lesions. This revealed substantial inter-patient heterogeneity in the magnitude of immune infiltration. Across the cohort, tumors could be broadly classified into three phenotypic categories. A subset of tumors displayed an immune-desert phenotype, characterized by a near-complete absence of peripheral immune cell infiltration across the whole tissue (Figure 14B). In contrast, other tumors exhibited an intermediate inflammatory state characterized by stromal immune infiltration composed predominantly of T cells and abundant macrophages (Figure 14C). Finally, a distinct group of tumors showed a highly inflamed phenotype with markedly denser immune infiltration, dominated by T cells and prominent B cell populations within the stromal compartment (Figure 14D).

Together, these spatial archetypes highlight the profound variability of the immune landscape across brain metastases and establish a framework for subsequent analysis of T cell localization and function.

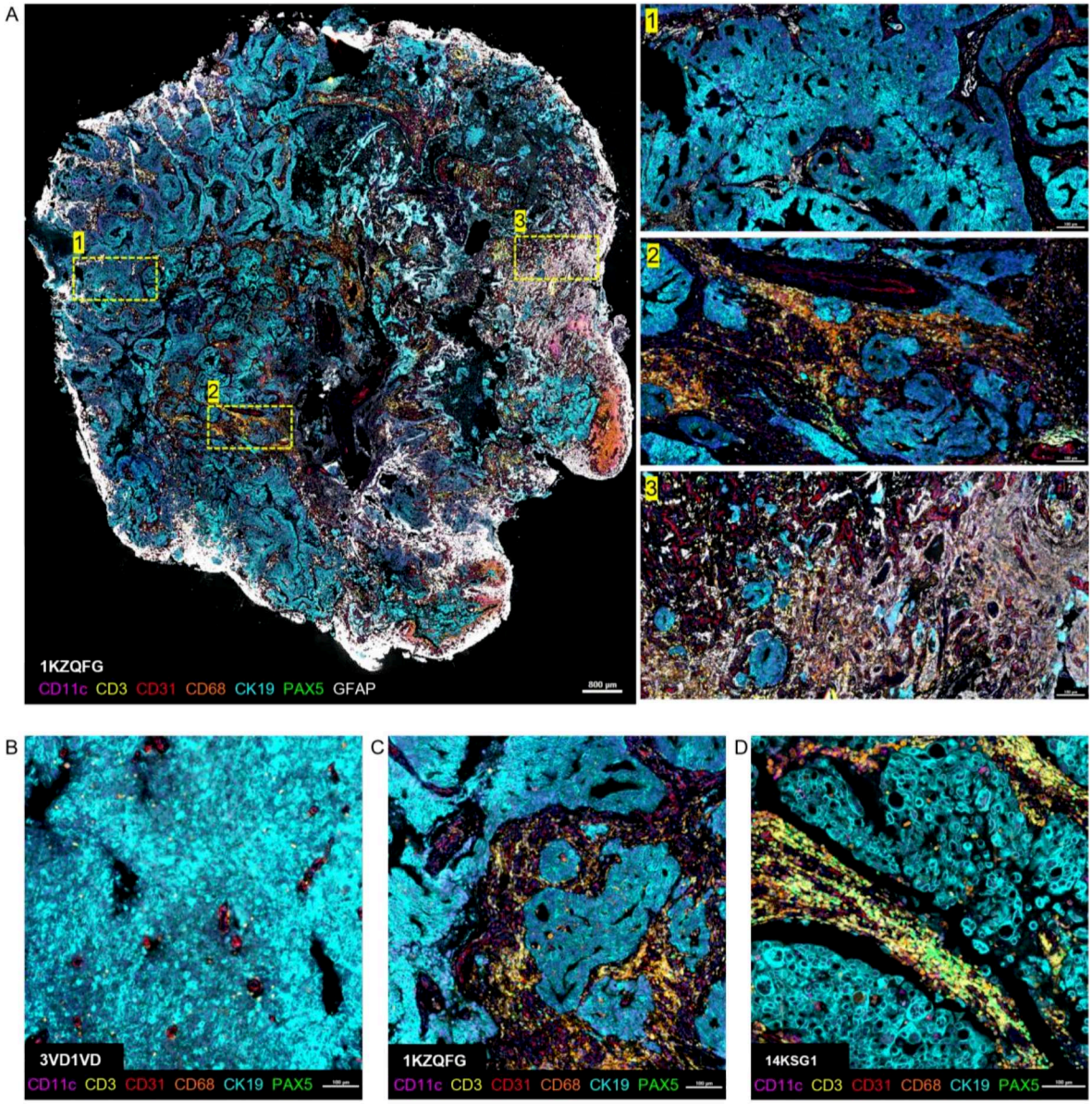


Figure 14: Spatial heterogeneity of immune infiltration in NSCLC brain metastases.

Representative CODEX images of brain metastases (BrM) tissues stained for dendritic cells (CD11c, magenta), T cells (CD3, yellow), vasculature (CD31, red), macrophages (CD68, orange), tumor cells (CK19, turquoise), B cells (PAX5, green), and astrocytes (GFAP, white). Nuclei are counterstained with DAPI (dark blue). (A) Whole-slide view of a representative BrM section illustrating spatially distinct microenvironmental niches, including immune-excluded tumor regions (1), inflamed stromal areas (2), and immune cell infiltration within astrocyte-rich regions (3). Scale bar, 800 µm. Magnified view, 100 µm. (B-D) Representative examples of distinct immune infiltration patterns across BrMs: immune-desert tumors (B), tumors with intermediate stromal infiltration dominated by T cells and macrophages (C), and highly inflamed tumors with dense T cell and B cell infiltration (D). Scale bars, 100 µm. Patient pseudonyms are indicated in the images; corresponding pathological classification are provided in Table M 2 and clinical characteristics in Table M 3.

4.3.3. Spatially defined barriers to T cell infiltration and function in brain metastases

Based on the pronounced inter-tumoral heterogeneity of immune infiltration described above, I investigated the structural and cellular determinants underlying these distinct spatial patterns.

Analysis of vascular architecture revealed three recurrent structural phenotypes associated with differential immune infiltration. In immune-desert tumors, the metastatic tissue formed a dense, stroma-poor lesion in which blood vessels were ensheathed by a continuous astrocytic layer, consistent with preservation of blood-brain barrier-like features. In these regions, immune cell infiltration was minimal, suggesting that intact vascular barriers restrict leukocyte extravasation (Figure 15A). In contrast, tumors with low to intermediate immune infiltration exhibited vessels directly adjacent to tumor cells but lacking a continuous astrocytic covering. This structural disruption was associated with detectable, albeit limited, immune cell extravasation into the tumor-adjacent stroma (Figure 15B). Highly inflamed tumors displayed a markedly altered vascular architecture characterized by abundant stromal regions and disorganized vessel networks, accompanied by extensive immune infiltration, including dense accumulations of T cells and macrophages (Figure 15C).

Beyond vascular entry, T cells encountered additional structural constraints at the tumor-stroma interface. In multiple samples, the invasive margin was characterized by a dense and continuous $CK19^{+}$ tumor cell layer forming a physical boundary separating tumor nests from the surrounding stroma. At sites where T cells penetrated tumor nests, I observed local disruption of this boundary (Figure 15D, arrows). Moreover, tumor cells at this tumor-stroma boundary exhibited elevated expression of CD138 (Syndecan-1), forming a gradient with highest expression at the stromal interface and decreasing toward the tumor core. Given the reported association of SDC1 expression with T cell exclusion (Y. Liu et al., 2024), this pattern suggests another potential barrier function at the tumor margin. Further analysis revealed that tumor cells at the stromal interface were largely non-proliferative, in contrast to highly proliferative regions within the tumor core, suggesting that tumor cells at the tumor-stroma boundary represent a distinct, spatially defined state compared to those in the core.

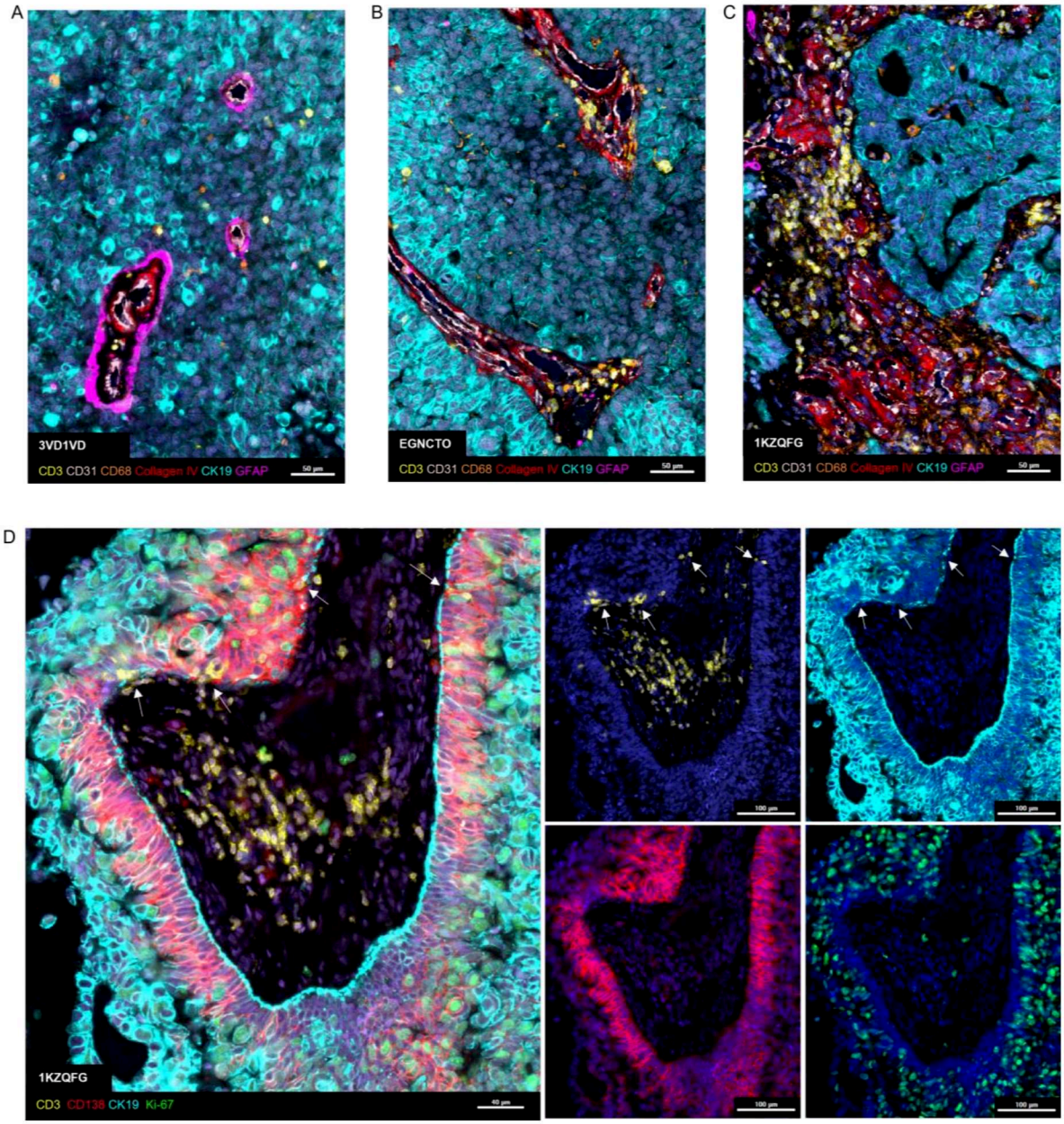


Figure 15: Structural barriers in NSCLC brain metastases.

(A-C) Representative CODEX images of brain metastases (BrM) tissues stained for T cells (CD3, yellow), vasculature (CD31, pink; Collagen IV, red), macrophages (CD68, orange), tumor cells (CK19, turquoise), and astrocytes (GFAP, magenta). Intact astrocyte-covered vasculature (A), blood vessels in direct contact with tumor cells lacking astrocytic coverage (B), and disorganized vascular structures with extensive stromal immune infiltration (C). Scale bars, 50 µm. (D) Tumor-stroma boundary stained for tumor cells (CK19, turquoise), CD138 (red), proliferating cells (Ki-67, green), and T cells (CD3, yellow). Arrows indicate sites of T cell infiltration. Scale bar, 800 µm. Magnified view, 100 µm. Patient pseudonyms are indicated in the images; corresponding pathological classification are provided in Table M 2 and clinical characteristics in Table M 3.

Strikingly, T cells infiltrating tumor nests differed markedly from those located within the stromal compartment. Tumor-infiltrating T cells were predominantly $CD8^+$ and exhibited a

tissue-resident phenotype, defined by CD103 expression (Figure 16A). These cells frequently expressed the cytotoxic effector molecule Granzyme B, indicating preserved effector potential, while only a small fraction expressed PD-1 (Figure 16B). Additional inhibitory receptors, including TIM-3 and LAG-3, were largely absent (not shown). This phenotype is consistent with an active cytotoxic state rather than canonical T cell exhaustion.

Together, these findings identify $CD103^{+}$ tissue-resident T cells as a dominant tumor-infiltrating population and indicate that their infiltration is shaped by structural barriers at both the vascular and tumor-stroma interface.

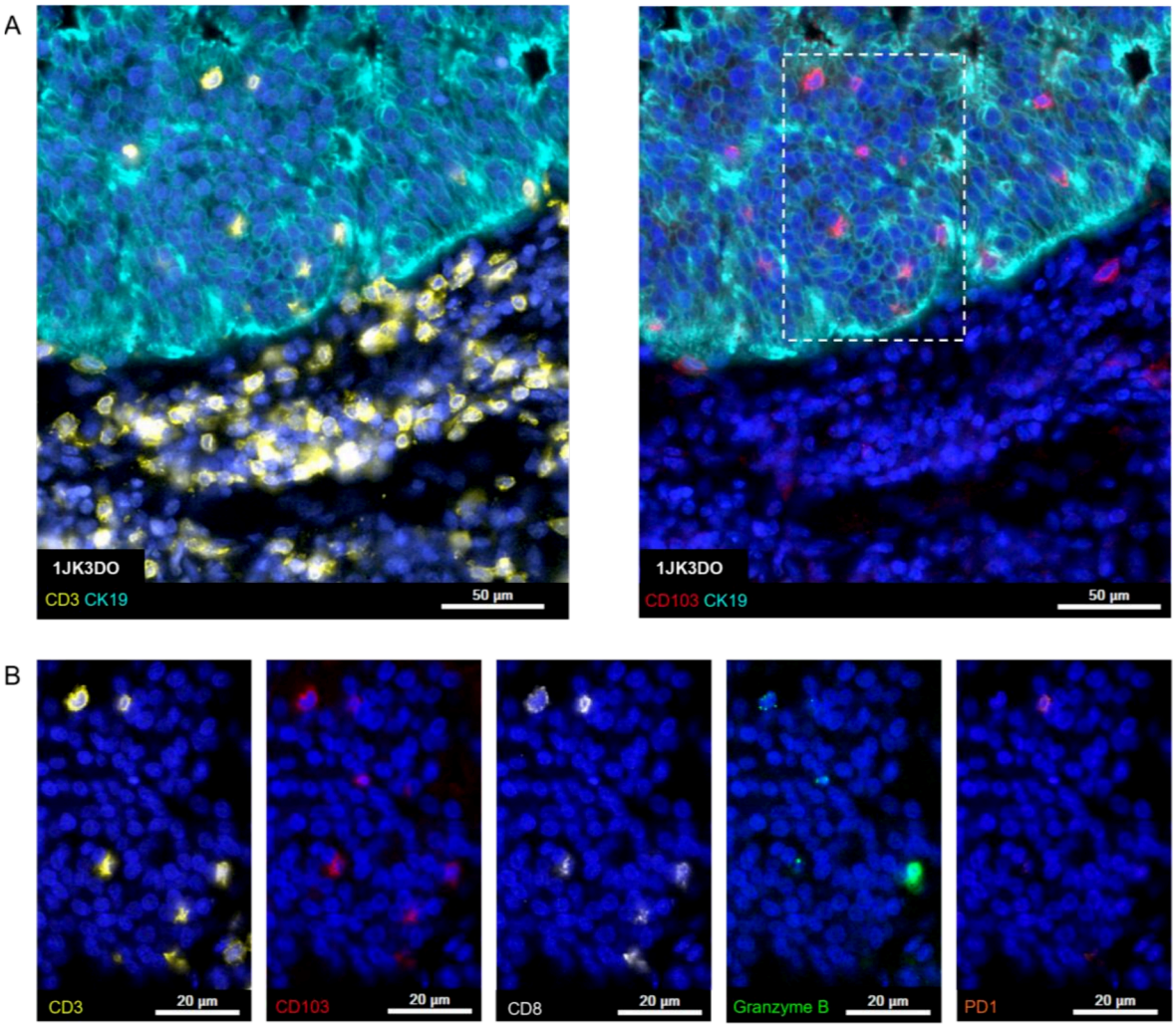


Figure 16: Phenotype of tumor-infiltrating T cells in NSCLC brain metastases.

(A) Representative CODEX image of BrM tissue showing T cells (CD3, yellow) located within the stromal compartment or infiltrating tumor regions (CK19, turquoise). T cell phenotypes are defined by CD103 (red), CD8 (white), Granzyme B (green), and PD-1 (orange) (B). Scale bar, 50 µm. Magnified view, 20 µm.
Nuclei are counterstained with DAPI (dark blue). Patient pseudonyms are indicated in the images; corresponding pathological classification are provided in Table M 2 and clinical characteristics in Table M 3.

4.3.4. Macrophage-driven T cell suppression and T_{REG} induced $CD8^+$ T cell apoptosis

While the previous section focused on structural barriers limiting T cell extravasation and tumor infiltration, these findings raised the question of whether T cells that successfully enter the tumor microenvironment remain functionally competent. Here, I investigated the local immunosuppressive interactions within the tumor stroma that may further constrain T cell activity.

Spatial profiling of exhaustion-associated markers revealed that TIM-3 expression was predominantly localized to $CD3^-$ cells rather than T cells. I identified these cells as $CD68^+$ macrophages co-expressing CD163, CD206, and IL4I1, consistent with an immunosuppressive M2-like phenotype. Notably, these TIM-3^+ macrophages accumulated at the vascular interface, forming a dense perivascular layer surrounding blood vessels (Figure 17A). This spatial organization places immunosuppressive myeloid cells at a critical entry point of the tumor, suggesting that infiltrating T cells encounter suppressive signals immediately upon extravasation into the BrM niche.

A central and previously unrecognized finding of this analysis is the high expression of IL4I1 by macrophages in NSCLC brain metastases. I observed that IL4I1$^+$ $CD68^+$ macrophages were consistently present across all analyzed samples and independent of overall immune infiltration levels and tumor cell density (Figure 17B, Figure 17C). Importantly, IL4I1-expressing macrophages were frequently found in direct physical contact with T cells and were co-expressing the typical tumor-associated macrophage marker CD206 and CD163 (Figure 17D). In contrast, metastatic tumor cells lacked detectable IL4I1 expression, indicating that this immunosuppressive pathway is not tumor-intrinsic but instead driven by infiltrating myeloid cells. Given the established role of IL4I1 in amino acid depletion and the generation of immunosuppressive metabolites (Sadik et al., 2020), these findings suggest that macrophage-derived IL4I1 represents a dominant metabolic mechanism limiting T cell proliferation and effector function within the BrM microenvironment. Consistent with their peripheral origin, these $CD68^+$ macrophages lacked expression of the microglia-specific marker TMEM119 (not shown), indicating recruitment from the circulation rather than local expansion of brain-resident cells.

In addition to myeloid-driven suppression, I identified direct immunoregulatory interactions between regulatory T cells (T_{REGs}) and $CD8^+$ T cells within the tumor stroma. High-resolution spatial analysis revealed close membrane apposition consistent with immunological synapse formation. T_{REGs} in direct contact with $CD8^+$ T cells exhibited Granzyme B expression, indicating a cytotoxic mechanism that may directly contribute to the elimination

of adjacent $CD8^+$ T cells. $CD8^+$ T cells engaged in these interactions displayed morphological alterations, including loss of a round cell shape and reduced cell size, which may be indicative of early apoptosis (Figure 17E).

Together, these findings demonstrate that, beyond structural barriers, T cell function within brain metastases is critically constrained by localized immunosuppressive interactions Immune suppression involved multiple mechanisms, including a metabolic axis mediated by IL4I1-expressing tumor-associated macrophages and T_{REG}-mediated cytotoxicity as an additional layer of immune regulation.

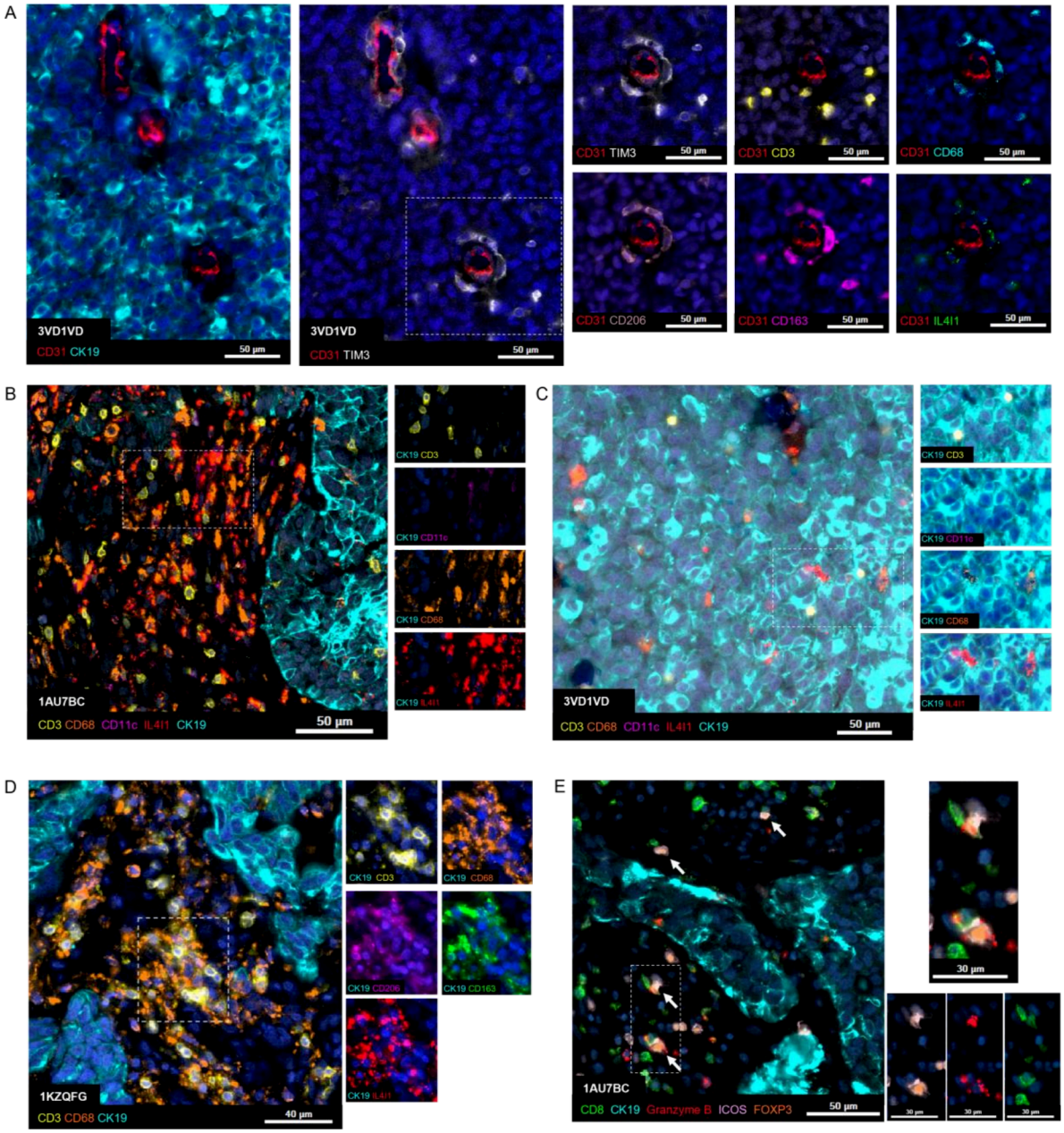


Figure 17: Spatial mapping of immunosuppressive interactions in NSCLC brain metastases.

(A) Blood vessels (CD31, red) surrounded by TIM-3$^+$ cells (white) co-expressing CD68 (turquoise), CD163 (magenta), CD206 (pink), and IL4I1 (green). Scale bar, 50 µm. (B, C) Representative CODEX images showing IL4I1 expression (red) in brain metastases with high (B), and low (C) general immune infiltration. T cells (CD3, yellow), macrophages (CD68, orange), dendritic cells (CD11c, magenta), and tumor cells (CK19, light blue) are indicated. Scale bars, 50 µm. (D) Spatial distribution of CD68$^+$ macrophages (orange) in proximity to T cells (CD3, yellow) and tumor cells (CK19, turquoise). Macrophages are of tumor-associated phenotype expressing CD163 (green), CD206 (magenta) and IL4I1 (red). Scale bar, 40 µm. (E) Representative image of direct cell-cell interactions between regulatory T cells (T_{REGs}; ICOS, pink; FOXP3, orange) and CD8$^+$ T cells (green). Granzyme B expression (red) is detected at sites of contact. Tumor cells are shown by CK19 (turquoise). Scale bar, 50 µm. Magnified view, 30 µm. Nuclei are counterstained with DAPI. Patient pseudonyms are indicated in the images; corresponding pathological classification are provided in Table M 2 and clinical characteristics in Table M 3.

4.3.5. Spatial analysis of tertiary lymphoid-like structures in brain metastases

Despite the presence of extensive structural barriers and immunosuppressive interactions, my single-cell transcriptomic and TCR analyses suggested ongoing T cell activation and clonal expansion within brain metastases. This raised the question of whether local T cell priming may occur directly within the tumor microenvironment. In this context, I investigated the spatial presence and organization of tertiary lymphoid-like structures (TLS) as potential sites of *in situ* immune activation.

Across the cohort, I identified lymphoid aggregates of varying sizes and cellular compositions, representing a continuum of architectural organization. The majority of these structures corresponded to early-stage TLS-like aggregates, characterized by loosely organized clusters of T cells with only sparse B cell infiltration (Figure 18A). In many of these early aggregates, dendritic cells (DCs) were absent, indicating limited potential for coordinated antigen presentation and T cell priming. In contrast, a subset of aggregates displayed increased structural organization, with clear compartmentalization of immune cell populations. These structures contained dense B cell regions interspersed with CD3$^+$ T cells and CD11c$^+$ DCs (Figure 18B).

Strikingly, in some cases, highly organized lymphoid structures were observed, consisting of a central core of CD138$^+$ plasma cells surrounded by CD20$^+$ B cells and associated CD3$^+$ T cell populations, consistent with germinal center-like architectures (Figure 18C). Phenotypic analysis of the T cell compartment within these structures revealed the presence of CD8$^+$ T cells and CD4$^+$ regulatory T cells. In addition, I identified a subset of

$CD4^+$ T cells co-expressing CXCL13 and ICOS, consistent with T follicular helper cells (Figure 18D). These cells were spatially localized within B cell-rich regions, in line with their known role in supporting B cell organization and function. Within the plasma cell compartment, I observed $CD138^+$ cells co-expressing the proliferation marker Ki-67. This phenotype has previously been associated with highly active plasma cells in specialized niches such as the bone marrow (Martinez-Murillo et al., 2016). The presence of proliferating plasma cells within these structures suggests ongoing local humoral immune activity within the tumor microenvironment.

Spatially, TLS-like structures were consistently located in close proximity to the tumor-associated vasculature. Analysis of the surrounding blood vessel network revealed that smaller vessels co-expressed CD31 and CD34 (Figure 18D), consistent with angiogenic vasculature. This spatial association suggests that TLS may depend on continuous cellular recruitment via the local vasculature.

Notably, canonical markers associated with fully mature TLS, including CD21 and LAMP3 (CD208), were not detected (not shown). CD21 staining was consistently absent across all analyzed tissues, whereas LAMP3 signal was detectable but did not co-localize with any other markers in the panel, preventing unambiguous assignment to a defined cell population. Nevertheless, the observed degree of cellular organization and compartmentalization indicates the presence of functionally relevant TLS-like structures within brain metastases.

Together, these findings demonstrate that, despite a highly immunosuppressive microenvironment, brain metastases can harbor spatially organized lymphoid aggregates with features consistent with local immune activation, supporting the possibility of in situ T cell priming and coordinated immune responses.

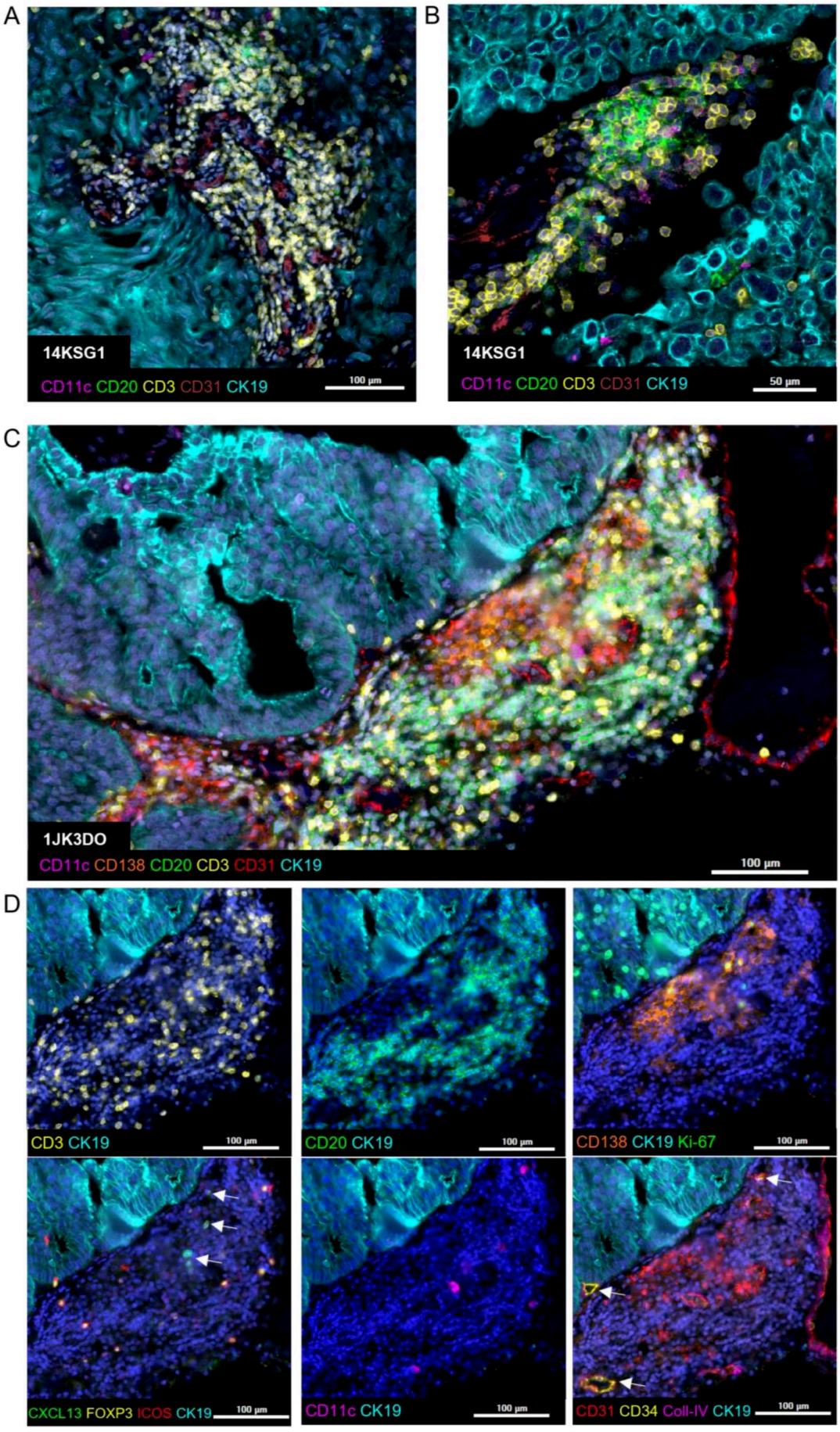

A
14KSG1
CD11c CD20 CD3 CD31 CK19
100 µm
B
14KSG1
CD11c CD20 CD3 CD31 CK19
50 µm
C
1JK3DO
CD11c CD138 CD20 CD3 CD31 CK19
100 µm
D
CD3 CK19
100 µm
CD20 CK19
100 µm
CD138 CK19 Ki-67
100 µm
CXCL13 FOXP3 ICOS CK19
100 µm
CD11c CK19
100 µm
CD31 CD34 Coll-IV CK19
100 µm

Figure 18: Tertiary lymphoid structures (TLS) in NSCLC brain metastases.

(A, B) Representative CODEX images of lymphoid aggregates in brain metastatic (BrM) tissue. (A) Early, unorganized aggregates composed predominantly of T cells (CD3, yellow) with sparse B cells (CD20, green). Scale bar: 100µm. (B) Organized lymphoid aggregate with compartmentalized architecture comprising a core of B cells (PAX5, green), surrounded by T cells (CD3, yellow), and a few DCs (CD11c, magenta). Scale bar: 100µm. (C) TLS comprising plasma cells (CD138, orange), B cells (CD20, green), T cells (CD3, yellow), and dendritic cells (CD11c, magenta). Tumor cells (CK19, light blue) and blood vessels (CD31, red) are indicated. Aggregates lacking dendritic cells (CD11c, magenta). Tumor cells are shown by CK19 (light blue), and blood vessels by CD31 (dark red). Scale bar: 50µm. (D) Single-channel and composite images showing of the structure shown in C showing the location of T cells and B cells, proliferating plasma cells (CD138, orange; Ki-67, green), T follicular helper cells indicated by arrows (CXCL13, green; ICOS, red), regulatory T cells (FOXP3,yellow; ICOS), and vascular structures (CD31, red; CD34, yellow; Collagen IV, magenta). Nuclei are counterstained with DAPI. Patient pseudonyms are indicated in the images; corresponding pathological classification are provided in Table M 2 and clinical characteristics in Table M 3.

5. Discussion

Historically, the brain was considered an immune-privileged organ, largely shielded from peripheral immune surveillance by the blood-brain barrier. This concept has been fundamentally revised. During the development of intracranial metastases, the blood-brain barrier is disrupted and remodeled into a more permeable blood-tumor barrier, thereby enabling immune cell infiltration into the metastatic niche (Lockman et al., 2010). In parallel, while surgical resection remains an important treatment modality, non-surgical management has shifted from a predominant reliance on radiotherapy and chemotherapy toward the integration of immunotherapy.

Clinical studies have shown that immune checkpoint blockade targeting the PD-1/PD-L1 axis, including pembrolizumab and atezolizumab, induces intracranial responses in a substantial proportion of patients, with response rates of 42% and 45%, respectively (Brastianos et al., 2023; Nadal et al., 2023). In addition, combination regimens with chemotherapy prolong survival compared with chemotherapy alone. These advances have led to the approval of multiple PD-1/PD-L1 inhibitors for metastatic NSCLC (Mansfield et al., 2018). Nevertheless, patient outcomes remain limited, with median overall survival ranging from 15 to 17 months (Peters et al., 2025).

Although insufficient drug penetration across the BTB may prevent therapeutics from reaching the metastatic niche at effective concentrations, this alone may not explain the limited response to immunotherapy in BrM. Increasing evidence indicates that the functional state, spatial organization, and cellular composition of tumor-infiltrating lymphocytes (TILs) within the brain microenvironment are critical determinants of therapeutic response. However, these parameters remain incompletely understood, particularly with respect to tumor-specific reactivity, clonal dynamics, and the spatial constraints shaping T cell behavior within brain metastatic lesions.

In this thesis, I addressed the unresolved question of whether T cells infiltrating NSCLC brain metastases include tumor-reactive populations or are predominantly bystanders, and which mechanisms within the metastatic niche restrict effective anti-tumor immunity. To this end, I combined single-cell transcriptomic and paired TCR profiling, functional TCR validation, and multiplexed spatial imaging to define the phenotypic states, clonal architecture, functional potential, and spatial organization of BrM-infiltrating T cells. I further investigated whether the BrM microenvironment contains lymphoid structures compatible with local immune activation and T cell priming. Focusing on a single primary tumor entity, NSCLC, minimizes confounding effects inherent to prior studies that aggregate brain

metastases across multiple cancer types (Gonzalez et al., 2022; Sudmeier et al., 2022; Wischnewski et al., 2023).

Collectively, the findings presented in this thesis provide a framework for understanding why T cell-mediated anti-tumor immunity remains poor in NSCLC brain metastases despite the presence of tumor-reactive clones. They also provide a rationale for combinatorial therapeutic strategies aimed at enhancing T cell infiltration, restoring effector function, and improving the efficacy of immune checkpoint blockade in brain metastasis.

5.1. Spatial organization of the brain metastatic niche constrains T cell access and function

The spatial organization of the brain metastatic niche imposes multiple, sequential constraints on T cell infiltration and function. In the following sections, I dissect these barriers at the level of vascular access, tissue architecture, and stromal immunosuppression.

5.1.1. Heterogeneous vascular remodeling enables but spatially restricts immune cell entry into brain metastases

Effective anti-tumor immunity in brain metastases first requires that circulating immune cells gain access to the metastatic niche. My whole-slide spatial analyses suggest that immune cell entry is not uniformly permitted, but varies substantially across and within individual NSCLC BrM lesions. Even within a single metastasis, regions differed markedly in immune cell density, stromal organization, vascular architecture, and the integration of brain-resident structures. This complexity underscores a major limitation of many previous spatial studies of brain metastases, which have relied on tissue microarrays or selected regions of interest and therefore cannot resolve the full architectural and immunological diversity of intact metastatic lesions (Álvarez-Prado et al., 2023; Biermann et al., 2022; Lu et al., 2021; Widodo et al., 2023).

A central determinant of immune cell entry in my dataset was the integrity of the perivascular astrocytic niche. In some regions, blood vessels remained tightly ensheathed by $GFAP^+$ astrocytes, consistent with preserved blood-brain barrier-like architecture, whereas other areas lacked this astrocytic boundary. Importantly, this variability occurred both within individual lesions and across patients. Some metastases showed partial loss of astrocytic

vessel coverage, particularly in the tumor core, whereas others retained dense astrocytic ensheathment throughout the whole lesion. Areas with preserved astrocytic vessel coverage were associated with minimal immune infiltration, whereas regions lacking this boundary showed markedly increased immune cell accumulation.

This pattern is consistent with the vascular evolution of brain metastases. Metastatic cells initially exploit pre-existing cerebral vessels through vascular co-option (Donnem et al., 2013), but progressive tumor growth can be accompanied by neoangiogenic remodeling, which alters vascular architecture and permeability to meet the increasing metabolic and nutrient demands of the expanding lesion. In line with this concept, I frequently observed $GFAP^+$ astrocytes displaced toward the tumor margins in lesions with higher immune accessibility. This spatially heterogeneous accessibility also provides an anatomical framework for the clinical observation that immune checkpoint blockade can induce intracranial responses in a subset of patients with BrM. My data suggest that regions permissive to immune cell extravasation are likely also more accessible to systemically administered therapeutics, whereas regions retaining intact blood-brain barrier-like structures may remain comparatively protected from both immune cell entry and drug delivery. However, these spatial constraints alone are unlikely to fully explain the limited efficacy of immunotherapy, indicating that additional suppressive mechanisms within the tumor microenvironment must further restrict effective anti-tumor immunity. This interpretation is consistent with clinical data demonstrating about 40% intracranial activity of PD-1- and PD-L1-directed therapies in NSCLC BrM (Brastianos et al., 2023; Nadal et al., 2023). Overall, my spatial data indicate that vascular remodeling in NSCLC BrM generates a mosaic of preserved and permissive vascular states rather than a uniform loss of barrier function. This heterogeneity defines where immune cells can extravasate into the metastatic niche and constitutes the first spatial checkpoint shaping the downstream anti-tumor response.

5.1.2. Structural barriers at the tumor-stroma interface restrict T cell infiltration into the metastatic parenchyma

Although vascular remodeling permits immune cell entry into parts of the lesion, my spatial analyses showed that the majority of infiltrating T cells remain confined to perivascular and stromal compartments and fail to penetrate deeply into tumor cell-dense regions. Thus, immune cell extravasation and effective tumor infiltration represent biologically distinct steps. At the tumor-stroma interface, I identified regions in which a dense and spatially continuous $CK19^+$ epithelial boundary sharply delineated the tumor border. The few sites at

which T cells appeared to penetrate the parenchyma coincided with localized disruptions of this structure, suggesting that the epithelial tumor margin itself may act as a physical barrier to infiltration. Although my data does not allow me to distinguish whether T cells actively remodel this interface or preferentially exploit pre-existing discontinuities, the spatial coincidence between barrier disruption and T cell entry strongly indicates that the tumor border is a biologically relevant regulator of T cell access to tumor cells.

A second key observation was the pronounced spatial gradient of CD138 (Syndecan-1, SDC1) across the tumor border, with highest expression at the tumor-stroma interface and a progressive decline toward the tumor core. Notably, infiltrating T cells were largely excluded from regions with high tumoral SDC1 expression and instead accumulated in areas where this signal was low or absent, suggesting a spatial association between SDC1 expression and immune exclusion. CD138/SDC1 is a multifunctional transmembrane proteoglycan which is widely used as a plasma cell marker due to its role in plasma cell homing and survival within the bone marrow niche (Ren et al., 2021). Beyond its role as a plasma cell marker, it has a broad regulatory capacity in tissue organization. Structurally, SDC1 consists of an extracellular domain carrying covalently attached glycosaminoglycan (GAG) chains, a transmembrane region, and a cytoplasmic tail. Through its GAG side chains, SDC1 can bind a wide range of ligands, including growth factors, cytokines, chemokines, and extracellular matrix components, thereby modulating signaling pathways that regulate cell adhesion, migration, and tissue architecture (Yang et al., 2022). In addition, proteolytic shedding of its extracellular domain generates a soluble form with autocrine, paracrine, and systemic signaling functions (Diab et al., 2024). Consistent with this broad interactome, syndecans have been reported to engage hundreds of molecular partners, underscoring their central role in coordinating cell-matrix interactions, adhesion and extracellular organization (Yang et al., 2022). In cancer, SDC1 is frequently overexpressed and has been linked to tumor cell proliferation, invasion, and metastatic behavior. High SDC1 expression has also been reported in brain metastases of breast cancer origin (Cerbelli et al., 2023). Moreover, recent studies have demonstrated that elevated SDC1 expression can directly impact anti-tumor immunity by limiting $CD8^+$ T cell infiltration, whereas its experimental depletion restores T cell entry, enhances cytotoxicity, and increases MHC class I expression on tumor cells (Y. Liu et al., 2024). In this context, the spatially organized SDC1 gradient observed in my dataset suggests that tumor-derived SDC1 may actively contribute to the establishment of a localized immune-excluded niche in NSCLC brain metastases. To my knowledge, such a spatially resolved pattern of tumoral SDC1 expression has not previously been described in this setting, identifying a potentially novel mechanism of immune regulation. Furthermore, the relevance of this finding may

extend beyond local T cell exclusion. In breast cancer, aberrant SDC1 expression has been implicated in brain tropism by facilitating both transmigration across the BBB and subsequent perivascular adhesion (Sayyad et al., 2019). In the same study, elevated SDC1 expression was associated with poor clinical outcome. In this light, SDC1 may represent a candidate mediator linking metastatic brain colonization with active immune evasion and immune exclusion once the lesion is established.

Interestingly, tumor cells forming the stromal-facing outer layer displayed a distinct morphology, characterized by tight epithelial organization and reduced proliferative activity compared with cells located deeper within the tumor bed. This observation aligns closely with work by Baldominos et al., who described quiescent tumor cell populations at the tumor margin that resist both immune infiltration and therapeutic intervention (Baldominos et al., 2022). The tumor border in my samples may therefore represent a specialized barrier state in which structural organization, reduced proliferation, and matrix-associated molecules such as SDC1 converge to create an interface that is simultaneously immune-restrictive and potentially therapy-resistant. Thus, even in lesions where vascular remodeling permits immune cell extravasation, effective access to tumor cells remains constrained at the level of tissue architecture. In this framework, the metastatic niche imposes a second spatial checkpoint after vascular entry.

5.1.3. Myeloid and regulatory T cells contribute to suppression of infiltrating T cells in the tumor stroma

Following extravasation into the metastatic niche, infiltrating T cells are immediately exposed to a highly immunosuppressive microenvironment. My spatial analyses showed that the stromal compartment of NSCLC BrM is densely populated by monocyte-derived $CD68^{+}TMEM119^{-}$ macrophages, which markedly outnumber resident $TMEM119^{+}$ microglia. These macrophages consistently exhibited a phenotype characterized by expression of CD206 and CD163, indicative of an immunoregulatory state. A particularly striking feature of these cells was their robust expression of IL4I1. IL4I1 is a secreted L-amino acid oxidase that primarily metabolizes aromatic amino acids. Through the generation of reactive oxygen species and metabolic intermediates, IL4I1 has been shown to inhibit T cell proliferation and effector function while also promoting tumor cell motility (Sadik et al., 2020). In line with these reports, the consistent presence of IL4I1-expressing macrophages across all analyzed BrM samples suggests that this pathway represents a conserved component of the immunosuppressive landscape in NSCLC brain metastases. Notably, in contrast to other tumor entities, in which IL4I1 expression has also been detected

in malignant cells, including glioma cells (Sadik et al., 2020), I observed IL4I1 expression to be restricted to the myeloid compartment in NSCLC BrM, with no detectable expression in metastatic tumor cells. To my knowledge, IL4I1 expression has not previously been described in the microenvironment of NSCLC brain metastases. This finding therefore identifies a previously unrecognized, macrophage-driven immunosuppressive pathway within the brain metastatic niche.

In a subset of tumors, particularly in immunologically cold lesions, some of these tumor-associated macrophages appeared as concentric perivascular accumulations, consistent with structures resembling the “perivascular cuffs” previously described in brain metastases (Sun et al., 2023). These structures are thought to trap newly extravasated immune cells in the immediate vicinity of blood vessels and thereby prevent further migration into the surrounding tissue.

While perivascular macrophages establish an immunosuppressive and spatially restrictive niche immediately following immune cell extravasation, my data indicate that this is not the only layer of regulation within the stromal compartment. Within the $CD4^+$ T cells of my scRNA-seq dataset, I identified a distinct cluster of T_{REGs} characterized by high activation signatures and robust expression of perforin (*PRF1*). Although perforin- and granzyme-mediated cytotoxicity is classically associated with cytotoxic $CD8^+$ T cells, previous studies have shown that activated T_{REGs} can use similar effector mechanisms to limit excessive immune responses by targeting activated T cells (Grossman et al., 2004). Based on this transcriptional profile, I hypothesized that a comparable mechanism may operate in the BrM microenvironment. My multiplex immunofluorescence data revealed close spatial proximity between T_{REGs} expressing granzyme B and adjacent $CD8^+$ T cells, frequently forming tight immunological synapse-like interactions. Notably, $CD8^+$ T cells engaged in these interactions frequently displayed altered cellular morphology, including loss of their typical rounded shape and reduced cell size, features consistent with cellular distress or apoptosis. The detection of *PRF1*-expressing T_{REGs} in my transcriptomic data, together with the spatial observation of targeted granzyme B deposition onto $CD8^+$ T cells, suggests that T_{REGs} in NSCLC brain metastases may engage the perforin/granzyme axis to directly modulate $CD8^+$ T cells. However, this interpretation remains tentative and requires direct functional validation before final conclusions can be made.

Together, these data support a model in which multiple layers of immunosuppression converge within the BrM microenvironment. Following vascular entry and partial stromal retention, infiltrating T cells are exposed not only to myeloid-derived suppressive signals, but also to localized regulatory T cell activity that may further limit their expansion and effector function.

While my multiplexed spatial imaging analyses revealed clear and reproducible patterns of cellular organization and interaction within NSCLC brain metastases, the current interpretation is solely based on qualitative assessment of spatial relationships. Systematic quantitative analyses, including cell-cell proximity measurements, neighborhood analyses, and cross-patient comparisons, were beyond the scope of this study but will be essential to rigorously validate and generalize these observations. In particular, quantitative characterization of $CD103^+$ T cell neighborhoods, spatial niches, such as perivascular myeloid structures, tumor-stroma interfaces, and TLS-like aggregates, will provide a more comprehensive understanding of the spatial determinants governing immune cell localization and function in the brain metastatic microenvironment.

5.2. Clonally expanded $CD103^+$ tissue-resident T cells define a spatially localized and tumor-reactive T cell compartment in NSCLC brain metastases

To better understand the functional capacity of T cells infiltrating NSCLC brain metastases, I characterized their transcriptional states using single-cell RNA sequencing. My analysis revealed multiple $CD8^+$ T cell populations with distinct functional profiles. Among these were classical memory-like populations, including T_{SCM} and T_{EM} clusters, within which a subset of cells was characterized by elevated expression of *GZMK* accompanied by low transcript levels of perforin (*PRF1*). Although $GZMK^+$ $CD8^+$ T cells have been described across multiple tumor types, their functional role remains incompletely understood. Recent studies challenge the classical view of GZMK as a purely cytotoxic effector molecule. In lung adenocarcinoma, GZMK has been shown to exert perforin-independent functions, including cleavage of protease-activated receptors on tumor cells, thereby inducing PD-L1 expression and promoting immune evasion (Feng et al., 2026). In colorectal cancer, GZMK produced by T_{EM} cells has been associated with reduced E-cadherin expression, tissue remodeling, and epithelial-to-mesenchymal transition-like features linked to tumor progression and poor clinical outcome (Tiberti et al., 2022). In this context, the $GZMK^+$ populations in my dataset may represent a functional state not primarily defined by cytotoxicity but rather associated with alternative roles in shaping the tumor microenvironment.

In contrast, I identified a distinct population of $CD8^+$ tissue-resident memory T cells, defined by high transcription of the residency marker *ITGAE* (CD103). CD103 is an integrin that binds E-cadherin and mediates tissue retention, enabling sustained interactions with target

cells within epithelial environments. At the transcriptional level, these cells displayed a highly activated phenotype characterized by robust expression of cytotoxic effector genes. A subset also exhibited features of active proliferation, consistent with ongoing local expansion within the metastatic niche. Notably, T_{RM} cells represented the predominant clonally expanded $CD8^+$ T cell population in BrM, with substantially higher clonal expansion than the $GZMK^+$ subsets. Despite their activated state, they displayed only moderate expression of canonical exhaustion markers and remained transcriptionally distinct from the T_{EX} cluster, indicating a functionally active, non-terminally exhausted phenotype.

Integration of transcriptomic data with spatial protein-level analyses further supported this interpretation. Although GZMK was not included in the multiplex imaging panel, evaluation of canonical exhaustion markers revealed that the majority of infiltrating T cells expressed only low levels of PD-1, TIM-3, and LAG-3. This finding was consistent with the transcriptional profiles and indicates that classical T cell exhaustion is not a dominant feature of the BrM-infiltrating T cell pool. Instead, exhaustion marker expression was restricted to a minor fraction of T cells, while TIM-3 expression was predominantly observed in the myeloid compartment. These observations are in line with previous reports demonstrating lower exhaustion marker expression in BrM compared to matched primary tumors (Lu et al., 2021). One explanation for this phenotype is the spatial organization of the tumor microenvironment. Because a large proportion of T cells remain confined to the stromal compartment and do not engage in sustained interactions with tumor cells, they may not receive the chronic antigen stimulation required to drive terminal exhaustion. In addition, tumor-intrinsic heterogeneity, including the presence of poorly immunogenic tumor cell states with reduced MHC class I expression, may further limit effective T cell activation (Gonzalez et al., 2022).

Importantly, the transcriptional profile of $CD103^+$ T_{RM} cells was consistent with tumor-reactive T cell populations. These cells co-expressed *CXCL13* and *ENTPD1* (CD39), a combinatorial signature that has emerged as a robust marker for tumor-specific $CD8^+$ T cells across multiple malignancies (Duhen et al., 2018; Hanada et al., 2022; Meng et al., 2023). The presence of this signature, together with their pronounced clonal expansion, strongly suggests antigen-driven proliferation within the metastatic niche. This interpretation is further supported by recent single-cell studies in brain metastases. Wischnewski et al. identified maximal clonal expansion specifically within T cell subsets co-expressing *CXCL13*, and cytotoxicity-associated genes (Wischnewski et al., 2023), a transcriptional profile highly consistent with the T_{RM} clusters observed in my dataset. Moreover, a recent meta-analysis across multiple tumor types demonstrated that *CXCL13* expression represents a key determinant distinguishing clonally expanded from non-expanded T cells

following immune checkpoint inhibitor treatment (Shorer et al., 2025) further reinforcing its association with antigen-driven T cell responses. These observations are consistent with findings by Jassowicz et al. in brain metastases of primary breast cancer, where single-nucleus sequencing identified a GZMK$^+$ CD8$^+$ T cell population and an unrelated distinct CD8$^+$ T_{RM} population with a proliferative subcluster and a transcriptional signature suggestive of tumor reactivity (Jassowicz et al., 2026, in press). In line with these findings, computational prediction approaches consistently assigned higher tumor reactivity scores to CD103$^+$ T_{RM} cells compared to other T cell subsets within my dataset.

My multiplexed imaging data enabled contextual validation of these findings. CD103 staining was used as a surrogate to identify the tissue-resident population corresponding to the clonally expanded cells observed in the transcriptomic data. CD103$^+$ T cells were predominantly located within the tumor parenchyma, in direct proximity to metastatic cells, whereas CD103$^-$ T cells were largely confined to the perivascular stroma. This spatial segregation is consistent with antigen-driven tissue retention, as CD103-mediated binding to E-cadherin facilitates stable interactions with epithelial target cells. Although technical limitations precluded simultaneous visualization of CD39 and CXCL13, the concordance between transcriptional identity, clonal expansion, and spatial localization supports a coherent model in which CD103$^+$ T_{RM} cells represent the primary tumor-reactive T cell population in NSCLC brain metastasis. Similar observations were reported by Jassowicz et al. in breast cancer brain metastases, where T_{RM} cells were found to predominantly infiltrate tumor cell-dense regions (Jassowicz et al., 2026, in press). Notably, a high T_{RM} signature was significantly associated with prolonged overall survival, further supporting the hypothesis that these cells represent a tumor-reactive T cell population.

5.2.1. Functional validation reveals tumor-reactive TCRs within the CD103$^+$ T_{RM} compartment but highlights technical and biological constraints

To directly assess whether the transcriptionally and spatially defined CD103$^+$ T_{RM} populations indeed contain tumor-reactive T cells, I functionally tested selected TCRs derived from clonally expanded T cell populations. Given the limited availability of viable tumor material, these experiments were restricted to two patient samples and required assay systems that could operate with very low target-cell numbers.

Interestingly, among the selected TCRs, I observed that several clones from the same patient shared identical *TRBV* gene usage while pairing with distinct *TRAV* genes. This observation can be explained by the sequential nature of TCR recombination, in which

rearrangement of the TCRβ locus precedes that of the TCRα locus. As a result, a single progenitor cell carrying a successfully rearranged β-chain can give rise to multiple daughter cells that each express a distinct α-chain, thereby generating a diverse set of TCRαβ combinations from a shared β-chain backbone (Dupic et al., 2019; Tanno et al., 2020). Since antigen specificity is determined by the combined configuration of the CDR3 regions of both TCR chains (Rossjohn et al., 2015), these receptors are expected to recognize distinct epitopes despite their shared β-chain usage.

TCR reactivity was assessed using a Jurkat-based reporter system that enables detection of NF-κB activation upon TCR engagement. Although this system provides high sensitivity, it also exhibited measurable baseline activation independent of antigen-specific stimulation. This background signal is likely attributable to technical factors, including transient calcium flux induced by electroporation and innate immune sensing of in vitro-transcribed mRNA, both of which can activate NF-κB signaling (Hanna et al., 2017; Kavaliauskaitė et al., 2021; Muslimov et al., 2023). Despite the baseline activity observed in the reporter system, one TCR derived from a clonally expanded T_{RM} population (NCH8937 TCR-1) showed a clear increase in reporter activation upon co-culture with autologous tumor material, indicating antigen-specific reactivity. This observation is consistent with previous reports identifying $CD103^+$ T cells as a bona fide tumor-reactive population in brain metastases (Wischnewski et al., 2023).

However, additional TCRs derived from T_{RM} clones (TCR-2 and TCR-3) did not show detectable activation in this assay. Several technical factors may account for this observation. The heterogeneous composition of the tumor cell suspension, combined with the stochastic distribution of cells within the Lightning^{TM} optofluidic system, likely reduces the probability of productive encounters between T cells and their tumor-associated antigen. Consistent with this, only a small fraction of NanoPens (9 out of 130) containing NCH8937 TCR1-transgenic Jurkat reporter cells exhibited TCR-induced reporter activation, and signal intensity varied considerably across positive pens. This variability is in line with differences in TCR affinity for cognate peptide-MHC complexes, which directly influence reporter signal strength in this system (Müller et al., 2020). Furthermore, in most positive pens, activation was observed in only a single TCR-transgenic cell, despite the fact that all carry the same TCR, suggesting that the corresponding antigen is not abundantly presented across the tumor cell population. Furthermore, tumor cells may evade immune recognition by downregulating antigen presentation via MHC class I. The consistently low levels of T cell exhaustion observed across both transcriptomic and protein-level datasets in my study support this interpretation, as insufficient antigen presentation would limit sustained T cell activation required to drive exhaustion.

At the same time, it remains possible that some T_{RM}-derived TCRs are not tumor-specific. Computational prediction models and transcriptional signatures, although informative, are not fully specific for tumor reactivity and may overestimate the likelihood of tumor-antigen recognition. For example, CD103 expression is not restricted to tumor-reactive T cells but can also be acquired by bystander memory T cells that establish tissue residency following prior antigen exposure (Simoni et al., 2018).

Consistent with this, I observed one TCR with known viral specificity within the tissue-resident compartment of sample NCH9587. While this may reflect long-lived tissue-resident memory T cells generated during prior infections, it also raises the possibility of cross-reactive TCR recognition, as described in glioblastoma (Naghavian et al., 2023). In such cases, T cells originally primed against viral antigens may be locally reactivated through recognition of structurally related tumor-derived peptides. The clonal expansion within the BrM in combination with the typical phenotype of tumor-reactivity T cells further support the possibility of such cross-reactivity. However, the proposed anti-tumor reactivity remains hypothetical and requires direct functional validation, which was not feasible in this study due to the lack of biological brain metastatic material of NCH9587.

On the other hand, in patient NCH9348, no TCR reactivity could be detected across all tested TCRs, including multiple candidates derived from T_{RM} populations. Importantly, the tumor material available for this sample consisted predominantly of non-viable cells, rendering antigen presentation non-functional and thereby preventing effective TCR-mediated T cell activation. In addition to the Jurkat reporter cell-based assay, the availability of endogenous T cells was used to set up an assay with a more physiological readout. Importantly, this approach increased the absolute number of tumor and T cells per well from low-input conditions on the Lightning platform (approximately 5 T cells and 10 tumor cells per co-culture) to 40,000 tumor cells and 40,000 T cells per co-culture. While increasing effector-to-target ratio this approach furthermore enhanced the probability of productive tumor-T cell interactions. Even under these modified conditions, no reactivity was observed. This is most likely attributable to the severely compromised viability of the tumor material, which limited the presence of functional antigen-presenting cells even at higher input numbers. These findings underscore the substantial technical challenges associated with functional TCR validation in human BrM samples, particularly with respect to the viability and integrity of tumor cells following surgical resection and processing.

However, the functional testing against the viral peptide pool enabled me to identify one TCR (NCH9348 TCR-9) as virus-specific, which will be further discussed in the later section 5.3.1.

Taken together, my functional data provide direct evidence that tumor-reactive TCRs are present within the clonally expanded T_{RM} compartment while also highlighting the substantial technical and biological constraints that limit comprehensive validation. Importantly, the identification of even a single tumor-reactive TCR within this population supports the conclusion that functional anti-tumor immunity is present within NSCLC brain metastases.

5.3. Integrated analysis of TCR repertoire and lymphoid architecture supports localized T cell immunity in NSCLC brain metastases

To determine whether anti-tumor T cell responses in NSCLC brain metastases are locally maintained or systemically derived, I integrated TCR repertoire analyses with spatial characterization of lymphoid structures within the metastatic niche.

5.3.1. Differential TCR repertoire overlap between peripheral blood and brain metastases suggests localized T cell responses

To determine whether anti-tumor T cell responses in NSCLC brain metastases are locally generated or systemically derived, I compared the TCR repertoires of BrM-infiltrating lymphocytes with those of matched peripheral blood samples. This analysis aimed to distinguish locally expanded, tumor-reactive populations from systemically primed T cells, including those activated in lymph nodes or the primary tumor, as well as non-specific bystander infiltration.

Across the analyzed patients, I observed a heterogeneous degree of TCR sharing between the peripheral and intracranial compartments. This variability extended beyond the absolute number of shared clonotypes to their clonal architecture and compartmental distribution. Notably, smaller clonotypes were detected at comparable frequencies across both compartments, whereas highly expanded clonotypes were typically skewed toward either the peripheral blood or the brain metastasis. Importantly, this skewing was mutually exclusive at the patient level, with no patient exhibiting dominant shared clonotypes in both compartments. Clonotypes predominantly detected in the circulation may reflect virus-specific effector memory T cells that infiltrate the BrM niche in response to inflammatory

cues, whereas clonotypes enriched within the brain compartment might be a result of local antigen-driven expansion.

However, both the antigen specificity and the origin of these shared clonotypes remain unresolved. It is unclear whether they represent tumor-reactive or bystander T cells. If tumor-reactive, it remains to be determined whether they are primed in peripheral lymphoid organs and subsequently expand within the metastatic niche, or whether they are locally primed within the brain metastasis, potentially in TLS-like structures, with limited recirculation into the peripheral blood. Furthermore, the phenotypic identity of shared clonotypes across compartments remains to be systematically resolved, which will require dedicated bioinformatic analyses beyond the scope of this study.

An important technical consideration is that single-cell TCR sequencing captures only a limited fraction of the highly diverse peripheral repertoire, potentially underestimating true clonal overlap. To address this limitation, I performed bulk TCRβ sequencing of the same PBMC samples. Despite the loss of α–β pairing information, this approach provides substantially increased sampling depth. Importantly, bulk TCRβ sequencing revealed highly similar patterns of clonal expansion across patients, validating that the single-cell data accurately reflect the peripheral T cell repertoire in this cohort.

Among the nine selected clonotypes tested in patient NCH9348, only those derived from the T_{SCM} GZMK population were detectable in the peripheral blood, whereas the remaining seven clonotypes originating from tumor-predicted CD103$^+$ T_{RM} clusters were not identified in the circulation. This dichotomy is consistent with previous reports demonstrating that T cells with features of chronic antigen exposure are enriched for tumor specificity, whereas cells with conventional memory phenotypes more frequently recognize viral antigens and thus represent bystander populations (Oliveira et al., 2021). In line with this, the CD103$^+$ T_{RM} cells identified in my dataset display hallmarks of local antigen engagement, including strong expression of cytotoxic effector genes and pronounced clonal expansion. Given that tissue residency is typically established following antigen recognition and sustained local stimulation, these observations support the interpretation that T_{RM} populations are driven by tumor-antigen-specific responses within the metastatic niche and are unlikely to recirculate into the peripheral compartment. In contrast, the T_{SCM} and T_{EM} subsets lack evidence of prominent local expansion in the BrM. Importantly, I functionally identified one of the shared clones between the peripheral CD8$^+$ T_{EM} compartment and the intro-cranial CD8$^+$ T_{SCM} GZMK compartment in the BrM (NCH9348 TCR-9) as virus-specific. This provides direct functional evidence that shared clonotypes between blood and BrM can represent non-tumor-reactive, virus-specific T cells. This observation further supports a functional and spatial separation between circulating memory-like T cells and tumor-resident populations.

Given that the viral peptide pool used in this study covered only 32 peptides, it remains possible that clone 8, which was as well shared between the two compartments, may also exhibit viral specificities which were not captured in this assay.

One limitation of the current analysis is that shared clonotypes in the peripheral compartment were inferred based on identical TRAV/TRBV gene usage and matching CDR3α sequences. Final confirmation of clonal identity requires the demonstration of identical paired CDR3α and CDR3β sequences, which was not resolved in the present dataset and will require further dedicated bioinformatic validation.

Taken together, these findings support a model in which a substantial fraction of $CD103^-$ T cells in NSCLC brain metastases represents transiently infiltrating bystander populations with viral specificity. This interpretation is consistent with previous studies demonstrating that 37-50% of tumor-infiltrating lymphocytes across solid malignancies are non-tumor-reactive bystander T cells, predominantly directed against viral epitopes (Simoni et al., 2018). In contrast, effective anti-tumor immunity has been shown to rely on the local expansion and maintenance of tumor-resident T cell populations rather than continuous recruitment from the circulation (Shorer et al., 2025). Consistently, high TCR sharing between tumor and blood has been associated with bystander infiltration and reduced responsiveness to immunotherapy.

Importantly, alternative explanations cannot be excluded. If future functional analyses were to demonstrate tumor reactivity of shared clonotypes, this could support a model of systemic anti-tumor immunity involving migration of tumor-experienced T cells either egressing from the primary tumor (Torcellan et al., 2017) or being primed in extracranial draining lymph nodes which then migrate to the metastatic site. However, limited sample availability precluded such comprehensive validation in the present study.

Overall, my findings support a model in which the T cell compartment in NSCLC brain metastases consists of two distinct populations. The first comprises peripheral bystander T cells that transiently infiltrate the tumor microenvironment without substantial expansion and may include virus-specific clones, as demonstrated by the functional validation of a viral-reactive T_{SCM} GZMK clonotype. The second represents a locally enriched $CD103^+$ T_{RM} population that exhibits features consistent with tumor-antigen-driven retention and clonal expansion, as demonstrated by the functional validation of a tumor-reactive T_{RM} clonotype.

5.3.2. TLS-like structures suggest local T cell activation within NSCLC brain metastases

The presence of clonally expanded and spatially localized CD103$^+$ T_{RM} cells within NSCLC brain metastases, together with limited overlap with the peripheral blood repertoire, raises the question of where these cells are activated and maintained within the brain metastatic lesion. While classical models of anti-tumor immunity place T cell priming primarily in secondary lymphoid organs, my data suggest that at least part of this immune organization may occur locally within the metastatic niche.

My scRNA-seq data provided an initial indication that BrM can support such local immune organization. Within the CD4$^+$ T cell compartment, I identified a distinct population with features consistent with T follicular helper (T_{FH}) cells. CXCL13 is a key chemokine that mediates the recruitment of CXCR5-expressing B cells and plays a central role in the formation and organization of tertiary lymphoid structures (TLS). In NSCLC, intratumoral T_{FH} cells and CXCL13-associated programs have been linked to improved prognosis and durable anti-tumor immunity, particularly in the context of immune checkpoint blockade (Gutiérrez-Melo & Baumjohann, 2023; W. Liu et al., 2024; Magen et al., 2023). Importantly, in my dataset, *CXCL13* expression was not confined to CD4$^+$ T_{FH} cells but was also observed in the clonally expanded CD8$^+$ T_{RM} compartment, suggesting that local immune organization in BrM may be reinforced by both helper and cytotoxic T cell populations.

These transcriptomic findings were strongly supported by my spatial analyses. Across the analyzed cohort, I identified lymphoid aggregates in all stages of organization, ranging from relatively loose perivascular accumulations of T and B cells to highly structured TLS-like formations with clear compartmentalization of immune cell subsets. These findings suggest that lymphoid organization in BrM exists along a continuum of maturation rather than as a strictly binary present-or-absent phenomenon. Interestingly, the presence of TLS in brain metastases of primary breast cancer has been associated with improved overall survival, highlighting the functional relevance of these lymphoid structures as sites of active anti-tumor immunity (Jassowicz et al., 2026, in press). A defining feature of the most organized aggregates was a dense core enriched for CD138$^+$ plasma cells, a subset of which displayed proliferative activity. Notably, a fraction of these cells co-expressed CD31, resulting in a CD138$^+$CD31$^+$ phenotype that is atypical in peripheral tissues. This phenotype has been primarily described in the bone marrow, where it is associated with plasma cells exhibiting exceptionally high antibody secretory capacity (Martinez-Murillo et al., 2016). In this context, the presence of CD138$^+$CD31$^+$ plasma cells suggest the existence of a highly active local humoral compartment within BrM. Spatially, this plasma cell-rich core was

positioned in close proximity to T_{FH} cells and surrounded by B cell-enriched regions, forming an architecture consistent with coordinated local humoral immune activity. Such locally produced antibodies may contribute to anti-tumor immunity, for example through antibody-dependent cellular cytotoxicity (ADCC) mediated by innate immune effector cells. In other solid tumors, in situ B cell maturation within TLS has been linked to plasma cell generation, IgG deposition on tumor cells, and improved overall survival (Kroeger et al., 2016b; Meylan et al., 2022). Notably, IgG-coated tumor cells were associated with increased tumor cell death, suggesting a functional role of antibody-mediated effector mechanisms. Mechanistically, these effects have been attributed to ADCC; however, they were not associated with natural killer (NK) cell abundance but instead with macrophage proximity, indicating a dominant role for macrophage-mediated phagocytosis (Meylan et al., 2022). This is particularly relevant in the context of my data, in which tumor-associated macrophages expressed TIM3, a molecule linked to enhanced phagocytic capacity in myeloid cells (Nakayama et al., 2009), as well as high levels of IL4I1, recently proposed as a marker of highly phagocytic macrophage states (Matusiak et al., 2024). Together, these findings suggest a potential mechanistic link between TLS-associated anti-tumor humoral immunity driving a pro-tumorigenic macrophage-driven effector function in NSCLC brain metastases.

At the same time, these structures did not fully conform to the classical definition of a mature germinal center-like TLS. In my dataset, $CD21^+$ follicular DCs and $LAMP3^+$ mature DCs were not detectable, in line with previous reports in BrM (Nohira et al., 2024; Zhao et al., 2022). However, my data argue that such a strict definition may underestimate functionally relevant local immune structures in the metastatic brain microenvironment.

Furthermore, I observed $CD31^+CD34^+$ vascular structures in close proximity to these lymphoid aggregates. Given the association of CD34 with endothelial progenitor-like states and neoangiogenic remodeling (Hassanpour et al., 2023), these vessels may facilitate continuous immune cell recruitment into the TLS-like niche. In this context, vascular remodeling likely contributes not only to the metabolic demands of the tumor, but also to the maintenance of organized immune cell accumulation. TLS are not only defined by the accumulation of B cells, T cells, and dendritic cells, but also by the presence of high endothelial venules (HEVs) (Vella et al., 2021), which represent specialized vascular structures that facilitate lymphocyte recruitment in secondary lymphoid organs. HEVs are characterized by high expression of L-selectin ligands, collectively referred to as peripheral node addressin (PNAd) (Browning et al., 2005; Hua et al., 2022). The PNAd glycan is assembled, among others, on CD34, which has been described as a binding partner for L-selectin (Baumhueter et al., 1994; Puri et al., 1995). This axis mediates the recruitment of

circulating naïve T cells into lymphoid structures. Although a specific HEV marker was not included in my CODEX panel, CD34 staining in the context of TLS-like structures may therefore serve as a surrogate indicator of specialized vascular features associated with lymphocyte recruitment. However, this does not allow for conclusive identification of HEVs in the present dataset.

Taken together, my data support the presence of spatially organized lymphoid structures within NSCLC brain metastases that are consistent with local immune activation. Notably, these structures contain a prominent plasma cell-rich $CD138^+$ core, which, to my knowledge, has not previously been described in the context of NSCLC BrM. This finding suggests that humoral immune responses may play a more substantial role in the brain metastatic niche than previously appreciated. More broadly, these TLS-like structures provide a plausible framework for the local generation and maintenance of tumor-reactive $CD103^+$ T_{RM} cells, although direct evidence for *de novo* priming remains beyond the scope of this study.

6. Conclusion and Perspectives

6.1. Summary of findings

This thesis establishes a mechanistic framework to explain why T cell-mediated anti-tumor immunity remains ineffective in NSCLC brain metastases despite detectable immune infiltration. By integrating single-cell transcriptomics, TCR profiling, spatial imaging, and functional validation, I dissect the cellular composition, spatial organization, and functional constraints of the brain metastatic immune microenvironment.

A central finding of this work is the identification of a clonally expanded $CD103^+$ tissue-resident memory (T_{RM}) $CD8^+$ T cell population that exhibits multiple features consistent with tumor reactivity. The convergence of transcriptional signatures, clonal expansion, spatial localization within the tumor parenchyma, and the direct functional validation of a tumor-reactive TCR provides converging evidence that tumor-reactive T cells are present within NSCLC brain metastases. This finding challenges the notion that ineffective immunity in the brain is primarily due to the absence of tumor-specific T cells and instead identifies a spatially confined, tissue-resident compartment as the key site of tumor-specific immune activity.

At the same time, this work resolves the apparent paradox that tumor-reactive T cells are present but fail to control tumor growth. My data reveal a multi-layered system of immune restriction that operates across distinct spatial scales. Vascular heterogeneity defines where immune cells can access the metastatic niche, while structural barriers at the tumor-stroma interface limit penetration into tumor cell-dense regions. Within the stromal compartment, infiltrating T cells are further constrained by immunosuppressive niches, including IL4I1-expressing pro-tumorigenic macrophages and cytotoxic T_{REGs} that engage the perforin/granzyme axis. Together, these mechanisms form a coordinated restrictive network that limits effective T cell infiltration, persistence, and effector function.

Beyond these suppressive constraints, this thesis provides evidence that the brain metastatic microenvironment supports localized immune organization. The limited overlap between peripheral and intracranial TCR repertoires, combined with the presence of structured, plasma cell-rich TLS-like aggregates, supports a model in which anti-tumor immunity is at least partially established and maintained locally. The identification of a plasma cell core within these structures further suggests that humoral immune responses may contribute to this local immune landscape, extending current concepts of BrM immunology beyond a purely T cell-centered view.

Collectively, these findings redefine the basis of immune dysfunction in NSCLC brain metastases. Rather than reflecting a lack of tumor-specific immunity or widespread terminal exhaustion, ineffective immune control emerges as a consequence of spatial restriction, localized immunosuppression, and constrained antigen exposure. By identifying the cellular and structural determinants that limit T cell function in the brain metastatic niche, this work provides a foundation for the development of therapeutic strategies aimed at overcoming these constrains and enabling effective anti-tumor immunity.

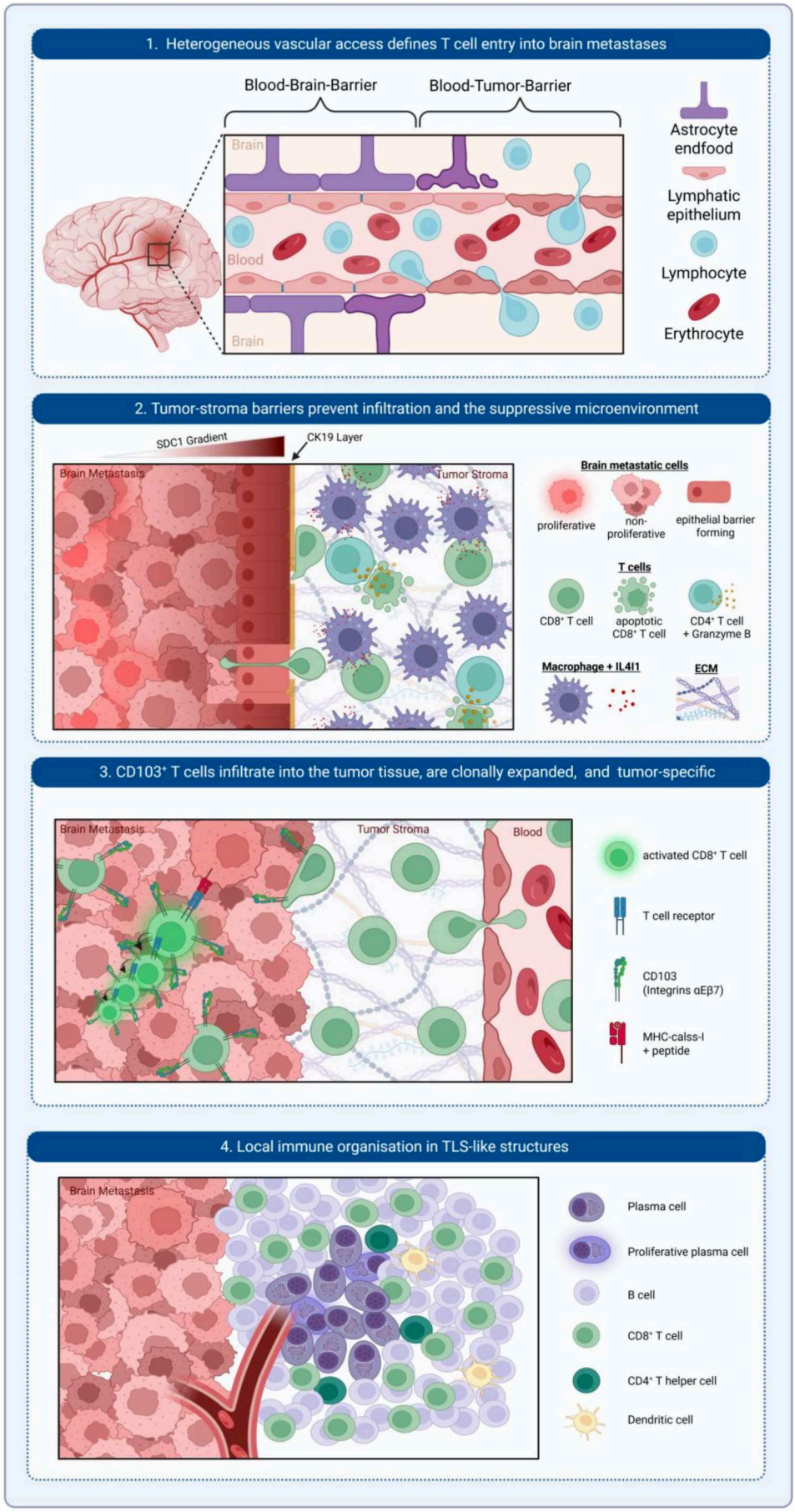

1. Heterogeneous vascular access defines T cell entry into brain metastases
Blood-Brain-Barrier
Blood-Tumor-Barrier
Brain
Blood
Brain
Astrocyte endfood
Lymphatic epithelium
Lymphocyte
Erythrocyte
2. Tumor-stroma barriers prevent infiltration and the suppressive microenvironment
SDC1 Gradient
CK19 Layer
Brain Metastasis
Tumor Stroma
Brain metastatic cells
proliferative
non-proliferative
epithelial barrier forming
T cells
CD8⁺ T cell
apoptotic CD8⁺ T cell
CD4⁺ T cell + Granzyme B
Macrophage + IL4I1
ECM
3. CD103⁺ T cells infiltrate into the tumor tissue, are clonally expanded, and tumor-specific
Brain Metastasis
Tumor Stroma
Blood
activated CD8⁺ T cell
T cell receptor
CD103 (Integrins αEβ7)
MHC-calss-I + peptide
4. Local immune organisation in TLS-like structures
Brain Metastasis
Plasma cell
Proliferative plasma cell
B cell
CD8⁺ T cell
CD4⁺ T helper cell
Dendritic cell

Figure 19: Integrated model of spatial and functional mechanisms of anti-tumor immunity in NSCLC brain metastases.

1. T cell entry into brain metastases is spatially heterogeneous and depends on the integrity of the perivascular niche. Regions with preserved astrocytic coverage maintain blood-brain barrier-like properties and restrict immune cell extravasation, whereas vascular remodeling associated with the blood-tumor barrier permits infiltration.
2. Following entry, T cells remain largely confined to the stromal compartment. At the tumor-stroma interface, a spatially organized $CK19^+$ barrier and an SDC1 (CD138) gradient restrict T cell penetration into the tumor parenchyma. Within the stroma, IL4I1-expressing macrophages and activated regulatory T cells further suppress T cell function, the latter via granzyme B-mediated mechanisms.
3. Despite these constraints, a subset of $CD103^+$ tissue-resident memory $CD8^+$ T cells localize within the tumor parenchyma. These cells exhibit clonal expansion, a transcriptional profile consistent with tumor reactivity, and include T cell receptors with confirmed tumor-specific activity, indicating the presence of functional anti-tumor immunity.
4. Spatially organized tertiary lymphoid structure (TLS)-like formations are present, characterized by a plasma cell-rich core surrounded by B cells, T cells, T_{FH} cells, and dendritic cells. These structures suggest local immune organizations and may support the generation and maintenance of tumor-reactive T cells.

6.2. Therapeutic perspectives and future directions

The findings of this thesis delineate distinct, targetable mechanisms that actively suppress anti-tumor immunity in NSCLC brain metastases while also uncovering additional layers of immune organization that remain incompletely understood. Rather than reflecting a passive failure of immune infiltration, my data identify defined structural and cellular barriers, including the tumor-stroma interface, and suppressive myeloid compartments. These findings define rational points of therapeutic intervention, while other observations, such as the presence of plasma cell-rich TLS-like structures, highlight independent areas that require further investigation.

A key next step will be the systematic quantitative analysis of the multiplexed spatial imaging data. This includes the application of computational approaches to define cell-cell interactions, spatial neighborhoods, and higher-order tissue structures across patients. In particular, quantitative assessment of $CD103^+$ T cell localization relative to tumor cells, macrophage-rich niches, and TLS-like structures will be critical to validate the spatial relationships described here and to determine their consistency across the cohort. Such analyses will also enable the identification of spatial correlations of T cell functionality and may uncover patient-specific differences in immune organization that are not captured by qualitative observation alone.

Beyond these methodological considerations, a central finding of this work is the identification of a previously unrecognized barrier at the tumor-stroma interface in BrM that actively restricts T cell entry into the tumor parenchyma. While SDC1 has been implicated in T cell exclusion in other tumor settings, my data reveal its spatially organized distribution at the tumor border as a key determinant of immune exclusion in NSCLC brain metastases, thereby defining a novel and targetable mechanism in this context. In solid tumor models, monoclonal antibodies targeting SDC1 have demonstrated potent anti-tumor activity by promoting $CD8^+$ T cell infiltration and inducing NK cell-mediated ADCC (Yang et al., 2026). However, in the context of brain metastases, such approaches require careful consideration. While systemic targeting of SDC1 may alleviate tumor-associated immune exclusion, it also risks disrupting plasma cells within TLS-like structures and thereby compromising local humoral immunity. In addition, the pleiotropic functions of SDC1 in tissue organization and its extensive interactome raise significant concerns regarding unintended off-target effects, complicating its use as a therapeutic target. A more selective strategy, such as the development of bispecific antibodies combining SDC1 targeting with a tumor-restricted epithelial marker, may allow disruption of the tumor barrier while preventing off-target effects.

In parallel, the suppressive stromal microenvironment represents a second key therapeutic axis. The identification of IL4I1-expressing macrophages as a conserved feature of NSCLC brain metastases suggests that metabolic immune suppression is a central component of the local niche (Matusiak et al., 2024; Sadik et al., 2020). Notably, specific IL4I1 inhibitors have already been developed, highlighting the translational potential of this pathway (Sabnis, 2023). Targeting IL4I1 may therefore restore T cell proliferation and effector function while limiting tumor cell motility. However, effective delivery remains a major challenge, particularly in regions with preserved barrier function. The use of targeted delivery systems, such as nanoparticle-based approaches, may in this context be required to achieve sufficient drug penetration (Cheng et al., 2014).

Beyond T cell-directed immunity, the identification of highly organized, plasma cell-rich TLS-like structures points to a previously underappreciated role of humoral immunity in brain metastases. Integrating single-cell RNA sequencing with B cell receptor (BCR) profiling will be critical to resolve the clonal architecture and somatic hypermutation dynamics of BrM-infiltrating B cells and plasma cells. This will provide key insights into their role in shaping anti-tumor immunity within the brain metastatic niche.

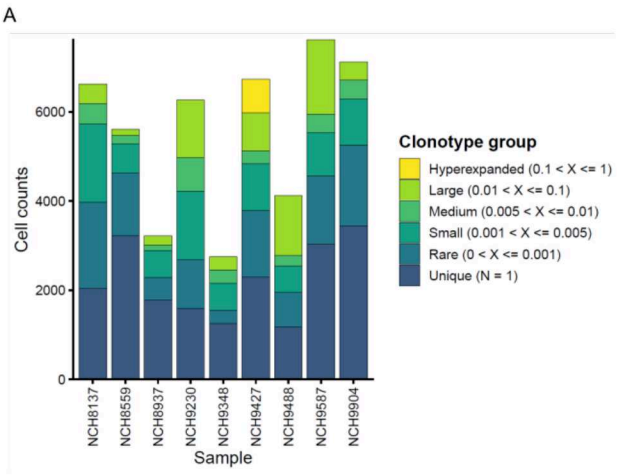
In addition to these therapeutic considerations, several targeted experimental approaches are required to further refine the mechanistic insights generated in this study. First, computational inference of cell-cell communication, for example using CellChat, should be

applied to the single-cell transcriptomic data to systematically characterize interactions between $CD8^+$ T cells and T_{REGs}. This would provide transcriptional-level support for the direct suppressive interaction suggested by spatial proximity and granzyme B deposition. Second, the antigen specificity of selected TCRs requires further clarification. The TCR identified as virus-reactive in patient NCH9348 should be cross-referenced against publicly available databases such as VDJdb to verify prior annotation and determine whether this TCR represents an already annotated virus-specific sequence. In parallel, the selected NCH9348 clonotype 9 from the BrM, which was validated to be viral-reactive, and which was observed to be also present in the peripheral blood based on concordant *TRAV* and *TRBV* gene usage and identical CDR3α sequences should be validated as true clone through comprehensive pairing analysis of the CDR3β region. Building on this, future analyses should systematically extend this approach to all clonotypes shared between brain metastases and peripheral blood across the four patients with matched sequencing data. In particular, it will be important to determine the extent to which these shared clonotypes correspond to previously annotated virus-specific sequences in VDJdb, and to define their phenotypic distribution within each compartment. Such analyses will provide critical insight into whether circulating-intratumoral overlap is predominantly driven by bystander, virus-specific T cells or includes clonotypes with potential tumor reactivity.

Third, the functional validation platform established in this study can be further strengthened by extending TCR testing of sample NCH8937 to PBMC-derived T cells. In particular, for patient NCH8937, where autologous PBMCs were not available, the use of HLA-matched healthy donor PBMCs would allow independent validation of the optofluidic assay results. Inclusion of viral peptide pools in this system would further allow for discrimination between tumor-specific and virus-specific TCR reactivity.

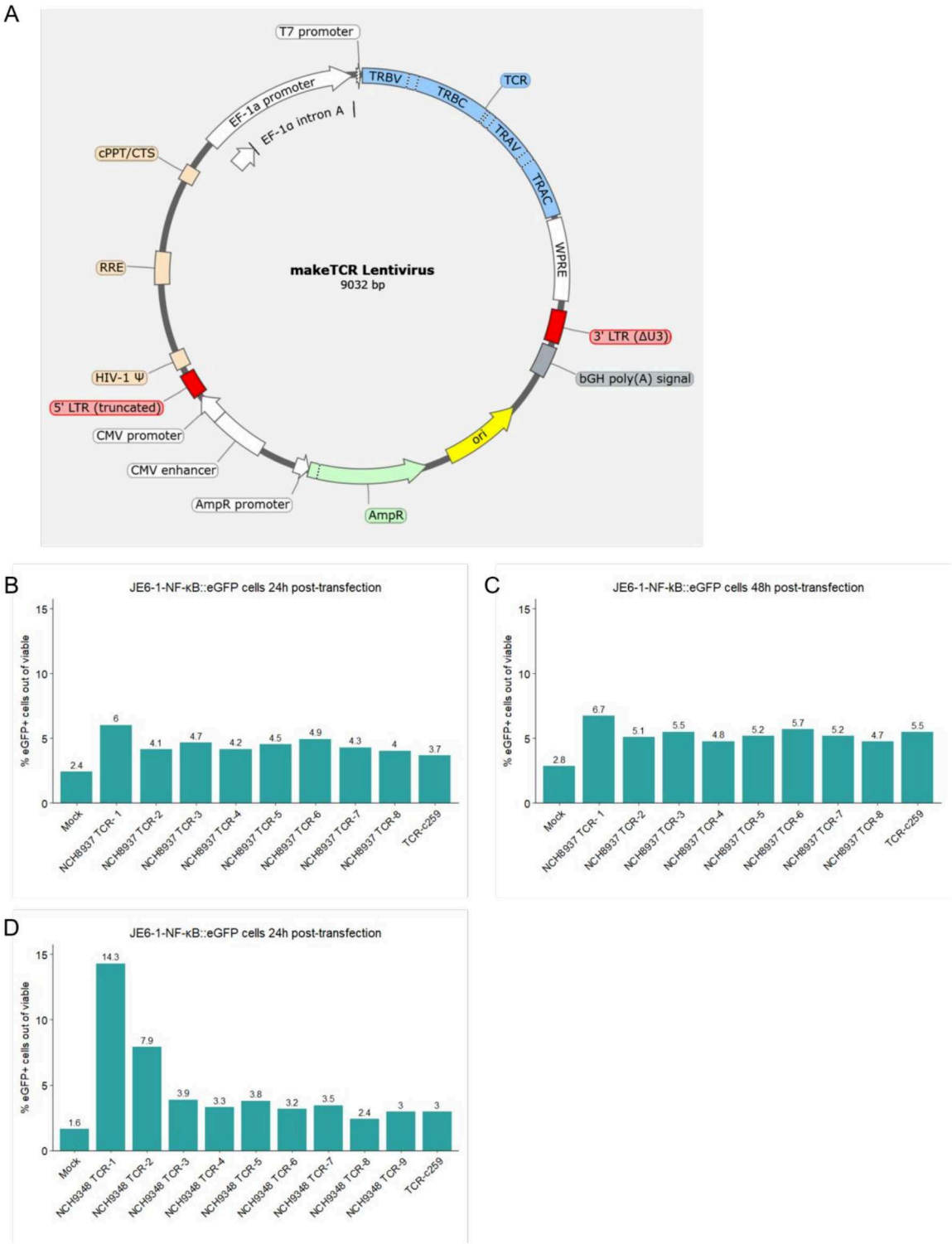
Taken together, these approaches will refine the mechanistic understanding of T cell function in NSCLC brain metastases and facilitate translation into clinically actionable strategies. By targeting the structural, cellular, and functional constraints identified in this work, future therapies may enable effective engagement of the resident tumor-reactive T cell compartment and thereby improve outcomes for patients with brain metastases.

7. Appendix



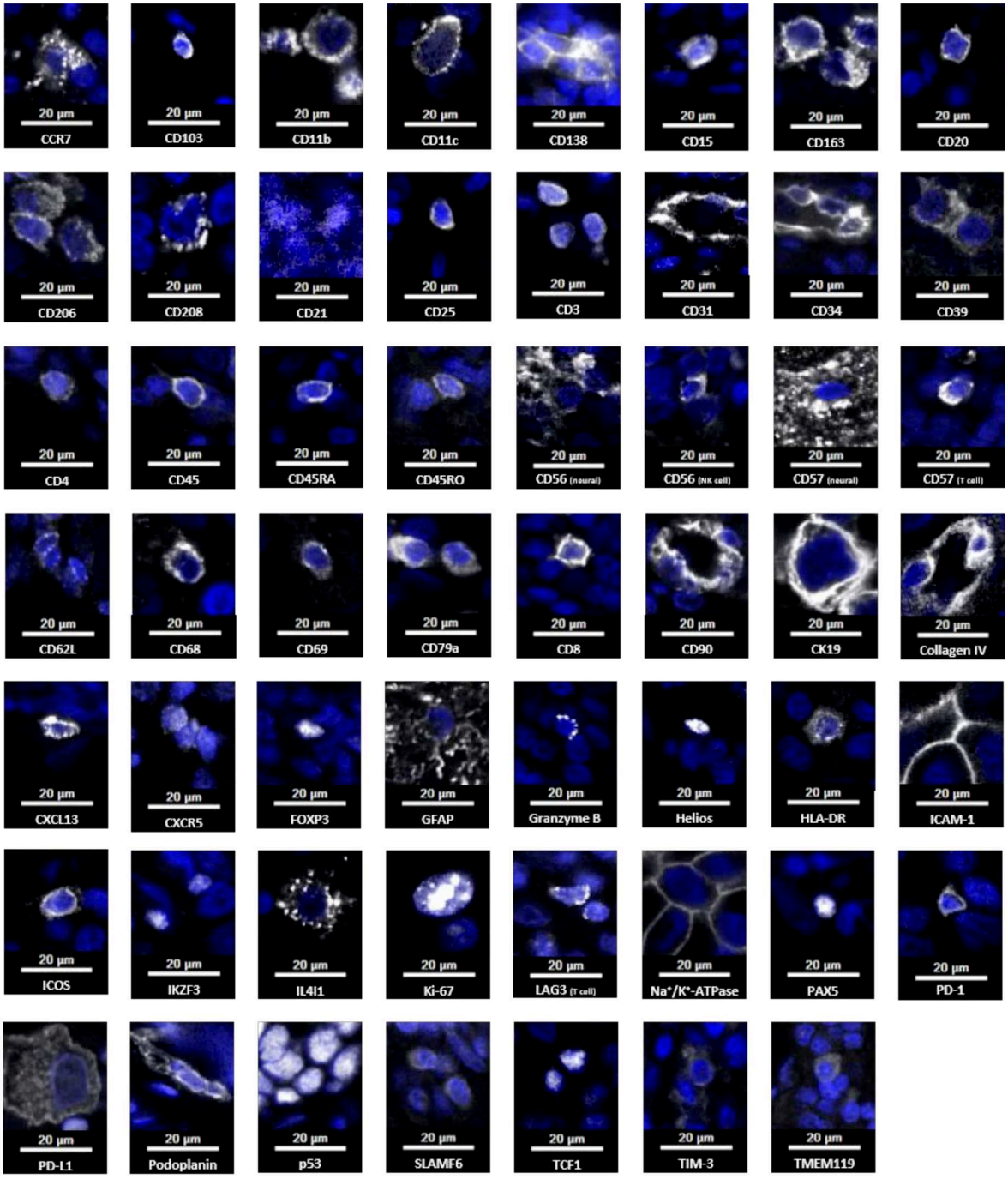
Appendix Figure 1: Cell count of T cells from scRNA/TCR-seq analysis including clonotype group

(A) Cell counts of BrM-infiltrating T cells with detectable TCR-sequence after quality control from the scRNA/TCR-seq dataset.



Appendix Figure 2: Lentiviral TCR construct and baseline reporter activation in JE6-1-NF-κB::eGFP cells

(A) Schematic representation of the lentiviral backbone used for cloning of TCR sequences of interest, combining *TRBV*, *TRBC*, *TRAV*, and *TRAC* within a single construct under the control of a T7 promoter. (B, D) Unspecific reporter activation, quantified as the percentage of eGFP$^+$ JE6-1-NF-κB::eGFP cells 24 h post-transfection with TCRs derived from sample NCH8937 (B) or NCH9348 (D), cultured in the absence of target cells. (C) Unspecific reporter activation, quantified as the percentage of eGFP$^+$ JE6-1-NF-κB::eGFP cells 48 h post-transfection with TCRs derived from sample NCH8937, cultured in the absence of target cells.



Appendix Figure 3: Representative multiplexed CODEX imaging of marker expression in brain metastases

Representative single-marker fluorescence images illustrating spatially resolved expression of selected markers within brain metastatic tissue. Signals are shown for individual markers, with nuclei counterstained by DAPI. Scale bars and marker identities are indicated.

8. List of publications

Alessia Floerchinger, Jan Philipp Schadendorf, Yuliia Borysovych, Min Gao, Hannah Briesch, Nicolas Aubert, Laura Llaó-Cid, **Liesa-Marie Pilger**, Cèlia Dobaño-López, Sama AlMehallawi, Evgeniya Nikolaeva, Yu-Qing Xie, Mei-Wen Peng, Manina Günter, Peter-Martin Bruch, Sascha Dietrich, Stella E. Autenrieth, Yugang Guo, Peter Lichter, Marc Zapatka, Li Tang, Martina Seiffert. IL-10 Limits T-Cell Exhaustion and Reprograms Monocytes to Enhance Immune Control and Ibrutinib Efficacy in Chronic Lymphocytic Leukemia. *Blood* (submitted)

Yael Zait, **Liesa-Marie Pilger**, Lea Monteran, Sameeha Mittwali, Nour Ershaid, Yeela Scharff, Elia Balouka, Keren Hareli, Gali Yanovich-Arad, Marva Langer, Omer Adler, Tamar Shami, Suzana Horn, Adva Levi-Barda, Yosef Laviv, Shlomit Yust-Katz, Tamar Geiger, Marc Zapatka, Yaron Carmi, Leeat Keren, Martina Seiffert and Neta Erez. Antigen-presenting astrocytes modulate anti-tumor immunity in brain metastasis. *Cancer Cell* (under revision)

Jawahar Kopparam, Gayathri Chandrasekaran, Danielle Hulsman, **Liesa-Marie Pilger**, Karen Stevers, Ji-Ying Song, Miguel Hernandez-Quiles, Jelmer Dijkstra, Jitendra Badhai, Nick Landman, Michiel Vermeulen, Maarten van Lohuizen. PRC2 loss impairs small cell lung cancer tumorigenesis and enhances sensitivity to G9a/GLP inhibition. *Communications Biology* (2026)

L Llaó-Cid, JKL Wong, I Fernandez Botana, Y Paul, M Wierz, **L-M Pilger**, A Floerchinger, CL Tan, S Gonder, G Pagano, M Chazotte, K Bestak, C Schifflers, M Iskar, T Roider, F Czernilofsky, P-M Bruch, JP Mallm, A Cosma, DE Campton, E Gerhard-Hartmann, A Rosenwald, D Colomer, E Campo, D Schapiro, EW Green, S Dietrich, P Lichter, E Moussay, J Paggetti, M Zapatka, M Seiffert. Integrative multi-omics reveals a regulatory and exhausted T-cell landscape in CLL and identifies galectin-9 as an immunotherapy target. *Nature Communications* (2025)

9. References

Allemani, C., Matsuda, T., Di Carlo, V., Harewood, R., Matz, M., Niksic, M., Bonaventure, A., Valkov, M., Johnson, C. J., Esteve, J., Ogunbiyi, O. J., Azevedo, E. S. G., Chen, W. Q., Eser, S., Engholm, G., Stiller, C. A., Monnereau, A., Woods, R. R., Visser, O.,…Group, C. W. (2018). Global surveillance of trends in cancer survival 2000-14 (CONCORD-3): analysis of individual records for 37 513 025 patients diagnosed with one of 18 cancers from 322 population-based registries in 71 countries. *Lancet*, *391*(10125), 1023–1075. https://doi.org/10.1016/S0140-6736(17)33326-3

Álvarez-Prado, Á. F., Maas, R. R., Soukup, K., Klemm, F., Kornete, M., Krebs, F. S., Zoete, V., Berezowska, S., Brouland, J.-P., Hottinger, A. F., Daniel, R. T., Hegi, M. E., & Joyce, J. A. (2023). Immunogenomic analysis of human brain metastases reveals diverse immune landscapes across genetically distinct tumors. *Cell Reports Medicine*, *4*(1), 100900. https://doi.org/10.1016/j.xcrm.2022.100900

Andersen, B. M., Faust Akl, C., Wheeler, M. A., Chiocca, E. A., Reardon, D. A., & Quintana, F. J. (2021). Glial and myeloid heterogeneity in the brain tumour microenvironment. *Nat Rev Cancer*, *21*(12), 786–802. https://doi.org/10.1038/s41568-021-00397-3

Baldominos, P., Barbera-Mourelle, A., Barreiro, O., Huang, Y., Wight, A., Cho, J. W., Zhao, X., Estivill, G., Adam, I., Sanchez, X., McCarthy, S., Schaller, J., Khan, Z., Ruzo, A., Pastorello, R., Richardson, E. T., Dillon, D., Montero-Llopis, P., Barroso-Sousa, R.,…Agudo, J. (2022). Quiescent cancer cells resist T cell attack by forming an immunosuppressive niche. *Cell*, *185*(10), 1694–1708.e1619. https://doi.org/10.1016/j.cell.2022.03.033

Barker, D. J., Natarajan, R. H. L., Cooper, M. A., Hopper, S. J. F., Yates, A. D., Parham, P., Marsh, S. G. E., & Robinson, J. (2025). The IPD-IMGT/HLA database: recent developments in sequence submission. *Nucleic Acids Res*. https://doi.org/10.1093/nar/gkaf1218

Baumhueter, S., Dybdal, N., Kyle, C., & Lasky, L. (1994). Global vascular expression of murine CD34, a sialomucin-like endothelial ligand for L-selectin. *Blood*, *84*(8), 2554–2565. https://doi.org/10.1182/blood.V84.8.2554.2554

Bertolini, A., Spallanzani, A., Fontana, A., Depenni, R., & Luppi, G. (2015). Brain metastases: an overview. *CNS Oncol.*, *4*(1), 37–46. https://doi.org/10.2217/cns.14.51

Biermann, J., Melms, J. C., Amin, A. D., Wang, Y., Caprio, L. A., Karz, A., Tagore, S., Barrera, I., Ibarra-Arellano, M. A., Andreatta, M., Fullerton, B. T., Gretarsson, K. H., Sahu, V., Mangipudy, V. S., Nguyen, T. T. T., Nair, A., Rogava, M., Ho, P., Koch, P. D.,…Izar, B. (2022). Dissecting the treatment-naive ecosystem of human melanoma brain metastasis. *Cell*, *185*(14), 2591–2608.e2530. https://doi.org/10.1016/j.cell.2022.06.007

Borst, J., Ahrends, T., Babala, N., Melief, C. J. M., & Kastenmuller, W. (2018). CD4(+) T cell help in cancer immunology and immunotherapy. *Nat Rev Immunol*, *18*(10), 635–647. https://doi.org/10.1038/s41577-018-0044-0

Brastianos, P. K., Kim, A. E., Giobbie-Hurder, A., Lee, E. Q., Lin, N. U., Overmoyer, B., Wen, P. Y., Nayak, L., Cohen, J. V., Dietrich, J., Eichler, A., Heist, R. S., Krop, I., Lawrence, D., Ligibel, J., Tolaney, S., Mayer, E., Winer, E., Bent, B.,…Sullivan, R. J. (2023). Pembrolizumab in brain metastases of diverse histologies: phase 2 trial results. *Nat Med*, *29*(7), 1728–1737. https://doi.org/10.1038/s41591-023-02392-7

Bray, F., Laversanne, M., Sung, H., Ferlay, J., Siegel, R. L., Soerjomataram, I., & Jemal, A. (2024). Global cancer statistics 2022: GLOBOCAN estimates of incidence and mortality worldwide for 36 cancers in 185 countries. *CA Cancer J Clin*, *74*(3), 229–263. https://doi.org/10.3322/caac.21834

Brizic, I., Susak, B., Arapovic, M., Huszthy, P. C., Hirsl, L., Kvestak, D., Juranic Lisnic, V., Golemac, M., Pernjak Pugel, E., Tomac, J., Oxenius, A., Britt, W. J., Arapovic, J., Krmpotic, A., & Jonjic, S. (2018). Brain-resident memory CD8(+) T cells induced by congenital CMV infection prevent brain pathology and virus reactivation. *Eur J Immunol*, *48*(6), 950–964. https://doi.org/10.1002/eji.201847526

Browning, J. L., Allaire, N., Ngam-Ek, A., Notidis, E., Hunt, J., Perrin, S., & Fava, R. A. (2005). Lymphotoxin-β Receptor Signaling Is Required for the Homeostatic Control of HEV Differentiation and Function. *Immunity*, *23*(5), 539–550. https://doi.org/10.1016/j.immuni.2005.10.002

Buell, J. F., Gross, T. G., & Woodle, E. S. (2005). Malignancy after transplantation. *Transplantation*, *80*(2 Suppl), S254–264. https://doi.org/10.1097/01.tp.0000186382.81130.ba

Bui, K. T., Cooper, W. A., Kao, S., & Boyer, M. (2018). Targeted Molecular Treatments in Non-Small Cell Lung Cancer: A Clinical Guide for Oncologists. *J Clin Med*, *7*(8). https://doi.org/10.3390/jcm7080192

Cameron, F. (2011). Ipilimumab: first global approval. *Grugs*, *71 (8)*. https://doi.org/10.2165/11594010-000000000-00000

Cerbelli, B., Pisano, A., Pignataro, M. G., Pernazza, A., Botticelli, A., Carosi, M., Costarelli, L., Allegretti, M., d'Amati, G., & Cordone, I. (2023). Overexpression in metastatic breast cancer supports Syndecan-1 as a marker of invasiveness and poor prognosis. *Clinical and Experimental Medicine*, *23*(5), 1641–1647. https://doi.org/10.1007/s10238-022-00880-7

Chen, D. S., & Mellman, I. (2013). Oncology meets immunology: the cancer-immunity cycle. *Immunity*, *39*(1), 1–10. https://doi.org/10.1016/j.immuni.2013.07.012

Chen, L., & Flies, D. B. (2013). Molecular mechanisms of T cell co-stimulation and co-inhibition. *Nat Rev Immunol*, *13*(4), 227–242. https://doi.org/10.1038/nri3405

Chen, X. T., Leisegang, M., Gavvovidis, I., Pollack, S. M., Lorenz, F. K. M., Schumacher, T. N., Daumke, O., & Blankenstein, T. (2024). Generation of effective and specific human TCRs against tumor/testis antigen NY-ESO-1 in mice with humanized T cell recognition system. *Front Immunol*, *15*, 1524629. https://doi.org/10.3389/fimmu.2024.1524629

Chen, Y.-T., Scanlan, M. J., Sahin, U., Türeci, Ö., Gure, A. O., Tsang, S., Williamson, B., Stockert, E., Pfreundschuh, M., & Old, L. J. (1997). A testicular antigen aberrantly expressed in human cancers detected by autologous antibody screening. *Proceedings of the National Academy of Sciences*, *94*(5), 1914–1918. https://doi.org/10.1073/pnas.94.5.1914

Cheng, Y., Dai, Q., Morshed, R. A., Fan, X., Wegscheid, M. L., Wainwright, D. A., Han, Y., Zhang, L., Auffinger, B., Tobias, A. L., Rincón, E., Thaci, B., Ahmed, A. U., Warnke, P. C., He, C., & Lesniak, M. S. (2014). Blood-Brain Barrier Permeable Gold Nanoparticles: An Efficient Delivery Platform for Enhanced Malignant Glioma Therapy and Imaging. *Small*, *10*(24), 5137–5150. https://doi.org/10.1002/smll.201400654

Christo, S. N., Park, S. L., Mueller, S. N., & Mackay, L. K. (2024). The Multifaceted Role of Tissue-Resident Memory T Cells. *Annu Rev Immunol*, *42*(1), 317–345. https://doi.org/10.1146/annurev-immunol-101320-020220

Curtsinger, J. M., & Mescher, M. F. (2010). Inflammatory cytokines as a third signal for T cell activation. *Curr Opin Immunol*, *22*(3), 333–340. https://doi.org/10.1016/j.coi.2010.02.013

Davies, M. J. (2019). PD-1/PD-L1 Inhibitors for Non-Small Cell Lung Cancer: Incorporating Care Step Pathways for Effective Side-Effect Management. *J Adv Pract Oncol*, *10*(Suppl 1), 21–35. https://doi.org/10.6004/jadpro.2019.10.2.11

Dhatchinamoorthy, K., Colbert, J. D., & Rock, K. L. (2021). Cancer Immune Evasion Through Loss of MHC Class I Antigen Presentation. *Front Immunol*, *12*, 636568. https://doi.org/10.3389/fimmu.2021.636568

Di Pilato, M., Kfuri-Rubens, R., Pruessmann, J. N., Ozga, A. J., Messemaker, M., Cadilha, B. L., Sivakumar, R., Cianciaruso, C., Warner, R. D., Marangoni, F., Carrizosa, E., Lesch, S., Billingsley, J., Perez-Ramos, D., Zavala, F., Rheinbay, E., Luster, A. D., Gerner, M. Y., Kobold, S.,…Mempel, T. R. (2021). CXCR6 positions cytotoxic T cells to receive critical survival signals in the tumor microenvironment. *Cell*, *184*(17), 4512–4530 e4522. https://doi.org/10.1016/j.cell.2021.07.015

Diab, L., Al Kattar, S., Oueini, N., Hawi, J., Chrabieh, A., Dosh, L., Jurjus, R., Leone, A., & Jurjus, A. (2024). Syndecan-1: a key player in health and disease. *Immunogenetics*, *77*(1), 9. https://doi.org/10.1007/s00251-024-01366-4

Djenidi, F., Adam, J., Goubar, A., Durgeau, A., Meurice, G., de Montpreville, V., Validire, P., Besse, B., & Mami-Chouaib, F. (2015). CD8+CD103+ tumor-infiltrating lymphocytes are tumor-specific tissue-resident memory T cells and a prognostic factor for survival in lung cancer patients. *J Immunol*, *194*(7), 3475–3486. https://doi.org/10.4049/jimmunol.1402711

Donnem, T., Hu, J., Ferguson, M., Adighibe, O., Snell, C., Harris, A. L., Gatter, K. C., & Pezzella, F. (2013). Vessel co-option in primary human tumors and metastases: an obstacle to effective anti-angiogenic treatment? *Cancer Medicine*, *2*(4), 427–436. https://doi.org/10.1002/cam4.105

Duhen, T., Duhen, R., Montler, R., Moses, J., Moudgil, T., de Miranda, N. F., Goodall, C. P., Blair, T. C., Fox, B. A., McDermott, J. E., Chang, S. C., Grunkemeier, G., Leidner, R., Bell, R. B., & Weinberg, A. D. (2018). Co-expression of CD39 and CD103 identifies tumor-reactive CD8 T cells in human solid tumors. *Nat Commun*, *9*(1), 2724. https://doi.org/10.1038/s41467-018-05072-0

Dunn, G. P., Old, L. J., & Schreiber, R. D. (2004). The three Es of cancer immunoediting. *Annu Rev Immunol*, *22*, 329–360. https://doi.org/10.1146/annurev.immunol.22.012703.104803

Dupic, T., Marcou, Q., Walczak, A. M., & Mora, T. (2019). Genesis of the αβ T-cell receptor. *PLOS Computational Biology*, *15*(3), e1006874. https://doi.org/10.1371/journal.pcbi.1006874

Feng, H.-M., Zhao, Y., Zhai, K.-R., Li, B., Song, T.-N., Meng, Y.-Q., Huang, H.-R., Li, Z., Cui, B.-Q., Yang, N., & Su, Z.-P. (2026). Extracellular granzyme K enhances PD-L1 transcription and stability via F2RL1 activation to facilitate tumor immune evasion in lung adenocarcinoma. *Journal for ImmunoTherapy of Cancer*, *14*(1), e013170. https://doi.org/10.1136/jitc-2025-013170

Flinsenberg, T. W., Spel, L., Jansen, M., Koning, D., de Haar, C., Plantinga, M., Scholman, R., van Loenen, M. M., Nierkens, S., Boon, L., van Baarle, D., Heemskerk, M. H., Boelens, J. J., & Boes, M. (2015). Cognate CD4 T-cell licensing of dendritic cells heralds anti-cytomegalovirus CD8 T-cell immunity after human allogeneic umbilical cord blood transplantation. *J Virol*, *89*(2), 1058–1069. https://doi.org/10.1128/JVI.01850-14

Fridman, W. H., Meylan, M., Petitprez, F., Sun, C. M., Italiano, A., & Sautes-Fridman, C. (2022). B cells and tertiary lymphoid structures as determinants of tumour immune contexture and clinical outcome. *Nat Rev Clin Oncol*, *19*(7), 441–457. https://doi.org/10.1038/s41571-022-00619-z

Fridman, W. H., Meylan, M., Pupier, G., Calvez, A., Hernandez, I., & Sautes-Fridman, C. (2023). Tertiary lymphoid structures and B cells: An intratumoral immunity cycle. *Immunity*, *56*(10), 2254–2269. https://doi.org/10.1016/j.immuni.2023.08.009

Friebel, E., Kapolou, K., Unger, S., Nunez, N. G., Utz, S., Rushing, E. J., Regli, L., Weller, M., Greter, M., Tugues, S., Neidert, M. C., & Becher, B. (2020). Single-Cell Mapping of Human Brain Cancer Reveals Tumor-Specific Instruction of Tissue-Invading Leukocytes. *Cell*, *181*(7), 1626–1642 e1620. https://doi.org/10.1016/j.cell.2020.04.055

Fu, B., Wang, F., Sun, R., Ling, B., Tian, Z., & Wei, H. (2011). CD11b and CD27 reflect distinct population and functional specialization in human natural killer cells. *Immunology*, *133*(3), 350–359. https://doi.org/10.1111/j.1365-2567.2011.03446.x

Galassi, C., Chan, T. A., Vitale, I., & Galluzzi, L. (2024). The hallmarks of cancer immune evasion. *Cancer Cell*, *42*(11), 1825–1863. https://doi.org/10.1016/j.ccell.2024.09.010

Gallimore, A. (1998). Induction and Exhaustion of Lymphocytic Choriomeningitis Virus–specific Cytotoxic T Lymphocytes Visualized Using Soluble Tetrameric Major Histocompatibility Complex Class I–Peptide Complexes. *J Exp Med*, *187 (9)*. https://doi.org/10.1084/jem.187.9.1383

Gan, D. X., Wang, Y. B., He, M. Y., Chen, Z. Y., Qin, X. X., Miao, Z. W., Chen, Y. H., & Li, B. (2020). Lung Cancer Cells-Controlled Dkk-1 Production in Brain Metastatic Cascade Drive Microglia to Acquire a Pro-tumorigenic Phenotype. *Front Cell Dev Biol*, *8*, 591405. https://doi.org/10.3389/fcell.2020.591405

Gillespie, C. S., Mustafa, M. A., Richardson, G. E., Alam, A. M., Lee, K. S., Hughes, D. M., Escriu, C., & Zakaria, R. (2023). Genomic Alterations and the Incidence of Brain Metastases in Advanced and Metastatic NSCLC: A Systematic Review and Meta-Analysis. *J Thorac Oncol*, *18*(12), 1703–1713. https://doi.org/10.1016/j.jtho.2023.06.017

Ginhoux, F. (2010). Fate Mapping Analysis Reveals That Adult Microglia Derive from Primitive Macrophages. *Science*, *330*. https://doi.org/10.1126/science.119463

Gong, J., Chehrazi-Raffle, A., Reddi, S., & Salgia, R. (2018). Development of PD-1 and PD-L1 inhibitors as a form of cancer immunotherapy: a comprehensive review of registration trials and future considerations. *Journal for ImmunoTherapy of Cancer*, *6*(1). https://doi.org/10.1186/s40425-018-0316-z

Gonzalez, H., Mei, W., Robles, I., Hagerling, C., Allen, B. M., Hauge Okholm, T. L., Nanjaraj, A., Verbeek, T., Kalavacherla, S., van Gogh, M., Georgiou, S., Daras, M., Phillips, J. J., Spitzer, M. H., Roose, J. P., & Werb, Z. (2022). Cellular architecture of human brain metastases. *Cell*, *185*(4), 729–745 e720. https://doi.org/10.1016/j.cell.2021.12.043

Grossman, W. J., Verbsky, J. W., Barchet, W., Colonna, M., Atkinson, J. P., & Ley, T. J. (2004). Human T Regulatory Cells Can Use the Perforin Pathway to Cause Autologous Target Cell Death. *Immunity*, *21*(4), 589–601. https://doi.org/10.1016/j.immuni.2004.09.002

Gutiérrez-Melo, N., & Baumjohann, D. (2023). T follicular helper cells in cancer. *Trends in Cancer*, *9*(4), 309–325. https://doi.org/10.1016/j.trecan.2022.12.007

Hamberger, M., Neuhoff, M. T., Pietrantonio, S. V., Boschert, T., Torres, C. M., Errerd, A., Tan, C. L., Lindner, J. M., Platten, M., & Green, E. W. (2025). https://doi.org/10.1101/2025.04.27.647198

Han, J., Zhao, Y., Shirai, K., Molodtsov, A., Kolling, F. W., Fisher, J. L., Zhang, P., Yan, S., Searles, T. G., Bader, J. M., Gui, J., Cheng, C., Ernstoff, M. S., Turk, M. J., & Angeles, C. V. (2021). Resident and circulating memory T cells persist for years in melanoma patients with durable responses to immunotherapy. *Nat Cancer*, *2*(3), 300–311. https://doi.org/10.1038/s43018-021-00180-1

Hanada, K. I., Zhao, C., Gil-Hoyos, R., Gartner, J. J., Chow-Parmer, C., Lowery, F. J., Krishna, S., Prickett, T. D., Kivitz, S., Parkhurst, M. R., Wong, N., Rae, Z., Kelly, M. C., Goff, S. L., Robbins, P. F., Rosenberg, S. A., & Yang, J. C. (2022). A phenotypic signature that identifies neoantigen-reactive T cells in fresh human lung cancers. *Cancer Cell*, *40*(5), 479–493 e476. https://doi.org/10.1016/j.ccell.2022.03.012

Hanahan, D., & Weinberg, R. A. (2000). The Hallmarks of Cancer. *Cell*, *100*, 57–70. https://doi.org/10.1016/S0092-8674(00)81683-9

Hanahan, D., & Weinberg, R. A. (2011). Hallmarks of cancer: the next generation. *Cell*, *144*(5), 646–674. https://doi.org/10.1016/j.cell.2011.02.013

Hanna, H., Andre, F. M., & Mir, L. M. (2017). Electrical control of calcium oscillations in mesenchymal stem cells using microsecond pulsed electric fields. *Stem Cell Res Ther*, *8*(1), 91. https://doi.org/10.1186/s13287-017-0536-z

Hao, Y., Baker, D., & Ten Dijke, P. (2019). TGF-beta-Mediated Epithelial-Mesenchymal Transition and Cancer Metastasis. *Int J Mol Sci*, *20*(11). https://doi.org/10.3390/ijms20112767

Hassanpour, M., Salybekov, A. A., Kobayashi, S., & Asahara, T. (2023). CD34 positive cells as endothelial progenitor cells in biology and medicine. *Frontiers in Cell and Developmental Biology*, *11*. https://doi.org/10.3389/fcell.2023.1128134

Heerboth, S., Housman, G., Leary, M., Longacre, M., Byler, S., Lapinska, K., Willbanks, A., & Sarkar, S. (2015). EMT and tumor metastasis. *Clin Transl Med*, *4*, 6. https://doi.org/10.1186/s40169-015-0048-3

Hodi, F. S. (2010). Improved Survival with Ipilimumab in Patients

with Metastatic Melanoma<NEJMoa1003466.pdf>. *The New England Journal of Medicine*, *363*. https://doi.org/10.1056/NEJMoa1003466

Hu, G., Zhong, K., Chen, W., Wang, S., & Huang, L. (2018). Podoplanin-positive cancer-associated fibroblasts predict poor prognosis in lung cancer patients. *Onco Targets Ther*, *11*, 5607–5619. https://doi.org/10.2147/ott.S175566

Hua, Y., Vella, G., Rambow, F., Allen, E., Antoranz Martinez, A., Duhamel, M., Takeda, A., Jalkanen, S., Junius, S., Smeets, A., Nittner, D., Dimmeler, S., Hehlgans, T., Liston, A., Bosisio, F. M., Floris, G., Laoui, D., Hollmén, M., Lambrechts, D.,…Bergers, G. (2022). Cancer immunotherapies transition endothelial cells into HEVs that generate TCF1+ T lymphocyte niches through a feed-forward loop. *Cancer Cell*, *40*(12), 1600–1618.e1610. https://doi.org/10.1016/j.ccell.2022.11.002

Ikarashi, D., Okimoto, T., Shukuya, T., Onagi, H., Hayashi, T., Sinicropi-Yao, S. L., Amann, J. M., Nakatsura, T., Kitano, S., & Carbone, D. P. (2021). Comparison of Tumor Microenvironments Between Primary Tumors and Brain Metastases in Patients With NSCLC. *JTO Clin Res Rep*, *2*(10), 100230. https://doi.org/10.1016/j.jtocrr.2021.100230

Jakel, S., & Dimou, L. (2017). Glial Cells and Their Function in the Adult Brain: A Journey through the History of Their Ablation. *Front Cell Neurosci*, *11*, 24. https://doi.org/10.3389/fncel.2017.00024

Jansen, C. S., Prokhnevska, N., Master, V. A., Sanda, M. G., Carlisle, J. W., Bilen, M. A., Cardenas, M., Wilkinson, S., Lake, R., Sowalsky, A. G., Valanparambil, R. M., Hudson, W. H., McGuire, D., Melnick, K., Khan, A. I., Kim, K., Chang, Y. M., Kim, A., Filson, C. P.,…Kissick, H. (2019). An intra-tumoral niche maintains and differentiates stem-like CD8 T cells. *Nature*, *576*(7787), 465–470. https://doi.org/10.1038/s41586-019-1836-5

Jassowicz, L., Feng, F., Warta, R., Heinicke, F., Wöllner, A., Briesch, H., Sor, F., Soller, J., Lotsch, C., Wong, J. K. L., Park, C., Aubert, N., Scheer, M., Hu, Z., Knoll, M., Schlegel, J., Frank, L., Trong, P. D., Jungwirth, G.,Herold-Mende, C. (2026, in press). Dissecting the cellular architecture of breast cancer brain metastases reveals prognostically distinct immune landscapes. *Cancer Cell*.

Ji, Y., Zhang, Y., Liu, S., Li, J., Jin, Q., Wu, J., Duan, H., Liu, X., Yang, L., & Huang, Y. (2025). The epidemiological landscape of lung cancer: current status, temporal trend and future projections based on the latest estimates from GLOBOCAN 2022. *J Natl Cancer Cent*, *5*(3), 278–286. https://doi.org/10.1016/j.jncc.2025.01.003

Jin, Y., Kang, Y., Wang, M., Wu, B., Su, B., Yin, H., Tang, Y., Li, Q., Wei, W., Mei, Q., Hu, G., Lukacs-Kornek, V., Li, J., Wu, K., Yuan, X., & Wang, W. (2022). Targeting polarized phenotype of microglia via IL6/JAK2/STAT3 signaling to reduce NSCLC brain metastasis. *Signal Transduct Target Ther*, *7*(1), 52. https://doi.org/10.1038/s41392-022-00872-9

Karimi, E., Yu, M. W., Maritan, S. M., Perus, L. J. M., Rezanejad, M., Sorin, M., Dankner, M., Fallah, P., Dore, S., Zuo, D., Fiset, B., Kloosterman, D. J., Ramsay, L., Wei, Y., Lam, S., Alsajjan, R., Watson, I. R., Roldan Urgoiti, G., Park, M.,…Walsh, L. A. (2023). Single-cell spatial immune landscapes of primary and metastatic brain tumours. *Nature*, *614*(7948), 555–563. https://doi.org/10.1038/s41586-022-05680-3

Kavaliauskaitė, J., Kazlauskaitė, A., Lazutka, J. R., Mozolevskis, G., & Stirkė, A. (2021). Pulsed Electric Fields Alter Expression of NF-κB Promoter-Controlled Gene. *Int J Mol Sci*, *23*(1). https://doi.org/10.3390/ijms23010451

Klemm, F., Maas, R. R., Bowman, R. L., Kornete, M., Soukup, K., Nassiri, S., Brouland, J. P., Iacobuzio-Donahue, C. A., Brennan, C., Tabar, V., Gutin, P. H., Daniel, R. T., Hegi, M. E., & Joyce, J. A. (2020). Interrogation of the Microenvironmental Landscape in Brain Tumors Reveals Disease-Specific Alterations of Immune Cells. *Cell*, *181*(7), 1643–1660 e1617. https://doi.org/10.1016/j.cell.2020.05.007

Kroeger, D. R., Milne, K., & Nelson, B. H. (2016a). Tumor-Infiltrating Plasma Cells Are Associated with Tertiary Lymphoid Structures, Cytolytic T-Cell Responses, and Superior Prognosis in Ovarian Cancer. *Clin Cancer Res*, *22*(12), 3005–3015. https://doi.org/10.1158/1078-0432.CCR-15-2762

Kroeger, D. R., Milne, K., & Nelson, B. H. (2016b). Tumor-Infiltrating Plasma Cells Are Associated with Tertiary Lymphoid Structures, Cytolytic T-Cell Responses, and Superior Prognosis in Ovarian Cancer. *Clinical Cancer Research*, *22*(12), 3005–3015. https://doi.org/10.1158/1078-0432.ccr-15-2762

Kudo, Y., Haymaker, C., Zhang, J., Reuben, A., Duose, D. Y., Fujimoto, J., Roy-Chowdhuri, S., Solis Soto, L. M., Dejima, H., Parra, E. R., Mino, B., Abraham, R., Ikeda, N., Vaporcyan, A., Gibbons, D., Zhang, J., Lang, F. F., Luthra, R., Lee, J. J.,…Wistuba, II. (2019). Suppressed immune microenvironment and repertoire in brain metastases from patients with resected non-small-cell lung cancer. *Ann Oncol*, *30*(9), 1521–1530. https://doi.org/10.1093/annonc/mdz207

Laaker, C., Baenen, C., Kovacs, K. G., Sandor, M., & Fabry, Z. (2023). Immune cells as messengers from the CNS to the periphery: the role of the meningeal lymphatic system in immune cell migration from the CNS. *Front Immunol*, *14*, 1233908. https://doi.org/10.3389/fimmu.2023.1233908

Layng, S. C., Betsock, A., Mansouri, A., Komiya, T., Miccio, J. A., Mahase, S. S., & Knisely, J. P. S. (2025). Brain metastases from lung cancer: recent advances and novel therapeutic opportunities. *Discov Oncol*, *16*(1), 157. https://doi.org/10.1007/s12672-025-01873-0

Lei, X., de Groot, D. C., Welters, M. J. P., de Wit, T., Schrama, E., van Eenennaam, H., Santegoets, S. J., Oosenbrug, T., van der Veen, A., Vos, J. L., Zuur, C. L., de Miranda, N., Jacobs, H., van der Burg, S. H., Borst, J., & Xiao, Y. (2024). CD4(+) T cells produce IFN-I to license cDC1s for induction of cytotoxic T-cell activity in human tumors. *Cell Mol Immunol*, *21*(4), 374–392. https://doi.org/10.1038/s41423-024-01133-1

Li, H., van der Leun, A. M., Yofe, I., Lubling, Y., Gelbard-Solodkin, D., van Akkooi, A. C. J., van den Braber, M., Rozeman, E. A., Haanen, J., Blank, C. U., Horlings, H. M., David, E., Baran, Y., Bercovich, A., Lifshitz, A., Schumacher, T. N., Tanay, A., & Amit, I. (2019). Dysfunctional CD8 T Cells Form a Proliferative, Dynamically Regulated Compartment within Human Melanoma. *Cell*, *176*(4), 775–789 e718. https://doi.org/10.1016/j.cell.2018.11.043

Li, J., Zhu, H., Sun, L., Xu, W., & Wang, X. (2019). Prognostic value of site-specific metastases in lung cancer: A population based study. *J Cancer*, *10*(14), 3079–3086. https://doi.org/10.7150/jca.30463

Liu, W., You, W., Lan, Z., Ren, Y., Gao, S., Li, S., Chen, W. W., Huang, C., Zeng, Y., Xiao, N., Wang, Z., Xie, H., Ma, H., Chen, Y., Wang, G., Chen, C., & Li, H. (2024). An immune cell map of human lung adenocarcinoma development reveals an anti-tumoral role of the Tfh-dependent tertiary lymphoid structure. *Cell Rep Med*, *5*(3), 101448. https://doi.org/10.1016/j.xcrm.2024.101448

Liu, Y., Xu, C., Zhang, L., Xu, G., Yang, Z., Xiang, L., Jiao, K., Chen, Z., Zhang, X., & Liu, Y. (2024). Syndecan-1 inhibition promotes antitumor immune response and facilitates the efficacy of anti-PD1 checkpoint immunotherapy. *Sci Adv*, *10*(37), eadi7764. https://doi.org/10.1126/sciadv.adi7764

Lockman, P. R., Mittapalli, R. K., Taskar, K. S., Rudraraju, V., Gril, B., Bohn, K. A., Adkins, C. E., Roberts, A., Thorsheim, H. R., Gaasch, J. A., Huang, S., Palmieri, D., Steeg, P. S., & Smith, Q. R. (2010). Heterogeneous blood-tumor barrier permeability determines drug efficacy in experimental brain metastases of breast cancer. *Clin Cancer Res*, *16*(23), 5664–5678. https://doi.org/10.1158/1078-0432.Ccr-10-1564

Loh, C. Y., Chai, J. Y., Tang, T. F., Wong, W. F., Sethi, G., Shanmugam, M. K., Chong, P. P., & Looi, C. Y. (2019). The E-Cadherin and N-Cadherin Switch in Epithelial-to-Mesenchymal Transition: Signaling, Therapeutic Implications, and Challenges. *Cells*, *8*(10). https://doi.org/10.3390/cells8101118

Lu, B. Y., Gupta, R., Aguirre-Ducler, A., Gianino, N., Wyatt, H., Ribeiro, M., Chiang, V. L., Contessa, J. N., Adeniran, A. J., Jilaveanu, L. B., Kluger, H. M., Schalper, K. A., & Goldberg, S. B. (2021). Spatially resolved analysis of the T cell immune contexture in lung cancer-associated brain metastases. *J Immunother Cancer*, *9*(10). https://doi.org/10.1136/jitc-2021-002684

Magen, A., Hamon, P., Fiaschi, N., Soong, B. Y., Park, M. D., Mattiuz, R., Humblin, E., Troncoso, L., D'Souza, D., Dawson, T., Kim, J., Hamel, S., Buckup, M., Chang, C., Tabachnikova, A., Schwartz, H., Malissen, N., Lavin, Y., Soares-Schanoski, A.,…Merad, M. (2023). Intratumoral dendritic cell–CD4+ T helper cell niches enable

CD8+ T cell differentiation following PD-1 blockade in hepatocellular carcinoma. *Nature Medicine*, *29*(6), 1389–1399. https://doi.org/10.1038/s41591-023-02345-0

Mansfield, A. S., Ren, H., Sutor, S., Sarangi, V., Nair, A., Davila, J., Elsbernd, L. R., Udell, J. B., Dronca, R. S., Park, S., Markovic, S. N., Sun, Z., Halling, K. C., Nevala, W. K., Aubry, M. C., Dong, H., & Jen, J. (2018). Contraction of T cell richness in lung cancer brain metastases. *Sci Rep*, *8*(1), 2171. https://doi.org/10.1038/s41598-018-20622-8

Martinez-Murillo, P., Pramanik, L., Sundling, C., Hultenby, K., Wretenberg, P., Spångberg, M., & Karlsson Hedestam, G. B. (2016). CD138 and CD31 Double-Positive Cells Comprise the Functional Antibody-Secreting Plasma Cell Compartment in Primate Bone Marrow. *Frontiers in Immunology*, *7*. https://doi.org/10.3389/fimmu.2016.00242

Mathiot, L., Nigen, B., Goronflot, T., Hiret, S., Doucet, L., Pons-Tostivint, E., Bennouna, J., Denis, M. G., Herbreteau, G., & Raimbourg, J. (2024). Prognostic Impact of TP53 Mutations in Metastatic Nonsquamous Non–small-cell Lung Cancer. *Clinical Lung Cancer*, *25*(3), 244–253.e242. https://doi.org/10.1016/j.cllc.2023.12.004

Matusiak, M., Hickey, J. W., van, I. D. G. P., Lu, G., Kidzinski, L., Zhu, S., Colburg, D. R. C., Luca, B., Phillips, D. J., Brubaker, S. W., Charville, G. W., Shen, J., Loh, K. M., Okwan-Duodu, D. K., Nolan, G. P., Newman, A. M., West, R. B., & van de Rijn, M. (2024). Spatially Segregated Macrophage Populations Predict Distinct Outcomes in Colon Cancer. *Cancer Discov*, *14*(8), 1418–1439. https://doi.org/10.1158/2159-8290.CD-23-1300

McLane, L. M., Abdel-Hakeem, M. S., & Wherry, E. J. (2019). CD8 T Cell Exhaustion During Chronic Viral Infection and Cancer. *Annu Rev Immunol*, *37*, 457–495. https://doi.org/10.1146/annurev-immunol-041015-055318

Mellman, I., Chen, D. S., Powles, T., & Turley, S. J. (2023). The cancer-immunity cycle: Indication, genotype, and immunotype. *Immunity*, *56*(10), 2188–2205. https://doi.org/10.1016/j.immuni.2023.09.011

Meng, Z., Rodriguez Ehrenfried, A., Tan, C. L., Steffens, L. K., Kehm, H., Zens, S., Lauenstein, C., Paul, A., Schwab, M., Förster, J. D., Salek, M., Riemer, A. B., Wu, H., Eckert, C., Leonhardt, C.-S., Strobel, O., Volkmar, M., Poschke, I., & Offringa, R. (2023). Transcriptome-based identification of tumor-reactive and bystander CD8 ⁺ T cell receptor clonotypes in human pancreatic cancer. *Science Translational Medicine*, *15*(722). https://doi.org/10.1126/scitranslmed.adh9562

Meylan, M., Petitprez, F., Becht, E., Bougoüin, A., Pupier, G., Calvez, A., Giglioli, I., Verkarre, V., Lacroix, G., Verneau, J., Sun, C.-M., Laurent-Puig, P., Vano, Y.-A., Elaïdi, R., Méjean, A., Sanchez-Salas, R., Barret, E., Cathelineau, X., Oudard, S.,Fridman, W. H. (2022). Tertiary lymphoid structures generate and propagate anti-tumor antibody-producing plasma cells in renal cell cancer. *Immunity*, *55*(3), 527–541.e525. https://doi.org/10.1016/j.immuni.2022.02.001

Miller, B. C., Sen, D. R., Al Abosy, R., Bi, K., Virkud, Y. V., LaFleur, M. W., Yates, K. B., Lako, A., Felt, K., Naik, G. S., Manos, M., Gjini, E., Kuchroo, J. R., Ishizuka, J. J., Collier, J. L., Griffin, G. K., Maleri, S., Comstock, D. E., Weiss, S. A.,…Haining, W. N. (2019). Subsets of exhausted CD8(+) T cells differentially mediate tumor control and respond to checkpoint blockade. *Nat Immunol*, *20*(3), 326–336. https://doi.org/10.1038/s41590-019-0312-6

Mogi, A., & Kuwano, H. (2011). TP53 Mutations in Nonsmall Cell Lung Cancer. *BioMed Research International*, *2011*(1), 1–9. https://doi.org/10.1155/2011/583929

Müller, T. R., Schuler, C., Hammel, M., Köhler, A., Jutz, S., Leitner, J., Schober, K., Busch, D. H., & Steinberger, P. (2020). A T-cell reporter platform for high-throughput and reliable investigation of TCR function and biology. *Clinical & Translational Immunology*, *9*(11). https://doi.org/10.1002/cti2.1216

Muslimov, A., Tereshchenko, V., Shevyrev, D., Rogova, A., Lepik, K., Reshetnikov, V., & Ivanov, R. (2023). The Dual Role of the Innate Immune System in the Effectiveness of mRNA Therapeutics. *Int J Mol Sci*, *24*(19). https://doi.org/10.3390/ijms241914820

Myall, N. J., Yu, H., Soltys, S. G., Wakelee, H. A., & Pollom, E. (2021). Management of brain metastases in lung cancer: evolving roles for radiation and systemic treatment in the era of targeted and immune therapies. *Neurooncol Adv*, *3*(Suppl 5), v52–v62. https://doi.org/10.1093/noajnl/vdab106

Nadal, E., Rodriguez-Abreu, D., Simo, M., Massuti, B., Juan, O., Huidobro, G., Lopez, R., De Castro, J., Estival, A., Mosquera, J., Sullivan, I., Felip, E., Blasco, A., Guirado, M., Pereira, E., Vilarino, N., Navarro, V., & Bruna, J. (2023). Phase II Trial of Atezolizumab Combined With Carboplatin and Pemetrexed for Patients With Advanced Nonsquamous Non-Small-Cell Lung Cancer With Untreated Brain Metastases (Atezo-Brain, GECP17/05). *J Clin Oncol*, *41*(28), 4478–4485. https://doi.org/10.1200/JCO.22.02561

Naghavian, R., Faigle, W., Oldrati, P., Wang, J., Toussaint, N. C., Qiu, Y., Medici, G., Wacker, M., Freudenmann, L. K., Bonté, P.-E., Weller, M., Regli, L., Amigorena, S., Rammensee, H.-G., Walz, J. S., Brugger, S. D., Mohme, M., Zhao, Y., Sospedra, M.,…Martin, R. (2023). Microbial peptides activate tumour-infiltrating lymphocytes in glioblastoma. *Nature*, *617*(7962), 807–817. https://doi.org/10.1038/s41586-023-06081-w

Nakayama, M., Akiba, H., Takeda, K., Kojima, Y., Hashiguchi, M., Azuma, M., Yagita, H., & Okumura, K. (2009). Tim-3 mediates phagocytosis of apoptotic cells and cross-presentation. *Blood*, *113*(16), 3821–3830. https://doi.org/10.1182/blood-2008-10-185884

Nicholson, A. G., Tsao, M. S., Beasley, M. B., Borczuk, A. C., Brambilla, E., Cooper, W. A., Dacic, S., Jain, D., Kerr, K. M., Lantuejoul, S., Noguchi, M., Papotti, M., Rekhtman, N., Scagliotti, G., van Schil, P., Sholl, L., Yatabe, Y., Yoshida, A., & Travis, W. D. (2022). The 2021 WHO Classification of Lung Tumors: Impact of Advances Since 2015. *J Thorac Oncol*, *17*(3), 362–387. https://doi.org/10.1016/j.jtho.2021.11.003

Nohira, S., Kuramitsu, S., Ohno, M., Fujita, M., Yamashita, K., Nagasaka, T., Haimoto, S., Sakakura, N., Matsushita, H., & Saito, R. (2024). Tertiary Lymphoid Structures in Brain Metastases of Lung Cancer: Prognostic Significance and Correlation With Clinical Outcomes. *Anticancer Res*, *44*(8), 3615–3621. https://doi.org/10.21873/anticanres.17184

Oliveira, G., Stromhaug, K., Klaeger, S., Kula, T., Frederick, D. T., Le, P. M., Forman, J., Huang, T., Li, S., Zhang, W., Xu, Q., Cieri, N., Clauser, K. R., Shukla, S. A., Neuberg, D., Justesen, S., Macbeath, G., Carr, S. A., Fritsch, E. F.,…Wu, C. J. (2021). Phenotype, specificity and avidity of antitumour CD8+ T cells in melanoma. *Nature*, *596*(7870), 119–125. https://doi.org/10.1038/s41586-021-03704-y

Paget, S. (1889). THE DISTRIBUTION OF SECONDARY GROWTHS IN CANCER OF THE BREAST. *The Lancet*, *133*. https://doi.org/10.1016/S0140-6736(00)49915-0

Pakkala, S., & Ramalingam, S. S. (2018). Personalized therapy for lung cancer: striking a moving target. *JCI Insight*, *3*(15). https://doi.org/10.1172/jci.insight.120858

Park, J., & Skalhegg, B. S. (2025). Combination of PD-1/PD-L1 and CTLA-4 inhibitors in the treatment of cancer - a brief update. *Front Immunol*, *16*, 1680838. https://doi.org/10.3389/fimmu.2025.1680838

Park, S. L., Gebhardt, T., & Mackay, L. K. (2019). Tissue-Resident Memory T Cells in Cancer Immunosurveillance. *Trends Immunol*, *40*(8), 735–747. https://doi.org/10.1016/j.it.2019.06.002

Peters, S., Paz-Ares, L. G., Reck, M., Carbone, D. P., Brahmer, J. R., Borghaei, H., Lu, S., O'Byrne, K. J., John, T., Ciuleanu, T. E., Schenker, M., Bernabe Caro, R., Nishio, M., Cobo, M., Lee, J. S., Zurawski, B., Pluzanski, A., Aoyama, T., Tschaika, M.,…Ramalingam, S. S. (2025). Long-Term Survival Outcomes With First-Line Nivolumab Plus Ipilimumab-Based Treatment in Patients With Metastatic NSCLC and Tumor Programmed Death-Ligand 1 Lower Than 1%: A Pooled Analysis. *J Thorac Oncol*, *20*(1), 94–108. https://doi.org/10.1016/j.jtho.2024.09.1439

Pocha, K., Mock, A., Rapp, C., Dettling, S., Warta, R., Geisenberger, C., Jungk, C., Martins, L. R., Grabe, N., Reuss, D., Debus, J., von Deimling, A., Abdollahi, A., Unterberg, A., & Herold-Mende, C. C. (2020). Surfactant Expression Defines an Inflamed Subtype of Lung Adenocarcinoma Brain Metastases that Correlates with Prolonged Survival. *Clin Cancer Res*, *26*(9), 2231–2243. https://doi.org/10.1158/1078-0432.CCR-19-2184

Puri, K. D., Finger, E. B., Gaudernack, G., & Springer, T. A. (1995). Sialomucin CD34 is the major L-selectin ligand in human tonsil high endothelial venules. *Journal of Cell Biology*, *131*(1), 261–270. https://doi.org/10.1083/jcb.131.1.261

Ramakrishna, R., & Rostomily, R. (2013). Seed, soil, and beyond: The basic biology of brain metastasis. *Surg Neurol Int*, *4*(Suppl 4), S256–264. https://doi.org/10.4103/2152-7806.111303

Recondo, G., Facchinetti, F., Olaussen, K. A., Besse, B., & Friboulet, L. (2018). Making the first move in EGFR-driven or ALK-driven NSCLC: first-generation or next-generation TKI? *Nature Reviews Clinical Oncology*, *15*(11), 694–708. https://doi.org/10.1038/s41571-018-0081-4

Recondo, G., Facchinetti, F., Olaussen, K. A., Besse, B., & Friboulet, L. (2018). Making the first move in EGFR-driven or ALK-driven NSCLC: first-generation or next-generation TKI? *Nat Rev Clin Oncol*, *15*(11), 694–708. https://doi.org/10.1038/s41571-018-0081-4

Ren, Z., Spaargaren, M., & Pals, S. T. (2021). Syndecan-1 and stromal heparan sulfate proteoglycans: key moderators of plasma cell biology and myeloma pathogenesis. *Blood*, *137*(13), 1713–1718. https://doi.org/10.1182/blood.2020008188

Rossjohn, J., Gras, S., Miles, J. J., Turner, S. J., Godfrey, D. I., & McCluskey, J. (2015). T cell antigen receptor recognition of antigen-presenting molecules. *Annu Rev Immunol*, *33*, 169–200. https://doi.org/10.1146/annurev-immunol-032414-112334

Roth, D. B. (2014). V(D)J Recombination: Mechanism, Errors, and Fidelity. *Microbiol Spectr*, *2*(6). https://doi.org/10.1128/microbiolspec.MDNA3-0041-2014

Rudolph, M. G., Stanfield, R. L., & Wilson, I. A. (2006). How TCRs bind MHCs, peptides, and coreceptors. *Annu Rev Immunol*, *24*, 419–466. https://doi.org/10.1146/annurev.immunol.23.021704.115658

Sabnis, R. W. (2023). Novel IL4I1 Inhibitors for Treating Cancer. *ACS Medicinal Chemistry Letters*, *14*(6), 700–701. https://doi.org/10.1021/acsmedchemlett.3c00180

Sadik, A., Somarribas Patterson, L. F., Ozturk, S., Mohapatra, S. R., Panitz, V., Secker, P. F., Pfander, P., Loth, S., Salem, H., Prentzell, M. T., Berdel, B., Iskar, M., Faessler, E., Reuter, F., Kirst, I., Kalter, V., Foerster, K. I., Jager, E., Guevara, C. R.,…Opitz,

C. A. (2020). IL4I1 Is a Metabolic Immune Checkpoint that Activates the AHR and Promotes Tumor Progression. *Cell*, *182*(5), 1252–1270 e1234. https://doi.org/10.1016/j.cell.2020.07.038

Sanromán, Á. F., Joshi, K., Au, L., Chain, B., & Turajlic, S. (2023). TCR sequencing: applications in immuno-oncology research. *Immuno-Oncology and Technology*, *17*, 100373. https://doi.org/10.1016/j.iotech.2023.100373

Sayyad, M. R., Puchalapalli, M., Vergara, N. G., Wangensteen, S. M., Moore, M., Mu, L., Edwards, C., Anderson, A., Kall, S., Sullivan, M., Dozmorov, M., Singh, J., Idowu, M. O., & Koblinski, J. E. (2019). Syndecan-1 facilitates breast cancer metastasis to the brain. *Breast Cancer Res Treat*, *178*(1), 35–49. https://doi.org/10.1007/s10549-019-05347-0

Scanlan, M. J., Gure, A. O., Jungbluth, A. A., Old, L. J., & Chen, Y. T. (2002). Cancer/testis antigens: an expanding family of targets for cancer immunotherapy. *Immunol Rev*, *188*, 22–32. https://doi.org/10.1034/j.1600-065x.2002.18803.x

Schenkel, J. M., & Masopust, D. (2014). Tissue-resident memory T cells. *Immunity*, *41*(6), 886–897. https://doi.org/10.1016/j.immuni.2014.12.007

Schniederjohann, C., Bruch, P. M., Dietrich, S., & Neumann, F. (2025). Multiplexed Immunophenotyping of Lymphoma Tissue Samples. *Methods Mol Biol*, *2865*, 375–393. https://doi.org/10.1007/978-1-0716-4188-0_16

Schwartz, R. H. (2003). T cell anergy. *Annu Rev Immunol*, *21*, 305–334. https://doi.org/10.1146/annurev.immunol.21.120601.141110

Sha, D., Jin, Z., Budczies, J., Kluck, K., Stenzinger, A., & Sinicrope, F. A. (2020). Tumor Mutational Burden as a Predictive Biomarker in Solid Tumors. *Cancer Discov*, *10*(12), 1808–1825. https://doi.org/10.1158/2159-8290.CD-20-0522

Shah, K., Al-Haidari, A., Sun, J., & Kazi, J. U. (2021). T cell receptor (TCR) signaling in health and disease. *Signal Transduct Target Ther*, *6*(1), 412. https://doi.org/10.1038/s41392-021-00823-w

Shah, S., Al-Omari, A., Cook, K. W., Paston, S. J., Durrant, L. G., & Brentville, V. A. (2023). What do cancer-specific T cells 'see'? *Discov Immunol*, *2*(1), kyac011. https://doi.org/10.1093/discim/kyac011

Shankaran, V. (2001). IFNg and lymphocytes prevent primary tumour development and shape tumour immunogenicity. *Nature*, *410 (6832)*. https://doi.org/10.1038/35074122

Shorer, O., Pinhasi, A., & Yizhak, K. (2025). Single-cell meta-analysis of T cells reveals clonal dynamics of response to checkpoint immunotherapy. *Cell Genomics*, *5*(5), 100842. https://doi.org/10.1016/j.xgen.2025.100842

Sim, M. J. W., & Sun, P. D. (2022). T Cell Recognition of Tumor Neoantigens and Insights Into T Cell Immunotherapy. *Front Immunol*, *13*, 833017. https://doi.org/10.3389/fimmu.2022.833017

Simoni, Y., Becht, E., Fehlings, M., Loh, C. Y., Koo, S.-L., Teng, K. W. W., Yeong, J. P. S., Nahar, R., Zhang, T., Kared, H., Duan, K., Ang, N., Poidinger, M., Lee, Y. Y., Larbi, A., Khng, A. J., Tan, E., Fu, C., Mathew, R.,…Newell, E. W. (2018). Bystander CD8+ T cells are abundant and phenotypically distinct in human tumour infiltrates. *Nature*, *557*(7706), 575–579. https://doi.org/10.1038/s41586-018-0130-2

Smalley, I., Chen, Z., Phadke, M., Li, J., Yu, X., Wyatt, C., Evernden, B., Messina, J. L., Sarnaik, A., Sondak, V. K., Zhang, C., Law, V., Tran, N., Etame, A., Macaulay, R. J. B., Eroglu, Z., Forsyth, P. A., Rodriguez, P. C., Chen, Y. A., & Smalley, K. S. M. (2021). Single-Cell Characterization of the Immune Microenvironment of Melanoma

Brain and Leptomeningeal Metastases. *Clinical Cancer Research*, *27*(14), 4109–4125. https://doi.org/10.1158/1078-0432.ccr-21-1694

Smith-Garvin, J. E., Koretzky, G. A., & Jordan, M. S. (2009). T cell activation. *Annu Rev Immunol*, *27*, 591–619. https://doi.org/10.1146/annurev.immunol.021908.132706

Smolarz, B., Lukasiewicz, H., Samulak, D., Piekarska, E., Kolacinski, R., & Romanowicz, H. (2025). Lung Cancer-Epidemiology, Pathogenesis, Treatment and Molecular Aspect (Review of Literature). *Int J Mol Sci*, *26*(5). https://doi.org/10.3390/ijms26052049

Smyth, M. J. (2000). Perforin-mediated Cytotoxicity Is Critical for Surveillance of Spontaneous Lymphoma. *J Exp Med.*, *192 (2)*. https://doi.org/10.1084/jem.192.5.755

Souza, V. G. P., de Araujo, R. P., Santesso, M. R., Seneda, A. L., Minutentag, I. W., Felix, T. F., Hamamoto Filho, P. T., Pewarchuk, M. E., Brockley, L. J., Marchi, F. A., Lam, W. L., Drigo, S. A., & Reis, P. P. (2023). Advances in the Molecular Landscape of Lung Cancer Brain Metastasis. *Cancers (Basel)*, *15*(3). https://doi.org/10.3390/cancers15030722

Spits, H. (2002). Development of alphabeta T cells in the human thymus. *Nat Rev Immunol*, *2*(10), 760–772. https://doi.org/10.1038/nri913

Steindl, A., Brunner, T. J., Heimbach, K., Schweighart, K., Moser, G. M., Niziolek, H. M., Moor, E., Kreminger, J., Starzer, A. M., Dieckmann, K., Gatterbauer, B., Widhalm, G., Preusser, M., & Berghoff, A. S. (2022). Changing characteristics, treatment approaches and survival of patients with brain metastasis: data from six thousand and thirty-one individuals over an observation period of 30 years. *Eur J Cancer*, *162*, 170–181. https://doi.org/10.1016/j.ejca.2021.12.005

Street, S. E., Trapani, J. A., MacGregor, D., & Smyth, M. J. (2002). Suppression of lymphoma and epithelial malignancies effected by interferon gamma. *J Exp Med*, *196*(1), 129–134. https://doi.org/10.1084/jem.20020063

Sudmeier, L. J., Hoang, K. B., Nduom, E. K., Wieland, A., Neill, S. G., Schniederjan, M. J., Ramalingam, S. S., Olson, J. J., Ahmed, R., & Hudson, W. H. (2022). Distinct phenotypic states and spatial distribution of CD8+ T cell clonotypes in human brain metastases. *Cell Reports Medicine*, *3*(5), 100620. https://doi.org/10.1016/j.xcrm.2022.100620

Sun, L., Kienzler, J. C., Reynoso, J. G., Lee, A., Shiuan, E., Li, S., Kim, J., Ding, L., Monteleone, A. J., Owens, G. C., Phillips, J. J., Everson, R. G., Nathanson, D., Cloughesy, T. F., Li, G., Liau, L. M., Hugo, W., Kim, W., & Prins, R. M. (2023). Immune checkpoint blockade induces distinct alterations in the microenvironments of primary and metastatic brain tumors. *Journal of Clinical Investigation*, *133*(17). https://doi.org/10.1172/jci169314

Suzuki, J., Aokage, K., Neri, S., Sakai, T., Hashimoto, H., Su, Y., Yamazaki, S., Nakamura, H., Tane, K., Miyoshi, T., Sugano, M., Kojima, M., Fujii, S., Kuwata, T., Ochiai, A., Tsuboi, M., & Ishii, G. (2021). Relationship between podoplanin-expressing cancer-associated fibroblasts and the immune microenvironment of early lung squamous cell carcinoma. *Lung Cancer*, *153*, 1–10. https://doi.org/10.1016/j.lungcan.2020.12.020

Tan, C. L., Lindner, K., Boschert, T., Meng, Z., Rodriguez Ehrenfried, A., De Roia, A., Haltenhof, G., Faenza, A., Imperatore, F., Bunse, L., Lindner, J. M., Harbottle, R. P., Ratliff, M., Offringa, R., Poschke, I., Platten, M., & Green, E. W. (2025). Prediction of tumor-reactive T cell receptors from scRNA-seq data for personalized T cell

therapy. *Nature Biotechnology*, *43*(1), 134–142. https://doi.org/10.1038/s41587-024-02161-y

Tanno, H., Gould, T. M., McDaniel, J. R., Cao, W., Tanno, Y., Durrett, R. E., Park, D., Cate, S. J., Hildebrand, W. H., Dekker, C. L., Tian, L., Weyand, C. M., Georgiou, G., & Goronzy, J. J. (2020). Determinants governing T cell receptor α/β-chain pairing in repertoire formation of identical twins. *Proceedings of the National Academy of Sciences*, *117*(1), 532–540. https://doi.org/10.1073/pnas.1915008117

Thandra, K. C., Barsouk, A., Saginala, K., Aluru, J. S., & Barsouk, A. (2021). Epidemiology of lung cancer. *Contemp Oncol (Pozn)*, *25*(1), 45–52. https://doi.org/10.5114/wo.2021.103829

Tiberti, S., Catozzi, C., Croci, O., Ballerini, M., Cagnina, D., Soriani, C., Scirgolea, C., Gong, Z., He, J., Macandog, A. D., Nabinejad, A., Nava Lauson, C. B., Quinte', A., Bertalot, G., Petz, W. L., Ravenda, S. P., Licursi, V., Paci, P., Rasponi, M.,…Manzo, T. (2022). GZMKhigh CD8+ T effector memory cells are associated with CD15high neutrophil abundance in non-metastatic colorectal tumors and predict poor clinical outcome. *Nature Communications*, *13*(1). https://doi.org/10.1038/s41467-022-34467-3

Torcellan, T., Hampton, H. R., Bailey, J., Tomura, M., Brink, R., & Chtanova, T. (2017). In vivo photolabeling of tumor-infiltrating cells reveals highly regulated egress of T-cell subsets from tumors. *Proceedings of the National Academy of Sciences*, *114*(22), 5677–5682. https://doi.org/10.1073/pnas.1618446114

Tsui, C., Kretschmer, L., Rapelius, S., Gabriel, S. S., Chisanga, D., Knopper, K., Utzschneider, D. T., Nussing, S., Liao, Y., Mason, T., Torres, S. V., Wilcox, S. A., Kanev, K., Jarosch, S., Leube, J., Nutt, S. L., Zehn, D., Parish, I. A., Kastenmuller, W.,…Kallies, A. (2022). MYB orchestrates T cell exhaustion and response to checkpoint inhibition. *Nature*, *609*(7926), 354–360. https://doi.org/10.1038/s41586-022-05105-1

Valiente, M., Ahluwalia, M. S., Boire, A., Brastianos, P. K., Goldberg, S. B., Lee, E. Q., Le Rhun, E., Preusser, M., Winkler, F., & Soffietti, R. (2018). The Evolving Landscape of Brain Metastasis. *Trends Cancer*, *4*(3), 176–196. https://doi.org/10.1016/j.trecan.2018.01.003

Valiente, M., Anders, C., Boire, A., Izar, B., Kotecki, N., Malladi, S., Massague, J., Moss, N. S., Neman, J., Preusser, M., Schagen, S., Siegel, P. M., Tawbi, H., Venkataramani, V., Winkler, F., Zadeh, G., & Joyce, J. A. (2025). The evolving landscape of brain metastasis: volume II. *Trends Cancer*. https://doi.org/10.1016/j.trecan.2025.11.007

Vardhana, S. A., Hwee, M. A., Berisa, M., Wells, D. K., Yost, K. E., King, B., Smith, M., Herrera, P. S., Chang, H. Y., Satpathy, A. T., van den Brink, M. R. M., Cross, J. R., & Thompson, C. B. (2020). Impaired mitochondrial oxidative phosphorylation limits the self-renewal of T cells exposed to persistent antigen. *Nat Immunol*, *21*(9), 1022–1033. https://doi.org/10.1038/s41590-020-0725-2

Vella, G., Guelfi, S., & Bergers, G. (2021). High Endothelial Venules: A Vascular Perspective on Tertiary Lymphoid Structures in Cancer. *Frontiers in Immunology*, *12*. https://doi.org/10.3389/fimmu.2021.736670

Weeden, C. E., Gayevskiy, V., Marceaux, C., Batey, D., Tan, T., Yokote, K., Ribera, N. T., Clatch, A., Christo, S., Teh, C. E., Mitchell, A. J., Trussart, M., Rankin, L., Obers, A., McDonald, J. A., Sutherland, K. D., Sharma, V. J., Starkey, G., D'Costa, R.,…Asselin-Labat, M. L. (2023). Early immune pressure initiated by tissue-resident memory T cells sculpts tumor evolution in non-small cell lung cancer. *Cancer Cell*, *41*(5), 837–852 e836. https://doi.org/10.1016/j.ccell.2023.03.019

Weiss, A., & Stobo, J. (1984). REQUIREMENT FOR THE COEXPRESSION OF T3 AND THE T CELL ANTIGEN RECEPTOR ON A MALIGNANT HUMAN T CELL LINE. *J. Exp. Med.*, *160*. https://doi.org/10.1084/jem.160.5.1284

Wherry, E. J., & Kurachi, M. (2015). Molecular and cellular insights into T cell exhaustion. *Nat Rev Immunol*, *15*(8), 486–499. https://doi.org/10.1038/nri3862

Widodo, S. S., Dinevska, M., Cuzcano, L., Papanicolaou, M., Cox, T. R., Stylli, S. S., & Mantamadiotis, T. (2023). Spatial analysis of the metastatic brain tumor immune and extracellular matrix microenvironment. *Advances in Cancer Biology - Metastasis*, *7*, 100096. https://doi.org/10.1016/j.adcanc.2023.100096

Wischnewski, V., Maas, R. R., Aruffo, P. G., Soukup, K., Galletti, G., Kornete, M., Galland, S., Fournier, N., Lilja, J., Wirapati, P., Lourenco, J., Scarpa, A., Daniel, R. T., Hottinger, A. F., Brouland, J. P., Losurdo, A., Voulaz, E., Alloisio, M., Hegi, M. E.,…Joyce, J. A. (2023). Phenotypic diversity of T cells in human primary and metastatic brain tumors revealed by multiomic interrogation. *Nat Cancer*, *4*(6), 908–924. https://doi.org/10.1038/s43018-023-00566-3

Xie, T., Qiu, B. M., Luo, J., Diao, Y. F., Hu, L. W., Liu, X. L., & Shen, Y. (2024). Distant metastasis patterns among lung cancer subtypes and impact of primary tumor resection on survival in metastatic lung cancer using SEER database. *Sci Rep*, *14*(1), 22445. https://doi.org/10.1038/s41598-024-73389-6

Yang, Z., Chen, S., Ying, H., & Yao, W. (2022). Targeting syndecan-1: new opportunities in cancer therapy. *American Journal of Physiology-Cell Physiology*, *323*(1), C29–C45. https://doi.org/10.1152/ajpcell.00024.2022

Yang, Z., Theardy, M. S., Chen, S., Wei, Y., Takeda, M., Zeng, Y., Wang, X., Yao, J., Li, J., Thirasastr, P., Park, J., Zheng, Y., Vien, L. T., Wani, K. M., Wang, H., Gao, S., Heffernan, T., Kwong, L., Wistuba, I. I.,…Yao, W. (2026). Syndecan-1-targeted therapeutic antibody impairs macropinocytosis and elicits antitumor immunity in pancreatic cancer. *Cell Reports Medicine*, *7*(2), 102613. https://doi.org/10.1016/j.xcrm.2026.102613

Yuan, C., & Zheng, H. (2024). Brain metastases in newly diagnosed lung cancer: epidemiology and conditional survival. *Transl Cancer Res*, *13*(10), 5417–5428. https://doi.org/10.21037/tcr-24-776

Zebley, C. C., & Youngblood, B. (2022). Mechanisms of T cell exhaustion guiding next-generation immunotherapy. *Trends Cancer*, *8*(9), 726–734. https://doi.org/10.1016/j.trecan.2022.04.004

Zhao, H., Wang, H., Zhao, Y., Sun, Q., & Ren, X. (2022). Tumor-Resident T Cells, Associated With Tertiary Lymphoid Structure Maturity, Improve Survival in Patients With Stage III Lung Adenocarcinoma. *Front Immunol*, *13*, 877689. https://doi.org/10.3389/fimmu.2022.877689

Zhu, W., Germain, C., Liu, Z., Sebastian, Y., Devi, P., Knockaert, S., Brohawn, P., Lehmann, K., Damotte, D., Validire, P., Yao, Y., Valge-Archer, V., Hammond, S. A., Dieu-Nosjean, M. C., & Higgs, B. W. (2015). A high density of tertiary lymphoid structure B cells in lung tumors is associated with increased CD4(+) T cell receptor repertoire clonality. *Oncoimmunology*, *4*(12), e1051922. https://doi.org/10.1080/2162402X.2015.1051922

Ziv, Y., Ron, N., Butovsky, O., Landa, G., Sudai, E., Greenberg, N., Cohen, H., Kipnis, J., & Schwartz, M. (2006). Immune cells contribute to the maintenance of neurogenesis and spatial learning abilities in adulthood. *Nat Neurosci*, *9*(2), 268–275. https://doi.org/10.1038/nn1629

10. Acknowledgements

This thesis would not have reached its final form without the support and contributions of many people, to whom I would like to express my sincere gratitude.

I am deeply grateful to PD Dr. Martina Seiffert for her supervision throughout my PhD. Her continuous support, and constructive perspective were essential, particularly during the more demanding phases of this work. I greatly valued her openness, her trust in my ideas, and the motivating and supportive environment she fostered.

I would also like to thank Prof. Dr. Peter Lichter for giving me the opportunity to pursue my PhD in his division. I am grateful for his openness in sharing his scientific insight and for offering advice on both research and career-related matters.

I am especially thankful to Dr. Marc Zapatka for his key contribution to the bioinformatic analyses. His readiness to invest additional time when it mattered most, together with his patience and dedication, had a decisive impact on this project. I greatly appreciated both his expertise and his collaborative mindset.

I thank the members of my Thesis Advisory Committee — Prof. Dr. Peter Angel, Prof. Dr. Peter Lichter, Prof. Dr. Christel Herold-Mende, and Dr. Chong Sun — for their valuable feedback and insightful discussions throughout my PhD. I am also grateful to Prof. Dr. Peter Angel, Prof. Dr. Peter Lichter, Prof. Dr. Benedikt Brors, and Prof. Dr. Nina Papavasiliou for serving on my examination committee and for their time and consideration in evaluating this thesis.

This work relied on the generous support of numerous collaborators. I am particularly grateful to Prof. Dr. Christel Herold-Mende and Dr. Dr. Lena Jassowicz for providing the single-cell patient samples and for sharing their expertise. I also thank PD Dr. Marc Schneider and Guddi Sharma for supplying the tissue samples that formed a central component of this study. Above all, I would like to acknowledge the patients and their families, whose willingness to contribute to research made this work possible.

I further benefited from the scientific exchange within the ImmuMet consortium and thank all its members for stimulating discussions and valuable input. I am particularly grateful to Dr. Fangyoumin Feng for initiating the scRNA-seq analysis with me and for always being willing to take some time to discuss ideas and offer support. I also thank Dr. Fatima Heinicke for her scientific curiosity and positive mindset, particularly when discussing my project and future career perspectives.

Many colleagues contributed essential experimental and technical expertise. I thank Christina Schniederjohann for performing tissue staining and imaging, and Verena Kalter for her support with FACS sorting. I am grateful to Dr. Edward Green and his group for their assistance with TCR cloning, and a special thanks to Felix Andres and Katharina von Werthern for their crucial role in establishing the functional assays. Their expertise and enthusiasm made this collaboration particularly rewarding. I also thank the group of Dr. Isabel Poschke for performing the bulk TCRβ sequencing.

I would like to acknowledge the excellent IT support provided by Michael Hain and Torben Wagner, whose assistance was indispensable. I am also grateful to Dr. Dr. Jan-Philipp Mallm and Denise Keitel from the ScOpenLab for their guidance in single-cell RNA sequencing, and to Dr. Angela Schulz and the High Throughput Sequencing Facility team at DKFZ for their reliable support.

I am very thankful to all current and former members of the group, especially Dr. Mariana Mendes Martins Coelho, Dr. Cèlia Dobaño López, Dr. Mathieu Virazels, Dr. Nicolas Aubert, Hannah Briesch, Alessia Flörchinger, Covadonga Castellanos González, Yuliia Borysovych, Carolin Brombach, Jan Schadendorf, and Dr. Rebecca Jones for their support, discussions, and for creating a welcoming and collaborative working atmosphere. Beyond science, I especially appreciated the shared breaks and conversations, which made this time both productive and enjoyable. I also thank the members of the B06x division for their contributions during seminars and retreats.

Outside the lab, I am grateful to my friends Michelle Kehr, Carolin Rother, Lilly Grünewald, Maximilian Rokuss, Leon Klimeck, Natalie Schoebe, and Cèlia Dobaño López for providing balance, encouragement, and many memorable moments throughout these years.

My deepest gratitude goes to my family. I thank my parents, Claudia and Klaus, for their unconditional support, constant encouragement, and strong belief in me at every stage of this journey. I am equally grateful to my brother Marvin and my grandparents Gerhard and Monika, whose support and confidence have always meant a great deal to me.

Finally, I would like to thank my partner Miquel Tibau Baltrons, who has accompanied me throughout this entire journey. I am deeply grateful to have been able to share both the rewarding and the challenging moments of this PhD with him. Thank you for always believing in me, for keeping me motivated and positive, and for knowing exactly when chocolate or a *Kaffee und Kuchen* break were needed to lift my spirits.